Max-Planck-Institut für Quantenoptik, Garching bei München
Physik-Department der Technischen Universität München
Fachbereich Physik der Philipps-Universität Marburg

Five-wave mixing investigation of electron dynamics at silicon surfaces

Carsten Voelkmann

Vollständiger Abdruck der von der Fakultät für Physik der Technischen Universität München zur Erlangung des akademischen Grades eines

Doktors der Naturwissenschaften

genehmigten Dissertation.

Vorsitzender:		Univ.-Prof. Dr. M. Kleber
Prüfer der Dissertation:	1.	Univ.-Prof. Dr. Dr. h.c. D. Menzel
	2.	Univ.-Prof. Dr. U. Höfer, Philipps-Universität Marburg

Die Dissertation wurde am 26.06.2001 bei der Technischen Universität München eingereicht und durch die Fakultät für Physik am 10.08.2001 angenommen.

Für meine Eltern
und
Imke

Summary

A surface-sensitive purely optical technique is demonstrated for the investigation of ultrafast relaxation processes of excited electronic surface states. We employed a synthesis of degenerate four-wave mixing (DFWM) and optical second-harmonic generation (SHG) to study the coherent and incoherent dynamics of dangling-bond states at silicon surfaces with femtosecond time-resolution. The resulting five-wave mixing process is characterized by a $\chi^{(4)}$-tensor; like the $\chi^{(2)}$-processes SHG or SFG it is dipole-forbidden in the bulk of centrosymmetric materials, like crystalline silicon. The surface-sensitive probe can be described by diffraction of photons at a transient population grating with their upconversion to the second harmonic.

The experiments were performed with a cavity-dumped Ti:sapphire laser that produced 14-fs pulses centered at a wavelength of 800 nm with pulse energies up to 50 nJ and repetition rates as high as 2 MHz. A comparison of the diffracted signal from clean and oxygen covered surfaces shows that under the experimental conditions electronic excitations in the metallic U_1/S_1-band of Si(111)7×7 and in the dangling bonds of Si(001) are responsible for the nonlinear response.

Two different excitation schemes were used: in a self-diffraction setup we worked with only two incident beams on the sample in ultrahigh vacuum by using one of the pump pulses simultaneously as a probe. A three-beam geometry yielded more information on the electronic relaxation behavior due to the two independently tunable time delays. With these two setups we were able to separate experimentally population relaxation (T_1) times on the order of 200 fs from dephasing (T_2) times around 10 fs. The T_1-times obtained with the coherent diffraction experiment are in excellent agreement with incoherent SHG pump–probe and time-resolved two-photon photoemission schemes.

For a qualitative physical understanding of the dynamical processes and the quantitative extraction of relaxation rates we employed a theoretical model based on the density-matrix formalism. An analytical treatment of the resulting differential equations for the induced polarizations and populations allowed the numerical simulation of the experimentally acquired data. The simulation made use of different phenomenological models: homogeneous broadening, inhomogeneous broadening, and continuum excitation.

Our experiments demonstrate that with the wide availability of high-intensity ultra-short laser pulses, this technique could thus become a valuable tool for the investigation of ultrafast dynamics at many surfaces and interfaces.

Zusammenfassung

Eine oberflächen-sensitive, rein optische Methode zur Untersuchung ultraschneller Relaxationsprozesse von angeregten elektronischen Oberflächenzuständen wird demonstriert. Wir verwendeten eine Synthese aus entarteter Vier-Wellen-Mischung (*degenerate four-wave mixing*, DFWM) und optischer Frequenzverdopplung (*second-harmonic generation*, SHG), um die kohärente und inkohärente Dynamik von *dangling bond*-Zuständen an Silizium-Oberflächen mit Femtosekunden-Zeitauflösung zu studieren. Der resultierende Fünf-Wellen-Mischprozess wird durch einen $\chi^{(4)}$-Tensor charakterisiert; genauso wie die $\chi^{(2)}$-Prozesse SHG und SFG ist dieser Vorgang dipol-verboten im Volumen zentrosymmetrischer Materialen, wie z. B. kristallinem Silizium. Der deshalb oberflächen-sensitive Prozess kann durch Beugung von Photonen an einem transienten Populationsgitter mit deren Hochkonversion zur Zweiten Harmonischen beschrieben werden.

Die Experimente wurden durchgeführt mit einem *cavity-dumped* Ti:Saphir-Laser, der 14-fs Pulse bei Wellenlängen um 800 nm mit Pulsenergien bis zu 50 nJ bei Repetitionsraten bis zu 2 MHz erzeugte. Ein Vergleich des gebeugten Signals von der sauberen und Sauerstoff-bedeckten Oberfläche zeigt, dass unter den experimentellen Bedingungen elektronische Anregungen im metallischen U_1/S_1-Band von Si(111)7×7 und in den *dangling bonds* von Si(001) für den nichtlinearen optischen Response verantwortlich sind.

Es wurden zwei unterschiedliche Anregungs-Geometrien benutzt: In einem Selbstbeugungs-Aufbau arbeiteten wir mit nur zwei auf die Probe im Ultrahochvakuum (UHV) einfallenden Strahlen, indem wir einen der beiden Anrege-Pulse simultan als Abfrage-Puls verwendeten. Eine Drei-Strahl-Geometrie lieferte noch mehr Informationen über das Relaxationsverhalten, auf Grund der zwei unabhängig voneinander durchstimmbaren Zeit-Verzögerungen. Mit diesen zwei Experimenten waren wir in der Lage, die Populations-Relaxationszeiten (T_1) um 200 fs von Dephasierungszeiten (T_2) der Größenordnung 10 fs experimentell zu separieren. Die T_1-Zeiten, die mit diesen kohärenten Beugungs-Techniken gemessen wurden, sind in sehr guter Übereinstimmung mit inkohärenten SHG Anrege–Abfrage-Experimenten und mit zeitaufgelöster Zwei-Photonen-Photoemission.

Um zu einem qualitativen physikalischem Verständnis der dynamischen Prozesse und zur quantitativen Bestimmung der Relaxations-Raten zu gelangen, verwendeten wir ein theoretisches Modell basierend auf einem Dichte-Matrix-Formalismus.

Eine analytische Behandlung der resultierenden Differenzial-Gleichungen für die induzierten Polarisationen und Populationen erlaubte die numerische Simulation der experimentell erhaltenen Daten. Der Simulation legten wir verschiedene phänomenologische Modelle zu Grunde: homogenes System, inhomogene Verbreiterung und Kontinuums-Anregung.

Unsere Experimente demonstrieren, dass mit der weiteren Verbreitung ultrakurzer Laser-Pulse hoher Intensität, diese Fünf-Wellen-Mischtechnik eine wertvolle Methode zur Untersuchung ultraschneller Dynamik an vielen Oberflächen und Grenzflächen werden kann.

Contents

Chapter 1

Introduction

One motivation for the study of carrier dynamics at surfaces is the desire for a physical understanding of the fundamental relaxation processes. In addition to the purely scientific perspective, these investigations are highly relevant for surface photochemistry, since the relaxation rate of photoexcited carriers can be a dominant factor for the yield of photochemical reactions at surfaces. A further field of application for the examination of surface carrier dynamics lies in the sector of semiconductor technology. For instance, accurate fundamental carrier scattering rates at surfaces are the prerequisite for a correct simulation of semiconductor devices.

Due to their generation of ultrashort light pulses, lasers represent a natural tool for time-resolved spectroscopy. In addition to their phenomenal time-resolution down to the femtosecond regime, lasers also provide an intense *coherent* source of radiation. In this case, the well-defined phase relationship between the wave functions of the states, that are coupled by the interaction with the light, can be exploited to gain additional, often complementary, information compared to methods that rely only on the measurement of intensities. Prominent examples in atomic, molecular, and condensed matter physics include coherent Raman scattering, quantum beat spectroscopy, as well as echo and induced grating experiments [1–3].

However, purely optical experiments are often more difficult to interpret than photoemission investigations. By analyzing the kinetic energy, the direction, and spin of the photoemitted electron, photoemission schemes can provide an integral characterization of the probed electronic states. Nevertheless, purely optical nonlinear methods, like second-harmonic generation (SHG), have several advantages compared to photoelectron techniques. Because of inversion symmetry breaking at surfaces of centrosymmetric media, SHG can provide a genuine surface signal. In addition, these methods are applicable at high excitation conditions, without being confronted with space-charge effects that destroy energy and momentum resolution in photoelectron experiments [4]. Due to their purely optical character, these methods can also be applied to interfaces between solid or liquid media, whereas photoemission is restricted to surfaces in UHV environments.

This thesis discusses a combination of SHG [5–7] with degenerate four-wave mixing (DFWM) for the acquisition of surface specific information about electron dynamics.

A transient population grating is generated at a surface by two ultrashort interfering laser pulses, giving rise to a spatial modulation of the nonlinear susceptibility $\chi_s^{(2)}$. A third synchronized pulse is diffracted from the transient grating, leading to second-harmonic light, which is detected. Since this five-wave mixing scheme is characterized by a $\chi^{(4)}$ tensor, it is intrinsically surface sensitive for centrosymmetric materials. Besides the precise determination of population relaxation times on the order of 200 fs, the technique also allowed to measure the timescale for the fundamental carrier scattering processes that occur immediately after the optical excitation and result in the loss of coherence between the electronic states coupled by the light pulse. This ultrafast coherent regime has been approached at surfaces only recently [8–11].

Among the few examples where coherence phenomena have been utilized for surface investigations is the pioneering study by Guyot-Sionnest, who employed infrared–visible sum-frequency up-conversion to follow the free-induction decay and photon echo of the H/Si(111) adsorbate–substrate stretching vibration in real time [12]. Remarkably, he succeeded in separating its genuine homogeneous dephasing time from inhomogeneous contributions [12]. Owrutsky *et al.* were able to observe the free-induction decay of vibrational excitations of CO on copper [13]. In another experiment, Chang, Xu, and Tom reported the coherent excitation and subsequent detection of surface optical phonons by time-resolved SHG [8]. An interferometric two-photon photoemission technique developed by Petek and coworkers allowed the investigation of hot electron dephasing on Cu(111) on a femtosecond timescale [9, 14]. In our own group, time-resolved two-photon photoemission in combination with the coherent excitation of several quantum states was employed by Höfer *et al.* to study the ultrafast electron dynamics of image-potential states on metal surfaces [10].

Following this introduction, the physical fundamentals of investigated systems and investigating methods are presented in Chap. 2. The discussion of fundamental structural and electronic properties of the silicon surfaces under examination – Si(111) and Si(001) – is an important prerequisite for the interpretation of their incoherent as well as coherent relaxation behavior. The understanding of the employed transient-grating technique is facilitated by the prior discussion of the underlying methods SHG and DFWM.

A description of the experimental setup used for the investigation is the topic of Chap. 3. After the presentation of the ultra-high vacuum system and the surface preparation procedures follows a characterization of the employed laser source with respect to parameters relevant to the study of relaxation dynamics. Important details of the optical setup are also described.

Following these experimental facts, the theoretical models for a qualitative description and quantitative simulation are presented and discussed in Chap. 4. Our five-wave mixing transient-grating experiments are treated within a semiclassical density-matrix formalism, which yields a system of differential equations for the induced polarizations and populations up to fourth order in terms of the incident electric fields. This presentation of the underlying theoretical framework is followed by a detailed discussion of its implications on the SH diffracted intensity.

The results of the discussion in Chap. 4 represent valuable information for the interpretation of the experimental data of the incoherent measurements, that are the subject of Chap. 5. After an in-depth treatment of the relevant excitation mechanism and a presentation of the population relaxation times obtained from SH pump–probe and SH three-beam diffraction schemes follows a comparative discussion with both experimental and theoretical results. Chap. 5 closes with an analysis of the microscopic relaxation mechanism.

Complementary information on the electronic relaxation behavior at the silicon surfaces investigated can be acquired through the examination of our coherent experiments in Chap. 6. By using the transient-grating approach in the two-beam self-diffraction setup and in the enhanced three-beam diffraction geometry we were able to obtain information on the dephasing time of the induced polarization. A discussion of different phenomenological models explains the inherent difficulty of a precise determination of dephasing rates.

Finally, two appendices cover the explicit and numerical integration of the system of differential equations for the induced polarizations and populations, respectively. The analytical treatment of the fourth-order polarization, which is responsible for the SH diffracted signal, for several limiting cases completes the scope of this thesis.

Chapter 2

Fundamentals

In order to gain surface-specific information on the ultrafast electron dynamics on Si(111) and Si(001) we employed the purely optical technique second-harmonic diffraction from a transient population grating of excited dangling bonds. This coherent method is a combination of second-harmonic generation (SHG) and degenerate four-wave mixing (DFWM). After an introduction into the relevant structural and electronic properties of the silicon surfaces studied (Sect. 2.1), we therefore continue with a brief description of SHG (Sect. 2.2) and DFWM (Sect. 2.3). Following the presentation of diffraction from transient surface gratings in Sect. 2.4 this chapter ends with a discussion of the nature of the relevant electronic excitations (Sect. 2.5).

2.1 Silicon surfaces

The elemental semiconductor silicon is the most intensely investigated and precisely characterized material [15]. The ultrahigh purity of silicon crystals, with defect and impurity concentrations in the ppb range and below, together with this thorough characterization make the material a model system for the study of ultrafast carrier dynamics [16–20]. Increasingly, the studies are extended from bulk electron dynamics to investigations of carrier scattering and relaxation processes at surfaces and interfaces [21–32], exploiting the reproducible preparability of very well defined, clean surfaces of silicon, compared to, *e.g.*, GaAs. These experiments are not only fascinating from a fundamental scientific point of view, but also provide valuable technologically relevant information – silicon being the core ingredient in most integrated circuits and electronic devices. A deeper understanding of electron dynamics facilitates proper estimates of device performance and reliability [33]. Due to the continuing process of miniaturization, the accurate quantitative determination of fundamental carrier scattering rates at surfaces grows to become a more and more crucial prerequisite for the correct simulation of semiconductor devices [34].

This section provides a short description of the geometric and electronic structure of the two types of silicon surfaces investigated in this thesis: Si(111) and Si(001) [35–37].

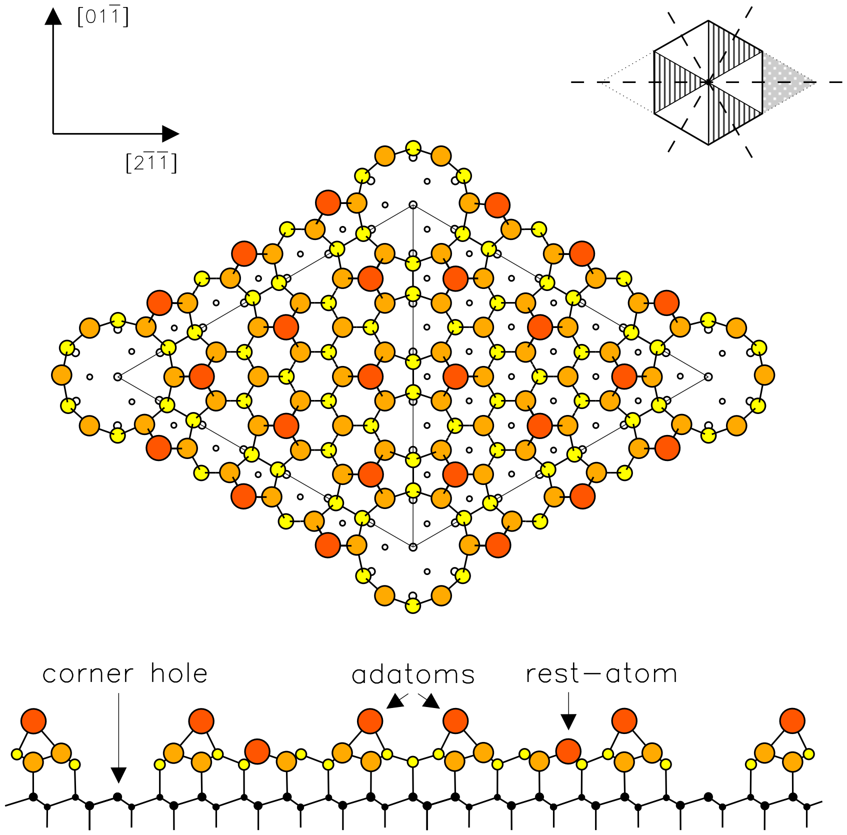

Fig. 2.1: Geometric structure of the Si(111)7×7 surface (top view and side view) according to the dimer–adatom–stacking fault (DAS) model after Takayanagi *et al.*, in which the total number of dangling bonds per unit cell is reduced from 49 to 19 [39]. Essential structural features of the unit cell are 9 Si–Si dimers between the two triangular subunits, 12 adatoms bonded to three otherwise broken bonds in the layer underneath, 6 restatoms, 1 corner-hole, and a stacking fault in one of the two triangular halves. Top right: Schematic representation of four 7×7 unit cells with the 3 mirror planes of the C_{3v} ($3m$) symmetry group.

2.1.1 Si(111)

The easiest cleavage planes in silicon are the {111} planes leading to a metastable 2×1 reconstruction. After annealing at elevated temperatures Si(111) forms the stable 7×7 reconstruction whose characteristic LEED pattern was discovered by Schlier and Farnsworth in 1959 [38]. Possessing the lowest surface energy of all silicon surfaces this reconstruction is not only worth investigating due to its intricate geometric structure but also because of the peculiar electronic behavior of the metallic dangling-bond surface band on top of the semiconducting bulk substrate.

The geometric structure of the Si(111)7×7 surface was elucidated in real space by scanning tunneling miscroscopy (STM) [40], scanning tunneling spectroscopy (STS) [41, 42], and atomic-force microscopy (AFM) [43–45], and in reciprocal space by glancing-incidence X-ray diffraction [46], Rutherford backscattering spectroscopy (RBS) [47–49], and low-energy electron diffraction (LEED) [50, 51]. Eventually, the analysis of transmission electron diffraction (TED) intensity distributions by Takayanagi *et al.* in 1985 resulted in the now fully accepted dimer–adatom–stacking fault (DAS) model of the Si(111)7×7 reconstruction [39, 52], that has since been confirmed by a variety of total energy minimization calculations [53–69]. Each unit cell (Fig. 2.1) is composed of 2 triangular subunits and contains 12 adatoms in T_4 sites in a 2×2 local arrangement, 6 restatoms between the adatoms in the layer below them and one corner-hole within a 12-member ring. One of the triangular halves contains a stacking-fault, which gives rise to 9 dimers connected by 8-member rings along the boundary of the triangles.

The origin of this complex atomic rearrangement lies in the interplay between a minimization of electronic energy through a reduction in the number of dangling bonds and the thereby resulting lattice strain. The predominant mechanism for the correlated lowering of the total energy is the presence of adatoms, each of which saturates three dangling bonds, while possessing only one. Nominally, the 12 adatoms in the 7×7 unit cell thus remove 24 broken bonds from a total of 49. The change in stacking from staggered to eclipsed in one of the two triangular subunits in conjunction with the thereby introduced dimers removes an additional number of 6 broken bonds. The remaining 19 dangling bonds imply a reduction in the areal density of broken bonds by a factor of 2.6, which overcompensates the substantial strain that goes along with the reconstruction.

Due to the presence of the stacking fault, the symmetry group of the 7×7 reconstruction is C_{3v} ($3m$), identical to the unreconstructed Si(111) surface. The second-order nonlinear susceptibility tensor $\chi^{(2)}$ is therefore composed of 4 nonvanishing independent components [70], that can be addressed individually through selecting the polarizations of the incident beam and the generated second-harmonic photons.

Along with the emergence of a structural understanding proceeded the investigation of the electronic properties of Si(111)7×7 in general, and of the different types of dangling bonds in particular. Fig. 2.2 shows the electronic band structure of Si(111)7×7 in an extended Brillouin zone scheme with the {111} projected bulk and valence bands (shaded) and the most important occupied (S_1, S_2, S_3) and unoccupied (U_1, U_2) surface bands of the 7×7 reconstruction. The origin of the surface states within the DAS model has been deduced from experiments that were able to connect structural with spectroscopic information: photoemission spectroscopy [73, 75–83], inverse photoemssion spectroscopy [84–87], scanning tunneling spectroscopy (STS) [41, 42, 88–90], electron energy-loss spectroscopy (EELS) [78, 91–94], and electron spin resonance (ESR) [95]. The 12 adatoms per 7×7 unit cell possess partially occupied dangling bonds that give rise to the surface band U_1/S_1 leading to the metallic char-

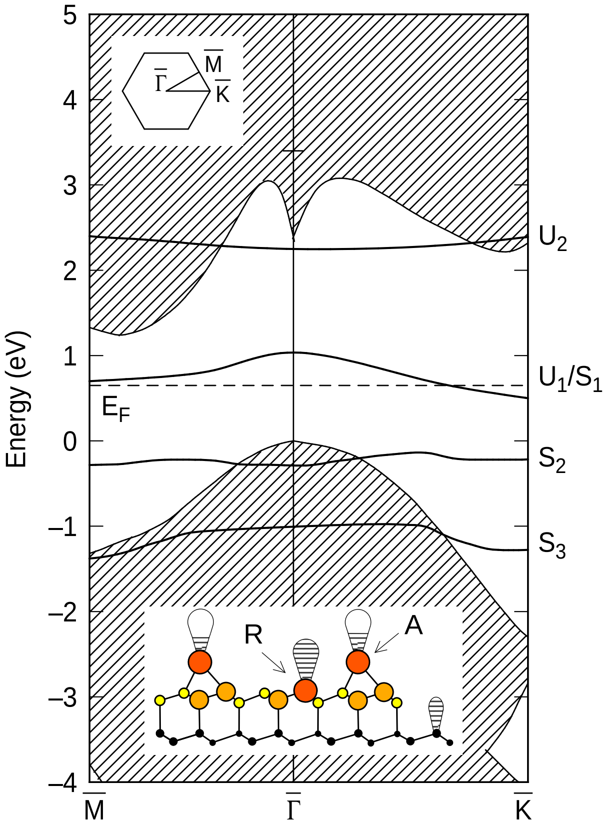

Fig. 2.2: Schematic electronic band structure of Si(111)7×7 in an extended Brillouin zone. The bulk valence and conduction bands projected onto Si(111) (after Refs. [71, 72]) are hatched. S_1, S_2, S_3 and U_1, U_2 denote occupied and unoccupied electronic surface states, respectively (after Refs. [73–75]). Inset: Side view of part of the Si(111)7×7 unit cell. The 12 adatoms (A) per unit cell that form the surface band U_1/S_1 have partially filled dangling bonds leading to a metallic character of the surface. Due to charge transfer from the adatoms to the 6 restatoms (R) that form the band S_2, the latter have fully occupied dangling bonds.

acter of the surface. Due to charge transfer from the adatoms to the 6 restatoms, the latter have fully occupied dangling bonds that form the band S_2. U_2 and S_3 denote surface states that are localized at the adatom back bonds to the restatom layer.

The experimental evidence for the metallicity of the two-dimensional adatom dangling-bond carrier gas on the semiconducting substrate stems from photoemission [73, 75–77, 80, 81] and STS [41, 88] data, that exhibit a finite electronic density of states (DOS) all the way to the Fermi level. A substantial DOS near the Fermi level is corroborated by the strong pinning of the surface Fermi level for both p- and n-type Si(111)7×7 [96, 97]. In addition, the asymmetric energy-loss lines observed in EELS experiments are characteristic of infinitesimal transitions across a metallic

Fermi level [78, 92–94]. Recent temperature-dependent measurements of the nuclear-spin relaxation rate of ^{8}Li probe atoms on the 7×7 surface using nuclear magnetic resonance (β-NMR) also indicated a metallic behavior [98]. A more direct proof for the metallicity of Si(111)7×7 was obtained by Heike and coworkers with STS using artificially produced insulating trenches in the surface [99]. By surrounding a part of the surface by a closed trench, they observed the naturally formed Schottky barrier between the surface states and the volume states with STM, which also allowed to estimate the 2D conductivity [99]. The formation of a tape-shaped trench allowed to measure the small but finite two-dimensional surface-state conductivity – mandatory for metallic behavior – of $8.7 \cdot 10^{-9}\ \Omega^{-1}$ [99].

At a temperature of $T_c \simeq 1100$ K, Si(111) displays a reversible phase transition from the ordered 7×7 reconstruction to the more disordered "1×1" structure, that was first reported by Lander in 1964 [100]. The "1×1" phase corresponds to an adatom gas in which the number of dangling bonds is increased by roughly 25% with respect to the 7×7 structure. This increase is reflected in a sudden rise in the SH intensity while heating through the phase transition [101]. The higher internal energy of the adatom gas that is due to the higher density of dangling bonds is overcompensated by the gain in entropy arising from the mobile adatoms.

2.1.2 Si(001)

Due to its technological importance for electronics applications, the Si(001) surface has been studied intensively over the last 40 years. Despite similar features, like the mechanism of free energy minimization by a reduction of dangling bond density, {001} surfaces of silicon display a number of very different properties compared to Si(111), both geometrically and electronically.

At room temperature Si(001) surfaces exhibit 2×1 reconstructions [38] composed of two 2×1 domains rotated by 90° with respect to each other. This structure arises from the pairing of neighboring silicon atoms to dimers via formation of a σ-bond, which reduces the dangling bond density from two to one per surface atom [38, 102–105]. The resulting rows of dimers along the [110] direction within the geometric structure of Si(001)2×1 are shown in Fig. 2.3. Since dimer rows on neighboring terraces divided by monolayer steps are oriented perpendicular to each other, the local C_{2v} ($2mm$) symmetry group gives rise to a macroscopic C_{4v} ($4mm$) symmetry. A Jahn-Teller-like distortion leads to a tilting of the dimers that has been observed in diffraction studies, ion scattering, and STM [37]. Molecular dynamics calculations revealed the tilted dimers to oscillate with a period in the subpicosecond range [106–109]. The finite correlation between the buckled dimers within and across dimer rows leads to a c(4×2) reconstruction at low temperatures, that corresponds to alternatingly buckled dimers (see Fig. 2.3). The structural order–disorder c(4×2) ↔ 2×1 phase transition that takes place around 150 K was followed *in situ* by LEED

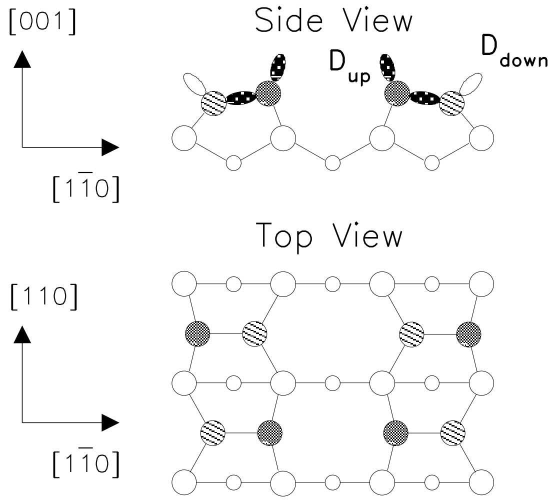

Fig. 2.3: Geometric structure of the Si(001)2×1 surface (side view and top view). Essential structural features of the reconstruction are rows of tilted silicon dimers along the [110] direction, which reduces the number of dangling bonds per surface atom from 2 to 1. Since dimer rows on neighboring terraces divided by monolayer steps are oriented perpendicular to each other, the local C_{2v} ($2mm$) symmetry group yields a macroscopic C_{4v} ($4mm$) symmetry. The correlation of the buckled dimers within and across dimer rows gives rise to a c(4×2) reconstruction below the order–disorder transition temperature of 150 K.

and X-ray diffraction [37].

The electronic structure of Si(001) has been studied extensively with angle-resolved photoelectron spectroscopy (ARPES) [82, 111, 112, 114], inverse photoemission (IPE) [85, 113, 115], electron energy-loss spectroscopy (EELS) [91, 116], and scanning tunneling spectroscopy (STS) [117, 118]. The experimental results have been confirmed by calculations [110, 119–124]. As a consequence of the Jahn-Teller rehybridization, charge is transferred from the depressed to the raised dimer atoms so that the latter ones exhibit completely filled dangling bonds, while the dangling bonds at the donating lowered dimer atoms are empty. Fig. 2.4 shows the schematic electronic band structure of Si(001)2×1 with the dangling bond surface bands arising from the raised (D_{up}) and lowered (D_{down}) dimer atoms. The two surface bands give rise to resonant optical transitions in the energy range 0.9–2.1 eV between D_{up} and D_{down}, with their joint density of states peaked at 1.65 eV (see Fig. 2.7). The relatively small dispersion of the dangling bond bands in the [1$\bar{1}$0] direction ($\overline{\Gamma}$–$\overline{J}$ and $\overline{K}$–$\overline{J'}$), *i.e.* perpendicular to the dimer rows, as compared to the [110] direction ($\overline{\Gamma}$–$\overline{J'}$ and $\overline{J}$–$\overline{K}$), parallel to the dimer rows, reflects the smaller coupling of the dangling bonds across dimer rows in contrast to within the dimer rows. The effective π-interaction between the dangling bonds in one dimer on the ideal Si(001) surface prevents the two band centers to come

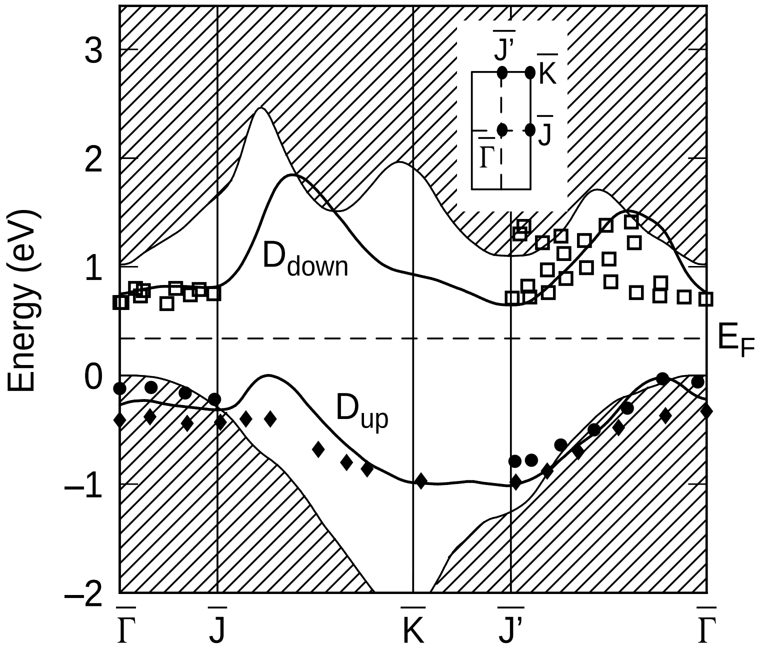

Fig. 2.4: Schematic electronic band structure of Si(001)2×1. The bulk valence and conduction bands projected onto Si(001) (after Ref. [110]) are shaded. D_{up} (D_{down}) denotes the occupied (unoccupied) dangling-bond state of the raised (lowered) silicon dimer atom, as shown in Fig. 2.3, calculated in the GW approximation [110]. The symbols refer to angle-resolved photoemission data of Ref. [111] (diamonds) and Ref. [112] (circles), and to k-resolved inverse photoemission data of Ref. [113] (open squares).

closer than 0.8 eV [110]. The electronic structure at steps, however, is different from the surface band structure at the terraces, enabling the bands to approach each other energetically [125], and thereby opening the way for a more efficient carrier relaxation mechanism at the steps.

2.2 Optical second-harmonic generation (SHG)

Carrier relaxation on the silicon surfaces that were described in the preceding section occurs on a femtosecond time scale. This suggests the application of an optical technique using ultrashort laser pulses, which also allows to utilize the coherence of the light field for the determination of dephasing times. Surface specifity of the measurement can be obtained by using an even-order *nonlinear* optical method, as the nonlinear optical susceptibilities $\chi^{(n)}$ with even n vanish in the volume of centrosymmetric materials, like crystalline silicon, but allow for finite $\chi^{(n)}$ at the surface, where inversion symmetry is broken. In order to gain surface specific information on carrier dynamics, we used a combination of the simplest of these techniques – second-harmonic generation (SHG) – with degenerate four-wave mixing (DFWM).

This section outlines the former, the following section the latter of the two methods.

The first SHG experiment was conducted in 1961 by Franken and coworkers using a quartz crystal [126]. After Bloembergen and Pershan theoretically treated SHG from surfaces of centrosymmetric materials [127], and this effect was observed experimentally by Brown *et al.* on silver [128], the technique was further developed and applied to various surfaces in the following decades by the group of Shen [6, 129–131].

Purely optical nonlinear methods, like SHG, have several advantages compared to photoelectron methods: Because of inversion symmetry breaking at every surface, SHG can provide a genuine surface signal. In addition, these methods are applicable at high excitation conditions, without being confronted with space-charge problems, as in the case of photoemission. Because of their purely optical character, they can also be applied to interfaces between solid media. However, purely optical experiments are often more difficult to interpret than photoemission investigations.

2.2.1 Macroscopic and microscopic description

Based on work by Bloembergen *et al.* [5, 127], Heinz developed a formalism for the macroscopic description of SHG from surfaces and interfaces [7, 70] that is outlined in the following. Approximating the interface by an infinitesimally thin sheet located at $z = 0$, the incident electric field $\mathbf{E}(t) = \mathbf{E}(\omega)\cos(\omega t)$ induces a nonlinear polarization $\mathbf{P}_\mathrm{s}^\mathrm{nls}$ in the sheet

$$\mathbf{P}_\mathrm{s}^\mathrm{nls}(\mathbf{r}, t) = \mathbf{P}_\mathrm{s}\delta(z)\mathrm{e}^{i\mathbf{k}_\parallel(\Omega)\mathbf{r}-i\Omega t} + \text{c.c.} \tag{2.1}$$

with $\Omega = 2\omega$. Considering the leading order term in a multipole expansion of the nonlinear polarization within the electric-dipole approximation, the nonlinear response of the polarization sheet is determined by the surface nonlinear susceptibility $\chi_\mathrm{s}^{(2)}$

$$\mathbf{P}_\mathrm{s}(\Omega) = \chi_\mathrm{s}^{(2)}(\Omega{=}2\omega) : \mathbf{E}(\omega)\mathbf{E}(\omega). \tag{2.2}$$

By solving Maxwell's equations with the appropriate boundary conditions, using $\mathbf{P}_\mathrm{s}^\mathrm{nls}$ as source term, one can obtain the radiation emitted from the polarization sheet and thus the intensity $I(\Omega)$ of the reflected second-harmonic radiation generated from a beam with intensity $I(\omega)$ [70]

$$I(\Omega) = \frac{8\pi^3\Omega^2\sec^2\theta_{2\omega}}{c^3\epsilon_1(\omega)[\epsilon_1(\Omega)]^{1/2}}\,|\mathbf{e}(\Omega)\cdot\chi_\mathrm{s}^{(2)} : \mathbf{e}(\omega)\mathbf{e}(\omega)|^2 I^2(\omega). \tag{2.3}$$

$\mathbf{e}(\Omega)$ and $\mathbf{e}(\omega)$ are transformed polarization vectors that are obtained from the unit polarization vectors $\hat{\mathbf{e}}(\omega)$ and $\hat{\mathbf{e}}(\Omega)$ of the incident and output fields by a Fresnel transformation $\mathbf{F}$, *e.g.* $\mathbf{e}(\omega) = \mathbf{F}(\omega)\hat{\mathbf{e}}(\omega)$.

In general, the nonlinear response of the bulk material also has to be taken into account. Since both the electric field $\mathbf{E}$ and the polarization $\mathbf{P}$ are polar vectors, *i.e.* change sign under a spatial inversion operation, Eq. (2.2) requires the nonlinear

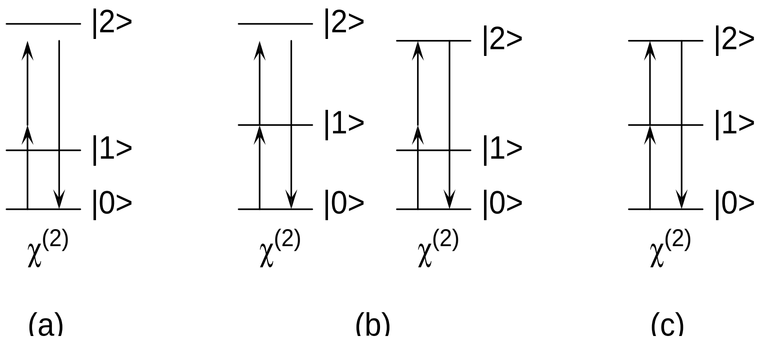

Fig. 2.5: Microscopic schemes of second-harmonic generation processes in nonresonantly (a), as well as singly (b), and twofold (c) resonantly excited three-level systems.

susceptibility $\chi^{(2)}$ to be a pseudotensor, *i.e.* also to change sign under the inversion. In the volume of centrosymmetric materials inversion symmetry simultaneously demands $\chi^{(2)}(\mathbf{r}) = \chi^{(2)}(-\mathbf{r})$. These two requirements imply $\chi^{(2)} \equiv 0$ in the bulk of centrosymmetric materials but allow for a non-vanishing $\chi_{\mathrm{s}}^{(2)}$ at the surface where inversion symmetry is broken [1, 70]. The leading terms in a multipole expansion of the nonlinear polarization are therefore [70]

$$\mathbf{P}_{\mathrm{s}}(\Omega) = \chi_{\mathrm{s}}^{(2)}(\Omega{=}\omega{+}\omega) : \mathbf{E}(\omega)\mathbf{E}(\omega) + \chi_{\mathrm{q}}^{(2)}(\Omega{=}\omega{+}\omega) : \mathbf{E}(\omega)\nabla\mathbf{E}(\omega), \tag{2.4}$$

where the first term is the surface electric-dipole contribution to SHG and the second term, that contains spatial derivatives of $\mathbf{E}$, describes volume-derived electric-quadrupole and magnetic-dipole contributions.

The second-order nonlinear optical susceptibility is a third-rank tensor composed of generally 18 elements $\chi_{\mathrm{s},ijk}^{(2)}$ for the triclinic C_1 (1) symmetry group. For surfaces of higher symmetry, the symmetry operations within the respective group reduce the number of independent, non-vanishing elements. The C_{3v} ($3m$) symmetry of Si(111)7×7 and the macroscopic C_{4v} ($4mm$) group of Si(001) give rise to 4 and 3 independent, nonvanishing $\chi_{\mathrm{s}}^{(2)}$ tensor components, respectively [70]. It is possible to selectively probe individual tensor elements by an appropriate choice of input and output polarizations.

In a microscopic description, SHG is the parametric conversion of two photons $\hbar\omega$ to one second-harmonic photon $2\hbar\omega$ in a three-wave mixing process (Fig. 2.5). Microscopic expressions for the nonlinear polarization $\mathbf{P}^{(2)}$ and the nonlinear susceptibility $\chi^{(2)}$ can be derived within a density-matrix formalism using a perturbation expansion up to second order in the electric field. The result for $\chi^{(2)}$ in explicit Cartesian tensor notation is the sum of 8 terms of the form [1]

$$\chi_{\mathrm{s},ijk}^{(2)}(\Omega{=}2\omega) = -N\frac{e^3}{\hbar^2}\sum_{g,n,n'}\left[\frac{\langle g|r_i|n\rangle\langle n|r_j|n'\rangle\langle n'|r_k|g\rangle}{(\Omega-\omega_{ng}+i\Gamma_{ng})(\omega-\omega_{n'g}+i\Gamma_{n'g})}+\cdots\right]\rho_g^{(0)} \tag{2.5}$$

with transition frequencies ω, line widths (relaxation rates) Γ and ground state population $\rho_g^{(0)}$. As the product of dipole matrix elements in the numerators of Eq. (2.5) suggests, this susceptibility describes a sequence of three transitions from an initially occupied electronic ground state $|g\rangle$ to unoccupied intermediate states $|n'\rangle$ and $|n\rangle$ by absorption of two photons $\hbar\omega$, followed by the emission of a second-harmonic photon $2\hbar\omega$, which returns the system to $|g\rangle$. As a consequence of the energy denominators in Eq. (2.5), $|\chi^{(2)}|$ becomes maximal and thus the SH intensity resonantly enhanced, whenever the fundamental and/or the SH frequency approximates a transition frequency between two real energy levels.

2.2.2 SHG from silicon surfaces

The presence of surface states within the volume band gap of silicon enables resonant optical transitions with photons in the visible and near infrared energy range (see Figs. 2.2 and 2.4). The resulting resonant enhancement of the SH intensity and the surface specifity of SHG due to the inversion symmetry of bulk silicon, together with the fs time-resolution through the application of ultrashort laser pulses form the basis for our investigation of the ultrafast relaxation dynamics of electronic excitations on silicon surfaces. With the help of a incoherent SH pump–probe setup it is possible to monitor the electronic population relaxation; the underlying coherent polarization dynamics remains inaccessible in such type of experiment [132,133]. Our combination of SHG with a coherent transient grating technique like degenerate four-wave mixing (DFWM) allowed the study of single, phase-destroying electronic scattering events.

For a qualitative understanding of the electronic excitation mechanism that is responsible for the second-harmonic five-wave mixing signal in our investigation, it is useful to study the dependence of the reflected SHG intensity on photon energy. The SH spectra of Si(111) in Fig. 2.6 obtained by Schmitt and Höfer reveal two resonant structures [74,134]. Similar SH spectroscopic information for Si(111) was also obtained experimentally by other groups [135–140] and was confirmed qualitatively by various calculations [141–144].

The broad feature below 1.5 eV disappears when hydrogen or oxygen is adsorbed. It originates from a resonant enhancement of SHG by the Si dangling-bond states, which are quenched upon hydrogen or oxygen adsorption. Sum-frequency experiments conducted by Schmitt showed that this broad feature is due to a one-photon resonance [134].

The peak around 1.7 eV, a two-photon resonance, is a consequence of the E_1 transition between the valence and conduction band of bulk silicon at 3.4 eV and arises because of the distortion of the bulk electronic structure at the surface [145]. It corresponds to a S_3–U_2 transition between the bonding and antibonding states of adatom backbonds [74]. Since the initial stage of oxygen adsorption on Si(111), the molecular precursor, is very stable at 80 K, the 7×7 surface structure remains

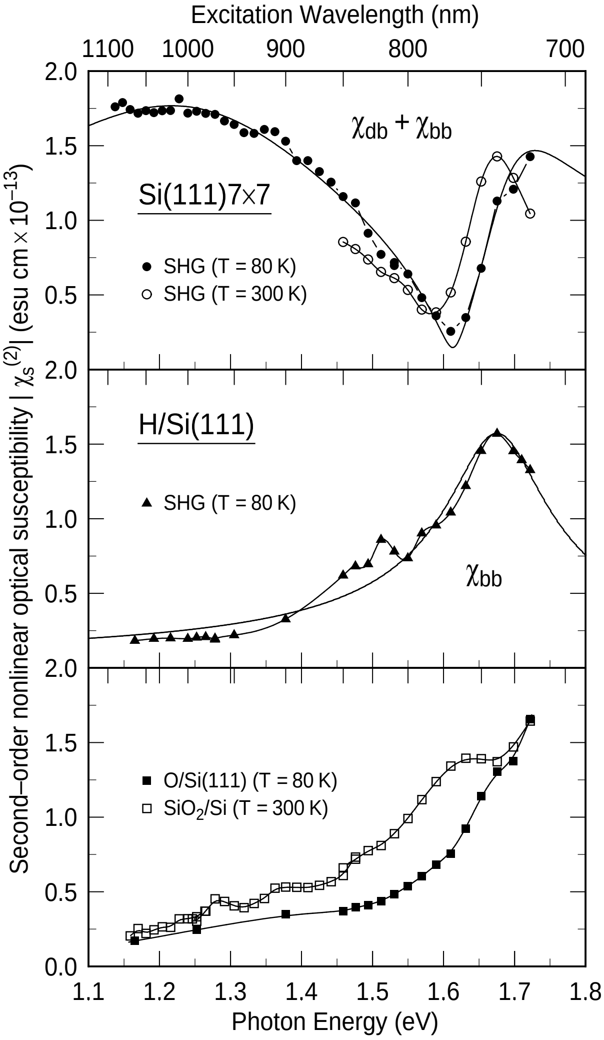

Fig. 2.6: Second-order nonlinear optical susceptibility $\chi_{\mathrm{s}}^{(2)}$ (anisotropic component $\chi_{\mathrm{s},xxx}^{(2)}$) as a function of photon energy for clean Si(111)7×7 (top) and for Si(111) surfaces with all dangling bonds saturated by hydrogen (center) and oxygen (bottom). The dangling-bond derived broad feature below 1.5 eV (χ_{db}) is quenched by hydrogen or oxygen adsorption, whereas the peak at 1.65 eV (χ_{bb}) exhibits relatively little sensitivity on adsorbates. (From Schmitt [134]).

intact for moderate exposures [146–150]. The E_1-related SH resonance peak therefore exhibits relatively little sensitivity on adsorbed oxygen.

Second-harmonic spectra of the clean Si(001) surface display qualitatively similar features: a broad dangling bond-derived structure between 1.1 eV and 1.6 eV that is quenched during oxygen adsorption, and a peak at 1.7 eV close to the E_1 transition [74,134,145,151–159]. The overall shape of these spectra was confirmed by calculations [143, 158–167].

Fig. 2.7 displays the joint density of states of the occupied/unoccupied $D_{\mathrm{up}}/D_{\mathrm{down}}$

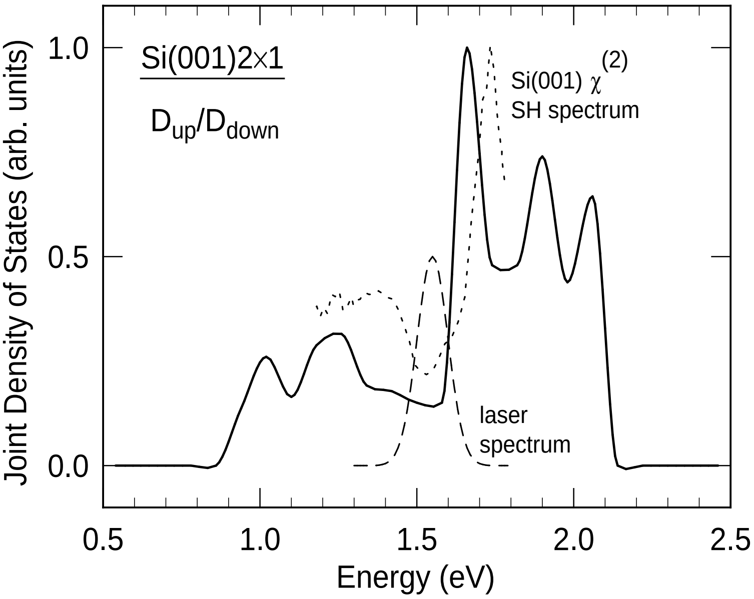

Fig. 2.7: Joint density of states of the occupied/unoccupied D_{up}/D_{down} dangling-bond states on Si(001) derived from the GWA calculated bands by Pollmann *et al.* shown in Fig. 2.4 [110]. This quantity respresents the influence of one-photon resonances in SHG that arise from the surface dangling-bond states, neglecting any transition matrix element effects. The $\chi^{(2)}$ SH spectrum of Si(001) (dotted line) obtained by Schmitt [134] agrees very well with the calculated bands, assuming an energetic offset of the calculation on the order of 100 meV. A more detailed analysis of the electronic band structure in Fig. 2.4 reveals that the excitation energy around 1.55 eV with a FWHM of 120 meV (dashed line) generates an excited dangling-bond population both near the center ($\overline{\Gamma}$) and at the surface Brillouin zone boundary near $\overline{J'}$.

dangling-bond states on Si(001) that are shown in Fig. 2.4. This spectrum reveals SHG processes to be resonantly enhanced in the broad range from 0.9 eV to 2.1 eV in accordance with experimental SHG spectra of Si(001) (dotted line) [134], indicating transitions between the D_{up} and D_{down} dangling-bond states to be the primary source of SH in that energy range. This interpretation is not unplausible due to the small spatial overlap of the surface states with the bulk states. Calculations by Rohlfing revealed that although the transition matrix elements between the D_{up} and D_{down} surface states are small compared to volume transitions, dipole selection rule considerations imply non-vanishing transition probabilites in most areas of the Si(001)2×1 Brillouin zone for specific input polarizations [168]. Taking into account the contributions of the two perpendicularly oriented surface domains, Rohlfing's calculations show non-zero transition amplitudes throughout the entire Brillouin zone [168]. The substantial quenching of the SH signal in the range 1.2–1.8 eV upon hydrogen adsorption on Si(001) [134] also corroborates the profound involvement of the dangling-bond

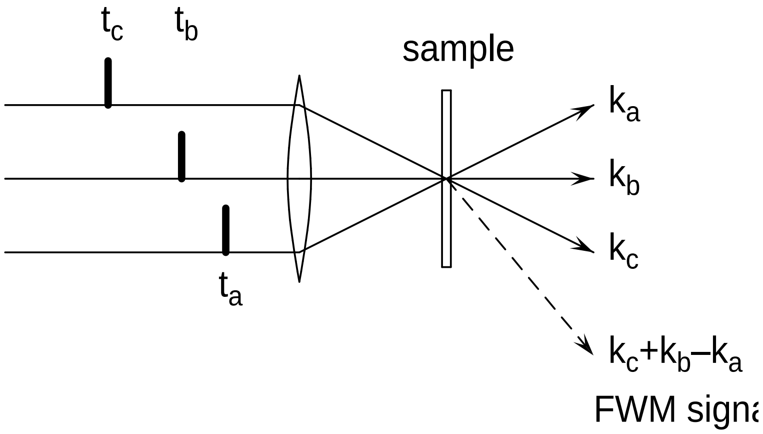

Fig. 2.8: Schematic representation of a four-wave mixing (FWM) experiment with three synchronized incident pulses $\mathbf{k}_\mathrm{a}$, $\mathbf{k}_\mathrm{b}$, and $\mathbf{k}_\mathrm{c}$. $\mathbf{k}_\mathrm{a}$ and $\mathbf{k}_\mathrm{b}$ generate a grating characterized by $\mathbf{k}_\mathrm{b} - \mathbf{k}_\mathrm{a}$, from which $\mathbf{k}_\mathrm{c}$ is diffracted into direction $\mathbf{k}_\mathrm{d} = \mathbf{k}_\mathrm{c} + \mathbf{k}_\mathrm{b} - \mathbf{k}_\mathrm{a}$. The intensity of this FWM signal as a function of the various time delays yields information about the relaxation behavior of the system investigated.

surface states in the SHG process.

As a more detailed analysis of the electronic band structure in Fig. 2.4 shows, the laser excitation energy centered around 1.55 eV with a FWHM of 120 meV produces an excited dangling bond population both near the center ($\overline{\Gamma}$) and at the surface Brillouin zone boundary near $\overline{J'}$. The delocalization of the electronic excitation in k-space complicates the interpretation of the measured relaxation times, since the purely optical experimental method integrates over the entire Brillouin zone.

2.3 Degenerate four-wave mixing (DFWM)

The degenerate five-wave mixing technique of our study is derived from both second-harmonic generation (SHG) and degenerate four-wave mixing (DFWM). Whereas SHG is responsible for the surface specifity, DFWM enables time-resolved measurements of population and polarization relaxation.

In DFWM the sample is excited by three beams with wave-vectors $\mathbf{k}_\mathrm{a}$, $\mathbf{k}_\mathrm{b}$, and $\mathbf{k}_\mathrm{c}$, which arrive at the sample at times t_a, t_b, and t_c [3, 169, 170], as shown schematically in Fig. 2.8. The diffracted radiation along the phasematched direction $\mathbf{k}_\mathrm{d} = \mathbf{k}_\mathrm{c} + \mathbf{k}_\mathrm{b} - \mathbf{k}_\mathrm{a}$ is measured as a function of the various time delays to obtain different information about the system that is investigated. In its simplest form, DFWM can be realized with only two incident beams, using $\mathbf{k}_\mathrm{c} = \mathbf{k}_\mathrm{b}$, which leads to a diffracted signal into direction $\mathbf{k}_\mathrm{d} = 2\mathbf{k}_\mathrm{b} - \mathbf{k}_\mathrm{a}$. Microscopic schemes of DFWM processes are depicted in Fig. 2.9.

The intensity of the diffracted beam depends on the time delay between the vari-

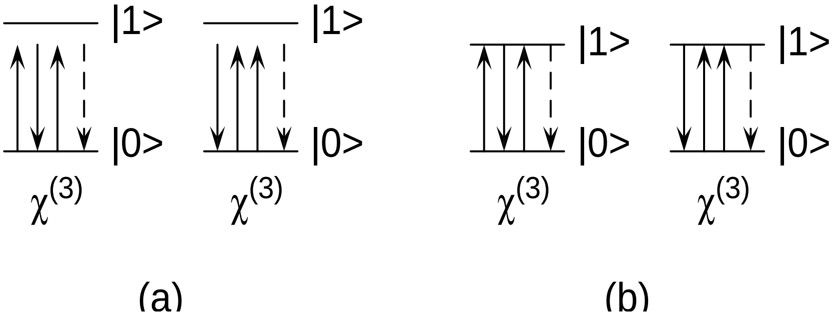

Fig. 2.9: Microscopic schemes of degenerate four-wave mixing processes in nonresonantly (a) and threefold resonantly (b) excited two-level systems.

ous pulses and the relaxation behavior of the electronic system (Fig. 2.10). One can distinguish two limiting cases: a homogeneous system and an inhomogeneously broadened system. With homogeneous broadening, the diffracted third-order signal decays exponentially with time after an exciting δ-pulse, whereas in the case of inhomogeneous broadening, there forms a so-called photon echo peaking at time $2\tau_{\mathrm{d}}$. This is because inhomogeneous broadening corresponds to a distribution of eigen-frequencies of the system. Due to this distribution, after an exciting pulse, the system dephases rapidly. A second pulse can partially rephase the system, which leads to the photon echo.

The intensity of the time-integrated signal is shown in the two lower parts of Fig. 2.10. In both cases the signal decays exponentially with time delay τ_{d}. In the homogeneous case with decay constant $T_2/2$, in the inhomogeneous case with $T_2/4$. From the simple exponential decays, the dephasing time T_2 can be determined, provided the nature of the line broadening is known.

The first experimental observation of a photon echo was reported by Kurnit and coworkers in 1964 for the case of ruby [171]. They explained the phenomenon in terms of a macroscopic oscillating electric dipole moment, which is momentarily reformed at the time the photon echo is observed [172, 173].

2.4 Diffraction from transient surface gratings

The combination of degenerate four-wave mixing, described in the preceding section, with another photon at the sample surface results in the five-wave mixing transient surface grating method, which is described in the following. Transient gratings have been widely used for the coherent spectroscopy of semiconductors and of molecules in liquid solutions [2, 3]. Two synchronized pump pulses of frequency ω and wave vectors $\mathbf{k}_{\mathrm{a}}$ and $\mathbf{k}_{\mathrm{b}}$ produce the electronic excitation. The grating results from the interference of the two beams, which gives rise to a spatial modulation of the linear

Homogeneous system

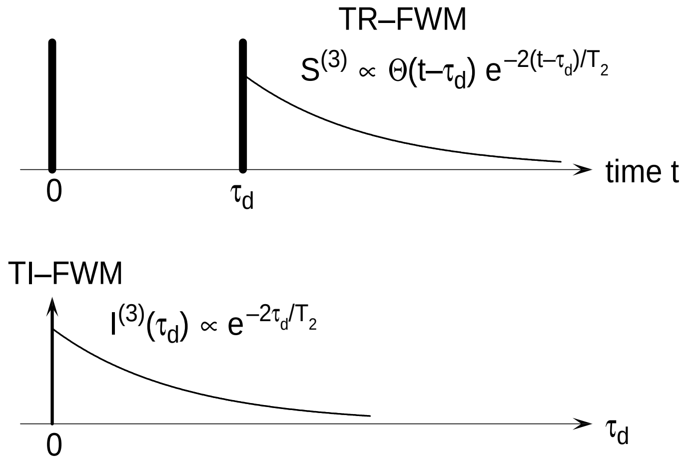

Inhomogeneously broadened system

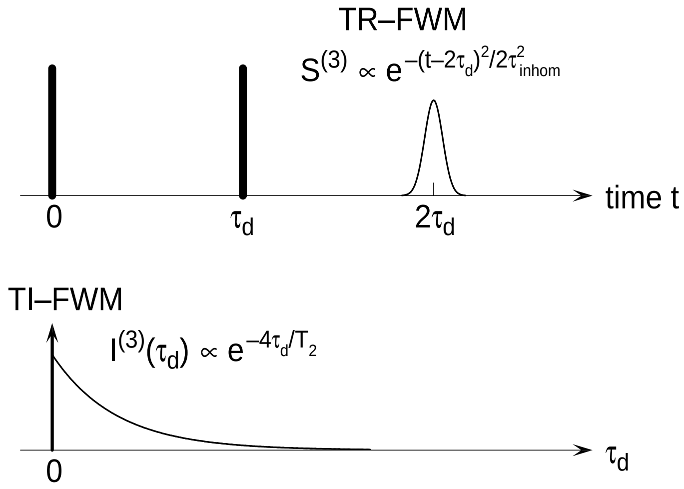

Fig. 2.10: Nonlinear third-order polarizations in degenerate four-wave mixing in the two-pulse self-diffraction geometry. Shown are the evolution of the time-resolved (TR) signal after the second excitation pulse and the dependence of the time-integrated (TI) signal as a function of time delay τ_d between the two excitation pulses. Top: Homogeneous system. Bottom: Inhomogeneously broadened system. With homogeneous broadening, the diffracted third-order signal decays exponentially with time-constant $T_2/2$. In the case of inhomogeneous broadening, there forms a photon echo peaking at time $2\tau_\mathrm{d}$. In both cases the time-integrated signal decays exponentially with time delay τ_d; in the homogeneous case with constant $T_2/2$, in the inhomogeneous case with $T_2/4$. (After Ref. [3]).

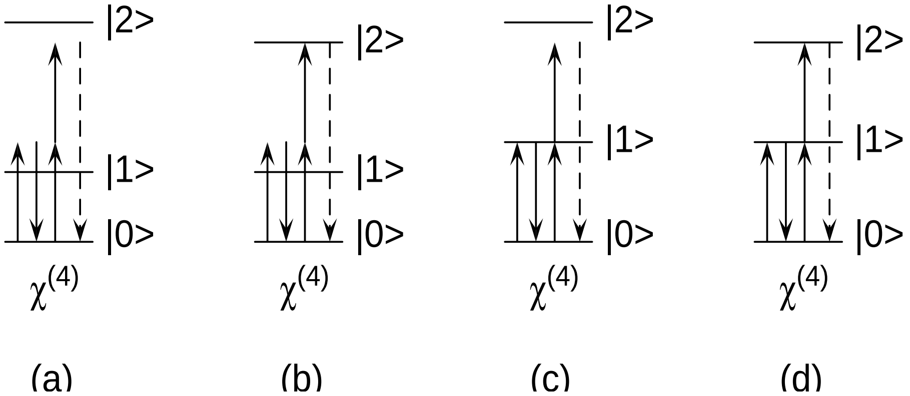

Fig. 2.11: Microscopic schemes of degenerate five-wave mixing processes in nonresonantly (a), singly (b), threefold (c), and fourfold (d) resonantly excited three-level systems.

absorption. In case of a surface experiment, the beams incident in the x-z plane (x denoting a direction parallel, z perpendicular to the surface) create a grating with k-vector $k_\mathrm{G} = k_{\mathrm{b},x} - k_{\mathrm{a},x}$. A synchronized probe pulse of the same frequency ω and wave vector $\mathbf{k}_\mathrm{p}$ is Bragg-diffracted from the transient grating into a direction determined by $k_{\mathrm{d},x} = k_{\mathrm{p},x} \pm k_\mathrm{G}$. The diffracted intensity is a function of the time delay between the incident pulses and of the relaxation dynamics of the electronic system.

The situation becomes most transparent for a resonantly excited two-level system with transition frequency $\omega_{01} = \omega$ in the limit of weak excitation. In this case it is sufficient to calculate the induced polarizations P and population changes N_{01} in the lowest order of the field E from a density matrix description [3, 174].

$$\frac{\partial}{\partial t} P_j^{(1)} = \frac{i\mu}{\hbar} E_j - \frac{1}{T_2} P_j^{(1)}, \qquad j = \mathrm{a}, \mathrm{b} \tag{2.6}$$

$$\frac{\partial}{\partial t} N_{01}^{(2)} = \frac{i\mu}{\hbar} (E_\mathrm{a} P_\mathrm{b}^{*(1)} - P_\mathrm{a}^{(1)} E_\mathrm{b}^{*}) + \mathrm{c.c.} - \frac{1}{T_1} N_{01}^{(2)} \tag{2.7}$$

$$\frac{\partial}{\partial t} P_\mathrm{d}^{(3)} = -2 \frac{i\mu}{\hbar} E_\mathrm{p} N_{01}^{(2)} - \frac{1}{T_2} P_\mathrm{d}^{(3)} \tag{2.8}$$

The first two equations (Eqs. 2.6 and 2.7) show that the spatial modulation of the population is *not* generated directly by an intensity grating of the interfering pump pulses but by the interference of the polarization induced by one excitation pulse with the field of the other. For the generation of the population grating $N(x) = N_{01}^{(2)} \cos(k_\mathrm{G} x)$, whose amplitude $N_{01}^{(2)}$ is assumed to decay exponentially with time constant T_1, it is thus not necessary that the two excitation pulses overlap in time. Instead $N_{01}^{(2)}$ depends on the ratio of the time delay between the pulses $|t_\mathrm{b} - t_\mathrm{a}|$ and the dephasing time of the polarization T_2. The polarization $P_\mathrm{d}^{(3)}$ induced by the interaction of the probe pulse with the grating gives rise to the diffracted radiation of frequency ω by dipole emission.

Depending on the temporal order of the various pulses one can gain different information from the diffracted signal. In one limiting case the two pump beams $\mathbf{k}_\mathrm{a}$ and $\mathbf{k}_\mathrm{b}$ coincide on the sample, $\tau_\mathrm{b}=0$, and after a time delay the probe pulse arrives on the surface, $\tau_\mathrm{probe}>0$. Since in this case the probe pulse samples the temporal decay of the transient grating, one measures T_1 population relaxation times and diffusivity. In another limiting case the second pump-pulse $\mathbf{k}_\mathrm{b}$ and the probe pulse hit the surface at the same time, but *after* the first pump pulse $\mathbf{k}_\mathrm{a}$, $\tau_\mathrm{b}>0$ and $\tau_\mathrm{probe}=\tau_\mathrm{b}$. In this case one measures dephasing times T_2.

$P_\mathrm{d}^{(3)}(\omega)$ is of third order in terms of the incident fields and thus not surface specific. Instead of the fundamental frequency ω of the diffracted pulse we detect its second-harmonic frequency 2ω. This radiation originates from an upconversion of $P_\mathrm{d}^{(3)}(\omega)$ with another probe photon at the surface. The polarization $P_\mathrm{d}^{(4)}(2\omega)$ is of fourth order in the incident fields and dipole-forbidden in the bulk of centrosymmetric materials. In the coherent experiments discussed in Chap. 6 we are interested mainly in the dephasing time T_2 rather than in the relaxation time T_1, which arises from a finite lifetime of the excited carriers and their diffusion. In this case it is possible to work with two incident beams and use one of the pump pulses, *e.g.* E_b, simultaneously as a probe. As one beam is diffracted here from a grating it generated itself, this is a case of self-diffraction.

The observed self-diffracted signal is determined by

$$\begin{aligned}\mathbf{P}_\mathrm{s}^{(4)}(\mathbf{K}_\mathrm{d}^{(+1)};2\omega) &= \chi_\mathrm{s}^{(4)}:\mathbf{E}_\mathrm{a}^{*}(\mathbf{k}_\mathrm{a})\mathbf{E}_\mathrm{b}^{3}(\mathbf{k}_\mathrm{b}) && (2.9)\\ K_{\mathrm{d},x}^{(+1)} &= 2k_{\mathrm{b},x}+(k_{\mathrm{b},x}-k_{\mathrm{a},x}). && (2.10)\end{aligned}$$

Its intensity $I_\mathrm{d}(2\omega)\propto|\mathbf{P}_\mathrm{s}^{(4)}(2\omega)|^2$ increases linearly with the intensity of pulse $\mathbf{k}_\mathrm{a}$ and with the third power of the intensity of pulse $\mathbf{k}_\mathrm{b}$. Its direction is given by Eq. (2.10) and the relationship $K_{\mathrm{d},x}^2+K_{\mathrm{d},z}^2=\epsilon(\frac{2\omega}{c})^2$. There is also a self-diffracted 2ω signal in the same order radiating into the direction given by $K_{\mathrm{d},x}^{(-1)}=2k_{\mathrm{b},x}-(k_{\mathrm{b},x}-k_{\mathrm{a},x})$. However, this signal is superimposed by the second-order sum-frequency response

$$\begin{aligned}\mathbf{P}_\mathrm{s}^{(2)}(\mathbf{K}_\mathrm{SF};2\omega) &= \chi_\mathrm{s}^{(2)}:\mathbf{E}_\mathrm{a}(\mathbf{k}_\mathrm{a})\mathbf{E}_\mathrm{b}(\mathbf{k}_\mathrm{b}) && (2.11)\\ K_{\mathrm{SF},x} &= k_{\mathrm{a},x}+k_{\mathrm{b},x}, && (2.12)\end{aligned}$$

which will completely dominate the 2ω signal in this direction in case of a weak grating.

A number of incoherent transient grating experiments on silicon have been performed in recent years by the group of Dai [25,27,28,31,175]. By detecting diffracted radiation from transient gratings at the *fundamental* photon frequency, they studied the dynamics of photoexcited carriers in the bulk and in the near-surface region of silicon on picosecond and femtosecond time scales. In contrast to our *second-harmonic* diffraction scheme, their experiments were not sensitive to genuine surface states, and they were not able to separate the coherent component of carrier relaxation.

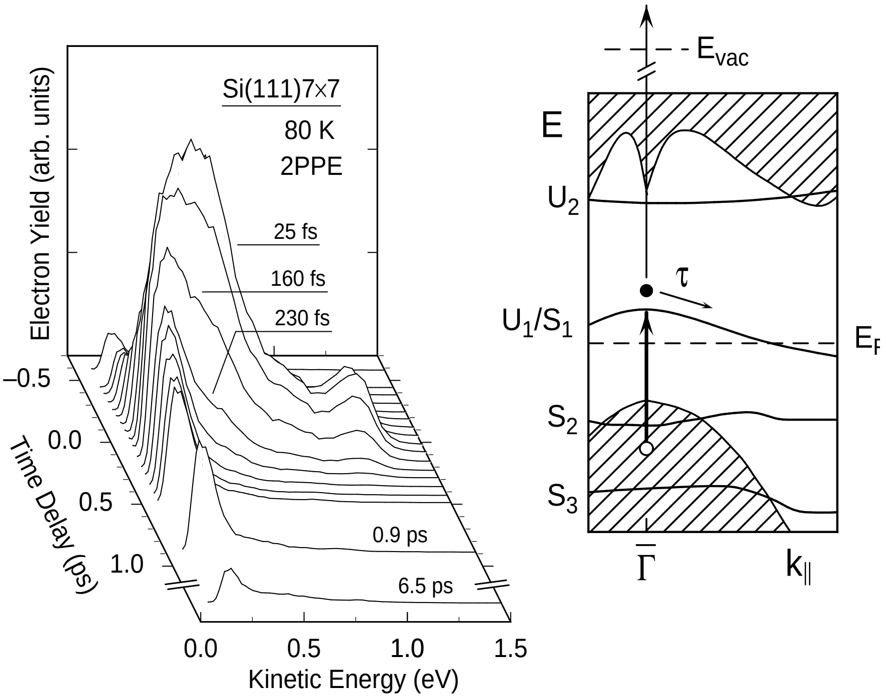

Fig. 2.12: Left: Transient electron population of usually unoccupied electronic states of Si(111)7×7 at 80 K above the Fermi level ($E_{\rm kin} \simeq 0.5$ eV) generated by 1.55 eV pump pulses and detected by photoemission with 4.65 eV probe pulses for $k_\| \approx 0$. Right: Schematic band structure of Si(111)7×7 in an extended Brillouin zone with the excitation produced by the pump pulse and its relaxation indicated by arrows. S_1 to S_3 and U_1, U_2 denote surface states; projected bulk states are hatched. (From Berthold [177]).

Recently, Kikteva *et al.* used surface-specific five-wave mixing spectroscopy to examine adsorbate dynamics at the fused silica/air interface [176]. Their transient grating approach allowed them to infer the dynamics of low-frequency intermolecular librational motion of different dye molecules at the sub-ps time scale [176].

2.5 Excitation of Si(111)7×7 dangling bonds

For the discussion of the actual diffraction experiment it is helpful to have some understanding of the nature of the relevant electronic excitations and their influence on the nonlinear optical response. For this purpose there were performed pump–probe experiments in our group at Si(111)7×7, using both 2PPE [177] and SHG [133]. The 2PPE investigations were conducted by Berthold and coworkers with the fundamental and frequency-tripled laser pulses of an amplified commercial Ti:sapphire laser (Quantronix RGA) operating at a wavelength of 800 nm and a repetition rate of 1 kHz. Pulse durations were 120 fs at the fundamental (IR) and 150 fs at the third-harmonic (UV) wavelength. The kinetic energy of the photoemitted electrons along the surface normal was measured by time-of-flight detection [178].

Fig. 2.12 shows that the IR pump pulses produce an electron distribution above the Fermi level in the bulk band gap that is probed by photoemission caused by the UV pulses. The 2PPE intensity is seen to decay as a function of pump–probe delay with rates that depend on the energy above the Fermi level. Since the only allowed states in this energy region are due to the U_1 surface band, which arises from partially occupied adatoms of Si(111)7×7 [87], we attribute the observed feature to excitation of this band near the $\overline{\Gamma}$ point and the fast decay to redistribution of the electrons within the band due to electron–electron scattering [177].

The qualitative conclusions on the excitation mechanism at Si(111)7×7 from the 2PPE experiments, as well as the observed population relaxation times on a picosecond and subpicosecond time scale were corroborated by time-resolved SH pump–probe measurements in our group conducted with the same laser system [133]. These findings will be discussed in more detail in Chap. 5.

The incoherent pump–probe experiments on Si(111)7×7 – two-photon photoemission and time-resolved second-harmonic generation – yield population relaxation times on the order of hundreds of femtoseconds to picoseconds. The origin of this relaxation is multiple scattering of excited electrons. In order to study single carrier scattering events one needs to probe a quantity that changes its magnitude significantly in every scattering process, such as the phase of the electronic wavefunction, that is addressed in coherent methods. By employing the technique diffraction from transient gratings in our study, we utilized one of these methods.

Chapter 3

Experimental setup

This chapter provides an account of the experimental setup that was employed in the investigation. Sect. 3.1 gives an overview of the ultra-high vacuum (UHV) system and the preparation procedure of the silicon surfaces. The cavity-dumped 10-fs Ti:sapphire laser system is the subject of Sect. 3.2. Closing this chapter is the description of the optical setup in Sect. 3.3.

3.1 Ultra-high vacuum system

The creation and maintaining of UHV conditions is the prerequisite for every investigation of atomically clean surfaces. This section presents a description of the UHV chamber and provides an account of the preparation procedures necessary to obtain clean, well-defined silicon surfaces.

3.1.1 UHV chamber

In order to enable optical measurements in UHV, a vacuum chamber built and previously operated by Mauerer [133] was modified in such a way that it could maintain a base pressure in the lower 10^{-11} mbar range. Reaching a low base pressure is the prerequisite for keeping the sample surface atomically clean over an entire measuring period. This issue is particularly crucial since the low optical signal of a few photons per second required extended periods of data acquisition around several 1000 seconds. The detailed characterization of the vacuum conditions and the inspection of the sample required the presence of several measurement instruments within the UHV chamber. The sample manipulator needed to provide a large number of translation and rotation degrees of freedom, while allowing for a large range of sample temperatures.

Fig. 3.1 provides a scheme of the UHV chamber (Varian) and its periphery. The system was baked at a temperature of 430 K, limited by the maximal allowable temperature of the rotary manipulator feedthrough, over a period of typically two days. Both sample and sample manipulator were degassed at 650 K during the entire bakeout period. The procedure resulted in a base pressure of typically 2×10^{-11} mbar. For

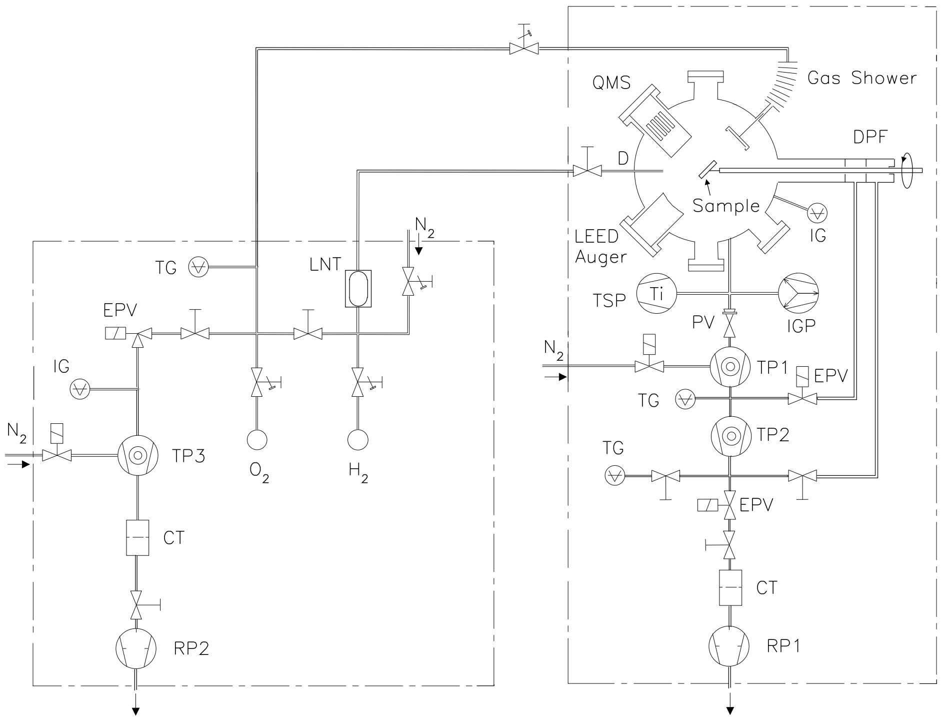

Fig. 3.1: Schematic representation of the UHV system consisting of the separately-pumped gas dosing system (left side) and the UHV chamber (right side) (adapted from Mauerer [133]). The abbreviations are explained in Tab. 3.1.

TP1, TP2, TP3	Turbomolecular pumps (Balzers), 500 l/s, 56 l/s, 190 l/s
TSP	Titanium sublimation pump (Varian), 2000 l/s
IGP	Ion getter pump (Varian), 200 l/s
RP1, RP2	Two-stage rotary vane pumps (Edwards), 30 m^3/h, 30 m^3/h
LNT	Liquid nitrogen trap
CT	Catalyzer trap
DPF	Differentially pumped feedthrough
IG	Ionization gauge
TG	Thermocouple gauge
PV	Plate valve CF 200
DV	UHV dosing valve
EPV	Electro-pneumatic protection valve
D	Doser with tungsten filament

Tab. 3.1: Vacuum components of the UHV system shown in Fig. 3.1. The combination of different pumps ensured the efficient and thorough pumping of the diverse molecules in the rest gas, that vary in mass and reactivity.

protection of the vacuum against power failure, loss of cooling water, or pump failure, the system is equipped with electro-pneumatic valves that are addressed by coupled circuits. A dosing system allows for the dosing of controlled amounts of research grade oxygen (purity 4.8, 99.998 Vol.-%) via a gas shower and hydrogen (purity 5.0, 99.999 Vol.-%) via a needle doser into the vacuum chamber. By resistive heating of a tungsten filament in front of the needle doser in the chamber, it is also possible to produce atomic hydrogen.

A quadrupole mass spectrometer (Balzers) is used for temperature-programmed desorption (TPD) measurements and for a precise determination of the various components of the rest gas in the chamber. For the characterization of the sample surface the chamber is equipped with a combined retarding-field 4-grid LEED/Auger instrument (Omicron, Spectaleed).

The optical measurements require the accurate positioning of the sample in space. This is especially important for the exact adjustment of both the plane of incidence and the polarization plane of the incoming light with respect to the surface orientation. The sample manipulator can be freely translated in x-, y-, and z-direction with an accuracy in the μm range. Rotations around the vertical axis are possible over the entire 360°; rotations around both horizontal axes can be performed over a range of 6° with a precision of 0.1 mrad.

For temperature dependent measurements and for the preparation procedure the temperature of the silicon sample could be varied from 80 K to 1600 K. The silicon samples are clamped onto two copper bars with spring-loaded molybdenum brackets. The sample is isolated from both copper and molybdenum with additional silicon spacer platelets. The two copper blocks are attached to a liquid-nitrogen cooled cryostat separated by an insulating sapphire disk. The high cooling efficiency of this construction enabled the cooling down of the silicon sample from room temperature to 80 K within 5 minutes; furthermore, it enabled the sample holder temperature to stay below 100 K even at the peaks of the sample heating cycles (1300 K). A more detailed description of the sample holder can be found in Ref. [179]. Direct resistive heating is used to control the silicon surface temperature. The surface temperature is measured with a NiCr/NiAl (type K) thermocouple that was cemented onto the rear side of the sample with a zirconium-oxide based ceramic glue (T-E-Klebetechnik). It is carefully ensured that there is no direct contact between thermocouple and silicon sample; therefore the thermocouple contact is fully embedded in the glue. It has been verified by Auger electron spectroscopy (AES) and low-energy electron diffraction (LEED) that no contaminants, in particular nickel, diffuse onto the front surface of the sample, even for the highest annealing temperatures. By checking with an infrared pyrometer (Keller) it was verified that the thermocouple correctly reproduces the actual surface temperature with an absolute accuracy of ±15 K and an estimated relative uncertainty within one experiment of ±5 K.

3.1.2 Silicon surface preparation

Besides very clean UHV conditions, the sample preparation procedure is of crucial importance for the production of atomically clean, well-ordered surfaces with few chemical and structural defects.

The base material was single-crystal, Czochralski (Cz) grown, n-type phosphorus-doped silicon (Virginia Semiconductor) with specified resistivities between 6 and 12 Ωcm corresponding to a P donor density $\sim 5 \times 10^{14}$ cm^{-3} [180]. The nominally flat wafers of 3” diameter and a thickness of 0.6 mm were single-side polished and oriented to within ±0.25° along the principal [111] or [001] axis, respectively. The Si(111) and Si(001) samples used for the experiments were cut with a diamond scribe from the wafers into strips of 45×9 mm^2 size. After rinsing in extra pure methanol and a careful visual inspection for scratches and dust residues, the samples were mounted directly onto the manipulator. No further treatment is required for the samples before insertion into UHV. This is because high-quality thermal oxide layers are grown on commercial silicon wafers under very clean process environments. These 'native' oxide layers protect the silicon from contamination. Therefore after outgassing the sample, the thermal decomposition of the oxide in UHV will remove the oxide together with contaminants on its outer surface.

Outgassing the sample and manipulator at 650 K during the entire bake-out period of the UHV chamber removed volatile adsorbates without desorbing the protective oxide layer. In the initial preparation after bake-out, the native oxide layer was removed by a series of heating cycles with peak temperatures rising in steps of 50 K and cooling rates of 2 Ks^{-1}. The maximal temperatures applied were 1300 K and 1200 K for Si(111) and Si(001), respectively; the chamber pressure stayed below 1×10^{-9} mbar at any time within the annealing cycles. Both duration and maximal values of the high-temperature annealing and cooling rates are critical parameters for the preparation of silicon surfaces with long-range ordered superstructure and small defect concentrations, as known from LEED and scanning tunneling microscopy (STM). Particularly in Si(001), extended annealing leads to surface roughening [181]. To protect the surface from adsorption of rest gas components, especially of non-volatile carbohydrates, the sample was passivated with an exposure of 10 Langmuir (1 L = 10^{-6} Torr·s) O_2 between measurement periods. Before the beginning of each measurement cycle the passivation layer of a few monolayers was desorbed by a single heating cycle peaking at 1300 K and 1200 K for Si(111) and Si(001), respectively.

After the preparation procedure the quality of the surface was inspected *in situ* by LEED and Auger electron spectroscopy (AES). The LEED pattern in Fig. 3.2 taken at a primary electron energy of 50 eV shows the sharp diffraction spots of the Si(111)7×7 reconstruction. An analysis of Auger electron spectra (Fig. 3.3) showed that the surface impurity density was below the detection limit of the retarding-field Auger spectrometer. In particular, the absence of carbon and oxygen on the surface

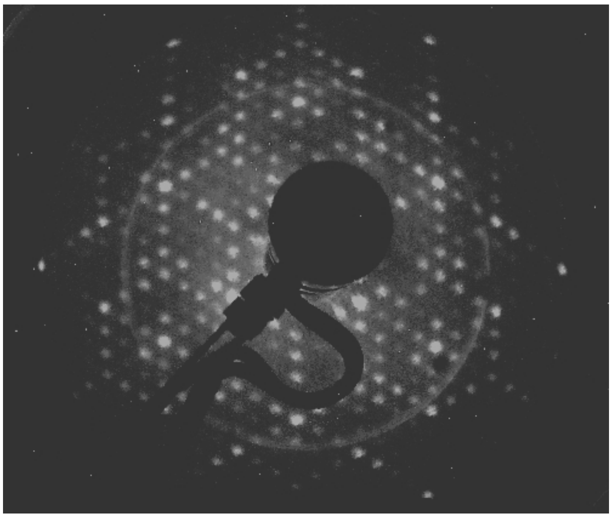

Fig. 3.2: LEED pattern of a clean Si(111)7×7 surface at 80 K taken at a primary electron energy of 50 eV. In addition to the intense hexagonal 1×1 spots, the sharp diffraction spots of the 7×7 reconstruction are clearly visible. The 2×2 pattern of the broken bonds inside each of the two triangular halves of the unit cell gives rise to enhanced diffraction intensities for diffraction spots close to 2×2 positions.

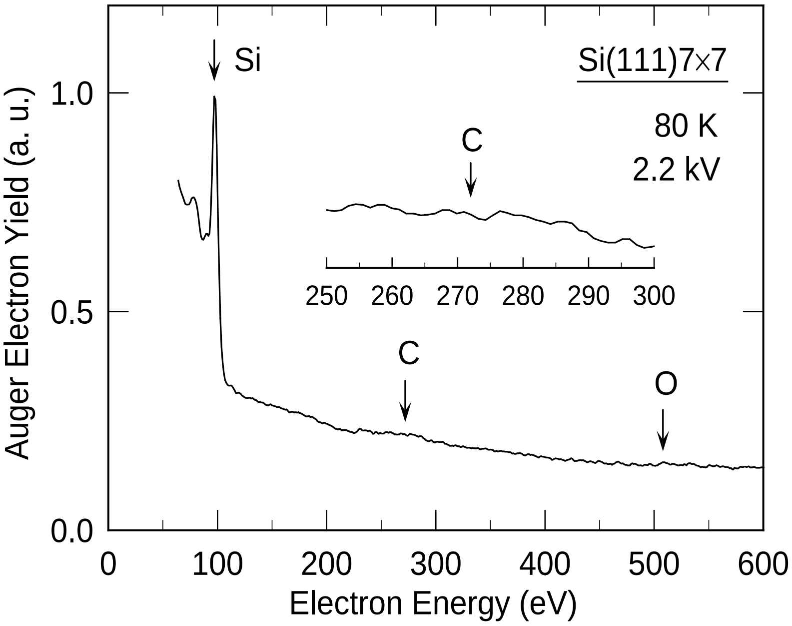

Fig. 3.3: Auger spectrum of a clean Si(111)7×7 surface at 80 K obtained with a primary electron energy of 2.2 kV. The energy positions of Auger electrons emitted from silicon (LMM), carbon (KLL), and oxygen (KLL) atoms are marked. Carbon and oxygen impurity concentrations are below the detection limit of a few percent of a monolayer.

was routinely checked by AES.

3.2 Cavity-dumped 10-fs laser

In order to deliver meaningful quantitative results from any optical experiment, it is necessary to characterize the light source employed. This section therefore provides an account of several methods used to gain information about temporal and spatial pulse shape, spectrum, pulse energy, pulse quality, and long-term stability of the Ti:sapphire laser with which the experiments were conducted. The investigation shows that the home-built laser yields 12.7-fs pulses around 800 nm with energies of 36 to 50 nJ at repetition rates from 100 kHz to 2 MHz.

In Kerr-lens mode-locked (KLM) Ti:sapphire oscillators a solitary wavepacket is generated by the interplay of self-phase modulation (SPM) and negative group velocity dispersion (GVD). The main limitations for shortening the pulse duration down to the 10 fs regime are the presence of GVD in the laser medium and third-order dispersion (TOD) in the cavity optics [182]. By using a short Ti:sapphire crystal and fused silica prisms, in order to reduce the gain medium GVD and cavity optics TOD, respectively, pulses of 11 fs duration could be obtained [183]. The pulse energies around a few nJ of typical Ti:sapphire laser oscillators are too small for the measurement of the highly nonlinear optical processes in our diffration experiment. For our experiments we used a cavity-dumped Ti:sapphire system that was home-built by Shumay and Berthold after a model from the group of Wiersma [184]. The technique of cavity dumping is capable to increase the pulse energy by about one order of magnitude through a reduction of the repetition rate while preventing any significant pulse broadening.

Fig. 3.4 shows a schematic representation of the cavity-dumped Ti:sapphire laser used for the SH self-diffraction experiments. The 4.5 mm short Brewster-cut Ti-doped sapphire crystal rod (Döhrer Elektrooptik) is optically pumped by a frequency-doubled (532 nm) Nd:YVO$_4$ laser (Spectra Physics, Millennia). The mode-locked pulses are compressed by two intra-cavity Brewster-cut fused silica prisms. For the cavity-dumping a 3 mm fused silica Bragg cell (Camac Systems) is used as acousto-optic modulator; the crystal was addressed by a radio-frequency driver (Camac Systems) that is fed with the output-coupled laser pulses taken by a photodiode.

Any quantitative discussion of optical time-domain experiments requires the accurate characterization of the temporal properties of the employed laser pulses. For the determination of the pulse duration and phase modulation we utilized two different second-harmonic autocorrelation approaches. Fig. 3.5 shows the interferometric autocorrelation of the cavity-dumped pulses obtained with a Michelson interferometer in which the second harmonic is generated collinearly in a 30 μm thin β-BaBO$_3$ (BBO) crystal (Optilab). A least-squares fit with a variable pulse duration τ_p using sech^2-pulses yields $\tau_\mathrm{p} = 12.7$ fs. From the shape of the envelope and the the-

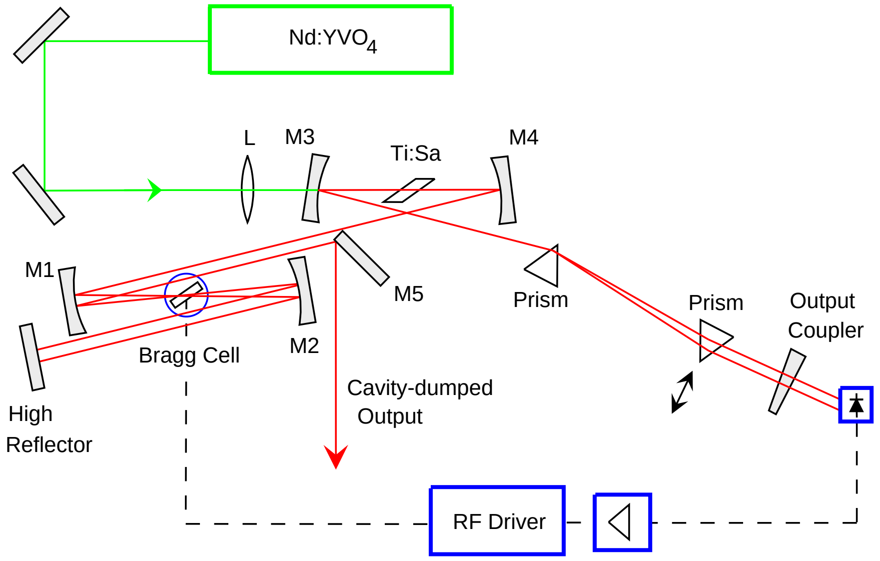

Fig. 3.4: Cavity-dumped Ti:sapphire laser used for the second-harmonic diffraction investigation. Since the technique of cavity-dumping enhances pulse energy by one order of magnitude compared to an ordinary laser oscillator, through a reduction of the repetition rate by a factor of 100, the second-harmonic diffracted signal from the highly nonlinear five-wave mixing process is intensified by two orders of magnitude.

oretically expected peak-to-background ratio of 8 to 1 the phase modulation of the pulses is concluded to be close to zero; the pulses are hence unchirped [185]. The inset of Fig. 3.5 shows the background-free intensity autocorrelation trace from the Si(001)c(4×2) surface at 80 K in UHV detected in the sum-frequency direction of two non-collinear beams. A sech^2 fit yields a pulse duration of 14.9 fs over three and a half orders of magnitude in intensity. The 4-mirror version, in which the ’Z’ with the Bragg cell is left away, produces unchirped pulses as short as 10 fs with 5 nJ of energy at a repetition rate of 82 MHz.

The gathering of spectral information of the laser pulses is important for the interpretation of results obtained from inhomogeneously broadened systems such as the U$_1$/S$_1$ surface band on Si(111)7×7. In combination with temporal data it is also possible to deduce the amount of frequency modulation (chirp) within the pulse. The spectrum of the cavity-dumped pulses taken by a photodiode array attached to a grating spectrometer is shown in Fig. 3.6. It displays a single clean peak over 4 orders of magnitude in intensity with its maximum at 809.5 nm and a full-width at half-maximum (FWHM) of 64.4 nm, which corresponds to a spectral bandwidth of 120 meV. Together with the pulse duration this result implies a duration–bandwidth product of $\Delta\nu\Delta t = 0.37$. As the product lies between the Fourier transform limit of 0.315 and $(2\ln 2)/\pi = 0.441$ for sech^2 and Gaussian pulses, respectively, the pulses

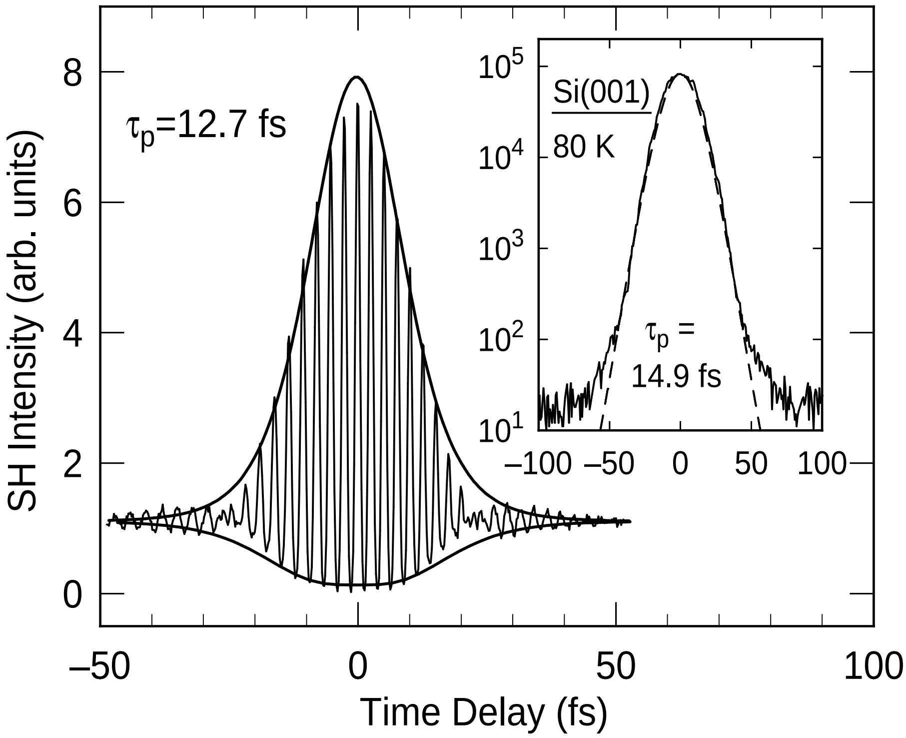

Fig. 3.5: Interferometric second-harmonic autocorrelation trace of the cavity-dumped pulses from the Ti:sapphire laser. A least-squares fit using sech^2 pulses yields a pulse duration of 12.7 fs. The shape of the pulse envelope together with the theoretically expected peak-to-background ratio of 8 to 1 implies the absence of significant phase modulation (chirp). Inset: Background-free intensity autocorrelation from the Si(001)c(4×2) surface at 80 K in UHV. A sech^2 pulse duration of 14.9 fs is shown over 3 and a half orders of magnitude in intensity.

are bandwidth-limited and therefore unchirped.

Besides the temporal and spectral characterization of the laser pulses, a spatial analysis of the beam is mandatory to ensure a smooth, time-independent distribution of intensity in space and thereby enabling a qualitative description of spatial pulse overlap in the focus on the silicon surface. The spatial beam profile of the cavity-dumped pulses taken with a CCD camera as displayed in Fig. 3.7 remained constant in time over periods of many hours. An analysis of the CCD images yielded a beam circularity of 85% and an excellent fit-accuracy to a Gaussian pulse shape of 95%.

The quality of the cavity-dumping process is monitored with a ns-fast photodiode. Fig. 3.8 shows the energy in the oscillator cavity and the cavity-dumped pulse as a function of time, displaying the oscillator roundtrip frequency of 82 MHz and a side-pulse suppression ratio of smaller than 1:30.

The low intensity of the highly nonlinear diffracted signal required measuring periods of the order of several 1000 s. Therefore the long-term stabilty of the light

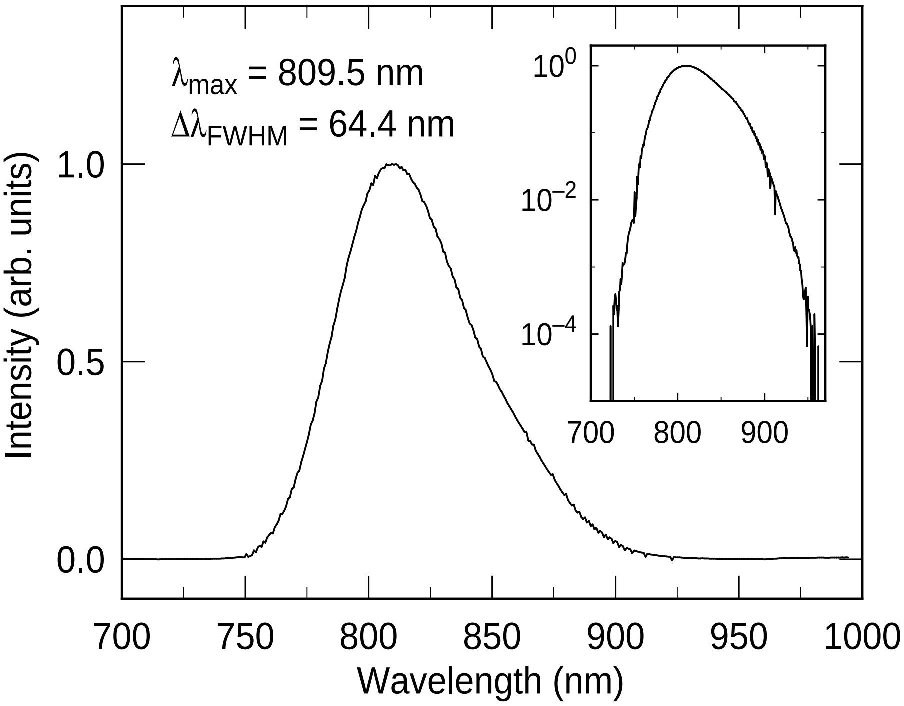

Fig. 3.6: Spectrum of the cavity-dumped pulses from the Ti:sapphire laser showing its peak intensity at 810 nm and a FWHM of 64 nm, which corresponds to a spectral bandwidth of 120 meV. Inset: Same spectrum on a logarithmic intensity scale displaying a clean single maximum over 4 orders of magnitude.

source employed is of crucial importance. The intensity of the cavity-dumped pulses from the Ti:sapphire laser is shown in Fig. 3.9 over a period of more than 2 hours.

The applications of such an intense, short-pulse, and coherent light source in surface science are multifarious. Besides the monitoring of electronic dephasing by SH diffraction, there is a variety of other scientific topics that can be advantageously addressed by this laser system. The investigation of ultrafast electron dynamics with time-resolved SHG and 2PPE and the generation and shaping of surface electron wavepackets are just two examples. One might also think about the mapping of excited state potential energy surfaces and the real-time study of elementary photochemical reactions. In combination with time-of-flight (TOF) photoelectron spectroscopy the system is also very well suited for probing sensitive adsorbate layers.

3.3 Optical setup

The optical setup of the SH self-diffraction experiment is shown in Fig. 3.10. The strategy for its design was driven by several stringent requirements that were a result of the aim of the experiment. The investigation was aimed at detecting a coherent,

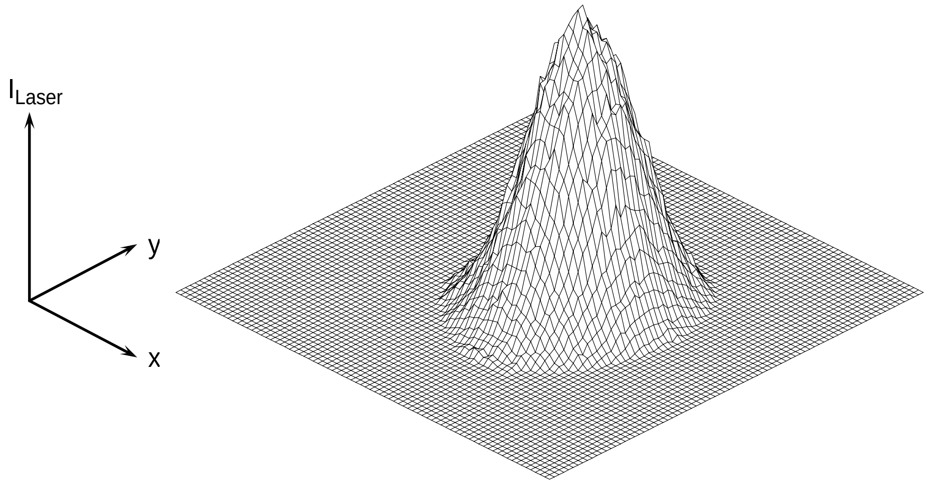

Fig. 3.7: Spatial intensity beam profile of the cavity-dumped pulses from the Ti:sapphire laser taken with a CCD camera. The intensity distribution in space was constant in time and showed a beam circularity of 85% as well as vertical and horizontal fit-accuracies to a Gaussian pulse shape of 95%.

ultrafast, highly nonlinear optical process that was resonant with optical transitions between electronic surface states on silicon. Coherent, femtosecond, intense light pulses should be delivered to a sample in UHV and the resulting optical signal of a few photons per second should be monitored. These goals determined the selection of the light source, the optical components in the beam path, and of the detection system.

The 13-fs, 800-nm pulses from our Ti:sapphire laser that were intensified by cavity-dumping to 50 nJ per pulse met all those requirements. The laser system was described in more detail in Sect. 3.2.

The function of the optical components in the beam path was twofold.

First, they should deliver the light from the source to the sample in UHV, preserving the pulses' extraordinary qualities. Light transmission through every material is accompanied by dispersion that leads to temporal broadening especially of ultrashort pulses. Therefore the number of transmissive elements in the beam path was kept to a minimum. In addition, the unavoidable transmissive elements – pulse-compression prisms, beam-splitters, half-wave plates, and UHV viewport – were carefully selected and tested. The prisms in the pulse compressor (Bernhard Halle Nachfl.) were made of fused silica (Suprasil 1). This material was chosen because it provides an extremely low third-order dispersion coefficient. The prisms were cut at their Brewster angle 69.06° for 800 nm light in order to minimize reflection losses. They were polished to a planarity of $\lambda/10$ to sustain the spatial coherence in the beam.

For the continuous rotation of the polarization, an isotropic material like fused

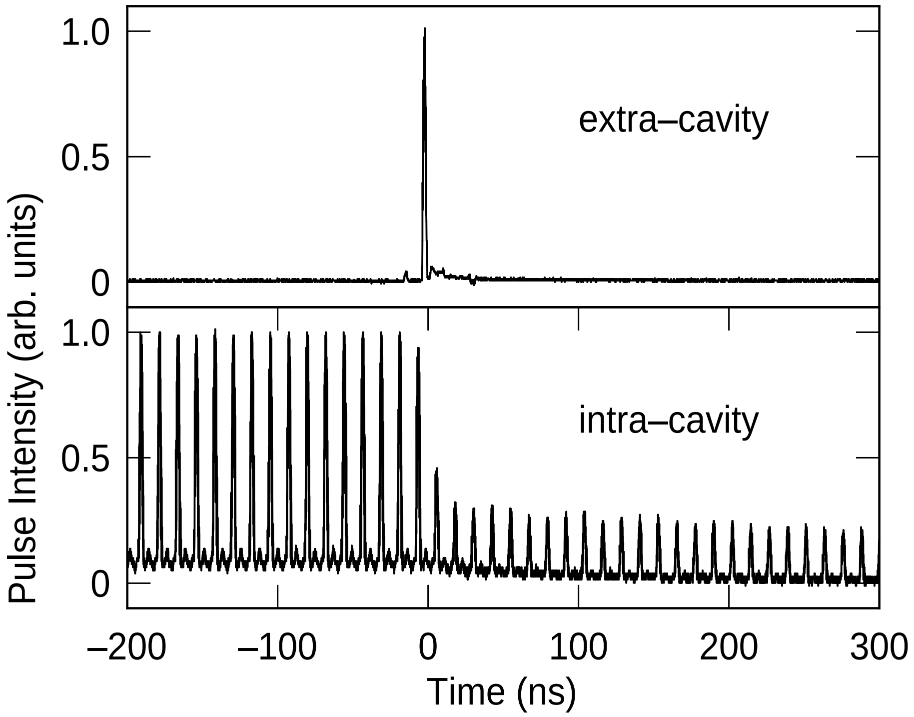

Fig. 3.8: Pulse energy in the oscillator cavity (bottom) and cavity-dumped pulse (top) from the Ti:sapphire laser as a function of time taken with a ns-fast photodiode. The oscillator roundtrip frequency of the mode-locked pulses is 82 MHz. From the shape of the cavity-dumped pulse a side-pulse suppression ratio of smaller than 1:30 can be deduced.

silica is unsuitable. Therefore the half-wave retardation plates for 800 nm (Bernhard Halle Nachfl.) were made of optically polished crystalline quartz. To minimize dispersion effects, they were specified low order to keep their thickness small (0.2 mm). In order to minimize reflection losses both sides of every plate were covered with an antireflection coating. The 3.3 mm thick, fused silica (Suprasil 1) UHV viewport (Caburn-MDC) was carefully checked for residual birefringence. Most parts in the beam path were reflecting mirrors. As the spectral bandwidth of dielectric mirrors was too small for the broadband ultrashort pulses, silver mirrors (Balzers) were employed. Their planarity was specified to better than $\lambda/20$ in order to preserve the spatial coherence of the beam.

Second, the optical elements should open the possibility to alter several properties of the photons in a controlled manner. The chirp of the pulses could be adjusted by translating one of the two compressor prisms. The direction of the linear polarization of all beams could be tuned continuously by changing the angle of the half-wave plates around the optical axis. For a variation of the time delay between the various pulses, tunable delay arms were inserted into the beam path. Besides the mechanical stability, the resolution of the delay stages is their most critical parameter. A temporal

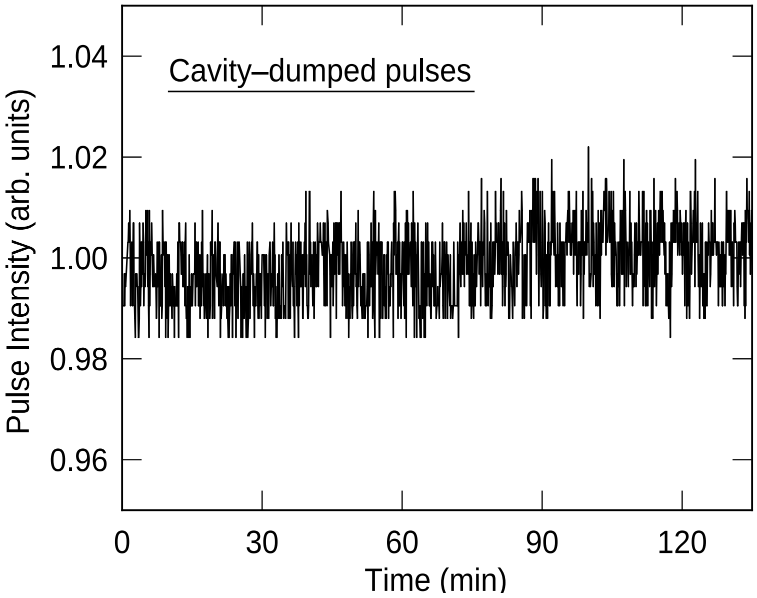

Fig. 3.9: Intensity of the cavity-dumped pulses from the Ti:sapphire laser over a period of 2 hours. The long-term stability of the laser pulses was an essential prerequisite, since the quantitative analysis of the low-level diffracted signal on the order of photons/sec depended on extended signal integration periods.

resolution of 1 fs corresponds to a spatial resolution of 0.15 μm. For this purpose, two microstepping motor driven positioning stages (Aerotech) with 0.1 μm resolution and a piezoelectrically driven translation stage (Physik Instrumente) with 2 nm resolution were employed.

The laser pulses were split with an intensity ratio of 3:7 in the two-beam pump–probe and self-diffraction setup, and of 2:1:1 in the three-beam geometry, leading to typical excitation fluences in the 100 μJ/cm^2 regime. The beams were recombined on the sample at angles of 22° and 24° (2 beams), and 19°, 22°, and 27° (3 beams) with respect to the surface normal. The plane of incidence was normal to the $[2\bar{1}\bar{1}]$ direction of Si(111) and normal to [110] for Si(001). Since after billions of shots onto the sample spot, the SH signal remained at the same level, we exclude any laser induced damage of the surface.

The detection system was optimized for the simultaneous monitoring of two beams of radiation with a wavelength around 400 nm at a rate ranging from 0.1 to 10^6 photons per second. The installation of two detection channels allowed the simultaneous recording of the sum-frequency cross-correlation with either a second-harmonic diffracted trace or a reflected SHG beam. This geometry allowed the independent determination of time-delay zero and thus corrected for delay shifts with time. After parallelization of all emerging beams from the surface with the help of a confocal fused silica lens two beams were selected by circular apertures of 3 mm diameter. Suppres-

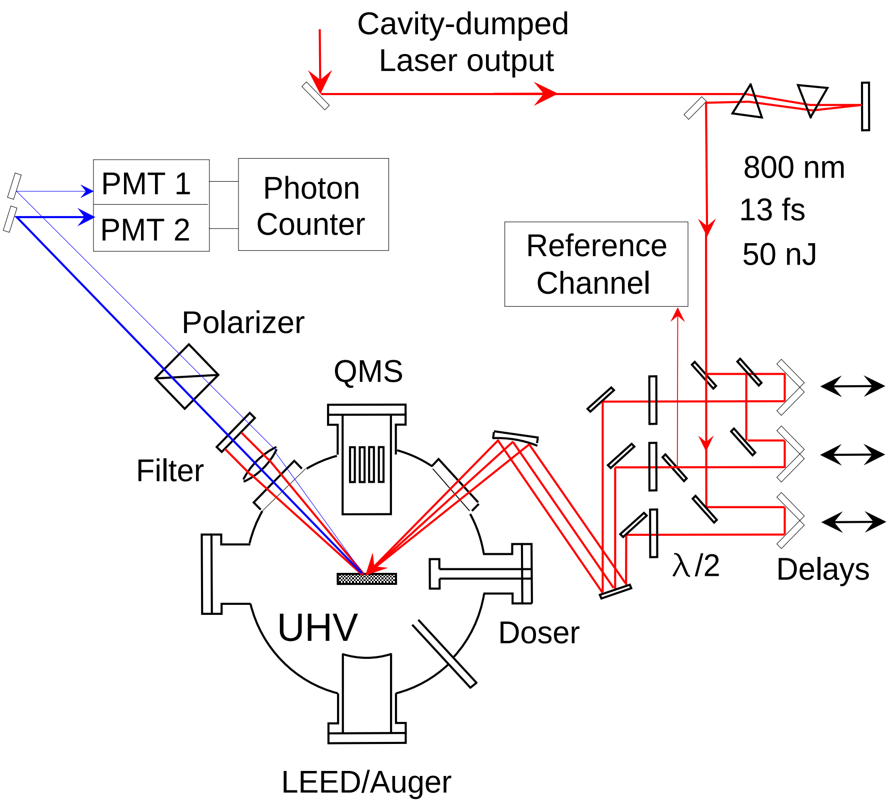

Fig. 3.10: Schematic representation of the optical setup for the second-harmonic diffraction experiment. After compression by two prisms, the pulses are split into two or three beams, which are focused onto the silicon surface in UHV. From the bunch of reflected and diffracted beams emerging from the surface, two second-harmonic rays are detected simultaneously and processed by a two-channel photon counter.

sion of the dominant fundamental radiation at 800 nm was achieved by spatial filtering with apertures as well as spectral selection with optical colored glass filters (Schott BG 39, 3 mm), and dielectric mirrors on fused silica substrates (Laser Components). The second-harmonic 400 nm photons were detected with two photon-counting type photomultiplier tubes (Hamamatsu R1527P) with specified dark currents of 0.1 nA, and counted in two separate channels by a pulse counter (Stanford Research Systems SR 400) that was time-gated at the laser repetition rate triggered by a photodiode. Dark count rates of 5 counts per minute with the laser pulses blocked and 0.2 to 4 counts per second unblocked that was due to unavoidable stray light from the surface were achieved; this threshold corresponds to the detection of a 100 W lightbulb at the distance Earth–Moon through the aperture of the PMT. Taking into account the 10^{17} photons per second emerging from the surface, the detectability threshold corresponds to a ratio of 10^{-17}.

Chapter 4

Theory and simulation

This chapter provides the theoretical background for the description of the diffracted radiation that originates from the surface. The density-matrix formalism that we employ is a semi-classical approach, in which the electromagnetic light field is treated classically, whereas the material system is described quantum-mechanically by its density operator [1]. The light–matter interaction Hamiltonian is inserted in the electric dipole approximation. The approach is mathematically equivalent to a second quantization method within the interaction picture that yields equations of motion derived from the Heisenberg equation [186]. We treat the relaxation of the system within a (Markovian) relaxation-time approximation. Sect. 4.1 starts with an introduction into the density-matrix formalism, which is then applied to an excited three-level system in the limit of weak excitation. An expansion in terms of the electric fields leads to the equations of motion for the nonlinear optical polarizations and populations up to the fourth order, in analogy to the optical Bloch equations [3]. In App. A we present the explicit integration of these iterative differential equations. We derive solutions for special pulse forms of the electric field and treat some special cases like vanishing relaxation times. The numerical integration of the diffracted fourth order signal is the topic of App. B. In Sect. 4.2 we discuss several aspects of the numerical simulation with respect to variations of various input parameters, based on the results of App. B.

4.1 Density matrix expansion

4.1.1 General considerations

The density operator ρ is defined as the ensemble average over the product of the ket and bra state vectors

$$\rho = \sum_j p_j |\psi_j\rangle\langle\psi_j| = \overline{|\psi\rangle\langle\psi|}. \tag{4.1}$$

The ensemble average of a physical quantity $\mathbf{P}$ is then given by

$$\langle\mathbf{P}\rangle = \overline{\langle\psi|\mathbf{P}|\psi\rangle} = \mathrm{Tr}(\rho\mathbf{P}). \tag{4.2}$$

The diagonal matrix elements ρ_{nn} represent the *population* of the system in state

$|n\rangle$, while the off-diagonal matrix elements $\rho_{nn'}$ designate a coherent *polarization*, also called *coherence*, between $|n\rangle$ and $|n'\rangle$.

From the definition of ρ (Eq. 4.1) and from the Schrödinger equation for $|\psi\rangle$ one can readily obtain the equation of motion for ρ,

$$\dot{\rho} = \frac{1}{i\hbar}[\mathcal{H}, \rho], \tag{4.3}$$

known as the Liouville-von Neumann equation. The Hamiltonian $\mathcal{H}$ is composed of three parts [1]

$$\mathcal{H} = \mathcal{H}_0 + \mathcal{H}_{\text{int}} + \mathcal{H}_{\text{random}}. \tag{4.4}$$

$\mathcal{H}_0$ is the Hamiltonian of the unperturbed material system with eigenstates $|n\rangle$ and eigenenergies E_n so that $\mathcal{H}_0|n\rangle = E_n|n\rangle$. Considering a system with three levels $|a\rangle$, $|b\rangle$, and $|c\rangle$,

$$\mathcal{H}_0 = \begin{pmatrix} E_a & . & . \\ . & E_b & . \\ . & . & E_c \end{pmatrix}. \tag{4.5}$$

$\mathcal{H}_{\text{int}}$ is the interaction Hamiltonian describing the interaction of light with matter. In the electric dipole approximation $\mathcal{H}_{\text{int}} = -\boldsymbol{\mu} \cdot \mathbf{E}$,

$$\mathcal{H}_{\text{int}} = \begin{pmatrix} . & \delta_{ab} & . \\ \delta_{ab}^* & . & \delta_{bc} \\ . & \delta_{bc}^* & . \end{pmatrix} \tag{4.6}$$

with components $\delta_{nk} = e\mathbf{r}_{nk} \cdot \mathbf{E}(\mathbf{R}, t)$.
$\mathcal{H}_{\text{random}}$ is a Hamiltonian describing the random perturbation on the system by the thermal reservoir around the system

$$\dot{\rho}_{\text{relax}} = \frac{1}{i\hbar}[\mathcal{H}_{\text{random}}, \rho]. \tag{4.7}$$

Within the Lindblad approach of the Markovian relaxation-time approximation this dissipation term becomes

$$\dot{\rho}_{\text{relax}} = -\Gamma \rho_{\text{relax}} \tag{4.8}$$

with a constant relaxation rate matrix Γ_{nk}. A perturbation expansion of Eq. (4.3) into a power series of $\mathbf{E}$ yields

$$\dot{\rho}^{(n)} = \frac{1}{i\hbar}\left([\mathcal{H}_0, \rho^{(n)}] + [\mathcal{H}_{\text{int}}, \rho^{(n-1)}]\right) - \frac{\rho^{(n)}}{T_i} \tag{4.9}$$

with

$$[\mathcal{H}_0, \rho^{(n)}] \;=\; \begin{pmatrix} E_a & . & . \\ . & E_b & . \\ . & . & E_c \end{pmatrix} \begin{pmatrix} \lambda & l & m \\ l^* & \mu & n \\ m^* & n^* & \nu \end{pmatrix} -$$

$$- \begin{pmatrix} \lambda & l & m \\ l^* & \mu & n \\ m^* & n^* & \nu \end{pmatrix} \begin{pmatrix} E_a & . & . \\ . & E_b & . \\ . & . & E_c \end{pmatrix} \tag{4.10}$$

$$= - \begin{pmatrix} . & (E_b - E_a)l & (E_c - E_a)m \\ -(E_b - E_a)l^* & . & (E_c - E_b)n \\ -(E_c - E_a)m^* & -(E_c - E_b)n^* & . \end{pmatrix} .$$

Eq. (4.9) can now be solved explicitly for $\rho^{(n)}$ in successive orders. The following sections derive differential equations for $\rho^{(n)}$ for $n \leq 4$. These equations are integrated explicitly in App. A and numerically in App. B.

4.1.2 Zeroth order

The usual initial condition reflects the unperturbed system in the ground state,

$$\rho^{(0)} = \begin{pmatrix} 1 & . & . \\ . & . & . \\ . & . & . \end{pmatrix} . \tag{4.11}$$

4.1.3 First order

From Eqs. (4.6) and (4.11) follows

$$\begin{aligned} [\mathcal{H}_{\text{int}}, \rho^{(0)}] &= \begin{pmatrix} . & \delta_{ab} & . \\ \delta_{ab}^* & . & \delta_{bc} \\ . & \delta_{bc}^* & . \end{pmatrix} \begin{pmatrix} 1 & . & . \\ . & . & . \\ . & . & . \end{pmatrix} - \\ &\quad - \begin{pmatrix} 1 & . & . \\ . & . & . \\ . & . & . \end{pmatrix} \begin{pmatrix} . & \delta_{ab} & . \\ \delta_{ab}^* & . & \delta_{bc} \\ . & \delta_{bc}^* & . \end{pmatrix} \\ &= \begin{pmatrix} . & -\delta_{ab} & . \\ \delta_{ab}^* & . & . \\ . & . & . \end{pmatrix} . \end{aligned} \tag{4.12}$$

With

$$\rho^{(1)} = \begin{pmatrix} . & p^{(1)} & . \\ p^{(1)*} & . & . \\ . & . & . \end{pmatrix} \tag{4.13}$$

and with Eq. (4.9), the equation of motion for the first-order polarization $p^{(1)}$ thus is

$$\boxed{\dot{p}^{(1)} = \left(-\frac{E_b - E_a}{i\hbar} - \frac{1}{T_{2,p(1)}} \right) p^{(1)} - \frac{\delta_{ab}}{i\hbar}} \tag{4.14}$$

4.1.4 Second order

From Eqs. (4.6) and (4.13) follows

$$\begin{aligned}
[\mathcal{H}_{\text{int}}, \rho^{(1)}] &= \begin{pmatrix} . & \delta_{ab} & . \\ \delta_{ab}^* & . & \delta_{bc} \\ . & \delta_{bc}^* & . \end{pmatrix} \begin{pmatrix} . & p^{(1)} & . \\ p^{(1)*} & . & . \\ . & . & . \end{pmatrix} - \\
&\quad - \begin{pmatrix} . & p^{(1)} & . \\ p^{(1)*} & . & . \\ . & . & . \end{pmatrix} \begin{pmatrix} . & \delta_{ab} & . \\ \delta_{ab}^* & . & \delta_{bc} \\ . & \delta_{bc}^* & . \end{pmatrix} \\
&= \begin{pmatrix} \delta_{ab} p^{(1)*} - \delta_{ab}^* p^{(1)} & . & -\delta_{bc} p^{(1)} \\ . & \delta_{ab}^* p^{(1)} - \delta_{ab} p^{(1)*} & . \\ \delta_{bc}^* p^{(1)*} & . & . \end{pmatrix}.
\end{aligned} \tag{4.15}$$

With

$$\rho^{(2)} = \begin{pmatrix} n^{(2)} & . & p^{(2)} \\ . & -n^{(2)} & . \\ p^{(2)*} & . & . \end{pmatrix} \tag{4.16}$$

and with Eq. (4.9), the equations of motion for the second-order population $n^{(2)}$ and polarization $p^{(2)}$ thus are

$$\boxed{\begin{aligned} \dot{n}^{(2)} &= -\frac{n^{(2)}}{T_{1,n(2)}} + \frac{\delta_{ab} p^{(1)*} - \delta_{ab}^* p^{(1)}}{i\hbar} \\ \dot{p}^{(2)} &= \left(-\frac{E_c - E_a}{i\hbar} - \frac{1}{T_{2,p(2)}} \right) p^{(2)} - \frac{\delta_{bc} p^{(1)}}{i\hbar} \end{aligned}} \tag{4.17}$$

4.1.5 Third order

From Eqs. (4.6) and (4.16) follows

$$\begin{aligned}
[\mathcal{H}_{\text{int}}, \rho^{(2)}] &= \begin{pmatrix} . & \delta_{ab} & . \\ \delta_{ab}^* & . & \delta_{bc} \\ . & \delta_{bc}^* & . \end{pmatrix} \begin{pmatrix} n^{(2)} & . & p^{(2)} \\ . & -n^{(2)} & . \\ p^{(2)*} & . & . \end{pmatrix} - \\
&\quad - \begin{pmatrix} n^{(2)} & . & p^{(2)} \\ . & -n^{(2)} & . \\ p^{(2)*} & . & . \end{pmatrix} \begin{pmatrix} . & \delta_{ab} & . \\ \delta_{ab}^* & . & \delta_{bc} \\ . & \delta_{bc}^* & . \end{pmatrix} \\
&= \begin{pmatrix} . & -2\delta_{ab} n^{(2)} - \delta_{bc}^* p^{(2)} & . \\ 2\delta_{ab}^* n^{(2)} + \delta_{bc} p^{(2)*} & . & \delta_{ab}^* p^{(2)} + \delta_{bc} n^{(2)} \\ . & -\delta_{bc}^* n^{(2)} - \delta_{ab} p^{(2)*} & . \end{pmatrix}.
\end{aligned} \tag{4.18}$$

With

$$\rho^{(3)} = \begin{pmatrix} . & p_{ab}^{(3)} & . \\ p_{ab}^{(3)*} & . & p_{bc}^{(3)} \\ . & p_{bc}^{(3)*} & . \end{pmatrix} \tag{4.19}$$

and with Eq. (4.9), the equations of motion for the third-order polarizations $p^{(3)}_{ab}$ and $p^{(3)}_{bc}$ thus are

$$\boxed{\begin{aligned}
\dot{p}^{(3)}_{ab} &= \left(-\frac{E_b - E_a}{i\hbar} - \frac{1}{T_{2,pab(3)}}\right) p^{(3)}_{ab} - \frac{2\delta_{ab} n^{(2)} + \delta^*_{bc} p^{(2)}}{i\hbar} \\
\dot{p}^{(3)}_{bc} &= \left(-\frac{E_c - E_b}{i\hbar} - \frac{1}{T_{2,pbc(3)}}\right) p^{(3)}_{bc} + \frac{\delta^*_{ab} p^{(2)} + \delta_{bc} n^{(2)}}{i\hbar}
\end{aligned}} \tag{4.20}$$

4.1.6 Fourth order

From Eqs. (4.6) and (4.19) follows

$$\begin{aligned}
[\mathcal{H}_{\text{int}}, \rho^{(3)}] &= \begin{pmatrix} \cdot & \delta_{ab} & \cdot \\ \delta^*_{ab} & \cdot & \delta_{bc} \\ \cdot & \delta^*_{bc} & \cdot \end{pmatrix} \begin{pmatrix} \cdot & p^{(3)}_{ab} & \cdot \\ p^{(3)*}_{ab} & \cdot & p^{(3)}_{bc} \\ \cdot & p^{(3)*}_{bc} & \cdot \end{pmatrix} - \\
&\quad - \begin{pmatrix} \cdot & p^{(3)}_{ab} & \cdot \\ p^{(3)*}_{ab} & \cdot & p^{(3)}_{bc} \\ \cdot & p^{(3)*}_{bc} & \cdot \end{pmatrix} \begin{pmatrix} \cdot & \delta_{ab} & \cdot \\ \delta^*_{ab} & \cdot & \delta_{bc} \\ \cdot & \delta^*_{bc} & \cdot \end{pmatrix} \\
&= \begin{pmatrix} \delta_{ab} p^{(3)*}_{ab} - \delta^*_{ab} p^{(3)}_{ab} & \cdot & \delta_{ab} p^{(3)}_{bc} - \delta_{bc} p^{(3)}_{ab} \\ \cdot & \begin{matrix} (\delta^*_{ab} p^{(3)}_{ab} - \delta_{ab} p^{(3)*}_{ab}) \\ +(\delta_{bc} p^{(3)*}_{bc} - \delta^*_{bc} p^{(3)}_{bc}) \end{matrix} & \cdot \\ \delta^*_{bc} p^{(3)*}_{ab} - \delta^*_{ab} p^{(3)*}_{bc} & \cdot & \delta^*_{bc} p^{(3)}_{bc} - \delta_{bc} p^{(3)*}_{bc} \end{pmatrix}.
\end{aligned} \tag{4.21}$$

With

$$\rho^{(4)} = \begin{pmatrix} n^{(4)}_a & \cdot & p^{(4)} \\ \cdot & n^{(4)}_b & \cdot \\ p^{(4)*} & \cdot & -n^{(4)}_a - n^{(4)}_b \end{pmatrix} \tag{4.22}$$

and with Eq. (4.9), the equations of motion for the fourth-order populations $n^{(4)}_a$ and $n^{(4)}_b$ and polarization $p^{(4)}$ thus are

$$\boxed{\begin{aligned}
\dot{n}^{(4)}_a &= -\frac{n^{(4)}_a}{T_{1,na(4)}} + \frac{\delta_{ab} p^{(3)*}_{ab} - \delta^*_{ab} p^{(3)}_{ab}}{i\hbar} \\
\dot{n}^{(4)}_b &= -\frac{n^{(4)}_b}{T_{1,nb(4)}} + \frac{(\delta^*_{ab} p^{(3)}_{ab} - \delta_{ab} p^{(3)*}_{ab}) + (\delta_{bc} p^{(3)*}_{bc} - \delta^*_{bc} p^{(3)}_{bc})}{i\hbar} \\
\dot{p}^{(4)} &= \left(-\frac{E_c - E_a}{i\hbar} - \frac{1}{T_{2,p(4)}}\right) p^{(4)} + \frac{\delta_{ab} p^{(3)}_{bc} - \delta_{bc} p^{(3)}_{ab}}{i\hbar}
\end{aligned}} \tag{4.23}$$

4.1.7 Summary of differential equations

It is convenient to introduce

$$\tilde{p}^{(1)} = p^{(1)} \mathrm{e}^{-i\omega t}$$

$$
\begin{aligned}
\tilde{p}^{(2)} &= p^{(2)}\mathrm{e}^{-i2\omega t} \\
\tilde{p}^{(3)}_{ab} &= p^{(3)}_{ab}\mathrm{e}^{-i\omega t} \\
\tilde{p}^{(3)}_{bc} &= p^{(3)}_{bc}\mathrm{e}^{-i\omega t} \\
\tilde{p}^{(4)} &= p^{(4)}\mathrm{e}^{-i2\omega t}
\end{aligned}
\tag{4.24}
$$

and detunings Δ between the incident field frequency and the different transition frequencies

$$
\begin{aligned}
\Delta_{ab} &= \omega - \frac{E_b - E_a}{\hbar} \\
\Delta_{bc} &= \omega - \frac{E_c - E_b}{\hbar} \\
\Delta_{ac} &= 2\omega - \frac{E_c - E_a}{\hbar} = \Delta_{ab} + \Delta_{bc}.
\end{aligned}
\tag{4.25}
$$

With electric fields in the slowly-varying-envelope approximation and couplings δ in the rotating-frame approximation

$$
\delta_{nk} = -\mu_{nk}\mathcal{E}(t)\mathrm{e}^{i\omega t},
\tag{4.26}
$$

assuming matrix elements μ and amplitude $\mathcal{E}$ to be real, and relaxation rates Γ as a function of the (longitudinal) population relaxation times $T_{1,a}$, $T_{1,b}$, $T_{1,c}$ and the (transverse) pure dephasing times $T^*_{2,a}$, $T^*_{2,b}$, $T^*_{2,c}$

$$
\begin{aligned}
\Gamma_{1,b} &= \frac{1}{T_{1,b}} \\
\Gamma_{1,c} &= \frac{1}{T_{1,c}} \\
\Gamma_{2,ab} &= \frac{1}{T^*_{2,a}} + \frac{1}{T^*_{2,b}} + \frac{1}{2T_{1,b}} \\
\Gamma_{2,bc} &= \frac{1}{T^*_{2,b}} + \frac{1}{T^*_{2,c}} + \frac{1}{2T_{1,b}} + \frac{1}{2T_{1,c}} \\
\Gamma_{2,ac} &= \frac{1}{T^*_{2,a}} + \frac{1}{T^*_{2,c}} + \frac{1}{2T_{1,c}},
\end{aligned}
\tag{4.27}
$$

Eqs. (4.14), (4.17), (4.20), and (4.23) can be summarized as

$$
\begin{aligned}
\dot{\tilde{p}}^{(1)} &= -(i\Delta_{ab}+\Gamma_{2,ab})\tilde{p}^{(1)} - \frac{i\mu_{ab}\mathcal{E}}{\hbar} \\
\dot{n}^{(2)} &= -\Gamma_{1,b}n^{(2)} - \frac{i\mu_{ab}\mathcal{E}}{\hbar}(\tilde{p}^{(1)} - \tilde{p}^{(1)*}) \\
\dot{\tilde{p}}^{(2)} &= -(i\Delta_{ac}+\Gamma_{2,ac})\tilde{p}^{(2)} - \frac{i\mu_{bc}\mathcal{E}}{\hbar}\tilde{p}^{(1)} \\
\dot{\tilde{p}}^{(3)}_{ab} &= -(i\Delta_{ab}+\Gamma_{2,ab})\tilde{p}^{(3)}_{ab} + \frac{2i\mu_{ab}\mathcal{E}}{\hbar}n^{(2)} - \frac{i\mu_{bc}\mathcal{E}}{\hbar}\tilde{p}^{(2)} \\
\dot{\tilde{p}}^{(3)}_{bc} &= -(i\Delta_{bc}+\Gamma_{2,bc})\tilde{p}^{(3)}_{bc} - \frac{i\mu_{bc}\mathcal{E}}{\hbar}n^{(2)} + \frac{i\mu_{ab}\mathcal{E}}{\hbar}\tilde{p}^{(2)} \\
\dot{n}^{(4)}_{a} &= -\frac{i\mu_{ab}\mathcal{E}}{\hbar}(\tilde{p}^{(3)}_{ab} - \tilde{p}^{(3)*}_{ab}) \\
\dot{n}^{(4)}_{b} &= -\Gamma_{1,b}n^{(4)}_{b} + \frac{i\mu_{ab}\mathcal{E}}{\hbar}(\tilde{p}^{(3)}_{ab} - \tilde{p}^{(3)*}_{ab}) - \frac{i\mu_{bc}\mathcal{E}}{\hbar}(\tilde{p}^{(3)}_{bc} - \tilde{p}^{(3)*}_{bc}) \\
\dot{\tilde{p}}^{(4)} &= -(i\Delta_{ac}+\Gamma_{2,ac})\tilde{p}^{(4)} - \frac{i\mu_{bc}\mathcal{E}}{\hbar}\tilde{p}^{(3)}_{ab} + \frac{i\mu_{ab}\mathcal{E}}{\hbar}\tilde{p}^{(3)}_{bc}.
\end{aligned}
\tag{4.28}
$$

The iterative differential equations (4.28) are equivalent to the expansion of the optical Bloch equations in terms of the electric field [3], named in analogy to the equations first derived by Bloch for non-dissipative independent two-level spin systems [187, 188].

4.2 Discussion of numerical simulations

In order to obtain analytical results, the excitation pulses $\mathcal{E}$ in the optical Bloch equations (4.28) are frequently assumed to be δ-pulses in time [189]. This treatment bears several inadequacies for the determination of the nonlinear optical populations and polarizations. Within this approximation the third and fourth order nonlinear optical polarizations are identically zero for negative time delays. In addition, there remain only two (one) non-vanishing terms in $p^{(4)}$ ($p^{(3)}$), out of six (two) terms altogether (see Sect. A.6). In consequence, the δ-pulse approximation only yields relevant results for time delays that are large compared to the pulse duration, since the different optical pulses do no longer overlap temporally in this case.

In order to acquire meaningful results at time delays small compared to the pulse width, it is thus mandatory to solve the optical Bloch equations (4.28) numerically. This is especially crucial in our investigation that experimentally delivers diffracted signal shifts on the order of the pulse duration (see Figs. 6.1 and 6.8). A detailed description of the numerical integration is the topic of App. B.

The following sections present results of the numerical treatment for the SH self-

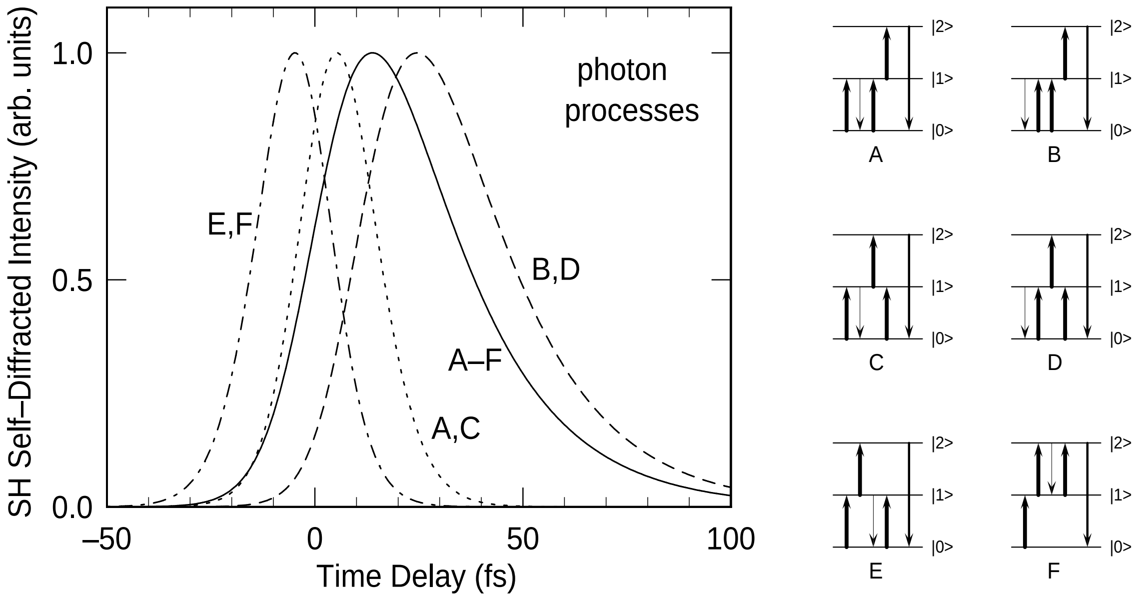

Fig. 4.1: Normalized SH self-diffracted intensity as a function of pump–probe time delay calculated for the six different photon processes A through F (Eqs. B.7–B.12) individually as shown schematically in Fig. 6.11, as well as for all six processes A–F combined (Eq. B.13). The calculation is performed for a homogeneous, resonantly excited three-level system for a pulse duration of 14 fs and T_1 and T_2^* times of 100 fs. The traces C, D, and F are almost identical to the traces A, B, and E, respectively. Both absolute magnitude and sign of the shifts with respect to time delay zero are plausible from the photon diagrams in Fig. 6.11, as explained in the text.

diffracted intensity as a function of time delay. Numerical results for the SH three-beam experiment are discussed in Chap. 6. The influence of several parameters and physical quantities on the diffracted signal is investigated, such as the behavior of the distinct photon process, pulse duration, detuning of the pulse with respect to the transition frequencies, and most importantly the relaxation times. This analysis yields important information for the interpretation of the experimental data.

4.2.1 Behavior of the different photon processes

The explicit integration of the optical Bloch equations (4.28) up to the fourth order polarization $p^{(4)}$ in App. A reveals the existence of six distinct terms contributing to the SH diffracted signal in each of the self-diffracted directions, *e.g.* $3\mathbf{k}_\mathrm{a}-\mathbf{k}_\mathrm{b}$ (see Eq. A.9). A schematic illustration of the emergence of the six different terms from the differential equations through four consecutive optical transitions between the three participating electronic levels is shown in Fig. 6.10. The six photon processes denoted A–F themselves are depicted in Fig. 6.11.

Fig. 4.1 shows the SH self-diffracted correlation traces calculated for the six distinct photon processes A through F individually (from Eqs. B.7–B.12), as well as for all six processes A–F combined (from Eq. B.13). Input parameters for the calculation that assumed a homogeneous, resonantly excited three-level system are a pulse duration of 14 fs, and all population relaxation times T_1 and pure dephasing times T_2^* of 100 fs. The correlation traces for the individual photon processes appear in three qualitatively different shapes, since the signals of C, D, and F are too close to the signals A, B, and E, respectively, to be distinguishable on the scale of Fig. 4.1.

Traces B and D, which differ only in the temporal sequence of the third and fourth incident photon (see Fig. 6.11), display the biggest shift to positive time delays. This is plausible due to the fact that all three photons of the second pulse temporally follow the photon of the first pulse. Therefore it is not necessary for the two pulses to temporally overlap for a finite SH self-diffracted signal to appear, as long as a finite dephasing time allows the coherent polarization to remain long enough in the surface to interact with the electric field of the second pulse. As a consequence, the shift of traces B and D with respect to time delay zero varies sensitively with the dephasing time T_2 of the polarization.

This is different to the situation for traces A and C, which also differ only in the sequence of photons three and four. Here, the three photons of pulse two both succeed *and* precede the incident photon of pulse one (see Fig. 6.11). Thus the SH self-diffracted signal is confined to the time interval of temporal overlap between pulses one and two, *i.e.* close to time delay zero. The processes A and C are therefore rather insensitive to the magnitude of the dephasing time.

Processes E and F differ only in the transition levels of photons three and four: between ground and intermediate level for process E, between intermediate and upper level for process F (see Fig. 6.11). Traces E and F are similar to traces A and C regarding the fact that photons of the second pulse arrive before and after the photon of the first incident pulse. In contrast to processes A and C, however, the majority of photons of the second pulse (*i.e.* two photons) arrive *before* the photon of the first pulse in processes E and F. These oberservations imply traces E and F also to be limited to the time interval of temporal overlap between pulses one and two, but with a *negative* shift with respect to time delay zero. Besides this inverted behavior, the similarity between processes E/F and A/C gives rise to a similar absolute magnitude of the temporal shift.

The overall trace A–F, as a coherent superposition of all six processes, displays an intermediate behavior. For the homogeneous system under consideration, the trace A–F thus shows a long-lived signal at positive time delays, due to the contribution of processes B and D. In an inhomogeneously broadened system, however, the superposition of the various eigenfrequencies leads to a more rapid decay of the SH self-diffracted signal, and thus to a less clear dependence of the shift on the dephasing time (see following subsections).

The following calculations were all performed taking into account the full set of

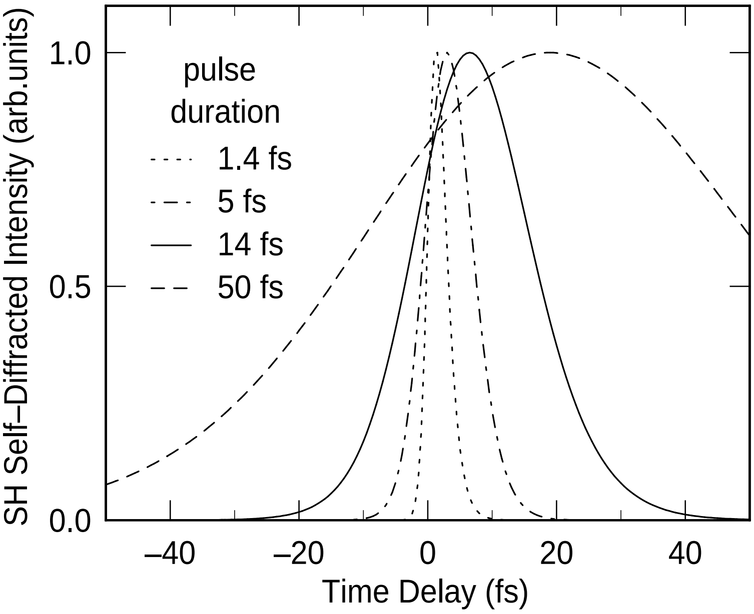

Fig. 4.2: Normalized SH self-diffracted intensity as a function of pump–probe time delay calculated for different durations of the sech^2 pulses. The calculation is performed for a homogeneous, resonantly excited three-level system for T_1 times of 200 fs and T_2^* times of 5 fs. Both shift and FWHM of the shown traces display a sensitive dependence on the duration of the incident pulses.

differential equations, corresponding to a coherent superposition of all six processes A–F.

4.2.2 Role of pulse duration

The analysis of the distinct traces in the preceding subsection revealed the significant influence of processes that yield a finite SH diffracted signal only in the case of temporal overlap between the two incident pulses. For a correct quantitative analysis of the diffracted signal it is thus necessary to investigate the effect of variable pulse duration on the temporal shape of the SH self-diffracted intensity.

In Fig. 4.2 the diffracted signal is displayed for different durations of the sech^2 pulses, calculated for a homogeneous, resonantly excited three-level system for T_1 times of 200 fs and pure dephasing times T_2^* for all three levels of 5 fs. The various pulse durations give rise to a pronounced variation in both temporal shift and width of the diffracted correlation trace.

This analysis shows the crucial importance of the *simultaneous* measurement of both SH self-diffracted intensity and SFG cross-correlation in the experiment (see Chap. 6). The accurate determination of the pulse duration from the SFG cross-correlation trace then allows to extract other quantities, such as the relaxation times,

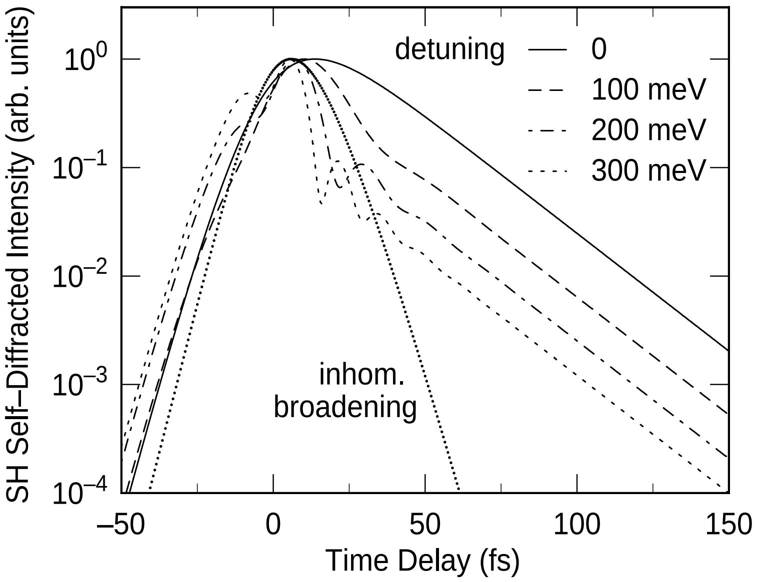

Fig. 4.3: Normalized SH self-diffracted intensity as a function of pump–probe time delay calculated for different detunings of the incident photon energy with respect to the $|0\rangle$–$|1\rangle$ eigenenergy of the three-level system, and also for an inhomogeneously broadened system with a 600 meV broad intermediate band $|1\rangle$ centered around the resonant photon energy. The calculation is performed for a pulse duration of 14 fs, T_1 times of 200 fs, and T_2^* times of 5 fs. The traces for the homogeneous system display an exponentially decreasing wing at positive time delays, whose magnitude decreases monotonically with the detuning.

from the self-diffracted signal.

4.2.3 Effects of detuning

The calculations presented up to this point were all conducted for a homogeneous, resonantly excited three-level system. A look at the physical systems under observation, namely the Si(111)7×7 and Si(001) surfaces, reveals both homogeneity and resonant excitation to be simplifications. The electronic band structures of the surfaces (Figs. 2.2 and 2.4) show a finite dispersion over the Brillouin zone, which leads to an inhomogeneous broadening in k-space. A further contribution to the finite distribution of transition energies in Si(111)7×7 comes from the presence of four different types of adatoms, corner and center adatoms on both triangular halves of the unit cell (see Fig. 2.1), that lead to four energetically different adatom dangling-bond bands. In Fig. 2.1 these bands are indicated schematically by just one band U_1/S_1.

In order to obtain meaningful quantitative results for the relaxation times it is thus useful to study the influence of off- and near-resonant excitation as well as excitation of an inhomogeneous distribution of uncoupled three-level systems. Excitation of a continuum of states is discussed in Chap. 6.

Fig. 4.3 shows the SH self-diffracted correlation trace for a homogeneous system with various detunings of the incident photon energy with respect to the $|0\rangle$–$|1\rangle$ eigenenergy of the three-level system, as well as for an inhomogeneously broadened system with a 600 meV broad intermediate band $|1\rangle$ centered around the resonant photon energy. The traces were calculated for a pulse duration of 14 fs, T_1 times of the intermediate and upper levels of 200 fs, and pure dephasing times of all three levels of 5 fs. The logarithmic scale on the y-axis reveals the exponentially decreasing tail at positive time delays, that is a consequence of the relaxation time approximation Eq. (4.8) employed in the Bloch equations (4.28), and thus is a signature of the population relaxation and dephasing times. The magnitude of the tails decreases with increasing detuning without affecting the slope that is determined by the relaxation times. In the region of temporal overlap of the two incident pulses a finite detuning leads to a modulation of the SH diffracted signal, whose amplitude decays to positive time delays.

The correlation trace from the inhomogeneously broadened system displays a different behavior. Although also being shifted to positive time delays, the interference within the distribution of eigenfrequency components eliminates the long-lived tail in the correlation trace in such a way that the correlation trace follows the behavior of the cross-correlation of the incident optical pulses. Similar results for degenerate *four*-wave mixing have been obtained by Weiner *et al.* [169] and Meier [190].

4.2.4 Influence of relaxation rates

Since the goal of our investigation is to acquire quantitative information on the relevant electronic relaxation processes, a sensitivity analysis of the calculated SH self-diffracted correlation traces with respect to the population relaxation as well as dephasing input parameters is mandatory.

The influence of different population relaxation times of the intermediate and upper level of an inhomogeneously broadened three-level system on the SH self-diffracted correlation trace is shown in Fig. 4.4. As in Fig. 4.3, the pulse duration was 14 fs, the pure dephasing time of all three levels 5 fs, and the broadening of the intermediate level 600 meV. For vanishing population relaxation times (which implies vanishing dephasing times as well, see Eq. 4.27), an explicit integration of the optical Bloch equations yields a symmetric SH self-diffracted correlation trace with a FWHM of $\sim$77% of the SFG cross-correlation width for ideal sech^2 pulses (see Sect. A.7, Eqs. A.12 and A.19). The fact that for population relaxation times small compared to the pulse duration the numerical simulation approximates the analytical result is a further verification of the validity of the numerical approach.

Finite T_1 times give rise to a shift of the SH self-diffracted signal to positive time delays. As Fig. 4.4 shows, the magnitude of the shift monotonically increases with rising T_1 from zero to a saturation value that is limited by the dephasing time. The

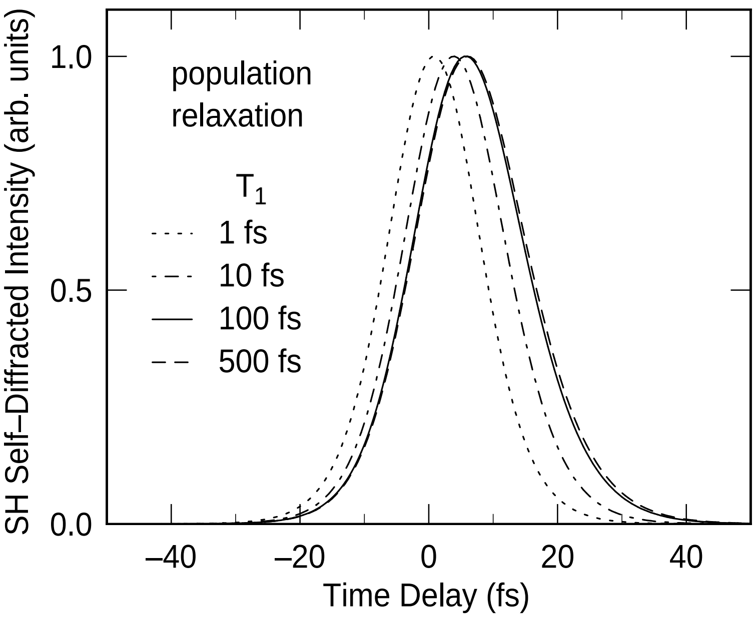

Fig. 4.4: Normalized SH self-diffracted intensity as a function of pump–probe time delay calculated for different population relaxation times T_1 of the intermediate and upper level of the inhomogeneously broadened three-level system. The pure dephasing times T_2^* were assumed to be 5 fs, with a pulse duration of 14 fs and a broadening of the intermediate level of 600 meV. The SH self-diffracted correlation trace shows a positive shift with respect to time delay zero, that is close to zero for very small T_1 times and increases to a saturation value at high T_1 times that is limited by the dephasing time.

saturation complies with the behavior for inhomogeneous systems as discussed in Fig. 4.3.

The small variation of the peak shift with respect to the pulse duration implies that the SH self-diffracted correlation trace is very insensitive to variations in T_1. Since, however, the population relaxation time T_1 can be obtained rather accurately from both the SH pump–probe and SH three-beam diffraction traces (see Figs. 5.9 and 5.10), the value for T_1 obtained from those experiments can be inserted into the simulation of the self-diffracted traces as fixed input parameter.

Fig. 4.5 shows the influence of different dephasing times on the behavior of the SH self-diffracted correlation traces. Although the temporal peak shift of the traces varies more significantly than for different T_1 times, the sensitivity of the variation on T_2 is still rather small, which complicates a precise evaluation of the dephasing time from the measured data. A similar result for degenerate *four*-wave mixing, that is applicable to dephasing of *bulk* states, was obtained by Weiner *et al.* [169]. A more quantitative analysis of the calculated diffraction traces in comparison with our measured data is discussed in Chap. 6 (see Fig. 6.2).

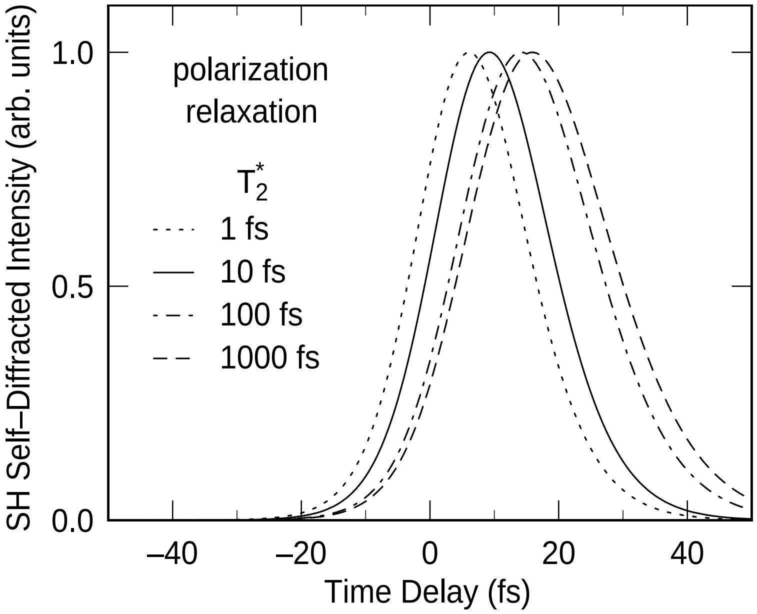

Fig. 4.5: Normalized SH self-diffracted intensity as a function of pump–probe time delay calculated for different pure dephasing times T_2^* of all three levels of the inhomogeneously broadened system. The population relaxation times T_1 were assumed to be 200 fs, with a pulse duration of 14 fs and a broadening of the intermediate level of 600 meV. The SH self-diffracted correlation trace is not very sensitive to changes in T_2, which complicates a precise determination of the dephasing time. Unlike the dependence on T_1 as shown in Fig. 4.4, the correlation trace displays a finite shift even for vanishing dephasing time, due to the finite remanence of the population.

Chapter 5

Incoherent dynamics

This chapter presents, models, and discusses the incoherent relaxation behavior of the excited dangling bond surface states on Si(111) and Si(001). The incoherent electron dynamics reflects the population relaxation of excited carriers that arises from multiple scattering processes of the carriers out of the optically coupled region in k-space. Two purely optical techniques are employed to monitor the population relaxation – which can be described in the Markovian relaxation-time approximation by a longitudinal relaxation time T_1 – with femtosecond time-resolution. The incoherent second-harmonic (SH) pump–probe experiment directly samples the decay of a surface-state population that is induced by a resonant or near-resonant pump pulse. The coherent SH diffraction method in the three-beam geometry also allows to follow the relaxation through sampling the decay of the induced surface-state population grating. Both methods yield identical temperature dependent T_1 relaxation times on the order of 100 fs for dangling-bond surface states on silicon.

Before the presentation of the time-dependent measurements, it is useful to have some insight into the nature of the excitation mechanism and into the influence of the electronic excitation on the nonlinear optical response. For this purpose, we have investigated in Sect. 5.1 the *static* dependence of the second-harmonic intensity on the density of unoccupied dangling bond states, which can be controlled by adsorption, heating to a different surface reconstruction, and optical pumping. After these prerequisites, Sect. 5.2 presents the time-resolved measurements on the dangling bond dynamics using both the incoherent SH pump–probe and the coherent SH diffraction methods. Sect. 5.3 terminates this chapter with a discussion of the relevant relaxation mechanism that is implied by the measured data.

5.1 Excitation mechanism

In order to elucidate the excitation mechanism relevant to the dynamic properties of the surface state carriers, this section investigates the *static* behavior of the SH intensity during oxygen adsorption, its laser pulse fluence dependence, and its reaction while heating through the Si(111)7×7 ↔ "1×1" phase transition. Polarization-dependent measurements that yield information on the nature of the transient grating are also presented.

5.1.1 Coverage dependence of the SH intensities

As discussed in Sect. 2.2, second-harmonic spectroscopic measurements [134] and hydrogen adsorption experiments [74, 191] reveal that the second-harmonic process on silicon surfaces with incident photon energies around 1.55 eV (800 nm) is not only resonantly enhanced by unoccupied dangling bond states; there exists a further contribution to $\chi_{\mathrm{s}}^{(2)}$ by the E_1 resonance that is due to perturbed Si–Si bonds in the surface layer. Since the adsorption of hydrogen or oxygen quenches the dangling bond states, while disturbing the Si–Si bonds only to a small extent, it is possible to experimentally distinguish between the two terms by studying the behavior of the second-harmonic intensity during adsorption.

Fig. 5.1 shows the SFG intensity and the SH self-diffracted intensity from Si(111) and Si(001) as a function of molecular oxygen exposure. The solid lines denote the SH signal into the sum-frequency direction. This signal first decreases as a function of oxygen exposure; there is a minimum at 1.3 Langmuir (2.2 L), then the signal increases again and saturates at 39% (11%) of its initial value, for Si(111) (Si(001)). This behavior is well understood from Eq. (5.1). The SH response of the clean surface is dominated by the dangling-bond derived term. As more and more dangling bonds saturate as a result of oxygen exposure the signal decreases monotonically until the dangling-bond contribution becomes comparable with the nonresonant term in $\chi_{\mathrm{s}}^{(2)}$. A phase shift between both contributions, which are complex quantities, leads almost to a cancellation at an intermediate coverage. At high coverages, after a complete passivation of the surface, all dangling bonds are quenched and the SH response is thus given by the nonresonant background term.

The circles in Fig. 5.1 correspond to the SH self-diffracted signal from both *p*-polarized beams. This signal is 3 orders of magnitude weaker than the SFG signal. It decreases monotonically to zero as a function of oxygen exposure. The fact that this signal does not exhibit a minimum for intermediate oxygen exposures is important because it demonstrates that the main effect of the interfering incident beams is indeed the generation of a population grating of the Si dangling bonds, since this term is monotonically reduced during adsorption. Other possible excitations that might cause a spatial modulation of the SH efficiency appear to be weak.

For a quantitative analysis of the population changes of the dangling-bond surface states as well as of the relative influence of the nonresonant background term, we express the dependence of the surface second-order nonlinear optical susceptibility $\chi_{\mathrm{s}}^{(2)}$ on coverage θ as a sum of two contributions [74]

$$\chi_{\mathrm{s}}^{(2)}(\theta) = \chi_{\mathrm{s,db}}^{(2)}(1-\theta) + \chi_{\mathrm{s,NR}}^{(2)}. \tag{5.1}$$

The first term on the right side is the resonant contribution proportional to the

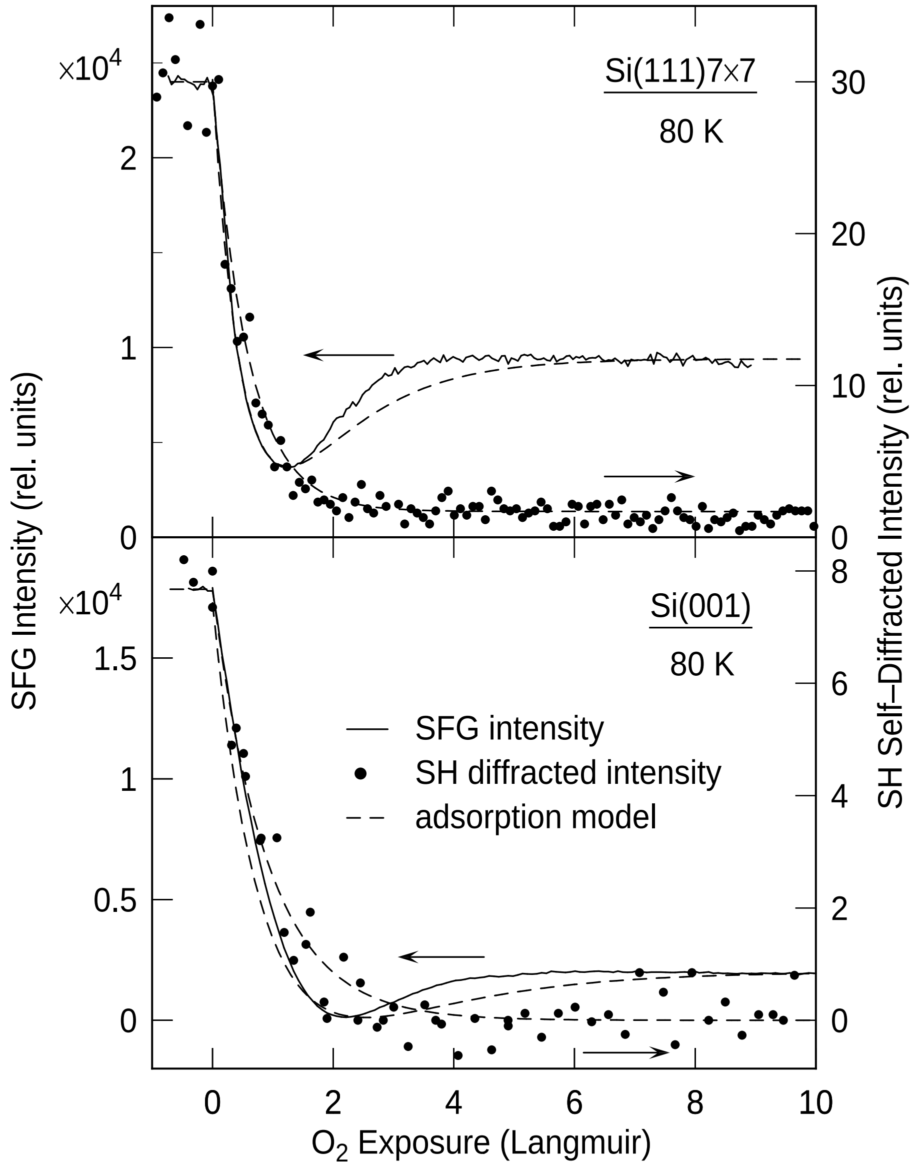

Fig. 5.1: Dependence of the sum-frequency intensity (solid lines, left scales) and SH self-diffracted intensity (circles, right scales) from Si(111)7×7 (top panel) and Si(001) (bottom panel) at 80 K for zero time delay on molecular oxygen exposure. The dashed lines are fits based on the Langmuir adsorption model discussed in the text. The minima in the SFG intensities display the destructive interference between the resonant dangling-bond derived term and the nonresonant background term in $\chi_{\mathrm{s}}^{(2)}$ during oxygen exposure. The fact that there is no minimum in the SH diffracted intensities implies that the only contribution to this signal arises from the dangling-bond term.

number of dangling bonds, that is $\chi_{\mathrm{s,db}}^{(2)}$ for the clean surface ($\theta = 0$) and zero for the passivated surface ($\theta = 1$). The nonresonant background term $\chi_{\mathrm{s,NR}}^{(2)}$ mainly arises from the two-photon resonance at $2\omega = 3.4$ eV of the E$_1$ transition [145], but also includes

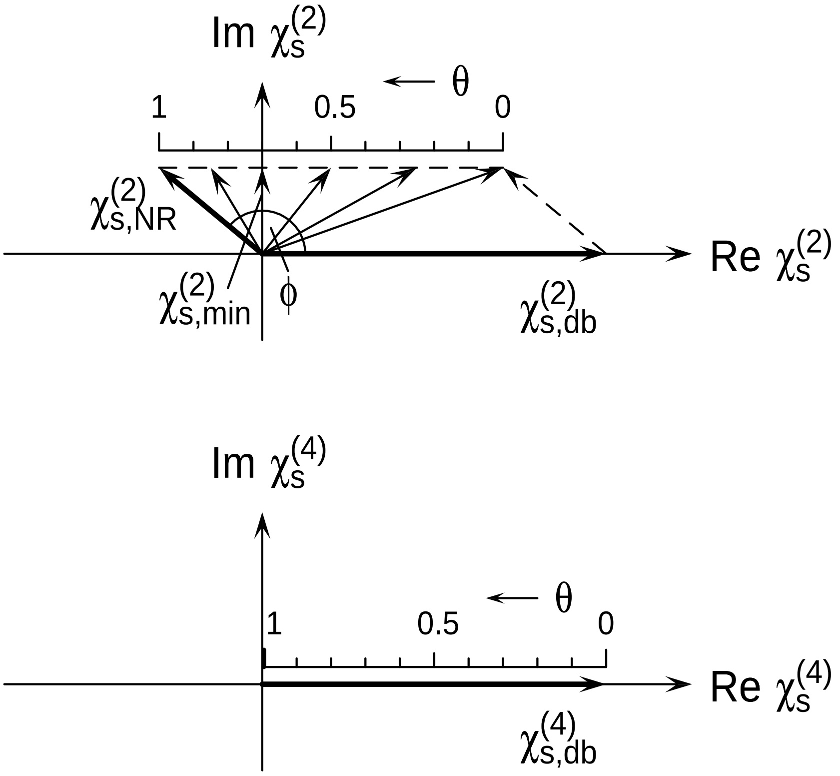

Fig. 5.2: Schematic visualization of the model for the dependence of the nonlinear optical susceptibilites $\chi_s^{(2)}$ (top) and $\chi_s^{(4)}$ (bottom) on coverage. The destructive interference between the dangling bond contribution and the nonresonant background leads to a minimum in the absolute magnitude of $\chi_s^{(2)}$ during adsorption, whereas the sole contribution of the dangling-bond term gives rise to the monotonic decrease in $\chi_s^{(4)}$ (see Fig. 5.1).

bulk quadrupolar and higher order surface and bulk contributions to SHG [70]. Since the coverage dependence of $\chi_{s,NR}^{(2)}$ is weak [134] and its contribution to the overall SH response is relatively small, this term is assumed to be independent of coverage. A schematic visualization of the behavior of $\chi_s^{(2)}$ during adsorption according to Eq. (5.1) is depicted in the upper part of Fig. 5.2.

The quadratic pulse fluence dependence of SHG on both clean and passivated silicon surfaces at our maximal fluences of 400 μJ/cm^2 (see Fig. 5.4 and Refs. [74, 133]) with the absence of any discernible saturation phenomena, indicates that these excitation conditions exert no significant influence on the population of dangling bonds. Both $\chi_{s,db}^{(2)}$ and $\chi_{s,NR}^{(2)}$ can therefore be assumed to be independent of fluence for our experimental conditions.

Considering the phase difference ϕ between the complex quantities $\chi_{s,db}^{(2)}$ and $\chi_{s,NR}^{(2)}$, Eq. (5.1) yields the nonlinear susceptibility (and thereby the relative SH intensities) from the clean surface, in the minimum of the adsorption curve, and at saturation

		Si(111)7×7	Si(001)
surface quantities	dangling bond density (cm^{-2})	$3.04 \cdot 10^{14}$	$6.78 \cdot 10^{14}$
measured quantities	$I_{\mathrm{SFG,min}}/I_{\mathrm{SFG}}(\theta\!=\!0)$	0.16	0.0069
	$I_{\mathrm{SFG}}(\theta\!=\!1)/I_{\mathrm{SFG}}(\theta\!=\!0)$	0.39	0.11
	$\theta_{\mathrm{SFG,min}}$	1.3 L	2.2 L
	$\theta_{\mathrm{diffr,decay}}$	0.59 L	0.91 L
calculated quantities (Langmuir adsorption kinetics)	$\lvert\chi^{(2)}_{\mathrm{s,db}}\rvert/\lvert\chi^{(2)}_{\mathrm{s,NR}}\rvert$	2.2	3.9
	(literature data)	3.3 [133], 2.6 (H_2) [192]	–
	ϕ	141°	166°
	(literature data)	164° [133], 132° [138], 160° [140], 160° (H_2) [192]	–
	s_0	0.7	1.0
	(literature data)	0.88 [193], 0.92 [179], 0.6 [133], 0.3 [140]	–

Tab. 5.1: Measured and calculated values, derived from Fig. 5.1, for the adsorption of molecular oxygen on Si(111)7×7 and Si(001) at 80 K compared to literature data.

coverage [133]

$$\begin{aligned}
\lvert\chi^{(2)}_{\mathrm{s}}(\theta\!=\!0)\rvert^2 &= \lvert\chi^{(2)}_{\mathrm{s,db}}\rvert^2 + 2\lvert\chi^{(2)}_{\mathrm{s,db}}\rvert\lvert\chi^{(2)}_{\mathrm{s,NR}}\rvert\cos\phi + \lvert\chi^{(2)}_{\mathrm{s,NR}}\rvert^2 \\
\lvert\chi^{(2)}_{\mathrm{s,min}}\rvert^2 &= \lvert\chi^{(2)}_{\mathrm{s,NR}}\rvert^2\sin^2\phi \\
\lvert\chi^{(2)}_{\mathrm{s}}(\theta\!=\!1)\rvert^2 &= \lvert\chi^{(2)}_{\mathrm{s,NR}}\rvert^2.
\end{aligned} \tag{5.2}$$

The measured values extracted from Fig. 5.1 for the relative magnitudes $\lvert\chi^{(2)}_{\mathrm{s}}(\theta\!=\!1)\rvert/\lvert\chi^{(2)}_{\mathrm{s}}(\theta\!=\!0)\rvert$ and $\lvert\chi^{(2)}_{\mathrm{s,min}}\rvert/\lvert\chi^{(2)}_{\mathrm{s}}(\theta\!=\!0)\rvert$ for Si(111) and for Si(001) are shown in Tab. 5.1. The insertion of these data into Eq. (5.2) yields for Si(111)

$$\begin{aligned}
\lvert\chi^{(2)}_{\mathrm{s,db}}\rvert/\lvert\chi^{(2)}_{\mathrm{s,NR}}\rvert &= 2.2 \\
\phi &= 141^\circ
\end{aligned} \tag{5.3}$$

and for Si(001)

$$\begin{aligned}
\lvert\chi^{(2)}_{\mathrm{s,db}}\rvert/\lvert\chi^{(2)}_{\mathrm{s,NR}}\rvert &= 3.9 \\
\phi &= 166^\circ.
\end{aligned} \tag{5.4}$$

The obtained values for the magnitude ratio and relative phase of the two contributions are in reasonable agreement with previously determined values (Refs. [133, 138, 140, 192]).

The dependence of the oxygen coverage θ on the impinging O_2 molecule flux Φ can be modeled with Langmuir adsorption kinetics, which assumes the sticking coefficient to be proportional to unoccupied adsorption sites, $s(\theta) = s_0 \cdot (1-\theta)$, and thus yields [194]

$$\theta = 1 - \exp(-s_0 \Phi t), \tag{5.5}$$

where the initial sticking coefficient s_0 is treated as a fit parameter.

An exposure of 1 L = 10^{-6} Torr·s corresponds to $3.58 \cdot 10^{14}$ cm^{-2} O_2 molecules striking the surface at a gas temperature of 300 K. In combination with the dangling bond densities of $3.04 \cdot 10^{14}$ cm^{-2} on Si(111)7×7 and of $6.78 \cdot 10^{14}$ cm^{-2} on Si(001), a fit to the SFG intensity yields $s_{0,(111)} = 0.7$ for Si(111) and $s_{0,(001)} = 1.0$ for Si(001). These obtained initial sticking coefficients are also in reasonable agreement with other investigations, using SHG [133, 179], SFG [140], XPS [146], and LITD [193].

The dashed lines for the SFG intensities in Fig. 5.1 result from the adsorption model based on Eq. (5.1) under the assumption of Langmuir kinetics. They are in excellent agreement with the measured data (solid lines in Fig. 5.1) up to the minimum in SFG intensity, corresponding to a coverage around 0.7 ML. The discrepancies between calculated and measured SFG intensities at coverages above the minimum may be due to the increasing non-validity of Langmuir kinetics at higher coverages caused by adsorbate interactions.

Modeling the coverage dependence of the nonlinear optical susceptibility $\chi_{\mathrm{s}}^{(4)}$ responsible for the SH diffracted radiation by a linear relation

$$\chi_{\mathrm{s}}^{(4)}(\theta) = \chi_{\mathrm{s,db}}^{(4)} \cdot (1-\theta), \tag{5.6}$$

where $\chi_{\mathrm{s,db}}^{(4)} = \chi_{\mathrm{s}}^{(4)}(\theta=0)$ is the fourth order response function of the clean surface that arises from the dangling bonds, we obtain from

$$I_{\mathrm{diffr}} \propto |\chi_{\mathrm{s}}^{(4)}|^2 \tag{5.7}$$

the SH diffracted intensity

$$I_{\mathrm{diffr}}(\theta) = I_{\mathrm{diffr}}(\theta=0) \exp(-2 s_0 \Phi t). \tag{5.8}$$

The dashed lines for the SH self-diffracted intensities in Fig. 5.1 are derived from Eq. (5.8), using the initial adsorption coefficients obtained from the fits to the SFG intensities. The fact that they are in excellent agreement with the measured diffracted signals (circles in Fig. 5.1) is a further indication for the validity of the SH coverage dependence model of Eq. (5.1).

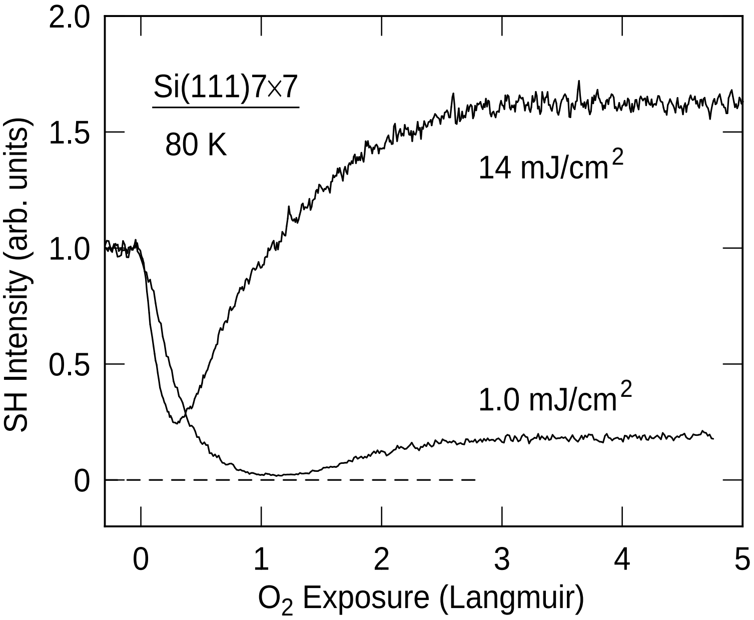

Fig. 5.3: Dependence of the specular reflected SH intensity from Si(111)7×7 at 80 K on oxygen exposure generated by 120-fs pulses at 800 nm with fluences of 1.0 mJ/cm^2 and 14 mJ/cm^2. Though both measurements display the characteristic minimum feature that was discussed in the preceding section (see Fig. 5.1), for the higher pulse fluence the minimum occurs for much smaller oxygen coverage and the response of the oxygen-saturated surface exceeds that of the clean surface. This is a consequence of the strong electronic excitation of the U$_1$ band by the 14 mJ/cm^2-pulse, which reduces the relative strength of $\chi^{(2)}_{\mathrm{s,db}}$ as compared to $\chi^{(2)}_{\mathrm{s,NR}}$. (From Mauerer [133]).

5.1.2 Fluence dependence of the SH intensities

Besides adsorption, a second independent means of reducing the dangling bond density is by resonant or near-resonant optical pumping. A sufficiently intense pump pulse can excite electrons from an occupied electronic surface band or from bulk valence states to a normally unoccupied dangling-bond surface band, thereby diminishing the SH nonlinear optical response. Fig. 5.3 shows the reflected SH intensity from Si(111)7×7 as a function of the exposure with molecular oxygen for two different laser pulse fluences, observed by Mauerer [133].

The SH signal generated by the 1.0 mJ/cm^2 beam first decreases as a function of oxygen exposure; there is a minimum for about 1 Langmuir, then the signal increases again and saturates at 20% of its initial value, similar to the data shown in Fig. 5.1. The quantitative differences to the measurements in Fig. 5.1 can be assigned to the different excitation pulse properties (120 fs, spectrally narrow, one order of magnitude higher pulse fluence) and different input and output polarizations.

For the reflected SH signal from the intense 14 mJ/cm^2 pulse, the minimum occurs

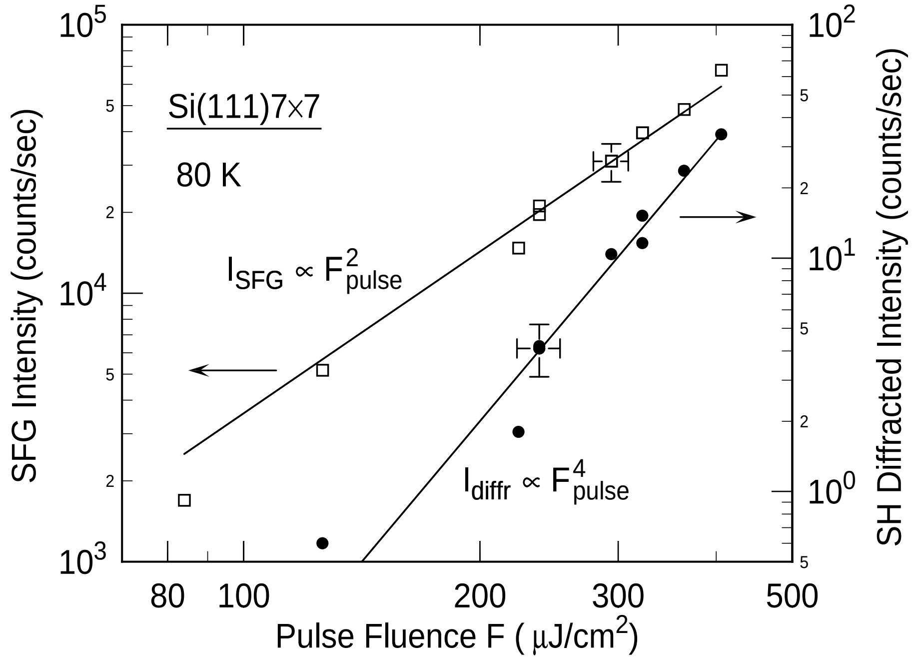

Fig. 5.4: SFG cross-correlation intensity (open squares, left scale) and SH self-diffracted intensity (circles, right scale) from a clean Si(111)7×7 surface as a function of laser pulse fluence F. The lines fitted to the data are proportional to F^2 and F^4, respectively.

for much smaller oxygen coverage and the response of the oxygen-saturated surface exceeds that of the clean surface. Here, the strong electronic excitation of the U_1 band by the pump pulse, that was directly observed in the 2PPE experiments by Berthold (Sect. 2.5, Fig. 2.12) [177], reduces the relative strength of $\chi^{(2)}_{s,db}$ as compared to $\chi^{(2)}_{s,NR}$. This is expected for a resonantly enhanced SHG process with the U_1 band acting as an intermediate state [1]. The same effect is exploited in SFG experiments of vibrational energy relaxation [6, 195]. Experiments with delayed probe pulses show that the SH-signal recovers on a timescale of 200 fs to 2 ps depending on the pump fluence (see Figs. 5.14 and 5.15). The corresponding incoherent scattering processes are characterized by a population decay time T_1 [196].

In order to confirm that the second-harmonic diffracted signal is really created in a $\chi^{(4)}$-process, we measured the dependence of the diffracted intensity on the laser pulse fluence F (Fig. 5.4). As expected from Eq. (2.9), the diffracted signal is proportional to F^4; similarly, Eq. (2.11) implies the observed F^2 dependence of the sum-frequency intensity, as expected for a two-photon absorption process. The power dependence plotted in Fig. 5.4 also demonstrates the importance of using a cavity-dumped system for these studies. Due to the high nonlinearity of the $\chi^{(4)}$-process, the diffracted signal delivers only few photons. As it scales with the fourth power of F, it would be very hard to detect without the cavity-dumping technique of our laser system, which enhances pulse energy more than one order of magnitude, while reducing the repetition rate. A usual Ti:sapphire oscillator with a factor of 100 higher repetition rate but 10 times lower energy per pulse would give a 100 times smaller diffracted signal.

The straight power law behavior of both SFG intensity and SH diffracted intensity up to a laser pulse fluence of 400 μJ/cm^2 implies the saturation regime for dangling-bond excitation to start above this maximum excitation fluence. Since a pump pulse fluence of 280 μJ/cm^2 already diminishes the SH response by 10% (see Fig. 5.9), however, the saturation threshold can be estimated to be around 1 mJ/cm^2. In fact, above 1.2 mJ/cm^2 Mauerer observed substantial deviations of the SH reflected intensity from the theoretically expected quadratic behavior [133], indicating the saturation of electronic transitions involving dangling-bond states during the finite pulse duration. This interpretation is confirmed by the observation of a square dependence of the SH intensity for the whole investigated fluence range up to 21 mJ/cm^2 from the *oxidized* Si(111) surface, on which the dangling bonds are quenched [133]. As in our investigations the sum of the pulse fluences of all incident beams on the silicon surface remained well below 500 μJ/cm^2, electronic saturation effects can legitimately be neglected in the interpretation of our SH reflection and diffraction observations.

5.1.3 Dangling-bond density dependence of the SH intensities

The model presented in the previous sections relates the nonlinear susceptibility $\chi_{\mathrm{s}}^{(2)}$ to the density of unoccupied dangling bonds (Eq. 5.1). In order to test the validity of the model, it is desirable to alter this density by a method different from adsorption. Si(111) displays a reversible phase transition from the 7×7 reconstruction to a more disordered "1×1" phase at a transition temperature of $T_{\mathrm{c}} \simeq 1100$ K that was first reported by Lander in 1964 [100]. Since the "1×1" phase corresponds to an adatom gas in which the areal dangling bond density is increased by roughly 25% with respect to the 7×7 structure [101], it is possible to corroborate the dangling-bond dependence of $\chi_{\mathrm{s}}^{(2)}$ by monitoring the SH response while heating Si(111) across T_{c}.

Fig. 5.5 shows the SH intensity in the sum-frequency direction from Si(111) in the surface temperature range from 1080 K to 1130 K with two *p*-polarized input beams and unpolarized detection. Due to the increasing background of black-body radiation from the silicon sample, it was not possible to discern the SH *diffracted* signal on the order of 10 photons/sec from the background noise above surface temperatures of 900 K. The SFG intensity in Fig. 5.5 displays a sudden rise of 45% at 1106 K, corresponding to the transition from the 7×7 reconstruction below, to the "1×1" phase above the transition temperature. The absolute accuracy of the temperature measurement is estimated to be ±15 K at 1100 K. Neglecting the nonresonant background term $\chi_{\mathrm{s,NR}}^{(2)}$ in Eq. (5.1) is equivalent to the approximation that $\chi_{\mathrm{s}}^{(2)}$ is proportional to the number of dangling bonds. The increase of the SH intensity by a factor of 1.45 at

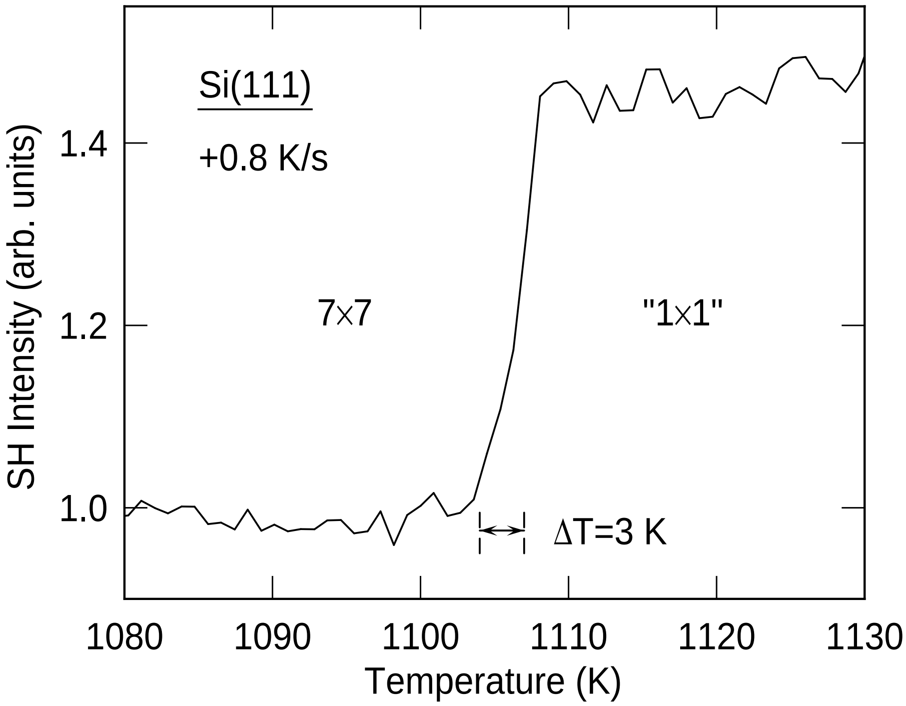

Fig. 5.5: SH intensity in the sum-frequency direction from Si(111) for heating through the 7×7 ↔ ”1×1” phase transition with a rate of 0.8 K/s. The rise of 45% at the transition temperature of 1106 K (±15 K) reflects the increase in the dangling bond density from 19/49 = 0.39 per Si(111) surface atom in the 7×7 phase to 0.50 in the ”1×1” phase.

the transition temperature corresponds to a change of $\sqrt{1.45} = 1.20$ in $\chi_s^{(2)}$. The rise in areal dangling bond density from 19/49 = 0.39 per Si(111) surface atom in the 7×7 phase to 0.50 in the ”1×1” phase would thus yield an increase of 0.50/0.39 = 1.28 in $\chi_s^{(2)}$. The slight difference of the experimental from the calculated factor may be a consequence of neglecting the nonresonant background term in $\chi_s^{(2)}$ at an incident photon energy of 1.55 eV (800 nm). The agreement between the factors can be enhanced by using incident photon energies that are farther apart from the E_1 resonance ($\hbar\omega = 1.7$ eV) (see Ref. [101]).

5.1.4 Temperature dependence of the SH intensities

A comparison of the surface temperature dependence of the SH reflected with the SH diffracted intensity provides a further means to examine the model developed in the preceding sections for $\chi_s^{(2)}$ and $\chi_s^{(4)}$. The nonlinear optical susceptibilities are sensitive to surface temperature due to temperature-dependent shifts in the energies of the surface electronic states. For the case of Si(111)7×7 a further contribution can result from changes in the thermal occupation of the narrow metallic surface states of the U_1/S_1 adatom dangling-bond band [78].

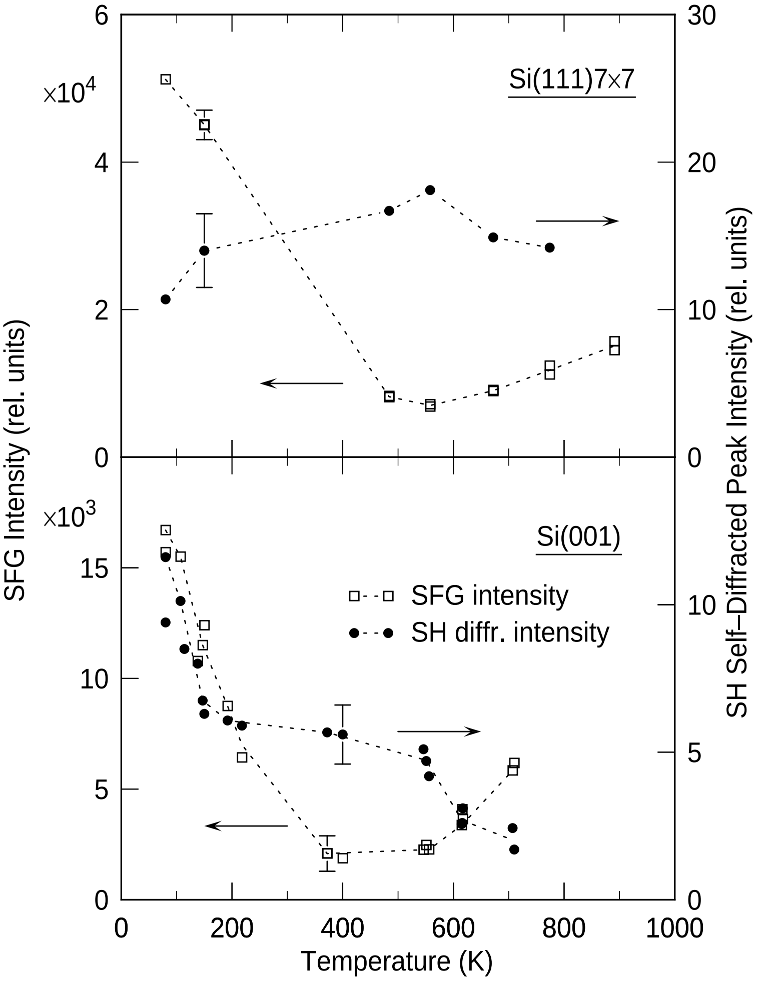

Fig. 5.6: SFG intensity (open squares, left scale) and SH self-diffracted peak intensity (circles, right scale) from Si(111)7×7 (top panel) and from Si(001) (bottom panel) as a function of surface temperature. In agreement with the interpretation of the coverage dependencies of $\chi_s^{(2)}$ and $\chi_s^{(4)}$ (see Fig. 5.1), the minima in the SFG intensities indicate the destructive interference of two contributions to $\chi_s^{(2)}$, whereas the monotonic behavior of the SH diffracted signals is consistent with just one contribution to $\chi_s^{(4)}$.

The dependencies of SFG intensity and SH diffracted intensity on surface temperature for both Si(111)7×7 and Si(001) show a markedly distinct behavior (Fig. 5.6). In agreement with previous observations [133, 134], the second-order SFG signal decreases from its maximum value at low temperatures to its minimum an order of magnitude smaller around 500 K and then increases again slightly with rising surface temperature. The fourth-order SH diffracted intensity, however, shows only negligible sensitivity to surface temperature in the entire accessible range from 80 K to 800 K for the case of Si(111)7×7, and a monotonic decrease for Si(001). This observation is in contrast to preliminary measurements by Mauerer with 120-fs pulses on Si(111)7×7,

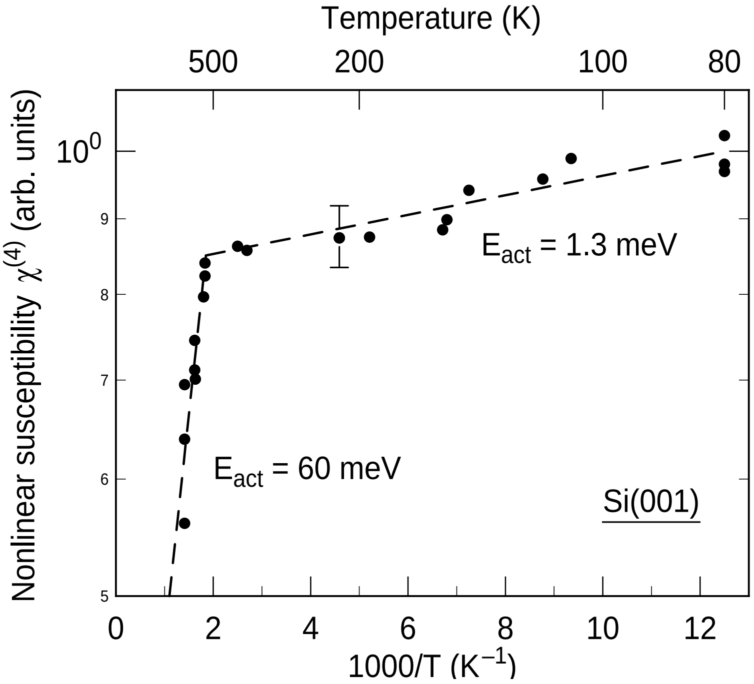

Fig. 5.7: Arrhenius plot of the surface temperature dependence of the fourth-order nonlinear optical susceptibility $\chi_s^{(4)}$ obtained from the self-diffracted peak intensity from Si(001) shown in Fig. 5.6 to the power 1/4. The diagram exhibits two activation energies of 1.3 meV and 60 meV.

who obtained a behavior very similar to the SH reflected data [133].

The qualitative difference between second-order SFG and fourth-order SH diffracted signals with respect to surface temperature in Fig. 5.6 supports the interpretation of the adsorption measurements in Fig. 5.1. Analogously, both adsorption measurements and temperature dependence exhibit marked minima in the SFG signals, as well as the contrasting monotonic behavior of the SH diffracted signals. Thus the conclusion obtained from the adsorption data – two contributions to $\chi_s^{(2)}$, whose destructive interference leads to a minimum in SH reflected intensity, and only one dangling bond-derived contribution to $\chi_s^{(4)}$ that leads to a monotonic behavior of the SH diffracted intensity – is corroborated by the temperature dependencies of the SH intensities.

Fig. 5.7 displays an Arrhenius plot of the surface temperature dependence of the fourth-order nonlinear optical susceptibility $\chi_s^{(4)}$ as obtained from the SH self-diffracted peak intensity from Si(001). The diagram shows that $\chi_s^{(4)}$ can be parametrized by a doubly exponentially activated behavior

$$\chi_s^{(4)} = A \exp(E_{\mathrm{act},1}/k_{\mathrm{B}}T) + B \exp(E_{\mathrm{act},2}/k_{\mathrm{B}}T) \tag{5.9}$$

with two activation energies $E_{\mathrm{act},1} = 1.3$ meV and $E_{\mathrm{act},2} = 60$ meV. The origin of the lower activation energy of 1.3 meV, that manifests itself at temperatures lower than

540 K in Fig. 5.7, may be due to the coupling between the silicon dimers across dimer rows, which is in the meV range. The source of the activation energy of 60 meV is probably a result of the interaction of the excited carriers with phonons. Not only bulk longitudinal and transverse optical phonons display peak densities of states at energies around 60 meV at the top of the continuum of volume states, there is also a surface mode above the optical continuum calculated to be at 61 meV [197] or 67 meV [109]. This mode corresponds to a subsurface phonon mode localized between the first and second layer of the Si(001) surface [109, 197].

5.1.5 Polarization dependence of the SH intensities

It is possible to learn more about the physical nature of the transient excitation by varying another accessible parameter of the incident photons: their polarization. Up to this point we only considered parallely polarized beams, which leads to a periodic spatial modulation of the electron population; such gratings are therfore called population or concentration gratings. Transient effects generated by orthogonally polarized beams were observed and discussed for the first time by Smirl and coworkers [198–200]. As the radiation intensity is not modulated for orthogonal polarizations, no concentration grating is formed. The vector sum of two orthogonally polarized electric fields varies periodically along the surface between linear and elliptical polarization. Since the strength of the resonant excitation for each position in k-space depends on the polarization of the electric field, the excited-state population will have a preferred orientation (*i.e.* quasi-momentum) in k-space at each position in real space. This form of excitation is labelled as anisotropic (in k-space) state-filling. Due to the spatial variation of the polarization, the position of the anisotropic state-filling in k-space will vary in real space, even though the *total* excited-state concentration (summed over all orientations) remains spatially uniform in the ideal case of absence of a population grating [199]. This is the origin of the orientation grating.

In contrast to the diffraction experiments at the fundamental photon frequency by Smirl *et al.*, we detected the second-harmonic signal, generated by an upconversion process. This process is resonantly enhanced by selected states in k-space whose occupation can be spatially modulated even in the case of an orientation grating, which then gives rise to a SH diffracted signal.

In order to study the possible influence of an orientation grating in relation to the anticipated population grating, we investigated the dependence of both sum-frequency and SH self-diffracted intensity on the relative polarization angle between the two linearly polarized excitation pulses (Fig. 5.8). As the incident polarizations determine the contributions of the different $\chi_s^{(2)}$ tensor components, the SFG intensity with orthogonal incident polarizations exhibits only 60% of its maximum magnitude at parallel polarizations. The SH self-diffracted intensity, however, drops to below the detection threshold with orthogonally polarized incident beams.

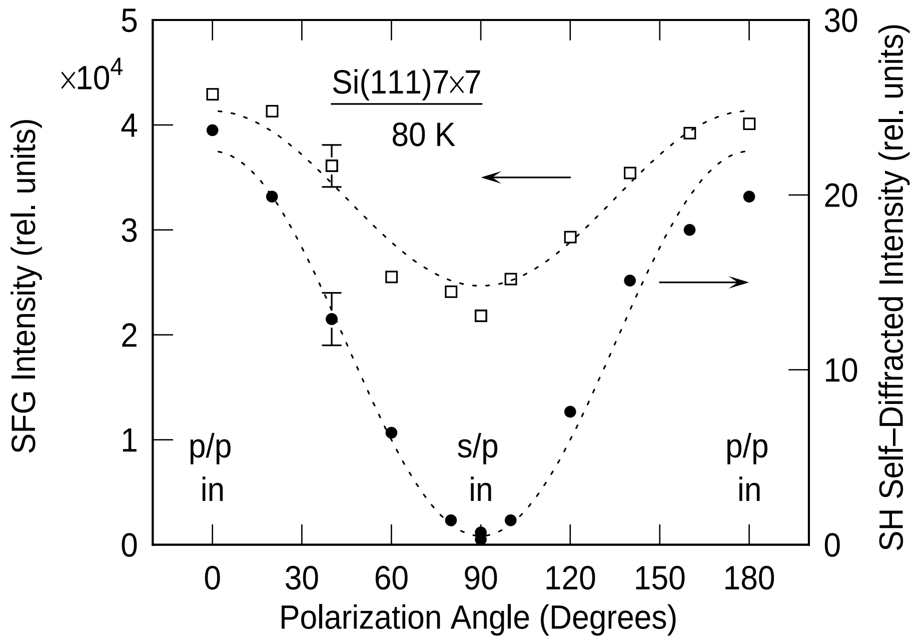

Fig. 5.8: Sum-frequency intensity (open squares, left scale) and SH self-diffracted intensity (circles, right scale) from Si(111)7×7 at 80 K as a function of the polarization angle of one of the two linearly polarized excitation pulses; the polarization plane of the other pulse remained fixed (p-polarized). The SFG intensity exhibits a finite minimum at orthogonal polarization of 60% of its maximum value at parallel polarization due to the different magnitudes of the contributing $\chi_s^{(2)}$ tensor components. In contrast, the SH self-diffracted intensity drops below the detection threshold with orthogonally polarized incident beams, thereby indicating the negligible influence of an orientational grating.

Buhleier *et al.* investigated an orientation grating in monocrystalline *bulk* silicon by degenerate four-wave mixing using 620-nm, 100-fs laser pulses [201]. Their study exhibited carrier momentum relaxation on a time scale of 10 fs. A similar investigation by Sjodin and coworkers with 800-nm pulses of 100 fs duration and 6.1 mJ/cm^2 fluence indicated that the momentum reorientation time and hence, dephasing time, is much faster than their pulse width [175]. Bergner *et al.* performed three-pulse transient grating experiments on crystalline silicon with excitation by 25-ps pulses at 532 nm and fluences up to 5 mJ/cm^2 [202]. They found the diffraction efficiency of the orientational grating (crossed polarizations) to be only 3% of the efficiency of the population grating (parallel polarizations). Since our experiment operates with two by a factor of 1.5 differing electric field magnitudes, instead of the ideally equal fields of Bergner *et al.*, and our detection threshold was around 5% of the maximum value at parallel polarizations, we can not exclude the existence of an orientational grating with our setup. Its influence on the SH diffracted signal produced by the population grating should, however, be negligible.

5.1.6 Conclusion

In order to elucidate the electronic excitation mechanism, being a prerequisite for the interpretation of dynamic relaxation data, this section presented a number of static nonlinear optical measurements. Aiming for an analysis how surface electronic states influence the SH response, we employed three physically different methods to control the areal density of unoccupied dangling bond states: adsorption, optical pumping, and heating through a structural phase transition.

The behavior of both second-order SFG and fourth-order SH diffracted intensities from Si(111) and Si(001) during oxygen adsorption agrees excellently with the notion that the dangling bond states are gradually quenched, following Langmuir kinetics. These adsorption measurements also show that the excited population grating contributing to second-harmonic diffracted radiation is located only in the $\mathrm{U}_1/\mathrm{S}_1$ surface band and not in other states, like the back bonds. The variation of the adsorption curves with increasing laser pulse fluence, as well as the drop in SH intensity following an optical pulse (see Fig. 5.9) reveal the excitation process by optical absorption that is responsible for the resonant enhancement of SHG. The straight power law dependences of SH reflected and diffracted signals on fluence, however, demonstrate the electronic system to be below the saturation regime. Heating Si(111) through the 7×7 ↔ "1×1" structural phase transition, thereby increasing the number of dangling bonds per unit area by 25% substantiates the approximate proportionality of both nonlinear optical susceptibilties $\chi_\mathrm{s}^{(2)}$ and $\chi_\mathrm{s}^{(4)}$ on surface dangling-bond density. The distinct behavior of SH reflected and SH diffracted signals with respect to surface temperature confirms the notion developed for the adsorption measurements of two destructively interfering contributions to $\chi_\mathrm{s}^{(2)}$ as opposed to only one dangling bond-derived contribution to $\chi_\mathrm{s}^{(4)}$. An investigation of the SH intensities on incident polarizations shows that the probe beam is diffracted from a transient *population* grating of dangling bonds, whereas the contribution of a hypothetical *polarization* grating is negligible.

These findings about the electronic excitation mechanism enable the interpretation of the time-resolved nonlinear optical experiments that are presented in the following sections.

5.2 Time-resolved second-harmonic generation

Due to the possibility to investigate electron dynamics at surfaces and interfaces with femtosecond time resolution, time-resolved SHG experiments gain increasing importance. A number of studies detected ultrafast, laser-induced order–disorder transitions in semiconductors by this technique [203–212]. In order to time-resolve the desorption of CO from Cu(111) Prybyla *et al.* utilized second-harmonic as a probe [213]. Matthias *et al.* used SH pump–probe to study ultrafast electron and magnetization dynamics in various metals [132,214–219]. Magnetization dynamics in NiFe films and single-crystal Ni were also investigated with time-resolved magnetization-induced SHG after ultra-short magnetic field pulses [220] and after optical excitation [221]. Similarly, the time-resolved photo-induced SH nonlinear magneto-optical Kerr effect was employed for the study of spin dynamics at a GaAs(001) surface [222]. Jong *et al.* studied the electric field dynamics at a metal–semiconductor Schottky interface with time-resolved SHG [223]. Analogously, Nahata and Heinz reported the application of electric-field-induced SHG as a new technique for measuring the field of freely propagating terahertz radiation [224,225]. Recently, time-resolved SHG was used by Tom *et al.* for coherent phonon spectroscopy on GaAs surfaces and interfaces [8,226–228], and by Rasing *et al.* for the detection of coherent plasmon–surface phonon oscillations in a Au/GaAs Schottky barrier interface [223,229]. Another recent experiment by Guo *et al.* investigated the ultrafast dynamics of electron thermalization in gold [230]. Their use of time-resolved SHG implied an electron temperature dependent enhancement of the SHG signal.

In order to study the population relaxation time T_1 of excited silicon dangling-bond surface states, we employed two different purely optical second-harmonic techniques. In the incoherent SH pump–probe method, an intense 800-nm pump pulse resonantly, or near-resonantly, excites the electronic surface states. A synchronized time-delayed, relatively weak 800-nm probe pulse then samples the excitation within the surface by generating specularly reflected SH radiation. The intensity of the SH light, monitored as a function of pump–probe time delay, yields information about the temporal decay of the excitation induced by the pump. The second technique is based on the generation of a transient population grating of the surface dangling-bond states by two coincident pump pulses. A synchronized probe pulse is diffracted from the grating leading to second-harmonic light. Again, the intensity of the SH radiation as a function of time delay is a measure for the relaxation of the transient grating. The two techniques are presented in more detail in the following.

A strong pump pulse that populates the U_1 state on Si(111)7×7 can cause the SHG signal from a weak probe pulse to decrease. This effect has been exploited to study the fluence dependent relaxation times employing the same laser system as for the 2PPE experiments discussed in Sect. 2.5 [196]. In Fig. 5.9 we show a similar experiment with the considerably shorter pulses from the cavity-dumped Ti:sapphire laser used for the diffraction experiments. After exciting the clean Si(111)7×7 surface with a pump pulse, we observe a decrease of the SH signal of 10%. The recovery of the SH signal with time constant 215 fs reflects the scattering time of the excited electrons out of the optically coupled region in k-space.

Due to the proportionality of the second-harmonic reflected intensity to the square of $\chi_{\mathrm{s}}^{(2)}$, the 10% drop of the SH signal implies an excitation density of 5% of the U_1 surface band and hence an excited adatom dangling bond population of $0.05\times1.92{\cdot}10^{14}$ $\mathrm{cm}^{-2} = 9.6\cdot10^{12}\ \mathrm{cm}^{-2}$. The incident photon flux of $1.13\cdot10^{15}\ \mathrm{cm}^{-2}$, corresponding to

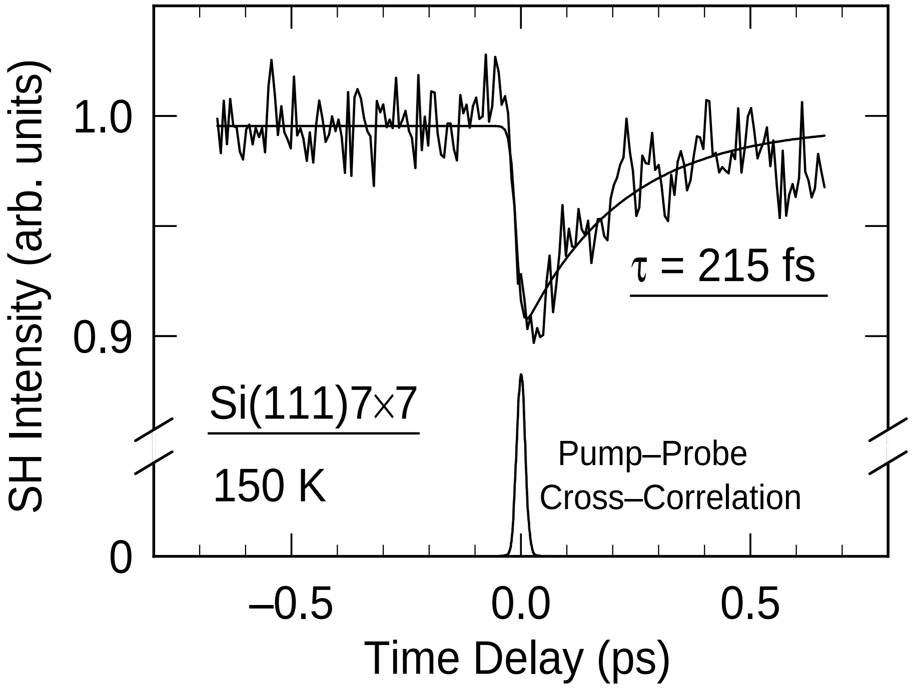

Fig. 5.9: Second-harmonic intensity from the Si(111)7×7 surface generated by a probe pulse (800 nm, 120 μJ/cm^2) as a function of time delay with respect to a pump pulse (800 nm, 280 μJ/cm^2). The line through the data is an exponential fit, which yields a time constant $\tau = 215$ fs. Also shown is the pump–probe sum-frequency cross-correlation.

the fluence of 280 μJ/cm^2 of the 1.55 eV photons, then gives a quantum yield for the excitation process of $1 \cdot 10^{-2}$. This is a very plausible value: under the assumption of an effective dangling bond absorption depth of 1 Å, the derived quantum yield implies an effective absorption coefficient of 10^6 cm^{-1}, which is the universal direct interband absorption constant for semiconductors [180].

The interpretation of SHG pump–probe experiments may be complicated by pump-induced changes of the bulk dielectric constant that effects the SHG process via Fresnel factors [132, 204, 210, 211, 231]. This effect is negligible in the present experiments because of the weak absorption of silicon, $\alpha^{-1}_{80\text{ K}} = 50$ μm, $\alpha^{-1}_{300\text{ K}} = 40$ μm, at a wavelength of 800 nm [180]. If present, it would result in a spatial modulation not only of $\chi^{(2)}_{\text{s,db}}$ but also of $\chi^{(2)}_{\text{s,NR}}$. The diffracted SH signal would then be affected by the (destructive) interference of both contributions to the SH response which is not observed. The absence of a significant difference in reflectivity before and after the pump pulse (see Fig. 5.14) supports this conclusion [133]. In addition, by measuring the oxygen coverage dependence of both the reflected SHG signal and the diffracted signal (see Sect. 5.1.1), a measurable bulk contribution to the observed pump–probe behavior or to the diffracted signal can be excluded [133, 232].

A time-resolved SH signal from Si(111)7×7 obtained with the coherent transient

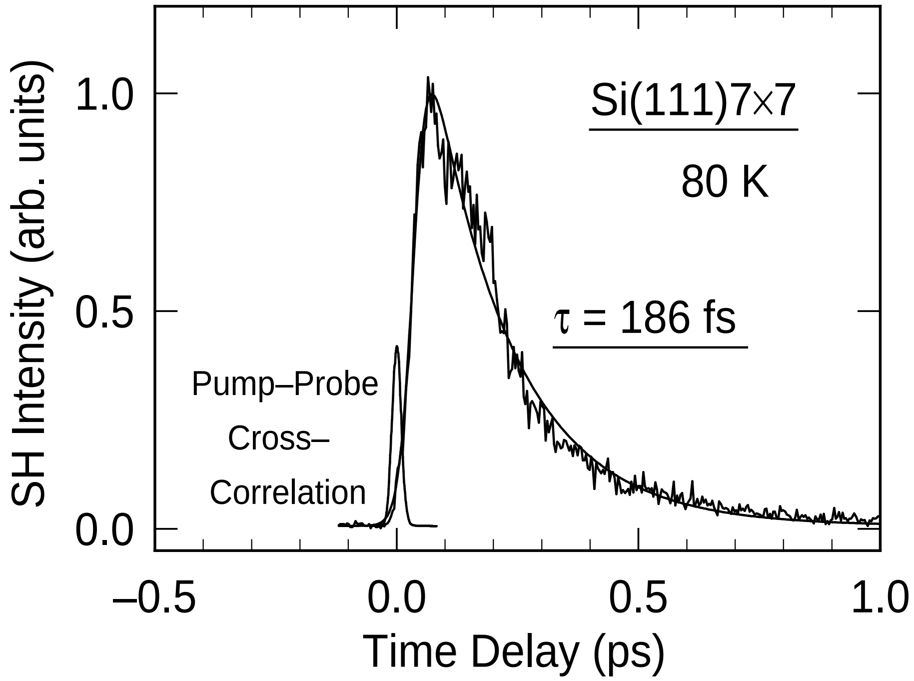

Fig. 5.10: Second-harmonic intensity from the Si(111)7×7 surface generated by a probe pulse (800 nm, 200 μJ/cm^2) diffracted from a transient population grating as a function of time delay with respect to a pair of coincident pump pulses (800 nm, 100 μJ/cm^2 each), that produce the grating. The line through the data is an exponential fit, which yields a time constant $\tau = 186$ fs. Also shown is the pump–probe sum-frequency cross-correlation.

grating technique is shown in Fig. 5.10. The SH signal observed into direction $2\mathbf{k}_c + \mathbf{k}_b - \mathbf{k}_a$ is the result of the SH diffraction of the probe beam $\mathbf{k}_c$ from the transient population grating characterized by $\mathbf{k}_b - \mathbf{k}_a$ that was generated by the two coincident pump pulses $\mathbf{k}_a$ and $\mathbf{k}_b$. An exponential fit through the data in Fig. 5.10 yields a population relaxation time of the grating of 186 fs.

The following two subsections investigate the surface temperature dependence of the population relaxation time T_1 obtained by both SH techniques for Si(111) and for Si(001).

5.2.1 Si(111)

The population relaxation time T_1 for Si(111)7×7 as a function of surface temperature obtained by both the incoherent SH pump–probe method and by the coherent transient-grating technique is shown in Fig. 5.11. For Si(111) there is a monotonic decrease in T_1 with rising temperature for both agreeing sets of data from second-harmonic reflection and diffraction. As the Debye temperature for bulk silicon is 640 K, one probable interpretation of the decrease in relaxation time is the interaction

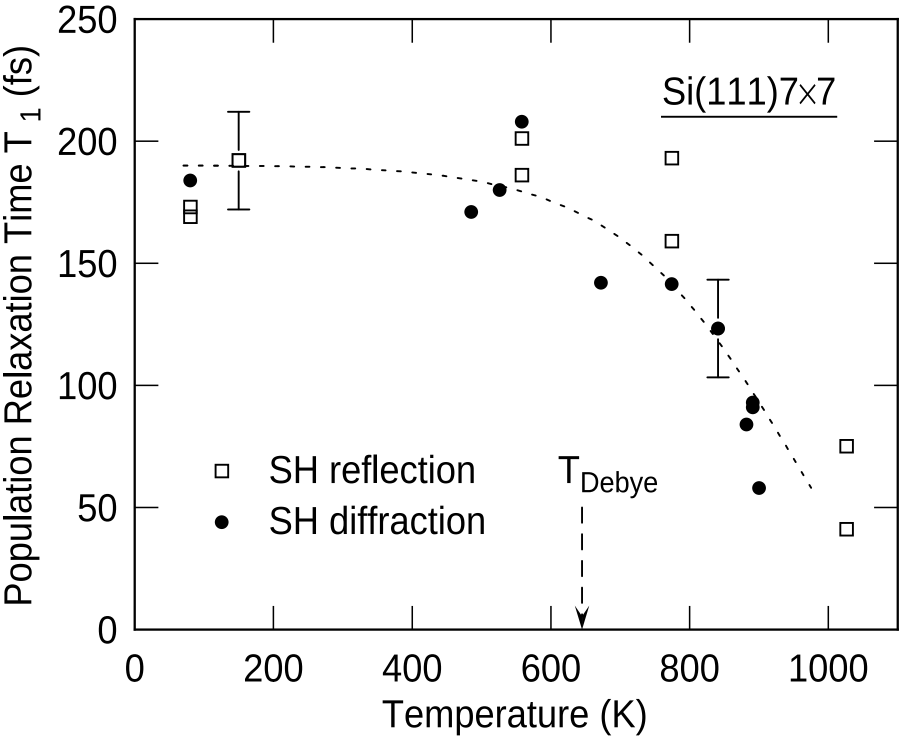

Fig. 5.11: Population relaxation time T_1 as a function of surface temperature for Si(111)7×7 measured with both incoherent pump–probe SH reflection (open squares) and coherent three-beam SH diffraction (circles). The monotonic decrease in T_1 with rising temperature for both agreeing sets of data indicates the increased interaction probability of the dangling-bond electrons with phonons at elevated temperatures. The dotted line is a guide to the eye.

of the dangling-bond electrons with optical phonons. A more detailed discussion of the relevant population relaxation processes in the electronic surface states is given in Sect. 5.3.

5.2.2 Si(001)

Due to the qualitative difference between the metallic Si(111)7×7 dangling-bond bands and the semiconducting Si(001) surface states, it is interesting to compare the T_1 relaxation times of Si(111) presented in the preceding section with the respective values for Si(001).

The population relaxation time T_1 as a function of surface temperature for Si(001) obtained with three-beam SH diffraction is shown in Fig. 5.12. For temperatures between 200 K and 600 K, T_1 is measured to be constant around 160 fs, which is only slightly smaller than the T_1 values for Si(111) around 180 fs, that behave similarly in this temperature range (cf. Fig. 5.11). Because of the increasing disturbing influence

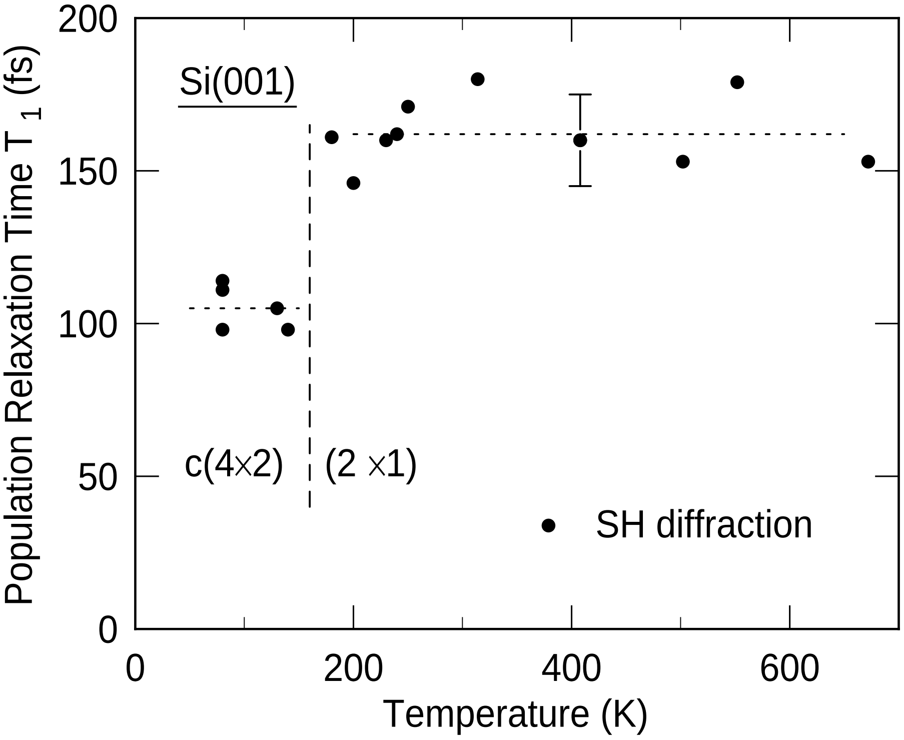

Fig. 5.12: Population relaxation time T_1 as a function of surface temperature for Si(001) measured with three-beam SH diffraction. The jump in T_1 at the transition temperature of the order–disorder c(4×2) ↔ 2×1 phase transition at 150 K indicates a more efficient transport mechanism to a fast recombination channel in the correlated dangling bond dimers of the low temperature phase. The dotted line is a guide to the eye.

of blackbody radiation from the surface at higher temperatures, it was not possible to obtain relaxation times above 700 K for Si(001).

The assignment of the relaxation to a specific surface band is more difficult on Si(001) than on Si(111). Whereas on Si(111) the dominant role of the U_1/S_1 adatom dangling-bond surface band for the SHG process with visible and near-infrared frequencies is evident [74], the relative contributions of the raised D_{up} and the lowered D_{down} dangling-bond states on Si(001) to the relaxation data is less clear. Our measured T_1 relaxation times on Si(001) in Fig. 5.12 are thus a mixture of hole dynamics within the normally occupied D_{up} dangling-bond band (initial state in SHG) and electron dynamics in the normally empty D_{down} band (intermediate state in SHG).

In the case of Si(001) there exists a well-known order–disorder phase transition around 150 K from a c(4×2) reconstruction to a primitive 2×1 structure [37]. Just at that temperature we observe a change in the T_1 relaxation time from 100 fs below to 160 fs above the transition temperature.

At first sight, it seems surprising that the relaxation time is higher in the more disordered 2×1 structure. One explanation, however, is the increased phase space for scattering due to the additional electronic surface bands shifted into the by a factor 2 smaller Brillouin zone of Si(001)c(4×2). Another interpretation assumes the existence of a fast carrier recombination channel that could be provided at defects or steps. This is a plausible assumption, since the energetic distance between the occupied D_{up} and the unoccupied D_{down} dangling-bond surface bands E_{gap}, which is centered around 1.7 eV at the Si(001) terraces (see Fig. 2.7) can be reduced considerably at steps by low energy distortions [125]. Since the radiative recombination time is proportional to E^3_{gap} and nonradiative processes, like multiphonon emission ($\tau \propto \exp(E_{\mathrm{gap}}/\hbar\Omega_{\mathrm{phon}})$) and recombination via defect states also show decreasing relaxation times with decreasing energetic distance between the bands, carrier recombination at steps is strongly favored. As the ordered structure at lower temperatures arises from a correlation of buckled dangling-bond dimers within and across dimer rows, the lower relaxation time then would indicate a more efficient carrier transport mechanism to the steps or to surface defects.

This interpretation is corroborated by the dependence of the SH self-diffracted peak shift from Si(001) as a function of oxygen exposure, that is displayed in Fig. 6.7. The fact that the magnitude of the peak shift increases with rising oxygen coverage is a clear indication of an increase in T_1. Since the oxygen atoms disrupt the ordered structure of the clean silicon surface, and thus impair the transport of the carriers to the recombination centers, the rise in T_1 is a natural consequence. One possibility to verify our interpretation would be the investigation of stepped Si(001) surfaces.

5.3 Discussion

This section includes a discussion of the obtained incoherent relaxation measurements that were presented in the preceding sections. A comparison of our data with other time-resolved investigations of the electronic structure of silicon surfaces facilitates the interpretation of our experiments. The metallicity of the U_1/S_1 surface band on Si(111)7×7 allows its theoretical description using a two-dimensional Fermi liquid model, yielding relaxation times similar to our measured ones.

Previous studies on carrier relaxation behavior at silicon surfaces can be classified into electronic experiments, employing two-photon photoemission (2PPE), and purely optical experiments, that rely on second-harmonic generation.

5.3.1 Photoemission

A number of time-resolved 2PPE investigations were performed in the group of Bokor on Si(111)2×1 [21–23] and on Si(001)2×1 [26, 32]. On cleavage in UHV to expose the (111) face, silicon crystals exhibit a metastable 2×1 structure, that transforms into the thermodynamically favored 7×7 reconstruction upon annealing. The electronic structure of the metastable phase displays an occupied surface state of bonding character π and an unoccupied state of antibonding character π^* [37]. Bokor *et al.* selectively photoexcited surface electrons into the normally empty antibonding surface state on Si(111)2×1 and followed the time decay of the excited population by time-resolved photoemission [21–23]. Due to their usage of laser pulse durations between 60 ps and 80 ps, they were only able to observe relaxation dynamics on a time scale of 100 ps. Bokor and coworkers explained their data using a transient surface recombination model between π and π^* via surface defect states [21–23]. In a similar study on the analogous Ge(111)2×1 surface Baeumler and Haight were able to follow the relaxation of the transient population in the normally unoccupied π^*-antibonding surface band with sub-picosecond time resolution [233].

In more recent time-resolved 2PPE experiments on Si(001)2×1, Bokor *et al.* obtained carrier relaxation in electronic surface states on a time scale of a few hundred femtoseconds to a few picoseconds, depending on the initial state energy [26, 32]. They concluded that the dominant contribution to the observed relaxation is associated with surface defect states [32]. New measurements conducted by Kutschera and coworkers on Si(001)2×1 implied a population relaxation time of the normally empty $\mathrm{D_{down}}$ dangling-bond states near the band bottom at $\overline{\Gamma}$ on the considerably longer time scale of 100 ps, which they attributed to phonon-assisted recombination [234]. Their results most relevant to our work, however, are their measured relaxation times obtained with off-normal detection, yielding electron dynamics information for $\mathrm{D_{down}}$ states far from the band bottom. For this case Kutschera *et al.* measured T_1 times in the range 150–300 fs, which is compatible with our results at Si(001) [234].

A further 2PPE study using laser pulses of 1–3 ps duration on various silicon surfaces by Rowe and coworkers showed that electron energy relaxation within the surface bands occurs on a time scale shorter than 3 ps [30]. Using the same technique, Goldman and Prybyla reported that the electron temperature inside the *bulk* conduction band decreases from 1500 K to 800 K in less than 60 fs after excitation [16, 17].

In order to study the population relaxation in the adatom dangling bond-derived $\mathrm{U_1}$ surface band of Si(111)7×7, Berthold conducted a detailed investigation using 2PPE, that was already presented in Sect. 2.5 [177]. The transient electron population within the bulk band gap generated by a pump pulse and detected by photoemission is shown in Fig. 2.12.

Exponential fits to the 2PPE data from Fig. 2.12 yield population life times T_1 as a function of electron energy for the $\mathrm{U_1}$ band of Si(111)7×7 at 80 K (Fig. 5.13). The data approximately comply with the $1/\mathrm{E}^2$ behavior predicted by a crude model of Fermi liquid theory (dashed line in Fig. 5.13) [235]. The highest lifetimes around 150 fs at energies very close to the Fermi level compare well with the population relaxation times of 180 fs that were obtained with the very different, purely optical techniques pump–probe SHG and SH diffraction for Si(111)7×7 at low temperatures (Fig. 5.11).

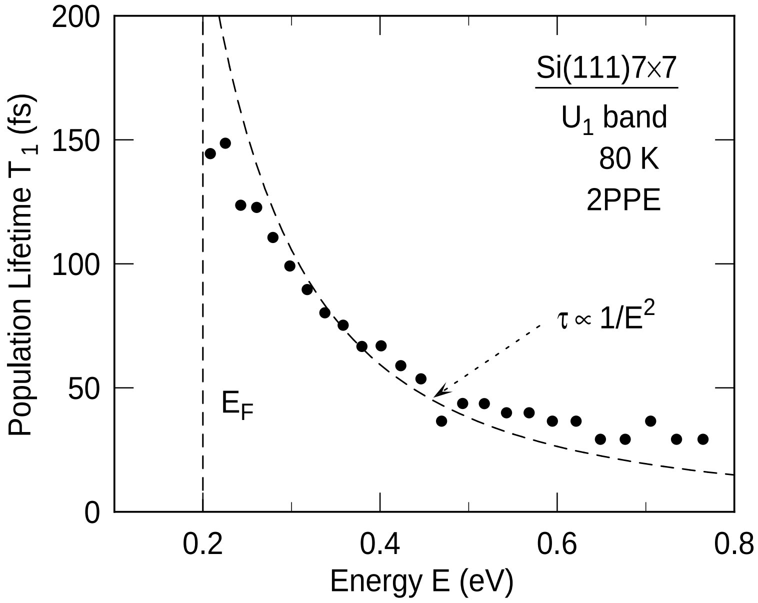

Fig. 5.13: Population lifetimes T_1 as a function of electron energy from the U_1 band of Si(111)7×7 at 80 K generated by 1.55 eV pump pulses and detected by photoemission with 4.65 eV probe pulses for $k_{\|} \approx 0$. The lifetimes were extracted by exponential fits to the two-photon photoemission data shown in Fig. 2.12. The Fermi level is located around $E = 0.2$ eV. The dashed line proportional to $1/E^2$ is an approximate result of Fermi liquid theory. (From Berthold [177]).

5.3.2 SHG

Due to the detailed characterizability of the final state, photoemission measurements are often easier to interpret compared to purely optical experiments. Optical techniques, however, that can take advantage of the genuine surface specifity of second-harmonic methods and that are also applicable at high excitation conditions, are more directly comparable to our investigation. Therefore in this subsection we present the findings of other relevant time-resolved purely optical studies on silicon and discuss them with with respect to our results.

Mauerer studied the fluence-dependence of the population relaxation times of the U_1/S_1 dangling-bond surface band on Si(111)7×7 using the SH pump–probe technique as presented in Sect. 5.2 (see Fig. 5.9) [133]. He employed the 800-nm, 120-fs laser pulses from a 1 kHz system consisting of a Ti:sapphire laser oscillator and a regenerative amplifier – the same laser system as for the 2PPE experiments by Berthold presented in Sect. 2.5 [133]. The beam was split into an intense pump beam of 14 mJ/cm^2 and a weak probe beam, that was limited to 1 mJ/cm^2 in order to evade the saturation threshold shown to be at 1.2 mJ/cm^2.

Fig. 5.14 shows the SH intensity of the probe pulse from the clean Si(111)7×7 as a function of time delay with respect to the pump pulse as obtained by Mauerer [133].

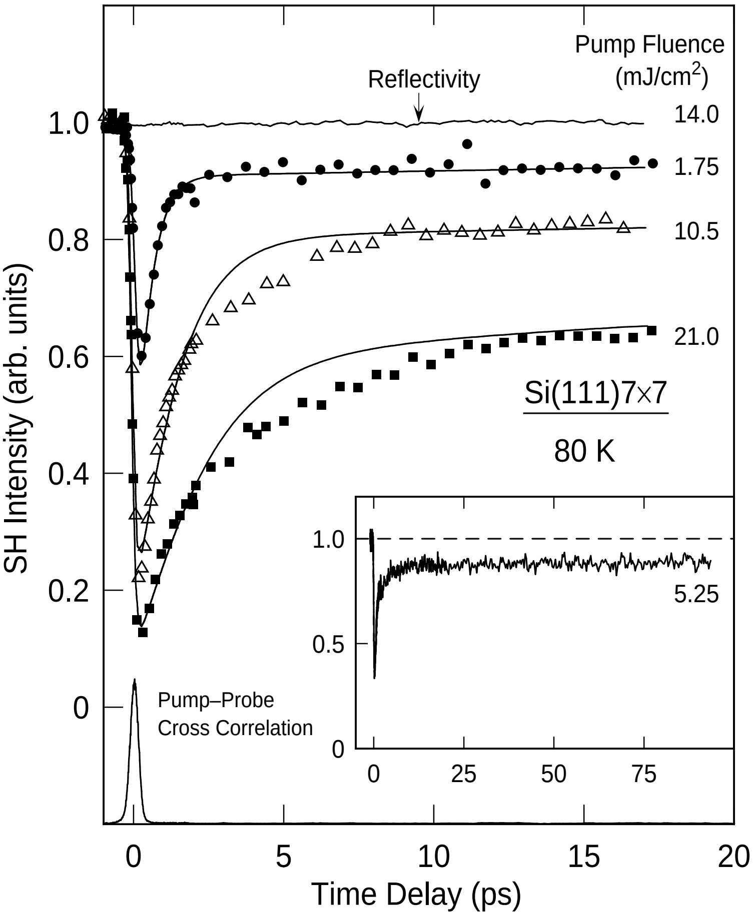

Fig. 5.14: Second-harmonic intensity from the Si(111)7×7 surface for a probe pulse (1 mJ/cm^2, 800 nm) as a function of time delay in respect to a pump pulse (800 nm) for the pump fluences indicated. The upper curve shows the linear reflectivity for a pump fluence of 14 mJ/cm^2. The lines through the curves are exponential fits. (From Mauerer [133]).

After the exciting pump pulse the SH probe signal decreases substantially by up to 90% after delays of about 200 fs and does not recover to its initial level even after a delay of 100 ps (see inset in Fig. 5.14), corresponding to a second relaxation channel with a time constant in the nanosecond range. The relaxation times on the sub-ps and ps time scale show an increase with pump fluence, that saturates above 21 mJ/cm^2. Since the linear reflectivity shown in Fig. 5.14 does not exhibit any variations in excess of 1.5%, bulk excitations are disqualified as origin for the considerable changes of the SH signal.

The comparatively large drop compared to our measured decrease on the order of 10% (see Fig. 5.9) is a natural consequence of the substantially higher pump pulse fluence applied by Mauerer, which is able to excite a significant fraction of the adatom dangling bonds responsible for the SH signal. Also the increased delay of minimum

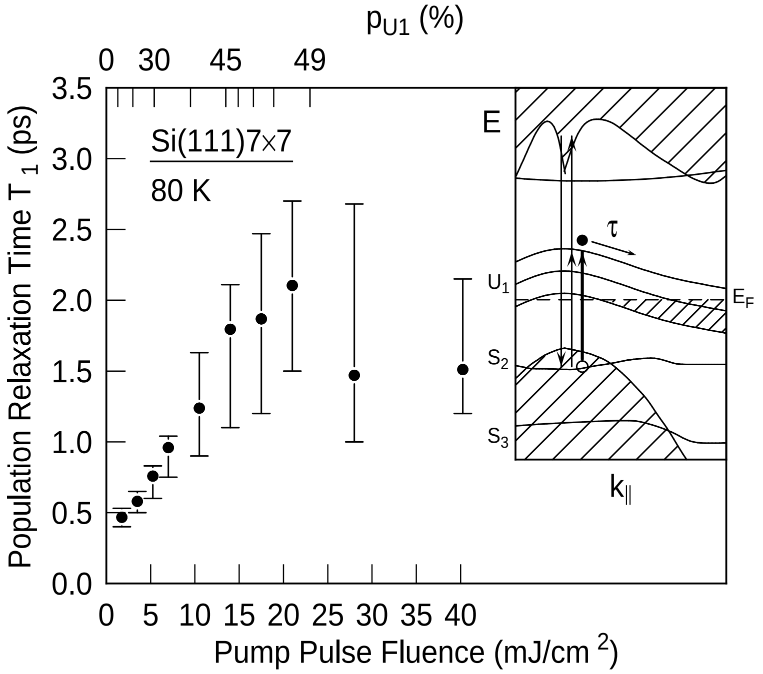

Fig. 5.15: Relaxation times of the SH signal from a Si(111)7×7 surface after excitation with pump pulses of various fluences. The values were extracted by exponential fits to the data like in Fig. 5.14. The upper axis relates the pump pulse fluence to the maximum population p_{U1} of the U_1 band using a two-level model. Inset: Schematic of the resonant enhancement of the SH-process via the adatom dangling bond states U_1 and the intraband electron–electron scattering, which leads to relaxation of the SH-signal after excitation by the pump pulse. Like in Figs. 2.2 and 2.12, U_1, S_2, S_3 are surface bands and the hatched areas show projected volume bands. (From Mauerer [133]).

SH intensity, which is due to the by an order of magnitude higher pulse duration compared to our study, is compatible with our result.

Fig. 5.15 shows the relaxation times of the SH signal as shown in Fig. 5.14 as a function of pump pulse fluence [133]. Mauerer observed a nearly linear increase of the relaxation times of the hot electrons from 470 fs up to 2.1 ps when increasing the pump fluences from 1.75 up to $\sim$ 21 mJ/cm^2. An extrapolation of Mauerer's data to our much smaller fluences of a few 100 μJ/cm^2 yields a relaxation time of 200 fs, in agreement with our SH pump–probe and three-beam diffraction measurements (see Fig. 5.11). The linear behavior is compatible to the direct proportionality between the quasiparticle lifetime and the 2D electronic density, as predicted by Fermi liquid theory (see Sect. 5.3.3). At pump fluences above 21 mJ/cm^2 the relaxation times and also the magnitudes of the pump-induced SH-dips saturate.

The gradual increase of the relaxation times with pump intensity is due to the reduction of phase space available for scattering processes, which is a direct consequence of the enhanced dangling-bond population at higher pump fluences. In addition, the exceedingly high excitation densities result in strong screening of the electron–electron interactions, which also contributes to the observed increase of the relaxation times [236].

5.3.3 Theory

For a complete discussion of the incoherent population relaxation times on silicon surfaces, it is desirable to compare our measured data with results that are obtained from a theoretical model. Following the experimental evidence for the metallicity of the Si(111)7×7 surface by electron-energy loss spectroscopy (EELS) [78, 92–94], scanning tunneling spectroscopy (STS) [41, 88], and recently nuclear magnetic resonance (β-NMR) [98], we modeled the adatom dangling-bond carriers in the U_1/S_1 surface band by a free electron gas on a semiconducting substrate. The validity of such a treatment is corroborated by STS experiments by Heike and coworkers, who observed the naturally formed Schottky barrier between the surface states and the bulk states by surrounding parts of the surface by a closed trench [99]. With their setup Heike *et al.* were also able to measure the small but finite surface conductivity [99].

It is thus natural to describe the surface in terms of two-dimensional Fermi liquid theory. The most simple approach within this framework is based on a perturbative approach within the random-phase approximation (RPA), which was used by Giuliani and Quinn to calculate the inelastic Coulomb lifetime of a quasiparticle near the Fermi surface [235]. The qualitative dependencies of the inverse inelastic quasiparticle lifetime $1/\tau_{\mathrm{ee}}$ near the Fermi level at zero temperature for the different dimensionalities are known to be

$$\text{(3D)} \quad \tfrac{1}{\tau_{\mathrm{ee}}} \propto (E - E_{\mathrm{F}})^2 \qquad [237, 238] \tag{5.10}$$

$$\text{(2D)} \quad \tfrac{1}{\tau_{\mathrm{ee}}} \propto (E - E_{\mathrm{F}})^2 \ln|E - E_{\mathrm{F}}| \qquad [235, 239] \tag{5.11}$$

$$\text{(1D)} \quad \tfrac{1}{\tau_{\mathrm{ee}}} \propto |E - E_{\mathrm{F}}| \qquad [238]. \tag{5.12}$$

The explicit two-dimensional electron-energy dependence of $1/\tau_{\mathrm{ee}}$ at $T = 0$ K is given by [235]

$$\frac{1}{\tau_{\mathrm{ee}}(E)} \simeq -\frac{E_{\mathrm{F}}}{4\pi\hbar}\left(\frac{E - E_{\mathrm{F}}}{E_{\mathrm{F}}}\right)^2 \left[\ln\left(\frac{E - E_{\mathrm{F}}}{E_{\mathrm{F}}}\right) - \frac{1}{2} - \ln\left(\frac{2k_{\mathrm{TF,2D}}}{k_{\mathrm{F}}}\right)\right], \tag{5.13}$$

with the Fermi wave vector k_{F} and the Thomas-Fermi screening wave vector in 2D

$$k_{\mathrm{TF,2D}} = \frac{2me^2}{4\pi\epsilon_0\hbar^2}. \tag{5.14}$$

At finite temperatures a result can be obtained only for quasiparticles very close to the Fermi surface, $|E - E_{\mathrm{F}}| \ll k_{\mathrm{B}}T$, by [235]

$$\frac{1}{\tau_{\mathrm{ee}}(T)} \simeq -\frac{E_{\mathrm{F}}}{2\pi\hbar}\left(\frac{k_{\mathrm{B}}T}{E_{\mathrm{F}}}\right)^2 \left[\ln\left(\frac{k_{\mathrm{B}}T}{E_{\mathrm{F}}}\right) - \ln\left(\frac{k_{\mathrm{TF,2D}}}{k_{\mathrm{F}}}\right) - \ln 2 - 1\right], \tag{5.15}$$

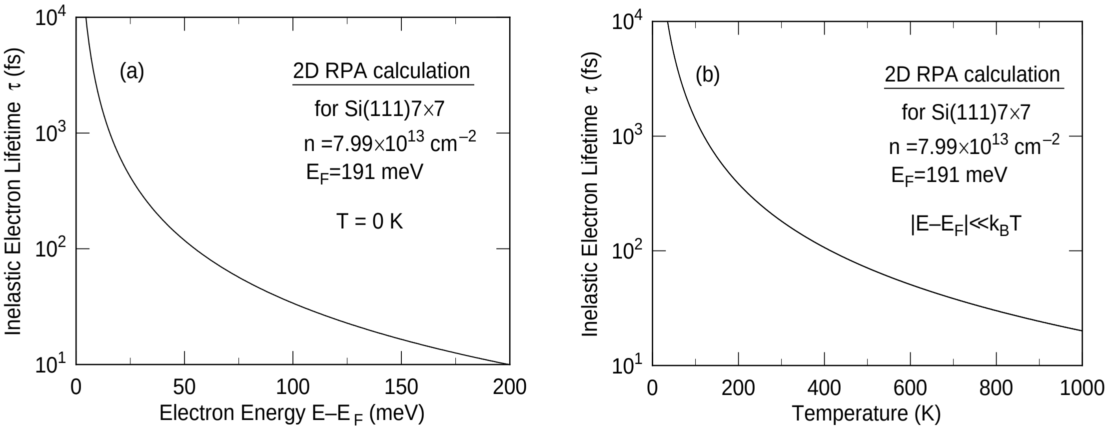

Fig. 5.16: Inelastic Coulomb lifetime of a quasiparticle near the Fermi surface of a two-dimensional electron gas with the carrier density of Si(111)7×7 adatom dangling-bond electrons. The data were calculated using equations by Giuliani and Quinn who employed a perturbative Fermi liquid approach based on the random-phase approximation (RPA) [235]. a) Quasiparticle energy dependence of the lifetime at 0 K. For electron energies about 40 meV above E_F the calculation yields relaxation times around 200 fs, comparable to our measured values (see Fig. 5.11). b) Temperature dependence of the lifetime for quasiparticles close to the Fermi surface ($|E - E_\mathrm{F}| \ll k_\mathrm{B}T$).

which is valid for temperatures $T \ll E_\mathrm{F}/k_\mathrm{B}$. Both equations imply that the quasiparticle lifetime τ_{ee} is directly proportional to the electronic density.

The Fermi energy for the case of Si(111)7×7 can be obtained from the 2D electron density in the adatom dangling-bond states that form the $\mathrm{U}_1/\mathrm{S}_1$ surface band. This density n is given by the product of the ratio electrons per surface atom times the 3D number-density of atoms in crystalline silicon times the average distance between $\{111\}$ lattice planes

$$n = \frac{5}{49} \times \frac{8}{a^3} \times \frac{a\sqrt{3}}{6} = 7.99 \cdot 10^{13}\ \mathrm{cm}^{-2}, \tag{5.16}$$

with the fcc lattice constant for silicon $a = 5.43 \cdot 10^{-10}$ m. With the Fermi wave vector that is given in two dimensions by $k_\mathrm{F} = \sqrt{2\pi n}$, the Fermi energy for the adatom dangling-bond system of Si(111)7×7 can be calculated to be $E_\mathrm{F} = 191$ meV.

The dependencies of the inelastic quasiparticle Coulomb lifetime for Si(111)7×7 on electron energy and on temperature, derived from Eqs. (5.14) and (5.15), respectively, are displayed in Fig. 5.16. Panel (a) shows that for electrons excited to energies about 40 meV above E_F, the calculation yields relaxation times around 200 fs, which is close to our measured values (see Fig. 5.11). The 2PPE data for the electron lifetimes by Berthold as shown in Fig. 5.13 [177], though generally half an order of magnitude larger than the calculated values in Fig. 5.16a, display a qualitatively similar behavior. The quantitative discrepancy is not surprising, since the intense excitation conditions in the 2PPE experiment lead to a substantial phase space reduction for carrier scattering processes, which eventually leads to the increased observed lifetimes.

The temperature-dependend lifetimes as shown in panel (b) of less than 100 fs for temperatures above 400 K, although lower than our data for Si(111)7×7 in Fig. 5.11, qualitatively agree with the decreasing behavior of T_1 with increasing temperature. Thus the enhanced phase space at elevated temperatures available for carrier scattering may provide a further contribution to the diminished population relaxation times above 600 K, in addition to optical phonon absorption and emission processes.

The quantitative discrepancy indicates that the relatively crude approximation of the free two-dimensional electron gas within the random-phase approach describes the electron dynamics on this surface only very roughly. The main flaws in this description are the neglect of both band-structure effects and finite coupling of the surface carriers to bulk electrons in the substrate. In addition, the picture of one single excited quasiparticle fails to describe the real situation with the excitation of interacting electrons in a substantial fraction of the adatom dangling bonds.

Due to the spatial complexity of the 7×7 superstructure it is very difficult to obtain quantitatively reliable results on the electronic properties of the surface dangling-bond states. Local-density approximation (LDA) calculations by Ortega and coworkers of the electronic surface band structure of Si(111)7×7 reveal the metallic character of the adatom dangling-bond surface states [240–242]. Among the 12 adatom surface bands, corresponding to the 12 adatom dangling bonds per unit cell, according to Ortega *et al.* only 2 bands lie in the vicinity of 10 meV around the Fermi level [241]. The fact that only part of the adatom dangling-bond electrons give rise to the metallicity of the surface implies a reduced metallic electronic density n and thus a reduced Fermi energy E_{F}. Since in both equations (5.14) and (5.15) the quasiparticle lifetimes are proportional to the electronic density, the calculations by Ortega *et al.* would imply smaller lifetimes than displayed in Fig. 5.16.

Despite the rough approximation of modeling the complex Si(111)7×7 surface by an idealized Fermi liquid approach, it has to be noted, however, that the RPA calculations yield the correct order of magnitude for the incoherent relaxation times and thus substantiate the experimentally observed indications for the metallicity of the dangling-bond bands on Si(111)7×7.

5.3.4 Scattering mechanism

From various SHG investigations, including adsorption [74], spectroscopy [134], and time-resolved experiments [133], and also from 2PPE studies performed under similar conditions [177] (Sect. 2.5), it is evident that for incident 1.55-eV (800-nm) photons the adatom dangling-bond states of Si(111)7×7 are the (near) resonant intermediate levels in the SH process. Their role is illustrated schematically in the inset of Fig. 5.15. An intense 1.55-eV pump pulse populates the partially unoccupied adatom dangling-bond states, whereas the relatively weak delayed probe pulse, that does not influence the dangling-bond population significantly, finds less unoccupied electronic states available for the enhancement of the SH process. The recoveries of the SH intensity with increasing probe delay time demonstrate the scattering times of the excited electrons out of the optically coupled region of adatom dangling-bond states in k-space.

In principle, the observed recovery of the SH signal in pump–probe experiments as well as the measured T_1 relaxation times obtained with the three-beam transient grating setup could be a result of carrier diffusion. However, since the adatom dangling-bond states are located energetically within the bulk band gap, diffusion or drift of the excited electrons normal to the surface into the volume is inhibited. In addition, the dynamics of space charges and the resulting band-bending and surface electric fields that lead to drift currents have been shown experimentally on Si(111) surfaces to lie between nanoseconds and microseconds [24, 29], far beyond the ps and sub-ps time scale of our experiments. *Lateral* carrier diffusion also occurs on time scales much longer than 1 ps for our spot sizes and grating periods on the order of 100 μm. Therefore the observed incoherent relaxation dynamics truly reflects population decay in k-space as opposed to diffusion in real space.

Candidates for scattering processes include Auger processes and radiative recombination. However, as these processes occur on much longer time scales than the femtosecond to picosecond range investigated in our study, they are irrelevant in our temporal regime. Radiative recombination times in *volume* semiconductors have been observed between nanoseconds in direct band-gap materials up to milliseconds in indirect semiconductors, in which the interaction with phonons is necessary for the recombination process [180]. The time scale of radiative recombination between *surface* states can be concluded from a 2PPE experiment by Bokor *et al.* on Si(111)2×1, that yielded the direct recombination between the antibonding π^* and the bonding π surface band in the sub-ns regime [21]. The relatively slow time dependence of direct recombination favors this process as key candidate for the long-time component on the nanosecond time-scale, that was observed by Mauerer (see inset of Fig. 5.14) and also in this work with both SH pump–probe experiments and the three-beam SH diffraction technique (barely visible in Figs. 5.9 and 5.10). Since lattice heating by the pump pulse can be estimated to be less than 25 K [133], thermal effects cannot be responsible for the long-time component in the SH signals. This slow component may be a result of the isotropic filling of the excited electrons within the U_1/S_1 adatom dangling-bond surface band after equilibration of the excited carriers. Once the band is isotropically filled in k-space, recombination leads to the relaxation of the long-time component on the nanosecond time scale.

Defects and impurities are both efficient centers for non-radiative recombination and scatterers for electrons. Although defect and impurity scattering occur mostly elastic, the significant wave vector change of the scattered electron can lead to its relocation out of the optically coupled region in k-space and thus to the observed relaxation of the SH signals in pump–probe and three-beam diffraction experiments (see Figs. 5.9 and 5.10). Experimentally, trapping and scattering times at defects and impurities on the Si(111)2×1 surface have been determined by 2PPE to be around 200 ps [21, 23], far beyond the time scale of femtoseconds to sub-picoseconds of our investigation. The irrelevance of defect and impurity scattering in our temporal regime is further corroborated by the independence of the population relaxation time with respect to oxygen coverage on Si(111)7×7 [133].

Another possibility for the relaxation mechanism of the excited electron population is the interaction with phonons. Due to the non-polarity of bulk silicon and thus the absence of any piezo-electric electron–phonon interaction, the interaction of the carriers with both acoustic and optical phonons is limited to deformation potential scattering. The weakly polar bonds at silicon surfaces, that are a result of charge transfer, are barely able to initiate any substantial piezo-electric contribution to the integral electron–phonon scattering rate. As a consequence of the typical scattering times of *acoustic* phonons in the nanosecond range [3], they play no role for the ultrashort relaxation component in our experiment.

The emission of *optical* phonons, on the other hand, has been shown to occur on a time scale of 100 fs in bulk silicon [3, 31]. The interaction with optical phonons is therefore a relevant candidate for our observed carrier relaxation time. The pronounced decrease in the population relaxation time for Si(111)7×7 at temperatures above 600 K (see Fig. 5.11) is an indication for the involvement of optical phonons at elevated temperatures. The observed decrease can, however, also be explained using a purely electronic phase space argument within Fermi liquid theory (see Fig. 5.16). However, since the screening of the deformation potential by high electronic densities is relatively weak [3], the electron–phonon interaction cannot account for the observed substantial increase in scattering time with increasing pump pulse fluence, as shown in Fig. 5.15 [133]. Nevertheless, it is very well possible that optical phonon scattering is the dominant relaxation process in Si(001).

For this reason, it is sensible to assign the fast relaxation of the SH signals in pump–probe and three-beam diffraction at the Si(111)7×7 surface to electron–electron scattering within the U_1/S_1 surface bands formed by the adatom dangling bonds. The quasi-elastic process of intraband electron–electron scattering (see inset of Fig. 5.15) implies that energy dissipation is not necessary in the fast relaxation process.

Chapter 6

Coherent dynamics

Although the incoherent population relaxation times as discussed in the preceding chapter yield valuable information about the carrier scattering machanism, one has to be aware, however, that the measured T_1 time is always a result of *multiple* scattering processes. This is a consequence of the experimental procedure of the SH pump–probe and SH three-beam diffraction schemes that both are sensitive to scattering of excited carriers out of the optically coupled region in k-space and thus yield average relaxation rates of a multi-step process. For the investigation of *single* carrier scattering instances it is necessary to employ an experimental technique that probes an electronic quantity which changes its value significantly in each interaction event. This one quantity is the phase of the electronic wavefunction that is addressed in coherent experiments. By measuring the dephasing times T_2 of induced electronic polarizations such methods gain important additional information on relaxation processes compared to incoherent techniques.

Carrier dephasing rates are important for understanding phenomena such as coherent generation and control of photocurrents in semiconductors [243, 244] as well as coherent optical switching by ultrafast pulses [245]. In order to determine the inelastic transport scattering time in semiconductor heterostructures independently of the elastic one, coherent techniques based on the observation of a current echo can be employed, as proposed theoretically by Niggemeier *et al.* [246]. Recently, Weinelt, Reuss, and coworkers studied the dephasing of image-potential states on Cu(001) by means of time- and energy-resolved two-photon photoemission [11, 247]. They obtained the influence of pure dephasing through the loss of coherence in quantum-beat spectroscopy and also from the results of linewidth and decay-rate measurements [11, 247].

Especially in solid-state investigations, photon echo experiments have been widely employed for the determination of dephasing times (see Sect. 2.3) [3]. To my knowledge, the only *surface-sensitive* experiment that makes use of the photon echo is the sum-frequency up-conversion scheme by Guyot-Sionnest, in which he studied the dephasing of the transient polarization of the Si–H adsorbate–substrate stretch vibration on Si(111) in real time [12]. With his setup, he succeeded in separating the dephasing due to the homogeneous linewidth from inhomogeneous broadening.

Whereas the extraction of quantitative population relaxation times T_1 from the time-resolved SH diffracted signal is relatively straight-forward (see Figs. 5.9 and 5.10), the deduction of dephasing times T_2 from the data is quite difficult. The reason for this difficulty is twofold: In the two-beam self-diffraction geometry, the temporal shift of the SH self-diffracted signal to positive time delays is mainly a function of the pulse duration (see Sect. 4.2), and depends only very insensitively on the dephasing time (see Fig. 6.2). Additionally, for both two-beam and three-beam setups, the determination of T_2 depends on the model used for the electronic system. Besides the qualitative fundamentals of this model (homogeneous, inhomogenous, or continuum model), the quantitative characteristics of the electronic band structure – which are not very well known for surface states – also influence the calculated dephasing times.

As already mentioned, we employed two methods to study the dephasing times T_2 of electronic surface states on Si(111) and Si(001). Sect. 6.1 presents the results of the two-beam SH self-diffraction experiment. In this set of measurements, the temporal shift of the diffracted signal with respect to the SFG cross-correlation time delay zero yields information about the order of magnitude of T_2 under the assumption of inhomogeneous broadening. The more advanced three-beam SH diffraction experiments with two independent time delays are the subject of Sect. 6.2. The use of three different incident directions together with the two independently tunable time delays provides a powerful tool to examine temporal relaxation behavior by means of spatial selection of the emerging beams. Finally, in Sect. 6.3 the different phenomenological models for the interpretation of the SH diffraction experiments are presented and discussed. The question which of these models – inhomogeneous broadening or continuum excitation – correctly describes the electronic systems under investigation, could be elucidated experimentally through the resolution of the SH diffracted signal in real time. This inherent uncertainty prevents the extraction of precise values for the dephasing times from our experimental data.

6.1 Second-harmonic self-diffraction

The second-harmonic self-diffraction setup is based on two synchronized incident optical pulses. The second pulse generates a transient population grating in the surface through interaction with the polarization in the material that was induced by the first pulse. In addition, photons from the second beam are diffracted from the transient grating, giving rise to second-harmonic light, which is detected as a function of time delay between the two pulses. A more qualitative description of the process was presented in Sect. 2.4.

With our experimental setup (Fig. 3.10) we were able to measure simultaneously the sum-frequency cross-correlation (Fig. 6.1a) and the correlation trace of the diffracted signal (Fig. 6.1b). Under the assumption of ideal sech^2 pulses, the width of 22 fs of the SFG cross correlation corresponds to a pulse duration of less than 14 fs

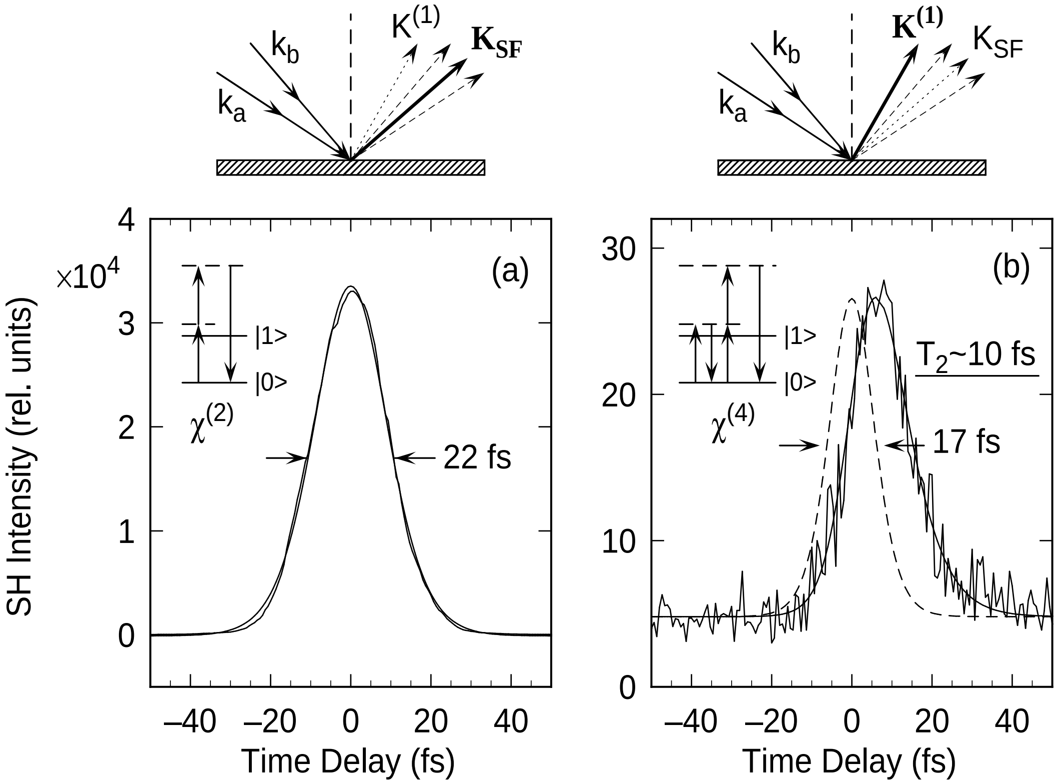

Fig. 6.1: a) SFG cross-correlation and b) self-diffracted SH signal from two beams incident on a clean Si(111)7×7 surface under 22° and 24°. The solid line through the data of the cross-correlation (a) and the dashed line in (b) indicate the calculated response of sech^2 pulses with a full width at half maximum of 14 fs. The shift and asymmetric broadening of the diffracted signal corresponds to a dephasing time around 10 fs under the assumption of an inhomogeneously broadened distribution of three-level systems [248].

– on the sample in UHV. With this cross-correlation we determined time delay zero. The most obvious characteristic of the diffracted signal is its shift to positive delay times. In addition, it exhibits a sharper rise than the SFG cross-correlation, and it is asymmetric. In the case of negligible relaxation times T_1 and T_2, one would expect a symmetric distribution with half-width of 17 fs (dashed line in Fig. 6.1b) for the sech^2 pulses that produce the SFG signal of Fig. 6.1a. This hypothetical correlation displays a narrower temporal width, because it corresponds to a four-photon absorption process, whereas in the SFG cross-correlation only two photons are absorbed. The shift to positive delays thus reflects the finite temporal response of the system. The best fit based on optical Bloch equations with variable finite decay time yields $\tau_\mathrm{d} \simeq 10$ fs under the assumption of inhomogeneous broadening.

Mauerer earlier conducted SH self-diffraction measurements on Si(111)7×7, but was not able to detect a finite temporal shift of the diffracted trace with respect to the SFG cross-correlation trace [133]. He observed neither the sharper temporal rise,

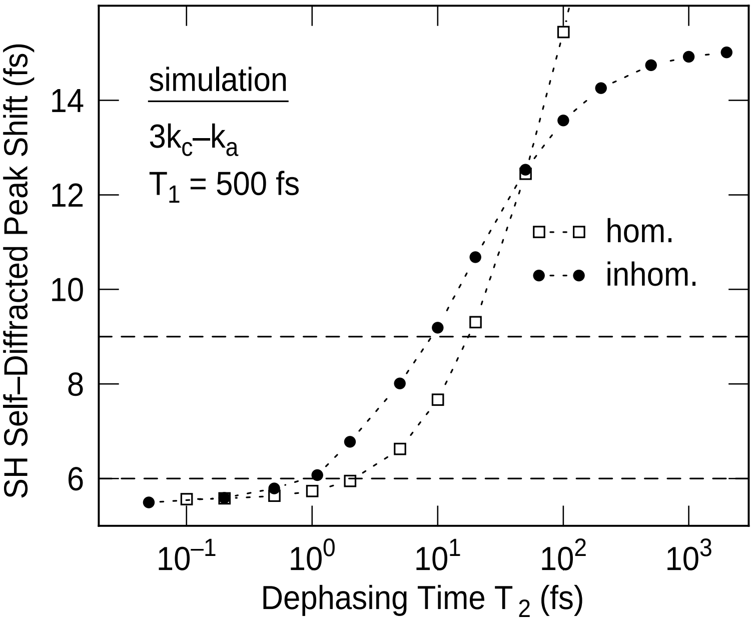

Fig. 6.2: Second-harmonic self-diffracted peak shift with respect to the SFG cross-correlation time delay zero as a function of dephasing time T_2, calculated within the density-matrix formalism as presented in Chap. 4. The calculations are based on independent three-level systems that model homogeneous behavior (open squares) as well as inhomogeneous broadening (circles). The measured shifts that are typically between 6 fs and 9 fs (between dashed horizontal lines) imply dephasing times on the order of 10 femtoseconds.

nor the asymmetry of the SH diffracted signal, which followed closely the shape of the SFG cross-correlation. The reason for his observation is probably the relatively long duration of his 120-fs pulses, that prevented the detection of relaxation phenomena on the femtosecond time scale.

Since the aim of this experimental scheme is to extract quantitative information about the dephasing processes, it is natural to take a look at the most prominent characteristic feature of the diffraction trace – the peak shift with respect to time delay zero – as a function of T_2. Fig. 6.2 shows the dependence of the peak shift as calculated within the density-matrix framework discussed in Chap. 4 on the dephasing time T_2 for both homogeneous and inhomogeneously broadened three-level systems. In both cases the dependence of the shift on T_2 is rather small, which complicates a precise determination of T_2 from the measured correlation traces. Qualitatively similar results for degenerate *four*-wave mixing were obtained by Weiner *et al.* [169]. Since typical diffracted shifts measured in our experiment lie between 6 fs and 9 fs (between dashed lines in Fig. 6.2), the dephasing time can, however, be extracted from the data to be on the order of 10 fs for both homogeneous and inhomogeneous model. Due to the insensitivity of the shift within the continuum model, that is discussed in Sect. 6.3, no information on T_2 can be extracted from the measured self-diffracted

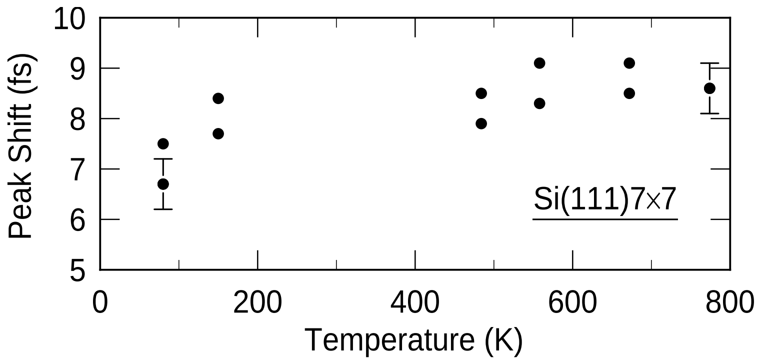

Fig. 6.3: SH self-diffracted peak shift from Si(111)7×7 with respect to the SFG time-delay zero as a function of surface temperature.

correlation traces in that case.

In the present self-diffraction experiment, however, the simultaneous measurement of the SFG cross-correlation (Fig. 6.1a) guarantees that shift and asymmetry of the diffracted signal (Fig. 6.1b) are caused by a finite intrinsic time constant. The deduced value of $T_2 \sim 10$ fs is smaller than the dephasing times observed for free-carrier dephasing in bulk semiconductors or semiconductor quantum wells [3] but larger than that of metallic systems [249]. Since the charge density in the dangling bonds of Si(111)7×7 is intermediate to those cases, this is the expected behavior.

The dependence of the SH self-diffracted temporal peak shift with respect to the SFG sum-frequency time delay zero is presented in Figs. 6.3–6.5 for Si(111)7×7 and in Figs. 6.6–6.7 for Si(001). Since the dependence of the shift on the various parameters is rather small or even absent, the insensitive shift-to-T_2 relation (see Fig. 6.2) did not allow to infer quantitative information on the variation of the dephasing time.

Fig. 6.3 shows the slight surface temperature dependence of the peak shift for Si(111)7×7. Due to the enhanced disturbing influence of black-body radiation from the surface at elevated temperature on the weak SH diffracted signal, it was not possible to extend the accessible temperature range beyond 800 K. The peak shift of 7 fs at 80 K is compatible with the low-temperature measurements with variable coverage (Fig. 6.4) and pulse fluence (Fig. 6.5), that were obtained with different silicon samples, and thus confirms the reproducibility of the measured data. The observed increase of the peak shift from 7 fs at 80 K to 9 fs at 800 K is probably a result of temperature-dependent variations in the energies of the surface electronic states. The resulting variations in the detuning of the incident photon energy relative to the distribution of transition energies lead to changes in the magnitude of the observed self-diffracted peak shift (see Fig. 4.3).

In Fig. 6.4 the dependence of the self-diffrated peak shift from Si(111)7×7 on oxygen exposure is displayed. A calibration of the coverage using the exposure-dependence of the diffracted intensity (Fig. 5.1) yields an oxygen coverage of almost

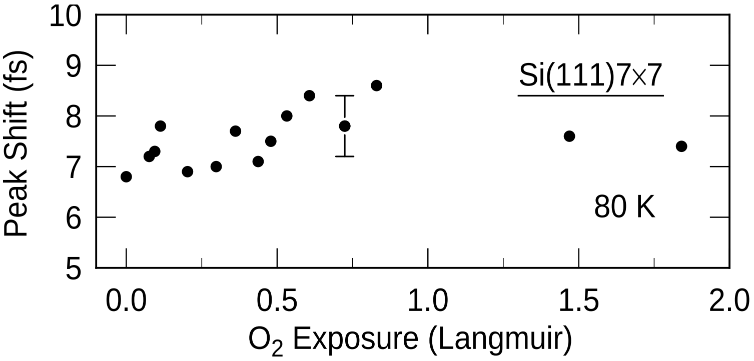

Fig. 6.4: SH self-diffracted peak shift from Si(111)7×7 at 80 K with respect to the SFG time-delay zero as a function of O_2 exposure. The data point of highest exposure (1.8 L) corresponds to an oxygen coverage on the order of 1 monolayer (see Sect. 5.1.1 and Fig. 5.1).

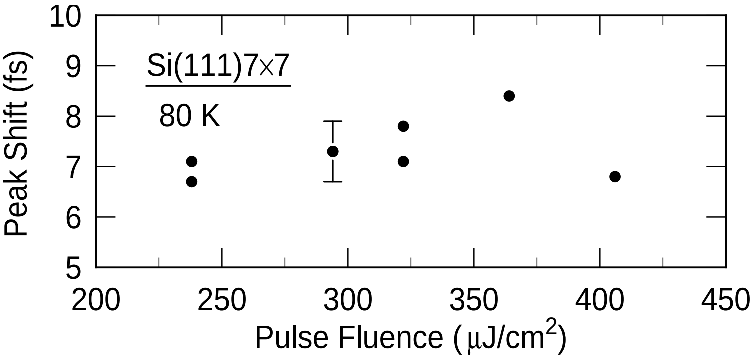

Fig. 6.5: SH self-diffracted peak shift from Si(111)7×7 at 80 K with respect to the SFG time-delay zero as a function of total pump and probe pulse fluence.

one monolayer for the data point of highest exposure (1.8 L). The absence of any significant variation of the shift in Fig. 6.4 does, however, not rule out a substantial decrease of the dephasing time due to the existence of efficient scatterers (*i.e.* oxygen atoms) on the surface. Since the magnitude of the peak shift stays at a finite minimum value even for vanishing dephasing time resulting from the finite population relaxation time (see Fig. 4.5), it is not possible to imply constant T_2 times from constant peak shift. In fact, Reuss, Weinelt, and coworkers studied the influence of surface defects and disorder on the dephasing rates of image-potential states on Cu(001) using two-photon photoemission [11, 247]. By adsorbing CO onto the copper surface, they observed a pronounced dependence of the dephasing rate on the degree of disorder on the surface [11, 247].

The pulse fluence dependence of the diffracted peak shift for Si(111)7×7 is shown in Fig. 6.5. In analogy to the discussion of Fig. 6.4, the constancy of the shift with respect to variations in pulse fluence does not allow to draw conclusions for the behavior of

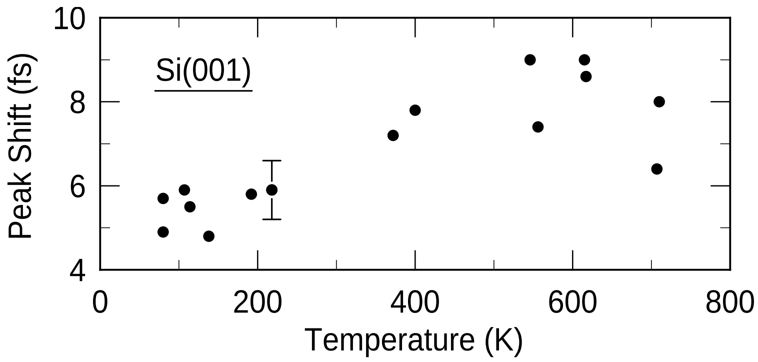

Fig. 6.6: SH self-diffracted peak shift from Si(001) with respect to the SFG time-delay zero as a function of surface temperature.

the dephasing rate. The behavior of the population relaxation time T_1 as a function of pump pulse fluence has been investigated by Mauerer [133] and was discussed in Sect. 5.3 (see Figs. 5.14 and 5.15).

In order to assess the experimental results for Si(111), it is useful to compare the SH self-diffracted data with identical measurements on Si(001). Fig. 6.6 shows the surface temperature dependence of SH self-diffracted peak shift for Si(001). Below 200 K Si(001) exhibits a peak shift around 5 fs, whereas at higher temperatures the shift is observed around 8 fs. The behavior complies with the measured population relaxation time T_1 as a function of temperature (Fig. 5.12), which shows a T_1 time of 100 fs in the low-temperature c(4×2) reconstruction, but an increased T_1 time of 160 fs in the high-temperature 2×1 phase. Since for small dephasing times the value of the T_1 time is a dominant contribution to the magnitude of the peak shift, its qualitative behavior as a function of temperature is not surprising. The reason for the relatively high transition temperature above 200 K in Fig. 6.6, as opposed to 150 K in Fig. 5.12 may be a result of the coexistence of both structures on the surface, which has been observed in earlier studies of the phase transition [37].

The oxygen exposure dependence of the peak shift for Si(001) is shown in Fig. 6.7. As in the case of Si(111), the data for low temperatures of clean Si(001) are consistent with each other (cf. Fig. 6.6). The fact that the peak shift of 5 fs at 80 K for Si(001) is smaller than the value of 7 fs for Si(111) is readily explained by the smaller low-temperature T_1 of 100 fs compared to 180 fs, respectively (see Fig. 5.11 and 5.12). The rising behavior of the peak shift with increasing coverage that is displayed in Fig. 6.7 indicates an increase in T_1, which complies with the carrier transport model to efficient recombination centers as discussed in Sect. 5.2. Since the adsorption of oxygen destroys the well-ordered surface structure of clean Si(001), the transport of surface carriers to the recombination centers (*e.g.* steps) is hindered. Therefore, the adsorption of oxygen on Si(001) increases the population relaxation time T_1, which appears as increasing magnitude of the peak shift in Fig. 6.7.

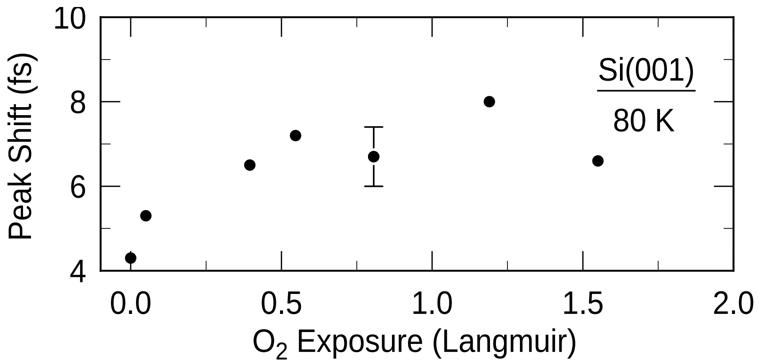

Fig. 6.7: SH self-diffracted peak shift from Si(001) at 80 K with respect to the SFG time-delay zero as a function of O_2 exposure. The data point of highest exposure (1.6 L) corresponds to an oxygen coverage around 0.5 monolayers (see Sect. 5.1.1 and Fig. 5.1).

The discussion in this section reveals, that our transient grating experiment in the SH self-diffracted two-beam geometry delivers only limited quantitative information about the dephasing time of the electronic surface states investigated. From the analysis of Fig. 6.2 it is only possible to deduce T_2 on the order of magnitude of 10 fs under the assumption of an inhomogeneously broadened distribution of three-level systems, that is characterized by vanishing coupling between the three-level systems. The introduction of finite coupling leads to a continuum model that is discussed in Sect. 6.3.

6.2 Second-harmonic three-beam diffraction

One possibility to extend the capabilities of the second-harmonic diffraction experiments in terms of extractability of physical relaxation parameters is the lifting of the spatial and temporal degeneracy of the incident excitation beams. In the *self*-diffraction setup, we used one of the two incident beams simultaneously as a pump pulse that generated the transient population grating together with the other pulse, and as a probe pulse that was diffracted from the grating it generated itself. In order to enhance the experimentally accessible degrees of freedom, we therefore extended the two-beam geometry with a spatially distinct synchronized third beam.

A special form of the SH three-beam diffraction scheme has already been presented in Chap. 5. The data in Fig. 5.10 have been obtained with the three-beam geometry, in which the two pump beams that produce the grating are temporally coincident, and the time delay with respect to the diffracted probe beam is varied. By using this setup it is possible to deduce population relaxation times directly from the SH diffraction trace (see Fig. 5.10).

A set of three-beam second-harmonic diffraction measurements into direction $2\mathbf{k}_c+$

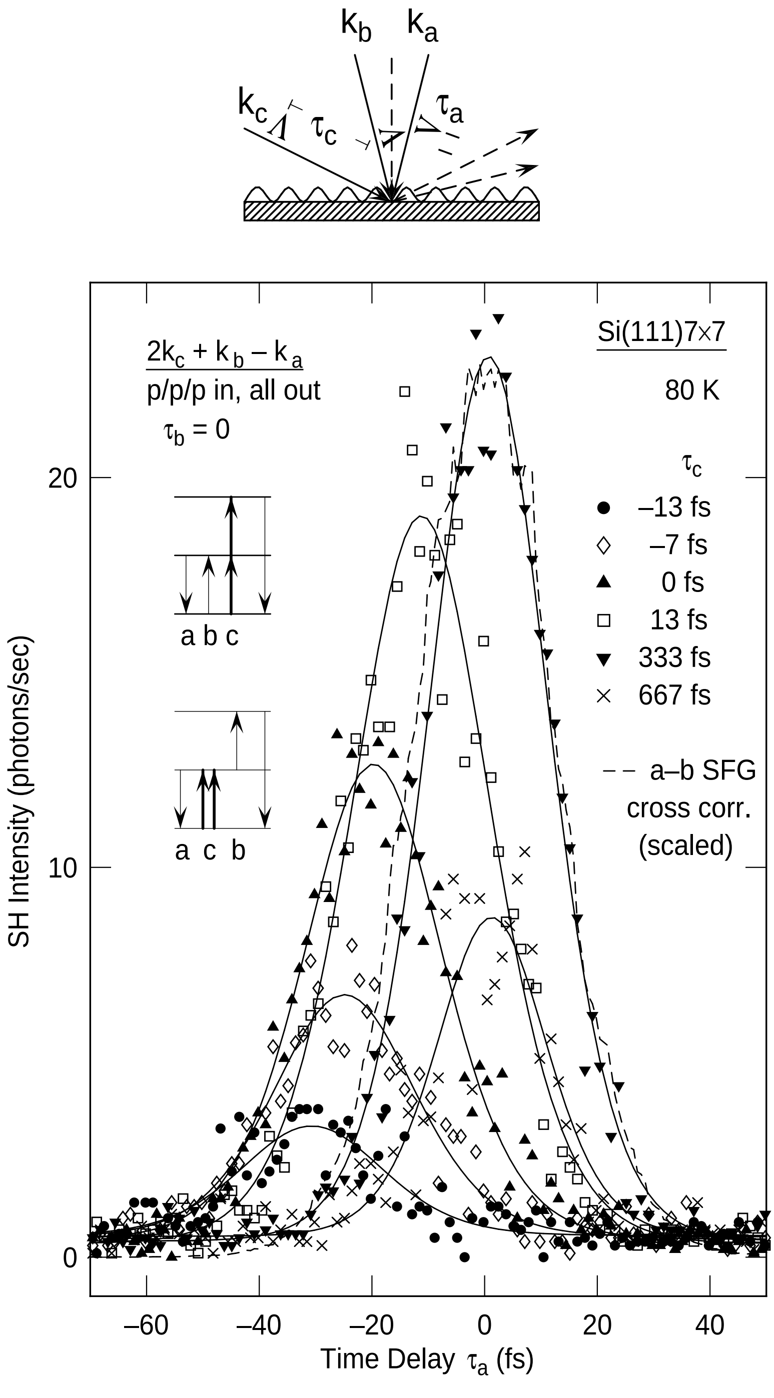

Fig. 6.8: Set of second-harmonic diffraction measurements from Si(111)7×7 at 80 K in the three-beam geometry detected in the direction $2\mathbf{k}_\mathrm{c} + \mathbf{k}_\mathrm{b} - \mathbf{k}_\mathrm{a}$. One of the two independently tunable time delays (τ_a) is displayed on the x-axis, while the other (τ_c) is chosen to be a parameter of the different curves. τ_b is set to zero. The dashed line is the measured SFG cross-correlation between the beams $\mathbf{k}_\mathrm{a}$ and $\mathbf{k}_\mathrm{b}$, that determines time delay τ_a zero. The solid lines through the data points are guides to the eye.

$\mathbf{k}_\mathrm{b} - \mathbf{k}_\mathrm{a}$ is shown in Fig. 6.8. Compared to two-beam self-diffraction, three-beam diffraction has one additional temporal degree of freedom, that is the additional second time delay. In Fig. 6.8 one delay is displayed on the x-axis, while the other is chosen to be a parameter of the different curves. With increasing delay τ_c the correlation traces shift from negative delays τ_a to zero, while rising in intensity. From τ_c values of a few 100 fs, the traces stay centered at $\tau_\mathrm{a} = 0$ and decay on the time scale of the population relaxation time.

This behavior can be understood qualitatively by a transient population grating generated by $\mathbf{k}_\mathrm{a}$ and $\mathbf{k}_\mathrm{b}$ from which $\mathbf{k}_\mathrm{c}$ is diffracted (upper photon diagram in Fig. 6.8). The lower photon diagram in Fig. 6.8 corresponds to the upconversion of a photon echo, that is not visible in our data. If present, a photon echo should appear in form of additional peaks near $\tau_\mathrm{a} = 2\tau_\mathrm{c}$ for negative time delays. However, this observation does not rule out an inhomogeneously broadened system, because small dephasing times T_2 give rise to temporal shifts of the echo and also to very small echo intensities. As already discussed in Sect. 5.2, the T_1 values deduced directly from the three-beam correlation traces are fully consistent with the ones that we observe with second-harmonic pump–probe (see Fig. 5.11).

A summary of the different purely optical second-harmonic experiments that we performed is displayed in Fig. 6.9. The incidence of three pulses onto the surface leads to a bunch of reflected and diffracted beams at the second-harmonic frequency (top panel in Fig. 6.9). The resulting second-harmonic beams emerge in four different categories: The open squares represent the reflected second-harmonic signal originating from two photons of one single beam ($2\mathbf{k}_\mathrm{a}$). It shows the characteristic dip after a pump pulse and the subsequent reincrease that is a measure for the population relaxation time T_1 (see Fig. 5.9). The dashed line around time delay zero is the sum-frequency cross-correlation trace that arises from the interaction of one photon of two distinct beams each ($\mathbf{k}_\mathrm{a}+\mathbf{k}_\mathrm{b}$). Its temporal position denotes time delay zero and its width allows to deduce the pulse duration. The solid line is the second-harmonic self-diffracted correlation trace shown already earlier in Fig. 6.1. It originates from three photons of one beam and one photon of another beam ($3\mathbf{k}_\mathrm{a} - \mathbf{k}_\mathrm{b}$). Its shift to positive time delays allows to infer T_2 dephasing times. The signal denoted by the circles is impossible to obtain in a two-beam self-diffraction geometry. It corresponds to a four-photon absorption process from three distinct beams, such as one beam contributes two photons ($2\mathbf{k}_\mathrm{c}+\mathbf{k}_\mathrm{b}-\mathbf{k}_\mathrm{a}$). Though the trace shown here allows to extract T_1 population relaxation times (also see Fig. 5.10), the freedom of two independently adjustable time delays also allows to obtain further information about dephasing processes characterized by T_2.

Before we discuss the applicability of several phenomenological models to our data in Sect. 6.3, the numerical simulation of the three-beam diffracted correlation traces under the assumption of inhomogeneous broadening is presented. For the accurate determination of the relaxation rates it is necessary to model the temporal evolution

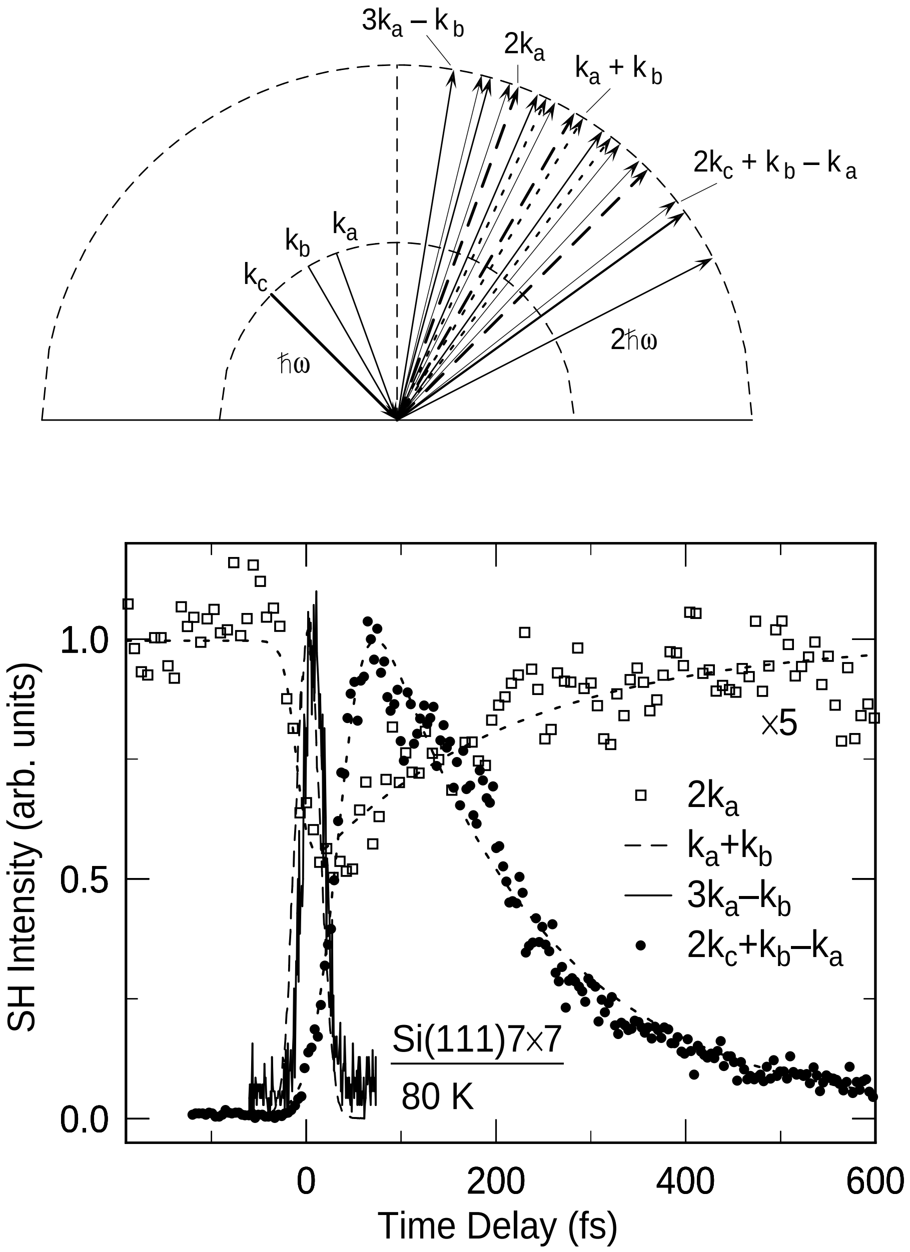

Fig. 6.9: SH signals into various directions. Top: The incidence of three pulses $\mathbf{k}_{\mathrm{a}}$, $\mathbf{k}_{\mathrm{b}}$, and $\mathbf{k}_{\mathrm{c}}$ onto the surface leads to a bunch of reflected and first-order diffracted beams at the second-harmonic frequency. Bottom: Example traces of the four different categories, in which the SH beams emerge from Si(111)7×7 at 80 K. Reflected SH signal after a pump pulse ($2\mathbf{k}_{\mathrm{a}}$, open squares), sum-frequency cross-correlation ($\mathbf{k}_{\mathrm{a}}+\mathbf{k}_{\mathrm{b}}$, dashed line), SH self-diffracted correlation trace ($3\mathbf{k}_{\mathrm{a}}-\mathbf{k}_{\mathrm{b}}$, solid line), and SH three-beam diffracted signal ($2\mathbf{k}_{\mathrm{c}}+\mathbf{k}_{\mathrm{b}}-\mathbf{k}_{\mathrm{a}}$, circles). The dotted lines through the data are fits.

of the diffracted SH signal by means of a density-matrix calculation, as discussed in Chap. 4. Such a description yields several terms of the form (2.9) for the nonlinear

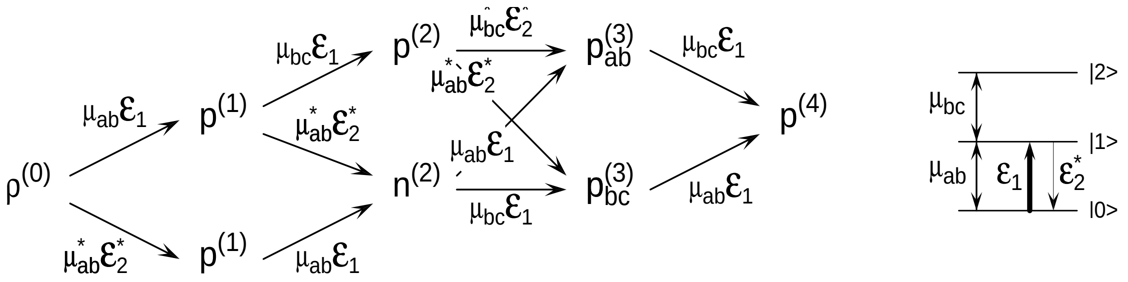

Fig. 6.10: Schematic summary of the photon processes A–F contributing to SH diffraction. Shown is the consecutive build-up of nonlinear polarization and population starting from the unperturbed ground state $\rho^{(0)}$ up to the fourth order nonlinear polarization $p^{(4)}$ into the self-diffracted direction $3\mathbf{q}_1 - \mathbf{q}_2$. Each of the 6 different pathways from $\rho^{(0)}$ to $p^{(4)}$ comprises three excitations by $\mathcal{E}_1$ and one excitation by $\mathcal{E}_2^*$ and corresponds to one photon diagram in Fig. 6.11.

polarization $\mathbf{P}_\mathrm{s}^{(4)}$ (see App. A). These terms correspond to different possibilities for the temporal order of the four incoming photons that contribute to the $\chi^{(4)}$ process.

Fig. 6.10 schematically displays the set of differential equations (B.13) for the polarizations and populations of first, second, third, and fourth order, that was derived in App. B. The consecutive absorption of four photons transform the ground state $\rho^{(0)}$ to the fourth order polarization $p^{(4)}$, giving rise to 6 different paths that lead from $\rho^{(0)}$ to $p^{(4)}$. Each of these paths corresponds to one distinct $\chi^{(4)}$ photon process shown in Fig. 6.11.

From the arrangement in Fig. 6.11 it is apparent that the second-harmonic diffraction process is not equivalent to a mere upconversion of the four-wave mixing signal like in two processes A and B. For a correct simulation of our experimental data we therefore take into account all six terms.

A result of a numerical calculation for the three-beam geometry as presented in Fig. 6.8 is shown in Fig. 6.12. Besides quantitative differences compared to the experimental data in Fig. 6.8, that arise from unprecise input parameters, the calculation shows all qualitative features of the measured correlation traces. Both, the behavior of the peak shift from negative values up to a saturation at zero, and also the rise and fall of the peak intensity with increasing τ_c are reproduced.

A more detailed comparison of experimental SH three-beam diffraction data, like in Fig. 6.8, with density-matrix based calculations (Fig. 6.12) is presented in Fig. 6.13. Shown are experimental results for Si(111)7×7 (circles) and Si(001) (open squares) at 80 K together with a simulation (solid line) assuming an inhomogeneous, 600 meV broad distribution of intermediate states, T_1 times of intermediate and upper level of 500 fs, and pure dephasing times T_2^* of 5 fs for all three levels. The data were derived from compilations like Fig. 6.8 by representing each correlation trace by its three most intuitive parameters: peak intensity, peak shift with respect to time delay

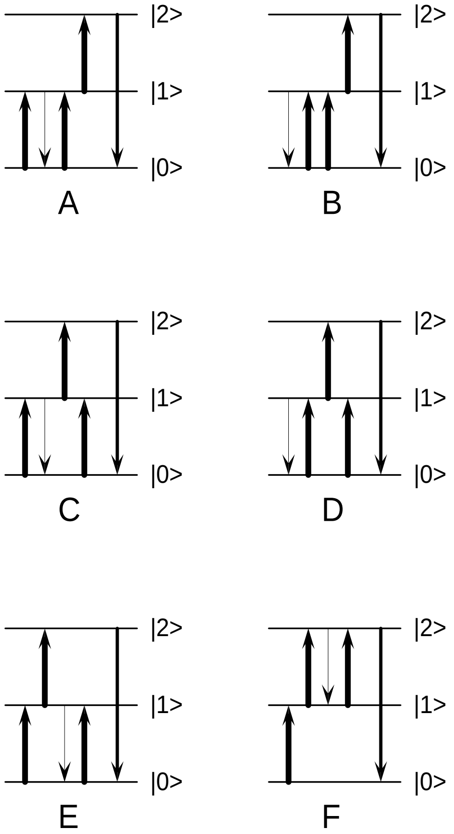

Fig. 6.11: Schematic representation of the 6 different $\chi^{(4)}$ photon processes A–F that constitute five-wave mixing in the second-harmonic self-diffraction geometry. Each process directly corresponds to one excitation path from the ground state to the fourth order polarization as depicted schematically in Fig. 6.10. From the arrangement it is apparent that the second-harmonic diffraction process is not equivalent to a mere upconversion of the four-wave mixing signal, like in the two processes A and B.

τ_a zero, and FWHM. The three values are displayed as a function of τ_c (the parameter of the different curves in Fig. 6.8) in the upper, center, and lower panel, respectively.

The peak intensity in the upper panel is similar to the diffraction trace at time delay $\tau_\mathrm{a} = 0$ shown in Fig. 5.10. It increases on the time scale of the pulse duration to its maximum value, before it decays on the time scale of the population relaxation time T_1. The experimental peak intensities match the simulated data fairly well.

The peak shift in the center panel of Fig. 6.13 shows an increase from negative values to its saturation value zero, which is reached around time delay $\tau_\mathrm{a} = 0$. The fit between the calculated curve and the experimental data is excellent, both in terms of the slope of the increase and the saturation behavior. However, both Si(111) and Si(001) display an overshoot to positive time delays, that is not reflected in the simulation. The distinct time scales of the temporal decay of the overshoot – on the order of several 100 fs for Si(111) but at least an order of magnitude more rapidly

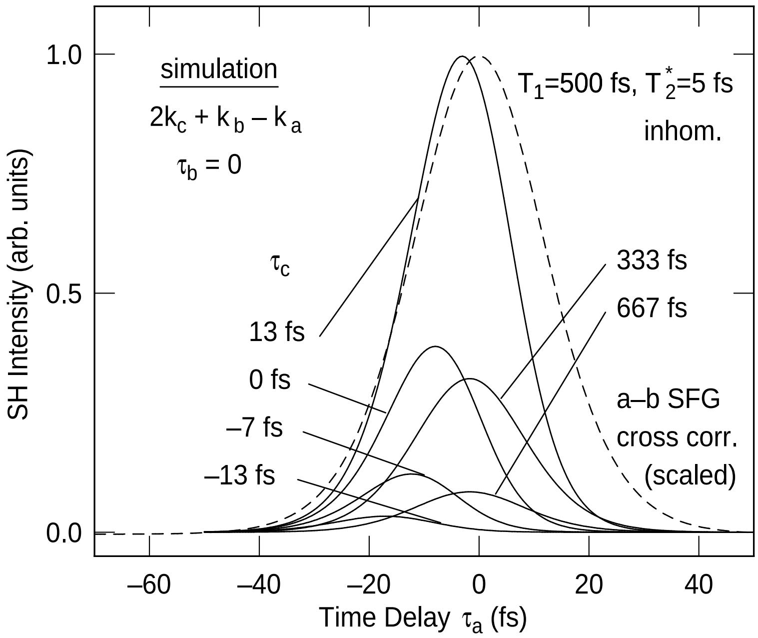

Fig. 6.12: Calculated set of second-harmonic three-beam diffraction traces into direction $2\mathbf{k}_c + \mathbf{k}_b - \mathbf{k}_a$. One of the two independently tunable time delays (τ_a) is displayed on the x-axis, while the other (τ_c) is chosen to be a parameter of the different curves. τ_b is set to zero. The dashed line is the calculated SFG cross-correlation between the beams $\mathbf{k}_a$ and $\mathbf{k}_b$, that determines time delay τ_a zero. Input parameters of the numerical calculation were T_1 times of the intermediate and upper level of 500 fs, pure dephasing times T_2^* for all three levels of 5 fs, a pulse duration of 14 fs, and a 600 meV broad inhomogeneous distribution of the intermediate level.

for Si(001) – may include important quantitative information about the dephasing rates. Since the overshoot is not existent in the simulation of the inhomogeneously broadened model, a calculation using the continuum model would be highly desirable (see Sect. 6.3).

The width of the correlation traces in the lower panel of Fig. 6.13 show little variation as a function of delay τ_c. The calculated values match the measured data better than 10%. Despite minor differences between the experimentally obtained SH three-beam diffraction traces and the density-matrix based calculations, the agreement between model and experiment affirms the validity of the theoretical approach.

6.3 Phenomenological models

For both, the physical understanding of the underlying fundamental relaxation processes and the correct theoretical treatment of the diffracted correlation traces, a *microscopic* description of the nonlinear optical and electronic processes at the inves-

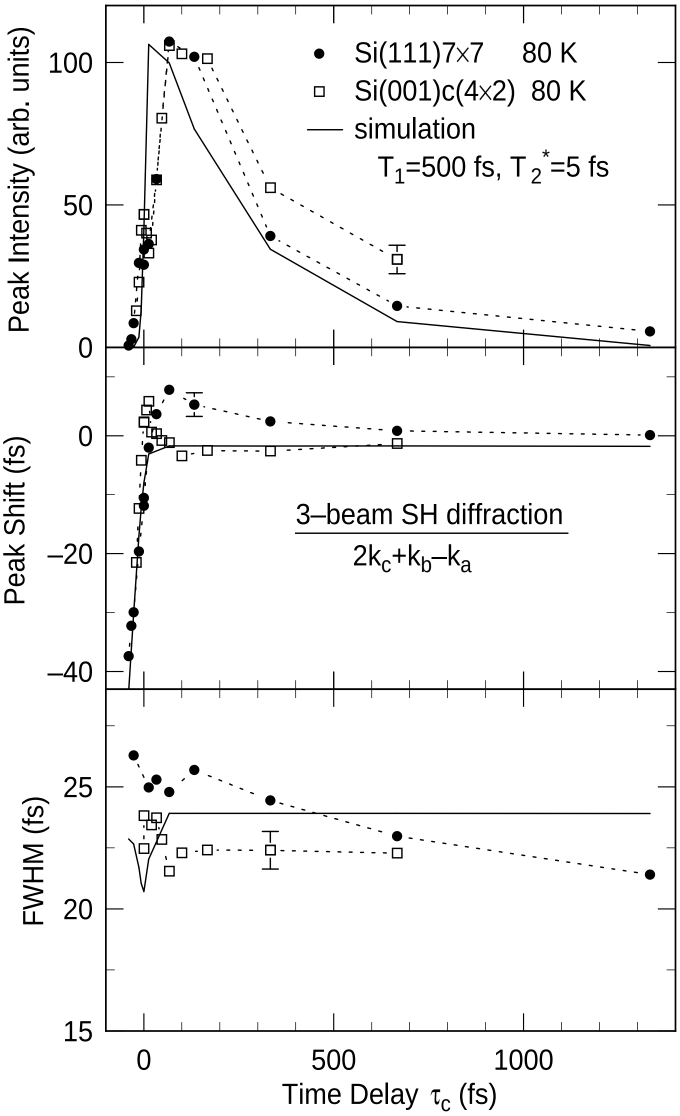

Fig. 6.13: Comparison of measured SH three-beam diffracted correlation traces as shown in Fig. 6.8 for Si(111)7×7 (circles) and Si(001) (open squares) at 80 K with calculations as shown in Fig. 6.12. The input parameters for the simulation are the same as in Fig. 6.12. Top panel: Peak intensity of the correlation traces. Center panel: Peak shift of the correlation traces with respect to time delay zero. Bottom panel: FWHM of the correlation traces.

tigated surfaces would be highly advantageous. However, the lack of precise experimental information and theoretical calculations of the electronic band structure of Si(111) and Si(001) and also the inavailability of certain degrees of freedom in our experiment – such as the impossibility to change the excitation wavelength – at the moment prevent the treatment on a microscopic level. Therefore, we are forced to rely on *phenomenological* models for the description of our experiment; three of these models are presented in Fig. 6.14.

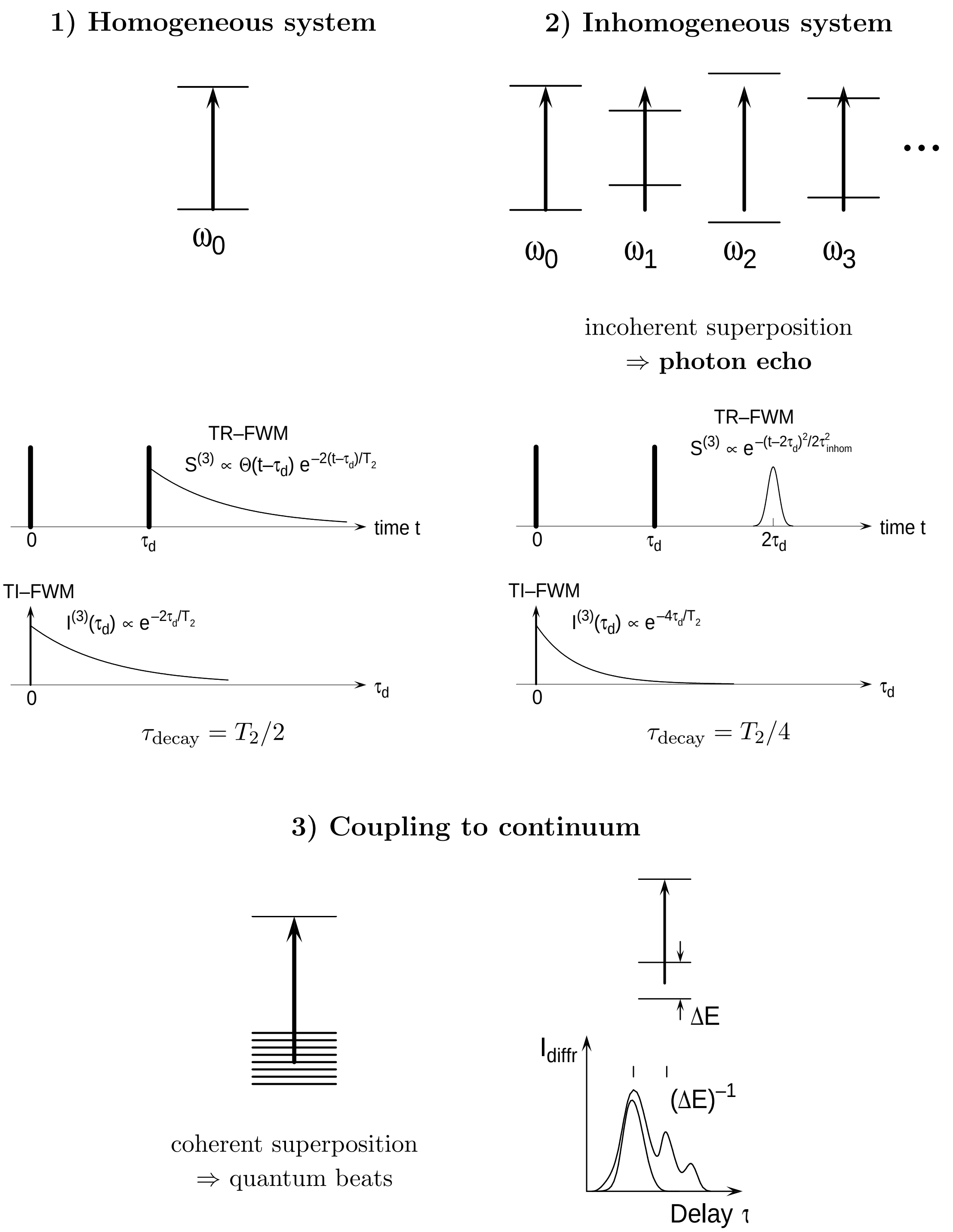

Fig. 6.14: Models for the phenomenological description of quantum systems. 1) Homogeneous system, consisting of a single transition frequency. 2) Inhomogeneous system, corresponding to a distribution of eigen-frequencies that are not coupled to each other. Only in this case a photon echo is possible. 3) Coupling to a continuum of states, leading to a rapid decay of the coherent polarization.

A relevant model would have to explain why the finite response time of the system that is clearly visible in the diffracted signal (Fig. 6.1b) does not appear in the SFG signal (Fig. 6.1a). If the polarization $\mathbf{P}_{\rm a}^{(1)}$ created by the pulse $\mathbf{k}_{\rm a}$ is present when the delayed pulse $\mathbf{k}_{\rm b}$ arrives at the surface, 2ω photons should be emitted. In fact, this has been exploited in IR–visible SFG experiments to measure the free induction decay of adsorbate vibrations [12, 13].

In the introduction to the transient grating experiment (Sect. 2.4) we assumed that the system is characterized by one resonantly excited transition frequency ω_{01} (homogeneous system in Fig. 6.14). In this case the polarization $\mathbf{P}_{\rm s}^{(4)}$ would decay with a time constant T_2 and the measured diffracted signal $I_{\rm d} \propto |\mathbf{P}_{\rm s}^{(4)}|^2$ with $T_2/2$. However, this situation is not directly applicable to our experiment. The 7×7 structure of Si(111) is characterized by four energetically inequivalent adatoms [87], the $\rm U_1$ band has a width of several 100 meV (cf. Fig. 2.12), and the valence band provides a wide energy range for the initial states of excitation. In addition, the electronic band structures of surface states on both Si(111) and Si(001) (see Figs. 2.2 and 2.4) display a finite dispersion within their respective Brillouin zones, that leads to a inhomogeneous broadening in k-space. Despite the short excitation pulses it is reasonable to assume that the inhomogeneous linewidth of the transition is larger than the spectral width of the pulse ($\sim$ 120 meV). Since the different excited eigenfrequency components evolve at different rates $\mathrm{e}^{i\omega_{01}t}$, the macroscopic polarization $\mathbf{P}_{\rm a}^{(1)}$ created by the first pulse will decay to zero within the pulse width, even in the absence of dephasing collisions (inhomogeneous system in Fig. 6.14). A delayed pulse $\mathbf{k}_{\rm b}$ cannot upconvert this polarization and generate 2ω radiation in the direction $K_{{\rm SF},x} = k_{{\rm a},x} + k_{{\rm b},x}$. In such a situation, small changes of the cross-correlation due to true dephasing processes are very difficult to detect even by means of interferometric measurements [250].

The diffracted signal, in contrast, is generated by a pulse sequence which causes transitions between $|0\rangle$ and $|1\rangle$. In the case of negligible coupling between the three-level systems (inhomogeneous broadening), the second pulse incident at $t = t_{\rm b}$ is able to reverse the phase evolution of the oscillating dipoles created by the first pulse at $t = t_{\rm a} = 0$. This leads to a photon echo which is peaked at $t = 2t_{\rm b}$ [171]. In the two-beam SH self-diffraction experiment the echo signal is not time-resolved. However, as its height is proportional to $\exp(-4t_{\rm b}/T_2)$ the echo leads to a decay of the diffracted signal with a time constant $T_2/4$, provided the broadening is truly inhomogeneous, which is equivalent to negligible coupling between the different three-level systems.

The identity of the initial state in the SH diffraction process is not well known. Considering our excitation energy of 1.55 eV, candidates for the initial state are both electronic surface states, such as $\rm S_2$ on Si(111)7×7 (Fig. 2.2) or $\rm D_{up}$ on Si(001) (Fig. 2.4), and volume states within the valence band of silicon. In case of excitation from bulk states, it is not clear that these transitions should be independent of each other. If we introduce a finite coupling between the different three-level systems, we end up with a continuum model, as shown at the bottom of Fig. 6.14. A continuum

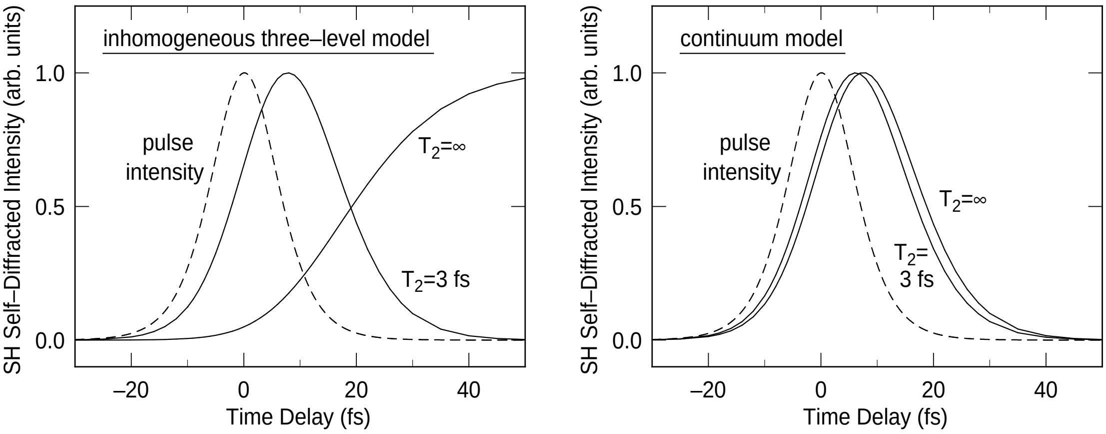

Fig. 6.15: Time-integrated SH self-diffracted intensity as a function of pump–probe time delay for infinite population relaxation times T_1 and different dephasing times T_2 calculated within the inhomogeneously broadened three-level model (left panel) and with the continuum model (right panel). The dashed lines denote the pulse intensity as a function of time. Whereas the peak of the diffracted signal shifts very sensitively with the dephasing time T_2 of the electronic system in the inhomogeneous model, the peak in the continuum model is relatively insensitive to changes in T_2. The different dependencies for the two models imply that the determination of T_2 by means of the self-diffracted data very susceptibly depends on the model employed. The time-*resolved* SH intensities for the two traces with infinite T_2 are depicted in Fig. 6.16. (From Reichelt [254]).

of quantum states can be approximated by a distribution of equally spaced levels in the limit of vanishing energetic separation between the states [251]. The coherent superposition of transitions from a set of levels with *finite* energy spacing ΔE results in the emergence of quantum beats in the coherent polarization with a temporal period proportional to $1/\Delta E$. The modulations can be observed experimentally by transient four-wave mixing with time-resolved detection of the coherent nonlinear signal [252].

The case of true continuum transitions displays a qualitatively different behavior compared to the finite number of levels. In 1980, Yeh and Eberly devised a model for continuum transitions in which they showed induced off-diagonal coherence to decay irreversibly [253]. Their model demonstrates that one cannot recover off-diagonal coherence by the application of subsequent radiative pulses, ruling out the occurence of long-time or repetitive transients, such as photon echoes [253]. Thus the continuum excitation yields a rapid decay of the nonlinear polarization on the time scale of the laser pulse due to the intrinsic destructive quantum interference between the coupled continuum levels (see bottom of Fig. 6.14). This behavior is a general effect that occurs whenever discrete transitions couple to a continuum of states [251].

The nature of the employed phenomenological model has a profound influence on the numerical simulation of the SH diffraction experiment. Whereas in the inhomoge-

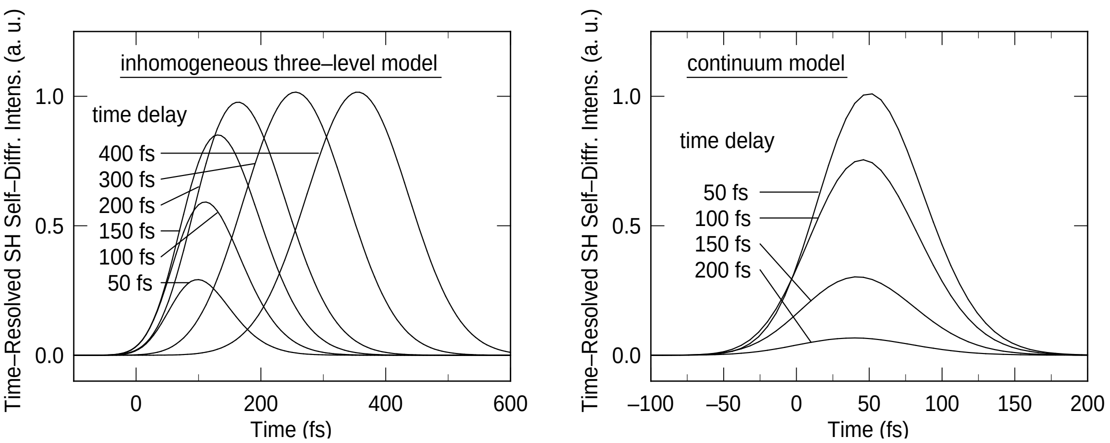

Fig. 6.16: Time-resolved SH self-diffracted intensity of the traces shown in Fig. 6.15 as a function of time for infinite population relaxation times T_1 and dephasing times T_2 calculated for a set of pump–probe time delays within the inhomogeneously broadened three-level model (left panel) and with the continuum model (right panel). Whereas the inhomogenous model displays a temporal peak shift with varying time delay in analogy to a photon echo, the peak position within the continuum model stays relatively constant. (From Reichelt [254]).

neous model the number of differential equations scales linearly with the number n of the three-level systems, it is proportional to n^2 for the continuum case, as a result of the generated coherences within the continuum. This relation limited our own computational efforts to the inhomogeneously broadened model, in which we calculated with a number of three-level systems of typically 100. A numerical approach of the continuum model was prevented by our limited computing capacities.

However, in order to compare predictions from the inhomogeneous model with excitation from a continuum, we received theoretical help from Reichelt and Meier, who performed calculations also for the continuum model [254]. Fig. 6.15 shows their results for the time-integrated SH diffracted signal in the two-beam self-diffraction geometry for infinite T_1 and two different dephasing times T_2. Whereas the diffracted signal for infinite relaxation times shows no decay with time delay in the inhomogeneous model, the continuum excitation gives rise to a rapid decay of the signal on the time of the laser pulse. The consequence of this behavior is a sensitive shift of the diffracted signal with the dephasing time T_2 (note: infinite T_1), whereas the peak in the continuum model is relatively insensitive to to changes in T_2. The distinct behavior in the two models implies that a precise determination of T_2 from the self-diffracted data depends on the correct phenomenological model. The case of inhomogeneous broadening yields a dephasing time T_2 on the order of 10 fs, whereas in the case of excitation from a continuum a quantification of T_2 is not possible.

For a first preliminary evaluation of results from the three-beam geometry, Reichelt and Meier also calculated the time-*resolved* SH diffracted intensity in the self-diffraction setup for infinite T_1 and T_2, as shown in Fig. 6.16 for several time delays [254]. The respective time-*integrated* diffraction traces for $T_2 = \infty$ were displayed in Fig. 6.15. For inhomogeneous broadening, the diffracted peak shifts with varying time delay (left panel in Fig. 6.16). This behavior is analogous to the photon echo in four-wave mixing. For the continuum model, however, a variation of time delay has almost no influence on the temporal position of the peak (right panel in Fig. 6.16). The principal effect of varying time delay is a change in the magnitude of the peak.

The qualitatively different behavior of the time-resolved calculations for the two models indicates the usefulness of the three-beam approach to decide, which of the phenomenological models correctly describes our experiments. Calculations of continuum excitation for the SH three-beam diffraction geometry are therefore a highly desirable goal for the near future. The determination of the relevant phenomenological model could then open the door for a more microscopic understanding of the relaxation processes on semiconductor surfaces.

Appendix A

Explicit integration of Bloch equations

This appendix presents the explicit integration of the iterative differential equations (4.28) for the nonlinear optical populations and polarizations that were derived in Sect. 4.1. After some general considerations in Sect. A.1 follows the consecutive integration from first to fourth order in terms of the incident fields (Sect. A.2–A.5). Analytic results for the fourth-order second-harmonic diffracted polarization $p^{(4)}$ for the complementary limiting cases of electric field pulse durations very short and very long compared to the relaxation times T_1 and T_2 of the electronic system are presented in Sects. A.6 and A.7.

A more general numerical solution of the differential equations for arbitrary pulse shapes $A(\mathbf{R}, t)$ is the topic of App. B.

A.1 General considerations

The explicit integration of the differential equations (4.28) that were derived in Sect. 4.1 utilizes that

$$\dot{n}(t) = -gn(t) + f(t) \tag{A.1}$$

has the solution

$$n(t) = \int_{-\infty}^{t} \mathrm{d}t_1 \mathrm{e}^{-g(t-t_1)} f(t_1). \tag{A.2}$$

In the two-pulse geometry, the electric field is given by

$$\mathcal{E}(t) = \mathcal{E}_1 A(\mathbf{R}, t) \mathrm{e}^{i\mathbf{q}_1 \cdot \mathbf{R}} + \mathcal{E}_2 A(\mathbf{R}, t - \tau_d) \mathrm{e}^{i\mathbf{q}_2 \cdot \mathbf{R}}, \tag{A.3}$$

where $\mathcal{E}_1$ ($\mathcal{E}_2$) is the amplitude of the first (second) electric field with wavevector $\mathbf{q}_1$ ($\mathbf{q}_2$) and $A(\mathbf{R}, t)$ is the electric field pulse shape at $\mathbf{R}$. Analogously, the electric field in the three-pulse geometry is a sum of three terms with two independent time delays.

A.2 First-order polarization

Using Eq. (A.2), the integration of Eq. (4.14) in Sect. 4.1 directly yields the first-order polarization $p^{(1)}$

$$\begin{array}{rcl} p^{(1)}(t) & = & \displaystyle\int_{-\infty}^{t} \mathrm{d}t_1 \mathrm{e}^{-\frac{t-t_1}{T_{2,p(1)}}} \mathrm{e}^{i\omega_{ab}(t-t_1)} \left(-\frac{\delta_{ab}(t_1)}{i\hbar}\right) \\ \Uparrow & = & \displaystyle \mathrm{e}^{i\omega t}\frac{ie}{\hbar} r_{ab} \int_{-\infty}^{t} \mathrm{d}t_1 \mathrm{e}^{-\frac{t-t_1}{T_{2,p(1)}}} \mathrm{e}^{-i\Delta_{ab}(t-t_1)} \Big[\mathcal{E}_1 A(\mathbf{R},t_1)\mathrm{e}^{i\mathbf{q}_1\cdot\mathbf{R}} + \\ \uparrow & & \displaystyle +\mathcal{E}_2 A(\mathbf{R},t_1-\tau_d)\mathrm{e}^{i\mathbf{q}_2\cdot\mathbf{R}}\Big] . \end{array} \tag{A.4}$$

$p^{(1)}$ is a sum of two terms that correspond to the polarizations induced by $\mathcal{E}_1$ and $\mathcal{E}_2$ radiated into directions $\mathbf{q}_1$ and $\mathbf{q}_2$, respectively. The factor preceding the integral in Eq. (A.4) shows that this polarization is emitted with the fundamental frequency ω. Since the first-order polarization corresponds to an excitation from the ground state $|a\rangle$ to the intermediate state $|b\rangle$, $p^{(1)}$ is proportional to the dipole matrix element r_{ab}.

A.3 Second order

The second-order population $n^{(2)}$ and polarization $p^{(2)}$ result from a further integration of $p^{(1)}$. In a physical picture this fact reflects the interaction of one excitation pulse with the polarization in the material induced by the other pulse, which leads to a population grating $n^{(2)}$ and a radiation emitted at the second-harmonic frequency $p^{(2)}$ (see also Fig. 6.10 in Sect. 6.2).

A.3.1 Population $n^{(2)}$

The integration of Eq. (4.17) in Sect. 4.1 yields the second-order population grating $n^{(2)}$

$$\begin{array}{rcl} n^{(2)}(t) & = & \displaystyle\int_{-\infty}^{t} \mathrm{d}t_1 \mathrm{e}^{-\frac{t-t_1}{T_{1,n(2)}}} \left(\frac{\delta_{ab}(t_1)p^{(1)*}(t_1) - \delta_{ab}^{*}(t_1)p^{(1)}(t_1)}{i\hbar}\right) \\ & = & \displaystyle -\frac{e^2|r_{ab}|^2}{\hbar^2}\int_{-\infty}^{t} \mathrm{d}t_1 \mathrm{e}^{-\frac{t-t_1}{T_{1,n(2)}}} \int_{-\infty}^{t_1} \mathrm{d}t_2 \mathrm{e}^{-\frac{t_1-t_2}{T_{2,p(1)}}} \times \\ \Uparrow\Downarrow & & \times \Big[\Big(\mathrm{e}^{i\Delta_{ab}(t_1-t_2)} + \mathrm{e}^{-i\Delta_{ab}(t_1-t_2)}\Big)\left(\mathcal{E}_1\mathcal{E}_1^{*}A(\mathbf{R},t_1)A(\mathbf{R},t_2) + \right. \\ \uparrow\downarrow & & \left. +\mathcal{E}_2\mathcal{E}_2^{*}A(\mathbf{R},t_1-\tau_d)A(\mathbf{R},t_2-\tau_d)\right) \\ \downarrow\Uparrow & & +\mathcal{E}_1\mathcal{E}_2^{*}\Big(\mathrm{e}^{i\Delta_{ab}(t_1-t_2)}A(\mathbf{R},t_1)A(\mathbf{R},t_2-\tau_d) + \\ \Uparrow\downarrow & & +\mathrm{e}^{-i\Delta_{ab}(t_1-t_2)}A(\mathbf{R},t_1-\tau_d)A(\mathbf{R},t_2)\Big)\mathrm{e}^{i(\mathbf{q}_1-\mathbf{q}_2)\cdot\mathbf{R}} \\ \Downarrow\uparrow & & +\mathcal{E}_1^{*}\mathcal{E}_2\Big(\mathrm{e}^{i\Delta_{ab}(t_1-t_2)}A(\mathbf{R},t_1-\tau_d)A(\mathbf{R},t_2) + \\ \uparrow\Downarrow & & +\mathrm{e}^{-i\Delta_{ab}(t_1-t_2)}A(\mathbf{R},t_1)A(\mathbf{R},t_2-\tau_d)\Big)\mathrm{e}^{i(\mathbf{q}_2-\mathbf{q}_1)\cdot\mathbf{R}}\Big] . \end{array} \tag{A.5}$$

$n^{(2)}$ is a sum of six terms that correspond to the difference-frequency signal known as optical rectification [1], induced by one excitation and one deexcitation of $\mathcal{E}_1$ and $\mathcal{E}_2$ separately (first two summands in Eq. (A.5)), plus the population grating induced by one excitation of $\mathcal{E}_1$ and $\mathcal{E}_2$ each, in the four possible combinations (summands 3 to 6 in Eq. (A.5)). Depending on the contribution of the two incident fields, the terms in $n^{(2)}$ are proportional to $\mathcal{E}_1\mathcal{E}_1^*$, $\mathcal{E}_2\mathcal{E}_2^*$, $\mathcal{E}_1\mathcal{E}_2^*$, and $\mathcal{E}_1^*\mathcal{E}_2$ with wavevectors 0, 0, $\mathbf{q}_1-\mathbf{q}_2$, and $\mathbf{q}_2-\mathbf{q}_1$, respectively.

The absence of a prefactor of the form $\exp(i\omega t)$ indicates that this population grating is stationary and therefore does not give rise to emitted radiation. Since $n^{(2)}$ corresponds to an excitation and deexcitation of the transition between states $|a\rangle$ and $|b\rangle$, Eq. (A.5) shows $n^{(2)}$ to be proportional to $r_{ab}\cdot r_{ab}^*=|r_{ab}|^2$.

A.3.2 Polarization $p^{(2)}$

The integration of Eq. (4.17) also yields $p^{(2)}$

$$\begin{aligned} p^{(2)}(t) &= \int_{-\infty}^{t} \mathrm{d}t_1 \mathrm{e}^{-\frac{t-t_1}{T_{2,p(2)}}} \mathrm{e}^{i\omega_{ac}(t-t_1)} \left(-\frac{\delta_{bc}(t_1)p^{(1)}(t_1)}{i\hbar}\right) \\ &= \mathrm{e}^{2i\omega t}\left(-\frac{e^2 r_{bc} r_{ab}}{\hbar^2}\right) \int_{-\infty}^{t} \mathrm{d}t_1 \mathrm{e}^{-\frac{t-t_1}{T_{2,p(2)}}} \mathrm{e}^{i(\omega_{ac}+2\omega)(t-t_1)} \times \\ &\quad \times \int_{-\infty}^{t_1} \mathrm{d}t_2 \mathrm{e}^{-\frac{t_1-t_2}{T_{2,p(1)}}} \mathrm{e}^{-i\Delta_{ab}(t_1-t_2)} \times \\ &\quad \times \Big[\mathcal{E}_1^2 A(\mathbf{R},t_1)A(\mathbf{R},t_2)\mathrm{e}^{2i\mathbf{q}_1\cdot\mathbf{R}} \\ &\quad\quad +\mathcal{E}_1\mathcal{E}_2\left(A(\mathbf{R},t_1)A(\mathbf{R},t_2-\tau_d)+A(\mathbf{R},t_1-\tau_d)A(\mathbf{R},t_2)\right)\mathrm{e}^{i(\mathbf{q}_1+\mathbf{q}_2)\cdot\mathbf{R}} \\ &\quad\quad +\mathcal{E}_2^2 A(\mathbf{R},t_1-\tau_d)A(\mathbf{R},t_2-\tau_d)\mathrm{e}^{2i\mathbf{q}_2\cdot\mathbf{R}}\Big]. \end{aligned} \tag{A.6}$$

The prefactor $\mathrm{e}^{2i\omega t}$ reveals $p^{(2)}$ to be induced radiation at the second-harmonic frequency. The four summands in Eq. (A.6) give rise to second-harmonic beams into reflected directions $2\mathbf{q}_1$ and $2\mathbf{q}_2$ (proportional to $\mathcal{E}_1^2$ and $\mathcal{E}_2^2$, respectively), and into the sum-frequency direction $\mathbf{q}_1+\mathbf{q}_2$ (two terms, proportional to $\mathcal{E}_1\mathcal{E}_2$).

Since $p^{(2)}$ corresponds to a sequence of two transitions from $|a\rangle$ to $|b\rangle$ to $|c\rangle$, its amplitude is proportional to the product of transition dipole matrix elements $r_{ab}r_{bc}$.

A.4 Third order

The two third-order polarizations $p_{ab}^{(3)}$ and $p_{bc}^{(3)}$ reflect the polarizations between levels $|a\rangle$ and $|b\rangle$, and between $|b\rangle$ and $|c\rangle$, repectively. These quantities result from the interaction of the induced second-order population grating $n^{(2)}$ and second-harmonic polarization $p^{(2)}$ with a further excitation photon (see also Fig. 6.10 in Sect. 6.2).

Due to the interaction of three incident and one emerging optical wave, the radiation resulting from $p^{(3)}$ is called four-wave mixing signal.

An expression for $p^{(3)}$ into a specific direction was obtained by Yajima and Taira [189]. Their result is a special case of the general result for $p^{(3)}$ presented in Eqs. (A.7) and (A.8). The resulting time-ordered triple integral for $p^{(3)}$ can also be obtained by a third-order perturbation formalism derived by Mukamel *et al.* [170].

A.4.1 Polarization $p_{ab}^{(3)}$

The polarization $p_{ab}^{(3)}$ is obtained through the integration of Eq. (4.20) in Sect. 4.1

$$
\begin{aligned}
p_{ab}^{(3)}(t) &= \int_{-\infty}^{t} \mathrm{d}t_1 \mathrm{e}^{-\frac{t-t_1}{T_{2,pab(3)}}} \mathrm{e}^{i\omega_{ab}(t-t_1)} \left(-\frac{2\delta_{ab}(t_1)n^{(2)}(t_1)+\delta_{bc}^{*}(t_1)p^{(2)}(t_1)}{i\hbar}\right) \\
&= \mathrm{e}^{i\omega t}\left(-\frac{ie^3 r_{ab}}{\hbar^3}\right) \int_{-\infty}^{t} \mathrm{d}t_1 \mathrm{e}^{-\frac{t-t_1}{T_{2,pab(3)}}} \mathrm{e}^{-i\Delta_{ab}(t-t_1)} \times \\
&\quad \times \Bigg(|r_{ab}|^2 \int_{-\infty}^{t_1} \mathrm{d}t_2 \mathrm{e}^{-\frac{t_1-t_2}{T_{1,n(2)}}} \int_{-\infty}^{t_2} \mathrm{d}t_3 \mathrm{e}^{-\frac{t_2-t_3}{T_{2,p(1)}}} \times \\
&\qquad \times \Big\{\Big[2\mathcal{E}_1 A(\mathbf{R},t_1)\Big(\mathrm{e}^{i\Delta_{ab}(t_2-t_3)}+\mathrm{e}^{-i\Delta_{ab}(t_2-t_3)}\Big) \times \\
&\qquad\qquad \times \left(\mathcal{E}_1\mathcal{E}_1^{*}A(\mathbf{R},t_2)A(\mathbf{R},t_3)+\mathcal{E}_2\mathcal{E}_2^{*}A(\mathbf{R},t_2-\tau_d)A(\mathbf{R},t_3-\tau_d)\right) + \\
&\qquad\quad +2\mathcal{E}_1\mathcal{E}_2\mathcal{E}_2^{*}A(\mathbf{R},t_1-\tau_d)\Big(\mathrm{e}^{i\Delta_{ab}(t_2-t_3)}A(\mathbf{R},t_2)A(\mathbf{R},t_3-\tau_d)+ \\
&\qquad\qquad\qquad +\mathrm{e}^{-i\Delta_{ab}(t_2-t_3)}A(\mathbf{R},t_2-\tau_d)A(\mathbf{R},t_3)\Big)\Big]\,\mathrm{e}^{i\mathbf{q}_1\cdot\mathbf{R}} \\
&\qquad\quad +\Big[2\mathcal{E}_1\mathcal{E}_1^{*}\mathcal{E}_2 A(\mathbf{R},t_1)\Big(\mathrm{e}^{i\Delta_{ab}(t_2-t_3)}A(\mathbf{R},t_2-\tau_d)A(\mathbf{R},t_3)+ \\
&\qquad\qquad\qquad +\mathrm{e}^{-i\Delta_{ab}(t_2-t_3)}A(\mathbf{R},t_2)A(\mathbf{R},t_3-\tau_d)\Big) + \\
&\qquad\qquad +2\mathcal{E}_2 A(\mathbf{R},t_1-\tau_d)\Big(\mathrm{e}^{i\Delta_{ab}(t_2-t_3)}+\mathrm{e}^{-i\Delta_{ab}(t_2-t_3)}\Big) \times \\
&\qquad\qquad\quad \times \left(\mathcal{E}_1\mathcal{E}_1^{*}A(\mathbf{R},t_2)A(\mathbf{R},t_3)+\right. \\
&\qquad\qquad\qquad \left.+\mathcal{E}_2\mathcal{E}_2^{*}A(\mathbf{R},t_2-\tau_d)A(\mathbf{R},t_3-\tau_d)\right)\Big]\,\mathrm{e}^{i\mathbf{q}_2\cdot\mathbf{R}} \\
&\qquad\quad +2\mathcal{E}_1^{2}\mathcal{E}_2^{*}A(\mathbf{R},t_1)\Big(\mathrm{e}^{i\Delta_{ab}(t_2-t_3)}A(\mathbf{R},t_2)A(\mathbf{R},t_3-\tau_d)+ \\
&\qquad\qquad\quad +\mathrm{e}^{-i\Delta_{ab}(t_2-t_3)}A(\mathbf{R},t_2-\tau_d)A(\mathbf{R},t_3)\Big)\,\mathrm{e}^{i(2\mathbf{q}_1-\mathbf{q}_2)\cdot\mathbf{R}} \\
&\qquad\quad +2\mathcal{E}_1^{*}\mathcal{E}_2^{2}A(\mathbf{R},t_1-\tau_d)\Big(\mathrm{e}^{i\Delta_{ab}(t_2-t_3)}A(\mathbf{R},t_2-\tau_d)A(\mathbf{R},t_3)+ \\
&\qquad\qquad\quad +\mathrm{e}^{-i\Delta_{ab}(t_2-t_3)}A(\mathbf{R},t_2)A(\mathbf{R},t_3-\tau_d)\Big)\,\mathrm{e}^{i(2\mathbf{q}_2-\mathbf{q}_1)\cdot\mathbf{R}} \ \Big\} \\
&\quad +|r_{bc}|^2 \int_{-\infty}^{t_1} \mathrm{d}t_2 \mathrm{e}^{-\frac{t_1-t_2}{T_{2,p(2)}}} \mathrm{e}^{-i\Delta_{ac}(t_1-t_2)} \int_{-\infty}^{t_2} \mathrm{d}t_3 \mathrm{e}^{-\frac{t_2-t_3}{T_{2,p(1)}}} \mathrm{e}^{-i\Delta_{ab}(t_2-t_3)} \times \\
&\qquad \times \Big\{\Big[\mathcal{E}_1^{2}\mathcal{E}_1^{*}A(\mathbf{R},t_1)A(\mathbf{R},t_2)A(\mathbf{R},t_3)+ \\
&\qquad\quad +\mathcal{E}_1\mathcal{E}_2\mathcal{E}_2^{*}A(\mathbf{R},t_1-\tau_d)\left(A(\mathbf{R},t_2)A(\mathbf{R},t_3-\tau_d)+\right. \\
&\qquad\qquad\qquad \left.+A(\mathbf{R},t_2-\tau_d)A(\mathbf{R},t_3)\right)\big]\,\mathrm{e}^{i\mathbf{q}_1\cdot\mathbf{R}} \\
&\qquad + \big[\mathcal{E}_1\mathcal{E}_1^{*}\mathcal{E}_2 A(\mathbf{R},t_1)\left(A(\mathbf{R},t_2)A(\mathbf{R},t_3-\tau_d)+A(\mathbf{R},t_2-\tau_d)A(\mathbf{R},t_3)\right) + \\
&\qquad\quad +\mathcal{E}_2^{2}\mathcal{E}_2^{*}A(\mathbf{R},t_1-\tau_d)A(\mathbf{R},t_2-\tau_d)A(\mathbf{R},t_3-\tau_d)\Big]\,\mathrm{e}^{i\mathbf{q}_2\cdot\mathbf{R}}
\end{aligned}
\tag{A.7}
$$

$$
\begin{aligned}
&+\mathcal{E}_1^2\mathcal{E}_2^* A(\mathbf{R},t_1-\tau_d)A(\mathbf{R},t_2)A(\mathbf{R},t_3)\mathrm{e}^{i(2\mathbf{q}_1-\mathbf{q}_2)\cdot\mathbf{R}}\\
&+\mathcal{E}_1^*\mathcal{E}_2^2 A(\mathbf{R},t_1)A(\mathbf{R},t_2-\tau_d)A(\mathbf{R},t_3-\tau_d)\mathrm{e}^{i(2\mathbf{q}_2-\mathbf{q}_1)\cdot\mathbf{R}} \;\Big\}\;\Big).
\end{aligned}
$$

The third-order polarization $p_{ab}^{(3)}$ is a sum of two contributions (see first line in Eq. (A.7)), that are visualized in Fig. 6.10. The first summand $2\delta_{ab}n^{(2)}$ reflects an upconversion of the second-order population grating $n^{(2)}$ with an excitation photon δ_{ab} inducing a polarization between levels $|a\rangle$ and $|b\rangle$. This contribution is thus proportional to $r_{ab}|r_{ab}|^2$. The second summand $\delta_{bc}^*p^{(2)}$ is a downconversion of the second-order second-harmonic polarization $p^{(2)}$ with a deexcitation photon δ_{bc}^* inducing a polarization between levels $|c\rangle$ and $|b\rangle$. This photon sequence is therefore proportional to $r_{ab}|r_{bc}|^2$.

$p_{ab}^{(3)}$ is radiated at the fundamental photon frequency (prefactor $\mathrm{e}^{i\omega t}$) into directions $\mathbf{q}_1$, $\mathbf{q}_2$, $2\mathbf{q}_1-\mathbf{q}_2$, and $2\mathbf{q}_2-\mathbf{q}_1$. Due to the intense first-order $p^{(1)}$ beams at fundamental frequency into $\mathbf{q}_1$ and $\mathbf{q}_2$, the relatively weak third-order signal from $p^{(3)}$ can be observed with less difficulty in the self-diffracted directions $2\mathbf{q}_1-\mathbf{q}_2$ and $2\mathbf{q}_2-\mathbf{q}_1$. Because of its third-order nature, all terms in $p_{ab}^{(3)}$ are proportional to $\mathcal{E}^3$.

A.4.2 Polarization $p_{bc}^{(3)}$

Eq. (4.20) can also be integrated to yield an integral expression for $p_{bc}^{(3)}$

$$
\begin{aligned}
p_{bc}^{(3)}(t) &= \int_{-\infty}^{t} \mathrm{d}t_1 \mathrm{e}^{-\frac{t-t_1}{T_{2,pbc(3)}}}\mathrm{e}^{i\omega_{bc}(t-t_1)}\left(\frac{\delta_{ab}^*(t_1)p^{(2)}(t_1)+\delta_{bc}(t_1)n^{(2)}(t_1)}{i\hbar}\right)\\
&= \mathrm{e}^{i\omega t}\left(\frac{ie^3 r_{bc}|r_{ab}|^2}{\hbar^3}\right)\int_{-\infty}^{t}\mathrm{d}t_1\mathrm{e}^{-\frac{t-t_1}{T_{2,pbc(3)}}}\mathrm{e}^{-i\Delta_{bc}(t-t_1)}\times\\
&\quad\times\left(\int_{-\infty}^{t_1}\mathrm{d}t_2\mathrm{e}^{-\frac{t_1-t_2}{T_{2,p(2)}}}\mathrm{e}^{-i\Delta_{ac}(t_1-t_2)}\int_{-\infty}^{t_2}\mathrm{d}t_3\mathrm{e}^{-\frac{t_2-t_3}{T_{2,p(1)}}}\mathrm{e}^{-i\Delta_{ab}(t_2-t_3)}\times\right.\\
&\qquad\times\Big\{\Big[\mathcal{E}_1^2\mathcal{E}_1^* A(\mathbf{R},t_1)A(\mathbf{R},t_2)A(\mathbf{R},t_3)+\\
&\qquad\qquad+\mathcal{E}_1\mathcal{E}_2\mathcal{E}_2^* A(\mathbf{R},t_1-\tau_d)\left(A(\mathbf{R},t_2)A(\mathbf{R},t_3-\tau_d)+\right.\\
&\qquad\qquad\qquad\left.+A(\mathbf{R},t_2-\tau_d)A(\mathbf{R},t_3)\right)\Big]\mathrm{e}^{i\mathbf{q}_1\cdot\mathbf{R}}\\
&\qquad+\Big[\mathcal{E}_1\mathcal{E}_1^*\mathcal{E}_2 A(\mathbf{R},t_1)\left(A(\mathbf{R},t_2)A(\mathbf{R},t_3-\tau_d)+A(\mathbf{R},t_2-\tau_d)A(\mathbf{R},t_3)\right)+\\
&\qquad\qquad+\mathcal{E}_2^2\mathcal{E}_2^* A(\mathbf{R},t_1-\tau_d)A(\mathbf{R},t_2-\tau_d)A(\mathbf{R},t_3-\tau_d)\Big]\mathrm{e}^{i\mathbf{q}_2\cdot\mathbf{R}}\\
&\qquad+\mathcal{E}_1^2\mathcal{E}_2^* A(\mathbf{R},t_1-\tau_d)A(\mathbf{R},t_2)A(\mathbf{R},t_3)\mathrm{e}^{i(2\mathbf{q}_1-\mathbf{q}_2)\cdot\mathbf{R}}\\
&\qquad+\mathcal{E}_1^*\mathcal{E}_2^2 A(\mathbf{R},t_1)A(\mathbf{R},t_2-\tau_d)A(\mathbf{R},t_3-\tau_d)\mathrm{e}^{i(2\mathbf{q}_2-\mathbf{q}_1)\cdot\mathbf{R}}\;\Big\}\\
&\quad+\int_{-\infty}^{t_1}\mathrm{d}t_2\mathrm{e}^{-\frac{t_1-t_2}{T_{1,n(2)}}}\int_{-\infty}^{t_2}\mathrm{d}t_3\mathrm{e}^{-\frac{t_2-t_3}{T_{2,p(1)}}}\times \qquad\qquad (A.8)\\
&\qquad\times\Big\{\Big[\mathcal{E}_1 A(\mathbf{R},t_1)\left(\mathrm{e}^{i\Delta_{ab}(t_2-t_3)}+\mathrm{e}^{-i\Delta_{ab}(t_2-t_3)}\right)\times\\
&\qquad\qquad\times\left(\mathcal{E}_1\mathcal{E}_1^* A(\mathbf{R},t_2)A(\mathbf{R},t_3)+\mathcal{E}_2\mathcal{E}_2^* A(\mathbf{R},t_2-\tau_d)A(\mathbf{R},t_3-\tau_d)\right)+
\end{aligned}
$$

$$
\begin{aligned}
&+\mathcal{E}_1\mathcal{E}_2\mathcal{E}_2^* A(\mathbf{R},t_1-\tau_d)\Big(\mathrm{e}^{i\Delta_{ab}(t_2-t_3)}A(\mathbf{R},t_2)A(\mathbf{R},t_3-\tau_d)+\\
&\qquad\qquad +\mathrm{e}^{-i\Delta_{ab}(t_2-t_3)}A(\mathbf{R},t_2-\tau_d)A(\mathbf{R},t_3)\Big)\Big]\,\mathrm{e}^{i\mathbf{q}_1\cdot\mathbf{R}}\\
&+\Big[\mathcal{E}_1\mathcal{E}_1^*\mathcal{E}_2 A(\mathbf{R},t_1)\Big(\mathrm{e}^{i\Delta_{ab}(t_2-t_3)}A(\mathbf{R},t_2-\tau_d)A(\mathbf{R},t_3)+\\
&\qquad\qquad\qquad +\mathrm{e}^{-i\Delta_{ab}(t_2-t_3)}A(\mathbf{R},t_2)A(\mathbf{R},t_3-\tau_d)\Big)+\\
&\qquad +\mathcal{E}_2 A(\mathbf{R},t_1-\tau_d)\Big(\mathrm{e}^{i\Delta_{ab}(t_2-t_3)}+\mathrm{e}^{-i\Delta_{ab}(t_2-t_3)}\Big)\times\\
&\qquad\qquad \times\left(\mathcal{E}_1\mathcal{E}_1^* A(\mathbf{R},t_2)A(\mathbf{R},t_3)+\right.\\
&\qquad\qquad\qquad \left.+\mathcal{E}_2\mathcal{E}_2^* A(\mathbf{R},t_2-\tau_d)A(\mathbf{R},t_3-\tau_d)\right)\big]\,\mathrm{e}^{i\mathbf{q}_2\cdot\mathbf{R}}\\
&+\mathcal{E}_1^2\mathcal{E}_2^* A(\mathbf{R},t_1)\Big(\mathrm{e}^{i\Delta_{ab}(t_2-t_3)}A(\mathbf{R},t_2)A(\mathbf{R},t_3-\tau_d)+\\
&\qquad\qquad\qquad +\mathrm{e}^{-i\Delta_{ab}(t_2-t_3)}A(\mathbf{R},t_2-\tau_d)A(\mathbf{R},t_3)\Big)\,\mathrm{e}^{i(2\mathbf{q}_1-\mathbf{q}_2)\cdot\mathbf{R}}\\
&+\mathcal{E}_1^*\mathcal{E}_2^2 A(\mathbf{R},t_1-\tau_d)\Big(\mathrm{e}^{i\Delta_{ab}(t_2-t_3)}A(\mathbf{R},t_2-\tau_d)A(\mathbf{R},t_3)+\\
&\qquad\qquad +\mathrm{e}^{-i\Delta_{ab}(t_2-t_3)}A(\mathbf{R},t_2)A(\mathbf{R},t_3-\tau_d)\Big)\,\mathrm{e}^{i(2\mathbf{q}_2-\mathbf{q}_1)\cdot\mathbf{R}}\ \Big\}\ \Big)\,.
\end{aligned}
$$

Similar to $p_{ab}^{(3)}$, the third-order polarization $p_{ab}^{(3)}$ is a sum of two contributions (see first line in Eq. (A.8)), as shown schematically in Fig. 6.10. The first summand $\delta_{ab}^* p^{(2)}$ is a downconversion of the second-harmonic polarization $p^{(2)}$ with a deexcitation photon δ_{ab}^* inducing a polarization between levels $|a\rangle$ and $|b\rangle$. The second summand $\delta_{bc}n^{(2)}$ reflects an upconversion of the second-order population $n^{(2)}$ with an excitation photon δ_{bc} inducing a polarization between levels $|c\rangle$ and $|b\rangle$. Both photon sequences are thus proportional to $|r_{ab}|^2 r_{bc}$.

Like $p_{ab}^{(3)}$, $p_{bc}^{(3)}$ is radiated at the fundamental photon frequency (prefactor $\mathrm{e}^{i\omega t}$) into directions $\mathbf{q}_1$, $\mathbf{q}_2$, $2\mathbf{q}_1-\mathbf{q}_2$, and $2\mathbf{q}_2-\mathbf{q}_1$. Due to its third-order nature, all terms in $p_{bc}^{(3)}$ are also proportional to $\mathcal{E}^3$.

A.5 Fourth-order polarization

The aim of this appendix is the derivation of an integral expression for the second-harmonic diffracted signal that arises from the fourth-order polarization $p^{(4)}$. In this case four incident and one outgoing optical wave give rise to a five-wave mixing signal, characterized by $p^{(4)}$. This polarization can be calculated by integrating Eq. (4.23), that was derived in Sect. 4.1

$$
\begin{aligned}
p^{(4)}(t) &= \int_{-\infty}^{t}\mathrm{d}t_1\mathrm{e}^{-\frac{t-t_1}{T_{2,p(4)}}}\mathrm{e}^{i\omega_{ac}(t-t_1)}\left(\frac{\delta_{ab}(t_1)p_{bc}^{(3)}(t_1)-\delta_{bc}(t_1)p_{ab}^{(3)}(t_1)}{i\hbar}\right)\\
&= \mathrm{e}^{2i\omega t}\frac{e^4 r_{bc}r_{ab}}{\hbar^4}\int_{-\infty}^{t}\mathrm{d}t_1\mathrm{e}^{-\frac{t-t_1}{T_{2,p(4)}}}\mathrm{e}^{-i\Delta_{ac}(t-t_1)}\times\\
&\quad\times\Bigg[\int_{-\infty}^{t_1}\mathrm{d}t_2\left\{|r_{ab}|^2\mathrm{e}^{-\frac{t_1-t_2}{T_{2,pbc(3)}}}\mathrm{e}^{-i\Delta_{bc}(t_1-t_2)}+|r_{bc}|^2\mathrm{e}^{-\frac{t_1-t_2}{T_{2,pab(3)}}}\mathrm{e}^{-i\Delta_{ab}(t_1-t_2)}\right\}\times
\end{aligned}
$$

$$
\begin{aligned}
&\times \int_{-\infty}^{t_2} \mathrm{d}t_3 \mathrm{e}^{-\frac{t_2-t_3}{T_{2,p(2)}}} \mathrm{e}^{-i\Delta_{ac}(t_2-t_3)} \int_{-\infty}^{t_3} \mathrm{d}t_4 \mathrm{e}^{-\frac{t_3-t_4}{T_{2,p(1)}}} \mathrm{e}^{-i\Delta_{ab}(t_3-t_4)} \times \\
&\quad \times \Big\{ \Big[\mathcal{E}_1^3 \mathcal{E}_1^* A(\mathbf{R},t_1) A(\mathbf{R},t_2) A(\mathbf{R},t_3) A(\mathbf{R},t_4) + \\
&\qquad + \mathcal{E}_1^2 \mathcal{E}_2 \mathcal{E}_2^* A(\mathbf{R},t_1) A(\mathbf{R},t_2-\tau_d) \left(A(\mathbf{R},t_3) A(\mathbf{R},t_4-\tau_d) + \right. \\
&\qquad\qquad\qquad \left. + A(\mathbf{R},t_3-\tau_d) A(\mathbf{R},t_4) \right) + \\
&\qquad + \mathcal{E}_1^2 \mathcal{E}_2 \mathcal{E}_2^* A(\mathbf{R},t_1-\tau_d) A(\mathbf{R},t_2-\tau_d) A(\mathbf{R},t_3) A(\mathbf{R},t_4) \Big] \mathrm{e}^{2i\mathbf{q}_1\cdot\mathbf{R}} \\
&\quad + \Big[\mathcal{E}_1 \mathcal{E}_1^* \mathcal{E}_2^2 A(\mathbf{R},t_1) A(\mathbf{R},t_2) A(\mathbf{R},t_3-\tau_d) A(\mathbf{R},t_4-\tau_d) + \\
&\qquad + \mathcal{E}_1 \mathcal{E}_1^* \mathcal{E}_2^2 A(\mathbf{R},t_1-\tau_d) A(\mathbf{R},t_2) \left(A(\mathbf{R},t_3) A(\mathbf{R},t_4-\tau_d) + \right. \\
&\qquad\qquad\qquad \left. + A(\mathbf{R},t_3-\tau_d) A(\mathbf{R},t_4) \right) + \\
&\qquad + \mathcal{E}_2^3 \mathcal{E}_2^* A(\mathbf{R},t_1-\tau_d) A(\mathbf{R},t_2-\tau_d) A(\mathbf{R},t_3-\tau_d) A(\mathbf{R},t_4-\tau_d) \Big] \mathrm{e}^{2i\mathbf{q}_2\cdot\mathbf{R}} \\
&\quad + \Big[\mathcal{E}_1^2 \mathcal{E}_1^* \mathcal{E}_2 A(\mathbf{R},t_1) A(\mathbf{R},t_2) \left(A(\mathbf{R},t_3) A(\mathbf{R},t_4-\tau_d) + \right. \\
&\qquad\qquad\qquad \left. + A(\mathbf{R},t_3-\tau_d) A(\mathbf{R},t_4) \right) + \\
&\qquad + \mathcal{E}_1 \mathcal{E}_2^2 \mathcal{E}_2^* A(\mathbf{R},t_1) A(\mathbf{R},t_2-\tau_d) A(\mathbf{R},t_3-\tau_d) A(\mathbf{R},t_4-\tau_d) + \\
&\qquad + \mathcal{E}_1^2 \mathcal{E}_1^* \mathcal{E}_2 A(\mathbf{R},t_1-\tau_d) A(\mathbf{R},t_2) A(\mathbf{R},t_3) A(\mathbf{R},t_4) + \\
&\qquad + \mathcal{E}_1 \mathcal{E}_2^2 \mathcal{E}_2^* A(\mathbf{R},t_1-\tau_d) A(\mathbf{R},t_2-\tau_d) \left(A(\mathbf{R},t_3) A(\mathbf{R},t_4-\tau_d) + \right. \\
&\qquad\qquad\qquad \left. + A(\mathbf{R},t_3-\tau_d) A(\mathbf{R},t_4) \right) \Big] \mathrm{e}^{i(\mathbf{q}_1+\mathbf{q}_2)\cdot\mathbf{R}} \\
&\quad + \mathcal{E}_1^3 \mathcal{E}_2^* A(\mathbf{R},t_1) A(\mathbf{R},t_2-\tau_d) A(\mathbf{R},t_3) A(\mathbf{R},t_4) \mathrm{e}^{i(3\mathbf{q}_1-\mathbf{q}_2)\cdot\mathbf{R}} \\
&\quad + \mathcal{E}_1^* \mathcal{E}_2^3 A(\mathbf{R},t_1-\tau_d) A(\mathbf{R},t_2) A(\mathbf{R},t_3-\tau_d) A(\mathbf{R},t_4-\tau_d) \mathrm{e}^{i(3\mathbf{q}_2-\mathbf{q}_1)\cdot\mathbf{R}} \quad \Big\} \\
&+ |r_{ab}|^2 \int_{-\infty}^{t_1} \mathrm{d}t_2 \left\{ \mathrm{e}^{-\frac{t_1-t_2}{T_{2,pbc(3)}}} \mathrm{e}^{-i\Delta_{bc}(t_1-t_2)} + \mathrm{e}^{-\frac{t_1-t_2}{T_{2,pab(3)}}} \mathrm{e}^{-i\Delta_{ab}(t_1-t_2)} \right\} \times \\
&\quad \times \int_{-\infty}^{t_2} \mathrm{d}t_3 \mathrm{e}^{-\frac{t_2-t_3}{T_{1,n(2)}}} \int_{-\infty}^{t_3} \mathrm{d}t_4 \mathrm{e}^{-\frac{t_3-t_4}{T_{2,p(1)}}} \times \qquad\qquad (\mathrm{A.9}) \\
&\quad \times \Big\{ \Big[2\mathcal{E}_1^2 A(\mathbf{R},t_1) A(\mathbf{R},t_2) \left(\mathrm{e}^{i\Delta_{ab}(t_3-t_4)} + \mathrm{e}^{-i\Delta_{ab}(t_3-t_4)} \right) \times \\
&\qquad\qquad \times \left(\mathcal{E}_1 \mathcal{E}_1^* A(\mathbf{R},t_3) A(\mathbf{R},t_4) + \right. \\
&\qquad\qquad\qquad \left. + \mathcal{E}_2 \mathcal{E}_2^* A(\mathbf{R},t_3-\tau_d) A(\mathbf{R},t_4-\tau_d) \right) + \\
&\quad + 2\mathcal{E}_1^2 \mathcal{E}_2 \mathcal{E}_2^* A(\mathbf{R},t_1) A(\mathbf{R},t_2-\tau_d) \Big(\mathrm{e}^{i\Delta_{ab}(t_3-t_4)} A(\mathbf{R},t_3) A(\mathbf{R},t_4-\tau_d) + \\
&\qquad\qquad + \mathrm{e}^{-i\Delta_{ab}(t_3-t_4)} A(\mathbf{R},t_3-\tau_d) A(\mathbf{R},t_4) \Big) + \\
&\quad + 2\mathcal{E}_1^2 \mathcal{E}_2 \mathcal{E}_2^* A(\mathbf{R},t_1-\tau_d) A(\mathbf{R},t_2) \Big(\mathrm{e}^{i\Delta_{ab}(t_3-t_4)} A(\mathbf{R},t_3) A(\mathbf{R},t_4-\tau_d) + \\
&\qquad\qquad + \mathrm{e}^{-i\Delta_{ab}(t_3-t_4)} A(\mathbf{R},t_3-\tau_d) A(\mathbf{R},t_4) \Big) \Big] \mathrm{e}^{i2\mathbf{q}_1\cdot\mathbf{R}} \\
&\quad + \Big[2\mathcal{E}_1 \mathcal{E}_1^* \mathcal{E}_2^2 A(\mathbf{R},t_1) A(\mathbf{R},t_2-\tau_d) \Big(\mathrm{e}^{i\Delta_{ab}(t_3-t_4)} A(\mathbf{R},t_3-\tau_d) A(\mathbf{R},t_4) + \\
&\qquad\qquad + \mathrm{e}^{-i\Delta_{ab}(t_3-t_4)} A(\mathbf{R},t_3) A(\mathbf{R},t_4-\tau_d) \Big) + \\
&\quad + 2\mathcal{E}_1 \mathcal{E}_1^* \mathcal{E}_2^2 A(\mathbf{R},t_1-\tau_d) A(\mathbf{R},t_2) \Big(\mathrm{e}^{i\Delta_{ab}(t_3-t_4)} A(\mathbf{R},t_3-\tau_d) A(\mathbf{R},t_4) + \\
&\qquad\qquad + \mathrm{e}^{-i\Delta_{ab}(t_3-t_4)} A(\mathbf{R},t_3) A(\mathbf{R},t_4-\tau_d) \Big) +
\end{aligned}
$$

$$
\begin{aligned}
&+2\mathcal{E}_2^2 A(\mathbf{R},t_1-\tau_d)A(\mathbf{R},t_2-\tau_d)\Big(\mathrm{e}^{i\Delta_{ab}(t_3-t_4)}+\mathrm{e}^{-i\Delta_{ab}(t_3-t_4)}\Big)\times\\
&\qquad\times\left(\mathcal{E}_1\mathcal{E}_1^* A(\mathbf{R},t_3)A(\mathbf{R},t_4)+\right.\\
&\qquad\quad\left.+\mathcal{E}_2\mathcal{E}_2^* A(\mathbf{R},t_3-\tau_d)A(\mathbf{R},t_4-\tau_d)\right)\Big]\,\mathrm{e}^{2i\mathbf{q}_2\cdot\mathbf{R}}\\
+&\Big[2\mathcal{E}_1^2\mathcal{E}_1^*\mathcal{E}_2 A(\mathbf{R},t_1)A(\mathbf{R},t_2)\Big(\mathrm{e}^{i\Delta_{ab}(t_3-t_4)}A(\mathbf{R},t_3-\tau_d)A(\mathbf{R},t_4)+\\
&\qquad+\mathrm{e}^{-i\Delta_{ab}(t_3-t_4)}A(\mathbf{R},t_3)A(\mathbf{R},t_4-\tau_d)\Big)+\\
&+2\mathcal{E}_1\mathcal{E}_2 A(\mathbf{R},t_1)A(\mathbf{R},t_2-\tau_d)\Big(\mathrm{e}^{i\Delta_{ab}(t_3-t_4)}+\mathrm{e}^{-i\Delta_{ab}(t_3-t_4)}\Big)\times\\
&\qquad\times\left(\mathcal{E}_1\mathcal{E}_1^* A(\mathbf{R},t_3)A(\mathbf{R},t_4)+\right.\\
&\qquad\quad\left.+\mathcal{E}_2\mathcal{E}_2^* A(\mathbf{R},t_3-\tau_d)A(\mathbf{R},t_4-\tau_d)\right)+\\
&+2\mathcal{E}_1\mathcal{E}_2 A(\mathbf{R},t_1-\tau_d)A(\mathbf{R},t_2)\Big(\mathrm{e}^{i\Delta_{ab}(t_3-t_4)}+\mathrm{e}^{-i\Delta_{ab}(t_3-t_4)}\Big)\times\\
&\qquad\times\left(\mathcal{E}_1\mathcal{E}_1^* A(\mathbf{R},t_3)A(\mathbf{R},t_4)+\right.\\
&\qquad\quad\left.+\mathcal{E}_2\mathcal{E}_2^* A(\mathbf{R},t_3-\tau_d)A(\mathbf{R},t_4-\tau_d)\right)+\\
&+2\mathcal{E}_1\mathcal{E}_2^2\mathcal{E}_2^* A(\mathbf{R},t_1-\tau_d)A(\mathbf{R},t_2-\tau_d)\Big(\mathrm{e}^{i\Delta_{ab}(t_3-t_4)}\times\\
&\qquad\qquad\times A(\mathbf{R},t_3)A(\mathbf{R},t_4-\tau_d)+\\
&\qquad+\mathrm{e}^{-i\Delta_{ab}(t_3-t_4)}A(\mathbf{R},t_3-\tau_d)A(\mathbf{R},t_4)\Big)\Big]\,\mathrm{e}^{i(\mathbf{q}_1+\mathbf{q}_2)\cdot\mathbf{R}}\\
+&2\mathcal{E}_1^3\mathcal{E}_2^* A(\mathbf{R},t_1)A(\mathbf{R},t_2)\Big(\mathrm{e}^{i\Delta_{ab}(t_3-t_4)}A(\mathbf{R},t_3)A(\mathbf{R},t_4-\tau_d)+\\
&\qquad+\mathrm{e}^{-i\Delta_{ab}(t_3-t_4)}A(\mathbf{R},t_3-\tau_d)A(\mathbf{R},t_4)\Big)\,\mathrm{e}^{i(3\mathbf{q}_1-\mathbf{q}_2)\cdot\mathbf{R}}\\
+&2\mathcal{E}_1^*\mathcal{E}_2^3 A(\mathbf{R},t_1-\tau_d)A(\mathbf{R},t_2-\tau_d)\Big(\mathrm{e}^{i\Delta_{ab}(t_3-t_4)}A(\mathbf{R},t_3-\tau_d)A(\mathbf{R},t_4)+\\
&\qquad+\mathrm{e}^{-i\Delta_{ab}(t_3-t_4)}A(\mathbf{R},t_3)A(\mathbf{R},t_4-\tau_d)\Big)\,\mathrm{e}^{i(3\mathbf{q}_2-\mathbf{q}_1)\cdot\mathbf{R}}\ \Big\}\ \Big].
\end{aligned}
$$

The fourth-order polarization $p^{(4)}$ is a sum of two contributions (see first line in Eq. (A.9)), shown schematically in Fig. 6.10). The first summand $\delta_{ab}p_{bc}^{(3)}$ corresponds to an interaction of third-order polarization $p_{bc}^{(3)}$ with an excitation photon δ_{ab} inducing a polarization between levels $|a\rangle$ and $|b\rangle$. The second summand $\delta_{bc}p_{ab}^{(3)}$ reflects an upconversion of the third-order polarization $p_{ab}^{(3)}$ with an excitation photon δ_{bc} inducing a polarization between levels $|c\rangle$ and $|b\rangle$.

As a consequence of the prefactor $\mathrm{e}^{2i\omega t}$ on the right side of Eq. (A.9), $p^{(4)}$ radiates at the second-harmonic frequency 2ω. The fourth-order polarization is emitted into the five different directions $2\mathbf{q}_1$, $2\mathbf{q}_2$, $\mathbf{q}_1+\mathbf{q}_2$, $3\mathbf{q}_1-\mathbf{q}_2$, and $3\mathbf{q}_2-\mathbf{q}_1$. Since all terms in $p^{(4)}$ are proportional to $\mathcal{E}^4$, the second-harmonic diffracted signal into the first three directions is dominated by the second-order reflected and sum-frequency polarizations, that are proportional to $\mathcal{E}^2$.

The analytic results of the following two sections and the numerical treatment described in App. B extract all summands of Eq. (A.9) that are radiated into direction $3\mathbf{q}_1-\mathbf{q}_2$. The six terms in Eq. (A.9) into this direction give rise to the six different photon processes A–F that are depicted schematically in Fig. 6.11.

A.6 Polarization $p^{(4)}$ with Dirac delta pulses

The iterative differential equations in Sect. 4.1, or equivalently, the integral equations derived in this appendix for the nonlinear optical polarizations and populations cannot be solved explicitly for any given pulse shape $A(\mathbf{R},t)$. This is a consequence of the multiple nested integrals, in which the integral boundary variables also appear as integration variables of the respective surrounding integral. Therfore a numerical integration is required, which is the topic of App. B. For a qualitative understanding of the second-harmonic diffracted signal, however, we consider in this section a simpler, analytically integrable case of pulses that can be described by Dirac δ-functions in time,

$$A(\mathbf{R},t) = \delta(t). \tag{A.10}$$

This assumption models the case in which the excitation pulses characterized by $A(\mathbf{R},t)$ are very short compared to the relaxation times T_1 and T_2. The component of the nonlinear optical polarization $p^{(4)}$ that is diffracted into the direction $3\mathbf{q}_1-\mathbf{q}_2$ is then given by Eq. (A.9) as

$$\begin{aligned}
p^{(4)}_{3\mathbf{q}_1-\mathbf{q}_2}(t) \;=\;& \mathrm{e}^{2i\omega t}\mathrm{e}^{i(3\mathbf{q}_1-\mathbf{q}_2)\cdot\mathbf{R}}\mathcal{E}_1^3\mathcal{E}_2^*\frac{e^4 r_{bc}r_{ab}}{\hbar^4}\int_{-\infty}^{t}\mathrm{d}t_1\mathrm{e}^{-\frac{t-t_1}{T_{2,p(4)}}}\mathrm{e}^{-i\Delta_{ac}(t-t_1)}\times\\
&\times\Bigg[\int_{-\infty}^{t_1}\mathrm{d}t_2\Bigg\{|r_{ab}|^2\mathrm{e}^{-\frac{t_1-t_2}{T_{2,pbc(3)}}}\mathrm{e}^{-i\Delta_{bc}(t_1-t_2)}+|r_{bc}|^2\mathrm{e}^{-\frac{t_1-t_2}{T_{2,pab(3)}}}\mathrm{e}^{-i\Delta_{ab}(t_1-t_2)}\Bigg\}\times\\
&\quad\times\int_{-\infty}^{t_2}\mathrm{d}t_3\mathrm{e}^{-\frac{t_2-t_3}{T_{2,p(2)}}}\mathrm{e}^{-i\Delta_{ac}(t_2-t_3)}\int_{-\infty}^{t_3}\mathrm{d}t_4\mathrm{e}^{-\frac{t_3-t_4}{T_{2,p(1)}}}\mathrm{e}^{-i\Delta_{ab}(t_3-t_4)}\times\\
&\qquad\times A(\mathbf{R},t_1)A(\mathbf{R},t_2-\tau_d)A(\mathbf{R},t_3)A(\mathbf{R},t_4)\\
&+|r_{ab}|^2\int_{-\infty}^{t_1}\mathrm{d}t_2\Bigg\{\mathrm{e}^{-\frac{t_1-t_2}{T_{2,pbc(3)}}}\mathrm{e}^{-i\Delta_{bc}(t_1-t_2)}+\mathrm{e}^{-\frac{t_1-t_2}{T_{2,pab(3)}}}\mathrm{e}^{-i\Delta_{ab}(t_1-t_2)}\Bigg\}\times\\
&\quad\times\int_{-\infty}^{t_2}\mathrm{d}t_3\mathrm{e}^{-\frac{t_2-t_3}{T_{1,n(2)}}}\int_{-\infty}^{t_3}\mathrm{d}t_4\mathrm{e}^{-\frac{t_3-t_4}{T_{2,p(1)}}}\times\\
&\qquad\times 2A(\mathbf{R},t_1)A(\mathbf{R},t_2)\Big(\mathrm{e}^{i\Delta_{ab}(t_3-t_4)}A(\mathbf{R},t_3)A(\mathbf{R},t_4-\tau_d)+\\
&\qquad\qquad+\mathrm{e}^{-i\Delta_{ab}(t_3-t_4)}A(\mathbf{R},t_3-\tau_d)A(\mathbf{R},t_4)\Big)\Bigg]\\
=\;& \mathrm{e}^{2i\omega t}\mathrm{e}^{i(3\mathbf{q}_1-\mathbf{q}_2)\cdot\mathbf{R}}\mathcal{E}_1^3\mathcal{E}_2^*\frac{e^4 r_{bc}r_{ab}}{\hbar^4}\int_{-\infty}^{t}\mathrm{d}t_1\mathrm{e}^{-\frac{t-t_1}{T_{2,p(4)}}}\mathrm{e}^{-i\Delta_{ac}(t-t_1)}\times\\
&\times\Bigg[\int_{-\infty}^{t_1}\mathrm{d}t_2\Bigg\{|r_{ab}|^2\mathrm{e}^{-\frac{t_1-t_2}{T_{2,pbc(3)}}}\mathrm{e}^{-i\Delta_{bc}(t_1-t_2)}+|r_{bc}|^2\mathrm{e}^{-\frac{t_1-t_2}{T_{2,pab(3)}}}\mathrm{e}^{-i\Delta_{ab}(t_1-t_2)}\Bigg\}\times\\
&\quad\times\mathrm{e}^{-\frac{t_2}{T_{2,p(2)}}}\mathrm{e}^{-i\Delta_{ac}t_2}\Theta(t_2)\Theta(0)A(\mathbf{R},t_1)A(\mathbf{R},t_2-\tau_d)\\
&+|r_{ab}|^2\int_{-\infty}^{t_1}\mathrm{d}t_2\Bigg\{\mathrm{e}^{-\frac{t_1-t_2}{T_{2,pbc(3)}}}\mathrm{e}^{-i\Delta_{bc}(t_1-t_2)}+\mathrm{e}^{-\frac{t_1-t_2}{T_{2,pab(3)}}}\mathrm{e}^{-i\Delta_{ab}(t_1-t_2)}\Bigg\}\times\\
&\quad\times 2\mathrm{e}^{-i\Delta_{ab}\tau_d}\mathrm{e}^{-\frac{t_2}{T_{1,n(2)}}}A(\mathbf{R},t_1)A(\mathbf{R},t_2)\times
\end{aligned}$$

$$\times \left(\Theta(t_2)\Theta(-\tau_d)\mathrm{e}^{\frac{\tau_d}{T_{2,p(1)}}} + \Theta(t_2-\tau_d)\Theta(\tau_d)\mathrm{e}^{\frac{\tau_d}{T_{1,n(2)}}}\mathrm{e}^{-\frac{\tau_d}{T_{2,p(1)}}}\right)\Bigg]$$

$$\begin{aligned}
= \;& \mathrm{e}^{2i\omega t}\mathrm{e}^{i(3\mathbf{q}_1-\mathbf{q}_2)\cdot\mathbf{R}}\mathcal{E}_1^3\mathcal{E}_2^*\frac{e^4 r_{bc}r_{ab}}{\hbar^4}\int_{-\infty}^{t}\mathrm{d}t_1\mathrm{e}^{-\frac{t-t_1}{T_{2,p(4)}}}\mathrm{e}^{-i\Delta_{ac}(t-t_1)}\times \\
& \times\Bigg[\Bigg\{|r_{ab}|^2\mathrm{e}^{-\frac{t_1-\tau_d}{T_{2,pbc(3)}}}\mathrm{e}^{-i\Delta_{bc}(t_1-\tau_d)} + |r_{bc}|^2\mathrm{e}^{-\frac{t_1-\tau_d}{T_{2,pab(3)}}}\mathrm{e}^{-i\Delta_{ab}(t_1-\tau_d)}\Bigg\}\times \\
& \quad\times\mathrm{e}^{-\frac{\tau_d}{T_{2,p(2)}}}\mathrm{e}^{-i\Delta_{ac}\tau_d}\Theta(t_1-\tau_d)\Theta(\tau_d)\Theta(0)A(\mathbf{R},t_1) \\
& +|r_{ab}|^2\left\{\mathrm{e}^{-\frac{t_1}{T_{2,pbc(3)}}}\mathrm{e}^{-i\Delta_{bc}t_1} + \mathrm{e}^{-\frac{t_1}{T_{2,pab(3)}}}\mathrm{e}^{-i\Delta_{ab}t_1}\right\}\times \\
& \quad\times 2\mathrm{e}^{-i\Delta_{ab}\tau_d}A(\mathbf{R},t_1)\Theta(t_1)\left(\Theta(0)\Theta(-\tau_d)\mathrm{e}^{\frac{\tau_d}{T_{2,p(1)}}} + \Theta(-\tau_d)\Theta(\tau_d)\mathrm{e}^{\frac{\tau_d}{T_{1,n(2)}}}\mathrm{e}^{-\frac{\tau_d}{T_{2,p(1)}}}\right)\Bigg] \\
= \;& \mathrm{e}^{2i\omega t}\mathrm{e}^{i(3\mathbf{q}_1-\mathbf{q}_2)\cdot\mathbf{R}}\mathcal{E}_1^3\mathcal{E}_2^*\frac{e^4 r_{bc}r_{ab}}{\hbar^4}\mathrm{e}^{-\frac{t}{T_{2,p(4)}}}\mathrm{e}^{-i\Delta_{ac}t}\times \\
& \times\Bigg[\Bigg\{|r_{ab}|^2\mathrm{e}^{\frac{\tau_d}{T_{2,pbc(3)}}}\mathrm{e}^{i\Delta_{bc}\tau_d} + |r_{bc}|^2\mathrm{e}^{\frac{\tau_d}{T_{2,pab(3)}}}\mathrm{e}^{i\Delta_{ab}\tau_d}\Bigg\}\times \\
& \quad\times\mathrm{e}^{-\frac{\tau_d}{T_{2,p(2)}}}\mathrm{e}^{-i\Delta_{ac}\tau_d}\Theta(t)\Theta(-\tau_d)\Theta(\tau_d)\Theta(0) \\
& +4|r_{ab}|^2\,\mathrm{e}^{-i\Delta_{ab}\tau_d}\Theta(t)\Theta(0)\left(\Theta(0)\Theta(-\tau_d)\mathrm{e}^{\frac{\tau_d}{T_{2,p(1)}}} + \Theta(-\tau_d)\Theta(\tau_d)\mathrm{e}^{\frac{\tau_d}{T_{1,n(2)}}}\mathrm{e}^{-\frac{\tau_d}{T_{2,p(1)}}}\right)\Bigg] \\
= \;& \mathrm{e}^{i\omega_{ac}t}\mathrm{e}^{-\frac{t}{T_{2,p(4)}}}\mathrm{e}^{i(3\mathbf{q}_1-\mathbf{q}_2)\cdot\mathbf{R}}\mathcal{E}_1^3\mathcal{E}_2^*\frac{e^4}{\hbar^4}r_{bc}r_{ab}|r_{ab}|^2\Theta(t)\Theta(-\tau_d)\mathrm{e}^{-i\Delta_{ab}\tau_d}\mathrm{e}^{\frac{\tau_d}{T_{2,p(1)}}}.
\end{aligned}$$

The result of this calculation for Dirac delta pulses is thus

With $A(\mathbf{R},t)=\delta(t)$:

$$\begin{aligned}
p^{(4)}_{3\mathbf{q}_1-\mathbf{q}_2}(t) \;=\;& \mathrm{e}^{i\omega_{ac}t}\mathrm{e}^{-\frac{t}{T_{2,p(4)}}}\Theta(t)\Theta(-\tau_d)\mathrm{e}^{-i\Delta_{ab}\tau_d}\mathrm{e}^{\frac{\tau_d}{T_{2,p(1)}}}\times \\
& \times\mathrm{e}^{i(3\mathbf{q}_1-\mathbf{q}_2)\cdot\mathbf{R}}\mathcal{E}_1^3\mathcal{E}_2^*\frac{e^4}{\hbar^4}r_{bc}r_{ab}|r_{ab}|^2. \qquad \text{(A.11)}
\end{aligned}$$

The time dependence of $p^{(4)}_{3\mathbf{q}_1-\mathbf{q}_2}$ shows in the first three factors of Eq. (A.11). The polarization radiates with frequency ω_{ac} between the lowest and highest energy level of the three-level system, which can be assumed to be at or near the second-harmonic frequency of the incident photons in case of finite pulse widths. $p^{(4)}_{3\mathbf{q}_1-\mathbf{q}_2}$ is zero for negative t and decays exponentially for positive t with constant T_2 between levels $|a\rangle$ and $|c\rangle$.

The next three factors display the dependence of the polarization on the time delay between the two contributing pulses $\mathcal{E}_1$ and $\mathcal{E}_2$. As a consequence of the Heaviside step function $\Theta(-\tau_d)$ in Eq. (A.11), the polarization is only non-vanishing, if $\mathcal{E}_2$ precedes

$\mathcal{E}_1$ ($\tau_d < 0$). Since the only photon processes in Fig. 6.11 in which one sort of photons ($\mathcal{E}_1$) succeeds the other sort of photons ($\mathcal{E}_2^*$) are processes B and D, these two sequences are the only non-vanishing contributions to $p^{(4)}_{3\mathbf{q}_1-\mathbf{q}_2}$. As in the processes A, C, E, and F, photons of one type ($\mathcal{E}_1$) both precede and succeed one photon of the other type ($\mathcal{E}_2$), these sequences yield zero for Dirac delta pulses.

From the processes B and D in Fig. 6.10 it is also obvious that $p^{(4)}_{3\mathbf{q}_1-\mathbf{q}_2}$ is proportional to both $\mathcal{E}_1^3\mathcal{E}_2^*$ and $r_{ab}|r_{ab}|^2 r_{bc}$.

A.7 Vanishing relaxation times

The complementary case to the preceding section assumes the electric field pulse duration to be very long compared to the relaxation times T_1 and T_2. In this case of vanishing relaxation times, *i.e.* all $T_1, T_2 \rightarrow 0$, the diffracted fourth-order polarization into direction $3\mathbf{q}_1-\mathbf{q}_2$ is given by Eq. (A.9) as

$$
\begin{aligned}
p^{(4)}_{3\mathbf{q}_1-\mathbf{q}_2}(t) \;=\; & \mathrm{e}^{2i\omega t}\mathrm{e}^{i(3\mathbf{q}_1-\mathbf{q}_2)\cdot\mathbf{R}}\mathcal{E}_1^3\mathcal{E}_2^*\frac{e^4 r_{bc} r_{ab}}{\hbar^4}\int_{-\infty}^{t}\mathrm{d}t_1\mathrm{e}^{-\frac{t-t_1}{T_{2,p(4)}}}\mathrm{e}^{-i\Delta_{ac}(t-t_1)}\times \\
& \times\left[\int_{-\infty}^{t_1}\mathrm{d}t_2\left\{|r_{ab}|^2\mathrm{e}^{-\frac{t_1-t_2}{T_{2,pbc(3)}}}\mathrm{e}^{-i\Delta_{bc}(t_1-t_2)}+|r_{bc}|^2\mathrm{e}^{-\frac{t_1-t_2}{T_{2,pab(3)}}}\mathrm{e}^{-i\Delta_{ab}(t_1-t_2)}\right\}\times\right. \\
& \quad\times\int_{-\infty}^{t_2}\mathrm{d}t_3\mathrm{e}^{-\frac{t_2-t_3}{T_{2,p(2)}}}\mathrm{e}^{-i\Delta_{ac}(t_2-t_3)}\int_{-\infty}^{t_3}\mathrm{d}t_4\mathrm{e}^{-\frac{t_3-t_4}{T_{2,p(1)}}}\mathrm{e}^{-i\Delta_{ab}(t_3-t_4)}\times \\
& \quad\quad\times A(\mathbf{R},t_1)A(\mathbf{R},t_2-\tau_d)A(\mathbf{R},t_3)A(\mathbf{R},t_4) \\
& +|r_{ab}|^2\int_{-\infty}^{t_1}\mathrm{d}t_2\left\{\mathrm{e}^{-\frac{t_1-t_2}{T_{2,pbc(3)}}}\mathrm{e}^{-i\Delta_{bc}(t_1-t_2)}+\mathrm{e}^{-\frac{t_1-t_2}{T_{2,pab(3)}}}\mathrm{e}^{-i\Delta_{ab}(t_1-t_2)}\right\}\times \\
& \quad\times\int_{-\infty}^{t_2}\mathrm{d}t_3\mathrm{e}^{-\frac{t_2-t_3}{T_{1,n(2)}}}\int_{-\infty}^{t_3}\mathrm{d}t_4\mathrm{e}^{-\frac{t_3-t_4}{T_{2,p(1)}}}\times \\
& \quad\quad\times 2A(\mathbf{R},t_1)A(\mathbf{R},t_2)\Big(\mathrm{e}^{i\Delta_{ab}(t_3-t_4)}A(\mathbf{R},t_3)A(\mathbf{R},t_4-\tau_d)+ \\
& \qquad\qquad\left.+\mathrm{e}^{-i\Delta_{ab}(t_3-t_4)}A(\mathbf{R},t_3-\tau_d)A(\mathbf{R},t_4)\Big)\right] \\
\propto\;\; & \mathrm{e}^{2i\omega t}\mathrm{e}^{i(3\mathbf{q}_1-\mathbf{q}_2)\cdot\mathbf{R}}\mathcal{E}_1^3\mathcal{E}_2^*\frac{e^4 r_{bc} r_{ab}}{\hbar^4}\int_{-\infty}^{t}\mathrm{d}t_1\delta(t-t_1)\times \\
& \times\left[\int_{-\infty}^{t_1}\mathrm{d}t_2\left\{|r_{ab}|^2+|r_{bc}|^2\right\}\delta(t_1-t_2)\int_{-\infty}^{t_2}\mathrm{d}t_3\delta(t_2-t_3)\int_{-\infty}^{t_3}\mathrm{d}t_4\delta(t_3-t_4)\times\right. \\
& \quad\times A(\mathbf{R},t_1)A(\mathbf{R},t_2-\tau_d)A(\mathbf{R},t_3)A(\mathbf{R},t_4) \\
& +|r_{ab}|^2\int_{-\infty}^{t_1}\mathrm{d}t_2 2\delta(t_1-t_2)\int_{-\infty}^{t_2}\mathrm{d}t_3\delta(t_2-t_3)\int_{-\infty}^{t_3}\mathrm{d}t_4\delta(t_3-t_4)\times \\
& \quad\left.\times 2A(\mathbf{R},t_1)A(\mathbf{R},t_2)\left(A(\mathbf{R},t_3)A(\mathbf{R},t_4-\tau_d)+A(\mathbf{R},t_3-\tau_d)A(\mathbf{R},t_4)\right)\right] \\
\propto\;\; & \mathrm{e}^{2i\omega t}A(\mathbf{R},t)^3A(\mathbf{R},t-\tau_d)\mathrm{e}^{i(3\mathbf{q}_1-\mathbf{q}_2)\cdot\mathbf{R}}\mathcal{E}_1^3\mathcal{E}_2^*\frac{e^4 r_{bc} r_{ab}}{\hbar^4}\left(9|r_{ab}|^2+|r_{bc}|^2\right).
\end{aligned}
$$

The result for vanishing relaxation times is thus

With all $T_1, T_2 \rightarrow 0$:

$$\begin{aligned} p^{(4)}_{3\mathbf{q}_1-\mathbf{q}_2}(t) &\propto \mathrm{e}^{2i\omega t} A(\mathbf{R},t)^3 A(\mathbf{R},t-\tau_d) \mathrm{e}^{i(3\mathbf{q}_1-\mathbf{q}_2)\cdot\mathbf{R}} \times \\ &\quad \times \mathcal{E}_1^3 \mathcal{E}_2^* \frac{e^4 r_{bc} r_{ab}}{\hbar^4} \left(9|r_{ab}|^2 + |r_{bc}|^2\right). \end{aligned} \tag{A.12}$$

For relaxation times very small compared to the electric field pulse duration, the fourth-order polarization into direction $3\mathbf{q}_1 - \mathbf{q}_2$ is thus proportional to the temporal overlap of one pulse shape to the third power $A(\mathbf{R}, t)^3$ with the other pulse $A(\mathbf{R}, t - \tau_d)$. With this result it is thus possible to calculate the relative widths of the diffracted correlation trace to the sum-frequency cross correlation by using the diffracted intensity

$$\begin{aligned} I^{2\omega}_{3\mathbf{q}_1-\mathbf{q}_2} &\propto \int_{-\infty}^{\infty} \mathrm{d}t |p^{(4)}_{3\mathbf{q}_1-\mathbf{q}_2}(t)|^2 \\ &\propto \int_{-\infty}^{\infty} \mathrm{d}t A(\mathbf{R},t)^6 A(\mathbf{R},t-\tau_d)^2. \end{aligned} \tag{A.13}$$

Assuming a Gaussian pulse shape

$$A(\mathbf{R}, t) = \mathrm{e}^{-(t/t_0)^2} \tag{A.14}$$

results in

$$\begin{aligned} I^{2\omega}_{3\mathbf{q}_1-\mathbf{q}_2} &\propto \int_{-\infty}^{\infty} \mathrm{d}t \mathrm{e}^{-6t^2/t_0^2} \mathrm{e}^{-2(t-\tau_d)^2/t_0^2} \\ &\propto \mathrm{e}^{-\frac{8}{t_0^2}(t-\tau_d/4)^2} \mathrm{e}^{\frac{\tau_d^2}{2t_0^2}} \mathrm{e}^{-\frac{2\tau_d^2}{t_0^2}} \\ &\propto \frac{\sqrt{\pi}}{2\sqrt{2}} t_0 \mathrm{e}^{-\frac{3\tau_d^2}{2t_0^2}}. \end{aligned} \tag{A.15}$$

As the SFG cross correlation intensity for Gaussian pulses is

$$\begin{aligned} I^{2\omega}_{\mathbf{q}_1+\mathbf{q}_2} &\propto \int_{-\infty}^{\infty} \mathrm{d}t \mathrm{e}^{-2t^2/t_0^2} \mathrm{e}^{-2(t-\tau_d)^2/t_0^2} \\ &\propto \mathrm{e}^{-\frac{4}{t_0^2}(t-\tau_d/2)^2} \mathrm{e}^{\frac{\tau_d^2}{t_0^2}} \mathrm{e}^{-\frac{2\tau_d^2}{t_0^2}} \\ &\propto \frac{\sqrt{\pi}}{2} t_0 \mathrm{e}^{-\frac{\tau_d^2}{t_0^2}}, \end{aligned} \tag{A.16}$$

the ratio of the FWHM of the two correlation traces for Gaussian pulses in the case of vanishing relaxation times is

$$\frac{\tau_{1/2,\mathrm{diffr}}}{\tau_{1/2,\mathrm{SFG}}} = \sqrt{2/3} \simeq 0.81650. \tag{A.17}$$

For sech pulses

$$A(\mathbf{R},t) = \operatorname{sech}(t/t_0), \tag{A.18}$$

a numerical treatment yields

$$\frac{\tau_{1/2,\mathrm{diffr}}}{\tau_{1/2,\mathrm{SFG}}} \simeq 0.77425. \tag{A.19}$$

The fact that the correlation trace of the diffracted signal displays a narrower temporal width than the SFG cross correlation is a consequence of the highly nonlinear nature of this signal. The a four-photon absorption process of the diffracted signal corresponds to a convolution of four peaked pulses, whereas in the SFG cross correlation, being a two-photon absorption process, only two pulses are convoluted.

It has to be emphasized, however, that this is only true in the limit of vanishing relaxation times. Finite decay times lead to a broadening of both correlation traces.

Appendix B

Numerical integration of Bloch equations

For a given pulse shape the iterative differential equations (4.28) for the nonlinear optical populations and polarizations can be solved numerically. We start this appendix with a classification of the photon processes that contribute to the fourth order polarization $p^{(4)}$ in direction $3\mathbf{q}_1 - \mathbf{q}_2$ (Sect. B.1). This allows the establishment of one set of differential equations for each photon process, as well as a set of all 6 processes combined (Sect. B.2). The numerical solution of these sets then requires a transformation of the complex variables n and p to real variables, shown in Sect. B.3. Finally, Sect. B.4 describes the numerical procedure that was applied to obtain reliable numerical results.

B.1 Classification of photon processes

From Sect. A.5 it can be seen that the fourth-order signal diffracted into direction $3\mathbf{q}_1 - \mathbf{q}_2$ is composed of 6 photon processes, named A, B, C, D, E, and F, which differ in the temporal order of the 4 incoming photons. In the following figures ⇑ (↓) corresponds to a photon with wavevector $\mathbf{q}_1$ ($\mathbf{q}_2$) and amplitude $\mathcal{E}_1$ ($\mathcal{E}_2^*$).

A)
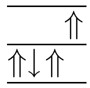

$$\rho^{(0)} \xrightarrow{\mu_{ab}\mathcal{E}_1} p^{(1)} \xrightarrow{\mu_{ab}\mathcal{E}_2^*} n^{(2)} \xrightarrow{\mu_{ab}\mathcal{E}_1} p_{ab}^{(3)} \xrightarrow{\mu_{bc}\mathcal{E}_1} p^{(4)} \tag{B.1}$$

B)
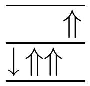

$$\rho^{(0)} \xrightarrow{\mu_{ab}\mathcal{E}_2^*} p^{(1)} \xrightarrow{\mu_{ab}\mathcal{E}_1} n^{(2)} \xrightarrow{\mu_{ab}\mathcal{E}_1} p_{ab}^{(3)} \xrightarrow{\mu_{bc}\mathcal{E}_1} p^{(4)} \tag{B.2}$$

C)
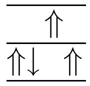

$$\rho^{(0)} \xrightarrow{\mu_{ab}\mathcal{E}_1} p^{(1)} \xrightarrow{\mu_{ab}\mathcal{E}_2^*} n^{(2)} \xrightarrow{\mu_{bc}\mathcal{E}_1} p_{bc}^{(3)} \xrightarrow{\mu_{ab}\mathcal{E}_1} p^{(4)} \tag{B.3}$$

D)
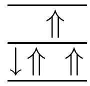

$$\rho^{(0)} \xrightarrow{\mu_{ab}\mathcal{E}_2^*} p^{(1)} \xrightarrow{\mu_{ab}\mathcal{E}_1} n^{(2)} \xrightarrow{\mu_{bc}\mathcal{E}_1} p_{bc}^{(3)} \xrightarrow{\mu_{ab}\mathcal{E}_1} p^{(4)} \tag{B.4}$$

E)
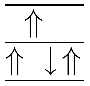

$$\rho^{(0)} \xrightarrow{\mu_{ab}\mathcal{E}_1} p^{(1)} \xrightarrow{\mu_{bc}\mathcal{E}_1} p^{(2)} \xrightarrow{\mu_{ab}\mathcal{E}_2^*} p_{bc}^{(3)} \xrightarrow{\mu_{ab}\mathcal{E}_1} p^{(4)} \tag{B.5}$$

F)
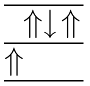

$$\rho^{(0)} \xrightarrow{\mu_{ab}\mathcal{E}_1} p^{(1)} \xrightarrow{\mu_{bc}\mathcal{E}_1} p^{(2)} \xrightarrow{\mu_{bc}\mathcal{E}_2^*} p_{ab}^{(3)} \xrightarrow{\mu_{bc}\mathcal{E}_1} p^{(4)} \tag{B.6}$$

A schematic representation of the consecutive buildup of nonlinear polarization and population from the unperturbed ground state up to the fourth-order polarization into the self-diffracted direction $3\mathbf{q}_1 - \mathbf{q}_2$ is depicted in Fig. 6.10. The 6 different paths from $\rho^{(0)}$ to $p^{(4)}$ correspond to the 6 photon processes A–F, which are also shown in Fig. 6.11.

B.2 Differential equations

As each photon process corresponds to a set of differential equations for the nonlinear optical polarizations and populations, Eq. (4.28) yields 6 sets (A, B, C, D, E, and F), that are shown in the following, together with the joint set of equations for all processes A–F combined.

A)

$$\begin{aligned}
\dot{\tilde{p}}^{(1)} &= -(i\Delta_{ab} + \Gamma_{2,ab})\tilde{p}^{(1)} - \frac{i\mu_{ab}\mathcal{E}_1}{\hbar} \\
\dot{n}^{(2)} &= -\Gamma_{1,b} n^{(2)} - \frac{i\mu_{ab}\mathcal{E}_2^*}{\hbar}\tilde{p}^{(1)} \\
\dot{\tilde{p}}_{ab}^{(3)} &= -(i\Delta_{ab} + \Gamma_{2,ab})\tilde{p}_{ab}^{(3)} - \frac{2i\mu_{ab}\mathcal{E}_1}{\hbar} n^{(2)} \\
\dot{\tilde{p}}^{(4)} &= -(i\Delta_{ac} + \Gamma_{2,ac})\tilde{p}^{(4)} - \frac{i\mu_{bc}\mathcal{E}_1}{\hbar}\tilde{p}_{ab}^{(3)}.
\end{aligned} \tag{B.7}$$

B)

$$\begin{aligned}
\dot{\tilde{p}}^{(1)} &= -(i\Delta_{ab} + \Gamma_{2,ab})\tilde{p}^{(1)} - \frac{i\mu_{ab}\mathcal{E}_2}{\hbar} \\
\dot{n}^{(2)} &= -\Gamma_{1,b} n^{(2)} + \frac{i\mu_{ab}\mathcal{E}_1}{\hbar}\tilde{p}^{(1)*} \\
\dot{\tilde{p}}_{ab}^{(3)} &= -(i\Delta_{ab} + \Gamma_{2,ab})\tilde{p}_{ab}^{(3)} - \frac{2i\mu_{ab}\mathcal{E}_1}{\hbar} n^{(2)} \\
\dot{\tilde{p}}^{(4)} &= -(i\Delta_{ac} + \Gamma_{2,ac})\tilde{p}^{(4)} - \frac{i\mu_{bc}\mathcal{E}_1}{\hbar}\tilde{p}_{ab}^{(3)}.
\end{aligned} \tag{B.8}$$

C)

$$\begin{aligned}
\dot{\tilde{p}}^{(1)} &= -(i\Delta_{ab}+\Gamma_{2,ab})\tilde{p}^{(1)} - \frac{i\mu_{ab}\mathcal{E}_1}{\hbar}\\
\dot{n}^{(2)} &= -\Gamma_{1,b}n^{(2)} - \frac{i\mu_{ab}\mathcal{E}_2^*}{\hbar}\tilde{p}^{(1)}\\
\dot{\tilde{p}}_{bc}^{(3)} &= -(i\Delta_{bc}+\Gamma_{2,bc})\tilde{p}_{bc}^{(3)} + \frac{i\mu_{bc}\mathcal{E}_1}{\hbar}n^{(2)}\\
\dot{\tilde{p}}^{(4)} &= -(i\Delta_{ac}+\Gamma_{2,ac})\tilde{p}^{(4)} + \frac{i\mu_{ab}\mathcal{E}_1}{\hbar}\tilde{p}_{bc}^{(3)}.
\end{aligned}\tag{B.9}$$

D)

$$\begin{aligned}
\dot{\tilde{p}}^{(1)} &= -(i\Delta_{ab}+\Gamma_{2,ab})\tilde{p}^{(1)} - \frac{i\mu_{ab}\mathcal{E}_2}{\hbar}\\
\dot{n}^{(2)} &= -\Gamma_{1,b}n^{(2)} + \frac{i\mu_{ab}\mathcal{E}_1}{\hbar}\tilde{p}^{(1)*}\\
\dot{\tilde{p}}_{bc}^{(3)} &= -(i\Delta_{bc}+\Gamma_{2,bc})\tilde{p}_{bc}^{(3)} + \frac{i\mu_{bc}\mathcal{E}_1}{\hbar}n^{(2)}\\
\dot{\tilde{p}}^{(4)} &= -(i\Delta_{ac}+\Gamma_{2,ac})\tilde{p}^{(4)} + \frac{i\mu_{ab}\mathcal{E}_1}{\hbar}\tilde{p}_{bc}^{(3)}.
\end{aligned}\tag{B.10}$$

E)

$$\begin{aligned}
\dot{\tilde{p}}^{(1)} &= -(i\Delta_{ab}+\Gamma_{2,ab})\tilde{p}^{(1)} - \frac{i\mu_{ab}\mathcal{E}_1}{\hbar}\\
\dot{\tilde{p}}^{(2)} &= -(i\Delta_{ac}+\Gamma_{2,ac})\tilde{p}^{(2)} - \frac{i\mu_{bc}\mathcal{E}_1}{\hbar}\tilde{p}^{(1)}\\
\dot{\tilde{p}}_{bc}^{(3)} &= -(i\Delta_{bc}+\Gamma_{2,bc})\tilde{p}_{bc}^{(3)} + \frac{i\mu_{ab}\mathcal{E}_2^*}{\hbar}\tilde{p}^{(2)}\\
\dot{\tilde{p}}^{(4)} &= -(i\Delta_{ac}+\Gamma_{2,ac})\tilde{p}^{(4)} + \frac{i\mu_{ab}\mathcal{E}_1}{\hbar}\tilde{p}_{bc}^{(3)}.
\end{aligned}\tag{B.11}$$

F)

$$\begin{aligned}
\dot{\tilde{p}}^{(1)} &= -(i\Delta_{ab}+\Gamma_{2,ab})\tilde{p}^{(1)} - \frac{i\mu_{ab}\mathcal{E}_1}{\hbar}\\
\dot{\tilde{p}}^{(2)} &= -(i\Delta_{ac}+\Gamma_{2,ac})\tilde{p}^{(2)} - \frac{i\mu_{bc}\mathcal{E}_1}{\hbar}\tilde{p}^{(1)}\\
\dot{\tilde{p}}_{ab}^{(3)} &= -(i\Delta_{ab}+\Gamma_{2,ab})\tilde{p}_{ab}^{(3)} - \frac{i\mu_{bc}\mathcal{E}_2^*}{\hbar}\tilde{p}^{(2)}\\
\dot{\tilde{p}}^{(4)} &= -(i\Delta_{ac}+\Gamma_{2,ac})\tilde{p}^{(4)} - \frac{i\mu_{bc}\mathcal{E}_1}{\hbar}\tilde{p}_{ab}^{(3)}.
\end{aligned}\tag{B.12}$$

A combination of all 6 of these processes yields a system of differential equations that describes the integral excitation of the three-level system

$$\boxed{\begin{aligned}
\dot{\tilde{p}}_1^{(1)} &= -(i\Delta_{ab} + \Gamma_{2,ab})\tilde{p}^{(1)} - \frac{i\mu_{ab}\mathcal{E}_1}{\hbar} \\
\dot{\tilde{p}}_2^{(1)} &= -(i\Delta_{ab} + \Gamma_{2,ab})\tilde{p}^{(1)} - \frac{i\mu_{ab}\mathcal{E}_2}{\hbar} \\
\dot{n}^{(2)} &= -\Gamma_{1,b}n^{(2)} - \frac{i\mu_{ab}\mathcal{E}_2^*}{\hbar}\tilde{p}_1^{(1)} + \frac{i\mu_{ab}\mathcal{E}_1}{\hbar}\tilde{p}_2^{(1)*} \\
\dot{\tilde{p}}^{(2)} &= -(i\Delta_{ac} + \Gamma_{2,ac})\tilde{p}^{(2)} - \frac{i\mu_{bc}\mathcal{E}_1}{\hbar}\tilde{p}_1^{(1)} \qquad \text{(B.13)} \\
\dot{\tilde{p}}_{ab}^{(3)} &= -(i\Delta_{ab} + \Gamma_{2,ab})\tilde{p}_{ab}^{(3)} - \frac{2i\mu_{ab}\mathcal{E}_1}{\hbar}n^{(2)} - \frac{i\mu_{bc}\mathcal{E}_2^*}{\hbar}\tilde{p}^{(2)} \\
\dot{\tilde{p}}_{bc}^{(3)} &= -(i\Delta_{bc} + \Gamma_{2,bc})\tilde{p}_{bc}^{(3)} + \frac{i\mu_{bc}\mathcal{E}_1}{\hbar}n^{(2)} + \frac{i\mu_{ab}\mathcal{E}_2^*}{\hbar}\tilde{p}^{(2)} \\
\dot{\tilde{p}}^{(4)} &= -(i\Delta_{ac} + \Gamma_{2,ac})\tilde{p}^{(4)} - \frac{i\mu_{bc}\mathcal{E}_1}{\hbar}\tilde{p}_{ab}^{(3)} + \frac{i\mu_{ab}\mathcal{E}_1}{\hbar}\tilde{p}_{bc}^{(3)}.
\end{aligned}}$$

B.3 Transformation to real variables

The numerical integration of the sets of differential equations for the 6 distinct photon processes and for the complete description of all 6 processes combined requires the transformation of the complex variables p and n to real variables Y, which is presented in this section.

B.3.1 Set of equations A

$$\begin{aligned}
\tilde{p}^{(1)} &= Y_1 + iY_2 \\
\tilde{n}^{(2)} &= Y_3 + iY_4 \\
\tilde{p}_{ab}^{(3)} &= Y_5 + iY_6 \\
\tilde{p}^{(4)} &= Y_7 + iY_8.
\end{aligned} \tag{B.14}$$

$$\begin{aligned}
\dot{Y}_1 &= -\Gamma_{2,ab}Y_1 + \Delta_{ab}Y_2 \\
\dot{Y}_2 &= -\Delta_{ab}Y_1 - \Gamma_{2,ab}Y_2 - \frac{\mu_{ab}\mathcal{E}_1}{\hbar} \\
\dot{Y}_3 &= +\frac{\mu_{ab}\mathcal{E}_2}{\hbar}Y_2 - \Gamma_{1,b}Y_3 \\
\dot{Y}_4 &= -\frac{\mu_{ab}\mathcal{E}_2}{\hbar}Y_1 - \Gamma_{1,b}Y_4 \qquad \text{(B.15)}
\end{aligned}$$

$$
\begin{aligned}
\dot{Y}_5 &= +2\frac{\mu_{ab}\mathcal{E}_1}{\hbar}Y_4 - \Gamma_{2,ab}Y_5 + \Delta_{ab}Y_6 \\
\dot{Y}_6 &= -2\frac{\mu_{ab}\mathcal{E}_1}{\hbar}Y_3 - \Delta_{ab}Y_5 - \Gamma_{2,ab}Y_6 \\
\dot{Y}_7 &= +\frac{\mu_{bc}\mathcal{E}_1}{\hbar}Y_6 - \Gamma_{2,ac}Y_7 + \Delta_{ac}Y_8 \\
\dot{Y}_8 &= -\frac{\mu_{bc}\mathcal{E}_1}{\hbar}Y_5 - \Delta_{ac}Y_7 - \Gamma_{2,ac}Y_8.
\end{aligned}
$$

B.3.2 Set of equations B

$$
\begin{aligned}
\tilde{p}^{(1)} &= Y_1 + iY_2 \\
\tilde{n}^{(2)} &= Y_3 + iY_4 \\
\tilde{p}^{(3)}_{ab} &= Y_5 + iY_6 \\
\tilde{p}^{(4)} &= Y_7 + iY_8.
\end{aligned}
\tag{B.16}
$$

$$
\begin{aligned}
\dot{Y}_1 &= -\Gamma_{2,ab}Y_1 + \Delta_{ab}Y_2 \\
\dot{Y}_2 &= -\Delta_{ab}Y_1 - \Gamma_{2,ab}Y_2 - \frac{\mu_{ab}\mathcal{E}_2}{\hbar} \\
\dot{Y}_3 &= +\frac{\mu_{ab}\mathcal{E}_1}{\hbar}Y_2 - \Gamma_{1,b}Y_3 \\
\dot{Y}_4 &= +\frac{\mu_{ab}\mathcal{E}_1}{\hbar}Y_1 - \Gamma_{1,b}Y_4 \\
\dot{Y}_5 &= +2\frac{\mu_{ab}\mathcal{E}_1}{\hbar}Y_4 - \Gamma_{2,ab}Y_5 + \Delta_{ab}Y_6 \\
\dot{Y}_6 &= -2\frac{\mu_{ab}\mathcal{E}_1}{\hbar}Y_3 - \Delta_{ab}Y_5 - \Gamma_{2,ab}Y_6 \\
\dot{Y}_7 &= +\frac{\mu_{bc}\mathcal{E}_1}{\hbar}Y_6 - \Gamma_{2,ac}Y_7 + \Delta_{ac}Y_8 \\
\dot{Y}_8 &= -\frac{\mu_{bc}\mathcal{E}_1}{\hbar}Y_5 - \Delta_{ac}Y_7 - \Gamma_{2,ac}Y_8.
\end{aligned}
\tag{B.17}
$$

B.3.3 Set of equations C

$$
\begin{aligned}
\tilde{p}^{(1)} &= Y_1 + iY_2 \\
\tilde{n}^{(2)} &= Y_3 + iY_4 \\
\tilde{p}^{(3)}_{bc} &= Y_5 + iY_6 \\
\tilde{p}^{(4)} &= Y_7 + iY_8.
\end{aligned}
\tag{B.18}
$$

$$
\dot{Y}_1 = -\Gamma_{2,ab}Y_1 + \Delta_{ab}Y_2
$$

$$\begin{aligned}
\dot{Y}_2 &= -\Delta_{ab}Y_1 - \Gamma_{2,ab}Y_2 - \frac{\mu_{ab}\mathcal{E}_1}{\hbar} \\
\dot{Y}_3 &= +\frac{\mu_{ab}\mathcal{E}_2}{\hbar}Y_2 - \Gamma_{1,b}Y_3 \\
\dot{Y}_4 &= -\frac{\mu_{ab}\mathcal{E}_2}{\hbar}Y_1 - \Gamma_{1,b}Y_4 \\
\dot{Y}_5 &= -\frac{\mu_{bc}\mathcal{E}_1}{\hbar}Y_4 - \Gamma_{2,bc}Y_5 + \Delta_{bc}Y_6 \\
\dot{Y}_6 &= +\frac{\mu_{bc}\mathcal{E}_1}{\hbar}Y_3 - \Delta_{bc}Y_5 - \Gamma_{2,bc}Y_6 \\
\dot{Y}_7 &= -\frac{\mu_{ab}\mathcal{E}_1}{\hbar}Y_6 - \Gamma_{2,ac}Y_7 + \Delta_{ac}Y_8 \\
\dot{Y}_8 &= +\frac{\mu_{ab}\mathcal{E}_1}{\hbar}Y_5 - \Delta_{ac}Y_7 - \Gamma_{2,ac}Y_8.
\end{aligned} \tag{B.19}$$

B.3.4 Set of equations D

$$\begin{aligned}
\tilde{p}^{(1)} &= Y_1 + iY_2 \\
\tilde{n}^{(2)} &= Y_3 + iY_4 \\
\tilde{p}^{(3)}_{bc} &= Y_5 + iY_6 \\
\tilde{p}^{(4)} &= Y_7 + iY_8.
\end{aligned} \tag{B.20}$$

$$\begin{aligned}
\dot{Y}_1 &= -\Gamma_{2,ab}Y_1 + \Delta_{ab}Y_2 \\
\dot{Y}_2 &= -\Delta_{ab}Y_1 - \Gamma_{2,ab}Y_2 - \frac{\mu_{ab}\mathcal{E}_2}{\hbar} \\
\dot{Y}_3 &= +\frac{\mu_{ab}\mathcal{E}_1}{\hbar}Y_2 - \Gamma_{1,b}Y_3 \\
\dot{Y}_4 &= +\frac{\mu_{ab}\mathcal{E}_1}{\hbar}Y_1 - \Gamma_{1,b}Y_4 \\
\dot{Y}_5 &= -\frac{\mu_{bc}\mathcal{E}_1}{\hbar}Y_4 - \Gamma_{2,bc}Y_5 + \Delta_{bc}Y_6 \\
\dot{Y}_6 &= +\frac{\mu_{bc}\mathcal{E}_1}{\hbar}Y_3 - \Delta_{bc}Y_5 - \Gamma_{2,bc}Y_6 \\
\dot{Y}_7 &= -\frac{\mu_{ab}\mathcal{E}_1}{\hbar}Y_6 - \Gamma_{2,ac}Y_7 + \Delta_{ac}Y_8 \\
\dot{Y}_8 &= +\frac{\mu_{ab}\mathcal{E}_1}{\hbar}Y_5 - \Delta_{ac}Y_7 - \Gamma_{2,ac}Y_8.
\end{aligned} \tag{B.21}$$

B.3.5 Set of equations E

$$\begin{aligned}
\tilde{p}^{(1)} &= Y_1 + iY_2 \\
\tilde{p}^{(2)} &= Y_3 + iY_4
\end{aligned} \tag{B.22}$$

$$\begin{aligned}
\tilde{p}^{(3)}_{bc} &= Y_5 + iY_6 \\
\tilde{p}^{(4)} &= Y_7 + iY_8.
\end{aligned}$$

$$\begin{aligned}
\dot{Y}_1 &= -\Gamma_{2,ab}Y_1 + \Delta_{ab}Y_2 \\
\dot{Y}_2 &= -\Delta_{ab}Y_1 - \Gamma_{2,ab}Y_2 - \frac{\mu_{ab}\mathcal{E}_1}{\hbar} \\
\dot{Y}_3 &= +\frac{\mu_{bc}\mathcal{E}_1}{\hbar}Y_2 - \Gamma_{2,ac}Y_3 + \Delta_{ac}Y_4 \\
\dot{Y}_4 &= -\frac{\mu_{bc}\mathcal{E}_1}{\hbar}Y_1 - \Delta_{ac}Y_3 - \Gamma_{2,ac}Y_4 \\
\dot{Y}_5 &= -\frac{\mu_{ab}\mathcal{E}_2}{\hbar}Y_4 - \Gamma_{2,bc}Y_5 + \Delta_{bc}Y_6 \\
\dot{Y}_6 &= +\frac{\mu_{ab}\mathcal{E}_2}{\hbar}Y_3 - \Delta_{bc}Y_5 - \Gamma_{2,bc}Y_6 \\
\dot{Y}_7 &= -\frac{\mu_{ab}\mathcal{E}_1}{\hbar}Y_6 - \Gamma_{2,ac}Y_7 + \Delta_{ac}Y_8 \\
\dot{Y}_8 &= +\frac{\mu_{ab}\mathcal{E}_1}{\hbar}Y_5 - \Delta_{ac}Y_7 - \Gamma_{2,ac}Y_8.
\end{aligned} \tag{B.23}$$

B.3.6 Set of equations F

$$\begin{aligned}
\tilde{p}^{(1)} &= Y_1 + iY_2 \\
\tilde{p}^{(2)} &= Y_3 + iY_4 \\
\tilde{p}^{(3)}_{ab} &= Y_5 + iY_6 \\
\tilde{p}^{(4)} &= Y_7 + iY_8.
\end{aligned} \tag{B.24}$$

$$\begin{aligned}
\dot{Y}_1 &= -\Gamma_{2,ab}Y_1 + \Delta_{ab}Y_2 \\
\dot{Y}_2 &= -\Delta_{ab}Y_1 - \Gamma_{2,ab}Y_2 - \frac{\mu_{ab}\mathcal{E}_1}{\hbar} \\
\dot{Y}_3 &= +\frac{\mu_{bc}\mathcal{E}_1}{\hbar}Y_2 - \Gamma_{2,ac}Y_3 + \Delta_{ac}Y_4 \\
\dot{Y}_4 &= -\frac{\mu_{bc}\mathcal{E}_1}{\hbar}Y_1 - \Delta_{ac}Y_3 - \Gamma_{2,ac}Y_4 \\
\dot{Y}_5 &= +\frac{\mu_{bc}\mathcal{E}_2}{\hbar}Y_4 - \Gamma_{2,ab}Y_5 + \Delta_{ab}Y_6 \\
\dot{Y}_6 &= -\frac{\mu_{bc}\mathcal{E}_2}{\hbar}Y_3 - \Delta_{ab}Y_5 - \Gamma_{2,ab}Y_6 \\
\dot{Y}_7 &= +\frac{\mu_{bc}\mathcal{E}_1}{\hbar}Y_6 - \Gamma_{2,ac}Y_7 + \Delta_{ac}Y_8 \\
\dot{Y}_8 &= -\frac{\mu_{bc}\mathcal{E}_1}{\hbar}Y_5 - \Delta_{ac}Y_7 - \Gamma_{2,ac}Y_8.
\end{aligned} \tag{B.25}$$

B.3.7 Combined set of equations

$$
\begin{aligned}
\tilde{p}_1^{(1)} &= Y_1 + iY_2 \\
\tilde{p}_2^{(1)} &= Y_3 + iY_4 \\
\tilde{n}^{(2)} &= Y_5 + iY_6 \\
\tilde{p}^{(2)} &= Y_7 + iY_8 \\
\tilde{p}_{ab}^{(3)} &= Y_9 + iY_{10} \\
\tilde{p}_{bc}^{(3)} &= Y_{11} + iY_{12} \\
\tilde{p}^{(4)} &= Y_{13} + iY_{14}.
\end{aligned}
\tag{B.26}
$$

$$
\begin{aligned}
\dot{Y}_1 &= -\Gamma_{2,ab}Y_1 + \Delta_{ab}Y_2 \\
\dot{Y}_2 &= -\Delta_{ab}Y_1 - \Gamma_{2,ab}Y_2 - \frac{\mu_{ab}\mathcal{E}_1}{\hbar} \\
\dot{Y}_3 &= -\Gamma_{2,ab}Y_3 + \Delta_{ab}Y_4 \\
\dot{Y}_4 &= -\Delta_{ab}Y_3 - \Gamma_{2,ab}Y_4 - \frac{\mu_{ab}\mathcal{E}_1}{\hbar} \\
\dot{Y}_5 &= +\frac{\mu_{ab}\mathcal{E}_2}{\hbar}Y_2 + \frac{\mu_{ab}\mathcal{E}_1}{\hbar}Y_4 - \Gamma_{1,b}Y_5 \\
\dot{Y}_6 &= -\frac{\mu_{ab}\mathcal{E}_2}{\hbar}Y_1 + \frac{\mu_{ab}\mathcal{E}_1}{\hbar}Y_3 - \Gamma_{1,b}Y_6 \\
\dot{Y}_7 &= +\frac{\mu_{bc}\mathcal{E}_1}{\hbar}Y_2 - \Gamma_{2,ac}Y_7 + \Delta_{ac}Y_8 \\
\dot{Y}_8 &= -\frac{\mu_{bc}\mathcal{E}_1}{\hbar}Y_1 - \Delta_{ac}Y_7 - \Gamma_{2,ac}Y_8 \\
\dot{Y}_9 &= +2\frac{\mu_{ab}\mathcal{E}_1}{\hbar}Y_6 + \frac{\mu_{bc}\mathcal{E}_2}{\hbar}Y_8 - \Gamma_{2,ab}Y_9 + \Delta_{ab}Y_{10} \\
\dot{Y}_{10} &= -2\frac{\mu_{ab}\mathcal{E}_1}{\hbar}Y_5 - \frac{\mu_{bc}\mathcal{E}_2}{\hbar}Y_7 - \Delta_{ab}Y_9 - \Gamma_{2,ab}Y_{10} \\
\dot{Y}_{11} &= -\frac{\mu_{bc}\mathcal{E}_1}{\hbar}Y_6 - \frac{\mu_{ab}\mathcal{E}_2}{\hbar}Y_8 - \Gamma_{2,bc}Y_{11} + \Delta_{bc}Y_{12} \\
\dot{Y}_{12} &= +\frac{\mu_{bc}\mathcal{E}_1}{\hbar}Y_5 + \frac{\mu_{ab}\mathcal{E}_2}{\hbar}Y_7 - \Delta_{bc}Y_{11} - \Gamma_{2,bc}Y_{12} \\
\dot{Y}_{13} &= +\frac{\mu_{bc}\mathcal{E}_1}{\hbar}Y_{10} - \frac{\mu_{ab}\mathcal{E}_1}{\hbar}Y_{12} - \Gamma_{2,ac}Y_{13} + \Delta_{ac}Y_{14} \\
\dot{Y}_{14} &= -\frac{\mu_{bc}\mathcal{E}_1}{\hbar}Y_9 + \frac{\mu_{ab}\mathcal{E}_1}{\hbar}Y_{11} - \Delta_{ac}Y_{13} - \Gamma_{2,ac}Y_{14}.
\end{aligned}
\tag{B.27}
$$

B.3.8 Time-integrated diffracted intensity

As the measured quantity is the time-integrated diffracted intensity

$$
I_{\mathrm{diff}}^{(4)}(\tau) = \int_{-\infty}^{\infty} |p^{(4)}(t,\tau)|^2 \mathrm{d}t,
\tag{B.28}
$$

we append each set of equations A–F by

$$\dot{Y}_9 = Y_7^2 + Y_8^2, \tag{B.29}$$

and the combined set of equations by

$$\dot{Y}_{15} = Y_{13}^2 + Y_{14}^2. \tag{B.30}$$

The measured time-integrated second-harmonic diffracted intensity is then given directly by $I_{\text{diff}}^{(4)} = Y_9$ and $I_{\text{diff}}^{(4)} = Y_{15}$, respectively.

B.4 Numerical procedure

The general structure of the linear differential equation systems of first-order in the preceding section is given by the initial value problem

$$\dot{\mathbf{Y}}(t) = \mathcal{M}(t)\mathbf{Y}(t) + \mathbf{a}(t), \tag{B.31}$$

with the vectors $\mathbf{Y}(t)$ (solution) and $\mathbf{a}(t)$ (inhomogeneity), the time-dependent matrix $\mathcal{M}(t)$, and the initial condition

$$\mathbf{Y}(t_0) = \mathbf{Y}_0. \tag{B.32}$$

Our calculations made use of the numerical integration package LSODE (Livermore solver for ordinary differential equations, double precision) by employing a routine based on Adam's method [255]. This technique works very efficiently due to the utilization of variable integration step widths.

Our code allowed us to calculate the SH diffracted intensity for both the two-beam self-diffraction setup and the three-beam geometry within the framework of inhomogeneous broadening. Due to the numerical complexity of the continuum model (see Chap. 6), that requires a set of at least 1000 differential equations to describe the coherent coupling between the interacting three-level systems, and thus demands substantial computing resources, this approach was not implemented by us. A simulation of the two-beam setup within the continuum framework was, however, provided by Reichelt and Meier (see Sect. 6.3) [254].

We could either choose one of the 6 different pulse sequences (see Sect. B.1) as well as the integrated set by a coherent summation over all 6 sequences combined. The optical pulse type could be chosen Gaussian or sech^2 and the input parameters included the durations of the various pulses, the respective time delays, as well as the energy detuning of the optical pulses with respect to the system transition energies. In order to simulate inhomogeneous broadening, we could also coherently sum over a range of both detunings. The electronic system parameters in the equations included the coupling constants μ between levels $|a\rangle$–$|b\rangle$ and $|b\rangle$–$|c\rangle$ (coupling $|a\rangle$–$|c\rangle$ chosen to be zero), the population relaxation times T_1 of levels $|b\rangle$ and $|c\rangle$, and the pure dephasing times T_2^* of all three levels.

The quality and accuracy of the complete numerical code was verified by the reproduction of various well-known results for the third-order polarization in four-wave mixing. Some of the results of the numerical simulation for the fourth-order polarization in *five*-wave mixing are presented in Sect. 4.2.

Bibliography

[1] Y. R. Shen, *The Principles of Nonlinear Optics* (Wiley, New York, 1984).

[2] W. Zinth and W. Kaiser, in *Ultrashort Laser Pulses – Generation and Applications*, Vol. 60 of *Topics in Applied Physics*, 2nd ed., edited by W. Kaiser (Springer-Verlag, Berlin, 1993), pp. 235–274.

[3] J. Shah, *Ultrafast Spectroscopy of Semiconductors and Semiconductor Nanostructures*, Vol. 115 of *Springer Series in Solid-State Sciences*, 2nd ed. (Springer-Verlag, Berlin, 1999).

[4] R. Haight, *Electron dynamics at surfaces*, Surf. Sci. Rep. **21**, 275 (1995).

[5] N. Bloembergen, R. K. Chang, S. S. Jha, and C. H. Lee, *Optical second-harmonic generation in reflection from media with inversion symmetry*, Phys. Rev. **174**, 813 (1968).

[6] Y. R. Shen, *Optical second harmonic generation at interfaces*, Ann. Rev. Phys. Chem. **40**, 327 (1989).

[7] G. A. Reider and T. F. Heinz, in *Photonic Probes of Surfaces*, Vol. 2 of *Electromagnetic Waves: Recent Developments in Research*, edited by P. Halevi (North-Holland, Amsterdam, 1995), Chap. 9, pp. 413–478.

[8] Y. M. Chang, L. Xu, and H. W. K. Tom, *Observation of coherent surface optical phonon oscillations by time-resolved surface second-harmonic generation*, Phys. Rev. Lett. **78**, 4649 (1997).

[9] S. Ogawa, H. Nagano, H. Petek, and A. P. Heberle, *Optical dephasing in Cu(111) measured by interferometric two-photon time-resolved photoemission*, Phys. Rev. Lett. **78**, 1339 (1997).

[10] U. Höfer, I. L. Shumay, C. Reuß, U. Thomann, W. Wallauer, and T. Fauster, *Time-resolved coherent photoelectron spectroscopy of quantized electronic states at metal surfaces*, Science **277**, 1480 (1997).

[11] C. Reuß, I. L. Shumay, U. Thomann, M. Kutschera, M. Weinelt, T. Fauster, and U. Höfer, *Control of dephasing of image-potential states by adsorption of CO on Cu(100)*, Phys. Rev. Lett. **82**, 153 (1999).

[12] P. Guyot-Sionnest, *Coherent processes at surfaces: Free-induction decay and photon echo of the Si-H stretching vibration for H/Si(111)*, Phys. Rev. Lett. **66**, 1489 (1991).

[13] J. C. Owrutsky, J. P. Culver, M. Li, Y. R. Kim, M. J. Sarisky, M. S. Yeganeh, A. G. Yodh, and R. M. Hochstrasser, *Femtosecond coherent transient infrared spectroscopy of CO on Cu(111)*, J. Chem. Phys. **97**, 4421 (1992).

[14] H. Petek, A. P. Heberle, W. Nessler, H. Nagano, S. Kubota, S. Matsunami, N. Moriya, and S. Ogawa, *Optical phase control of coherent electron dynamics in metals*, Phys. Rev. Lett. **79**, 4649 (1997).

[15] *Properties of Silicon*, Vol. 4 of *EMIS Datareviews Series* (INPSEC, The Institution of Electrical Engineers, London, 1988).

[16] J. R. Goldman and J. A. Prybyla, *Ultrafast hot-electron dynamics in silicon*, Semicond. Sci. Technol. **9**, 694 (1994).

[17] J. R. Goldman and J. A. Prybyla, *Ultrafast dynamics of laser-excited electron distributions in silicon*, Phys. Rev. Lett. **72**, 1364 (1994).

[18] B. B. Hu, E. A. de Souza, W. H. Knox, J. E. Cunningham, M. C. Nuss, A. V. Kuznetov, and S. L. Chuang, *Identifying the distinct phases of carrier transport in semiconductors with 10 fs resolution*, Phys. Rev. Lett. **74**, 1689 (1995).

[19] J. von Behren, Y. Kostoulas, K. B. Üçer, and P. M. Fauchet, *The femtosecond optical response of porous, amorphous and crystalline silicon*, J. Non-Cryst. Solids **198–200**, 957 (1996).

[20] J. Zielbauer and M. Wegener, *Ultrafast optical pump THz-probe spectroscopy on silicon*, Appl. Phys. Lett. **68**, 1223 (1996).

[21] J. Bokor, R. Storz, R. R. Freeman, and P. H. Bucksbaum, *Picosecond surface electron dynamics on photoexcited Si(111)2×1 surfaces*, Phys. Rev. Lett. **57**, 881 (1986).

[22] J. Bokor, *Ultrafast dynamics at semiconductor and metal surfaces*, Science **246**, 1130 (1989).

[23] N. J. Halas and J. Bokor, *Surface recombination on the Si(111)2×1 surface*, Phys. Rev. Lett. **62**, 1679 (1989).

[24] J. P. Long, H. R. Sadeghi, J. C. Rife, and M. N. Kabler, *Surface space-charge dynamics and surface recombination on Silicon (111) surfaces measured with combined laser and synchrotron radiation*, Phys. Rev. Lett. **64**, 1158 (1990).

[25] C. M. Li, Z. C. Ying, T. Sjodin, and H. L. Dai, *Measuring photocarrier diffusivity near a Si(111) surface by reflective two-color transient grating scattering*, Appl. Phys. Lett. **66**, 3501 (1995).

[26] S. Jeong, H. Zacharias, and J. Bokor, *Ultrafast carrier dynamics on the Si(100)2×1 surface*, Phys. Rev. B **54**, R17300 (1996).

[27] C. M. Li, T. Sjodin, Z. C. Ying, and H. L. Dai, *Photoexcited carrier diffusion near a Si(111) surface and in the Si bulk*, Appl. Surf. Sci. **104–105**, 57 (1996).

[28] C. M. Li, T. Sjodin, and H. L. Dai, *Photoexcited carrier diffusion near a Si(111) surface: Non-negligible consequence of carrier–carrier scattering*, Phys. Rev. B **56**, 15252 (1997).

[29] M. Marsi, M. E. Couprie, L. Nahon, D. Garzella, T. Hara, R. Bakker, M. Billardon, A. Delboulbé, G. Indlekofer, and A. Taleb-Ibrahimi, *Surface states and space charge layer dynamics on Si(111)2×1: A free electron laser–synchrotron radiation study*, Appl. Phys. Lett. **70**, 895 (1997).

[30] M. W. Rowe, H. Liu, G. P. Williams, Jr., and R. T. Williams, *Picosecond photoelectron spectroscopy of excited states at Si(111)*$\sqrt{3}\times\sqrt{3}R30^o$*-B, Si(111)7×7, Si(100)2×1, and laser-annealed Si(111)1×1 surfaces*, Phys. Rev. B **47**, 2048 (1993).

[31] T. Sjodin, H. Petek, and H.-L. Dai, *Ultrafast carrier dynamics in silicon: A two-color transient reflection grating study on a (111) surface*, Phys. Rev. Lett. **81**, 5664 (1998).

[32] S. Jeong and J. Bokor, *Ultrafast carrier dynamics near the Si(100)2×1 surface*, Phys. Rev. B **59**, 4943 (1999).

[33] M. V. Fischetti, S. E. Laux, and D. J. DiMaria, *The physics of hot-electron degradation of Si MOSFETs: can we understand it?*, Appl. Surf. Sci. **39**, 578 (1989).

[34] M. V. Fischetti, S. E. Laux, and E. Crabbé, *Understanding hot-electron transport in silicon devices: Is there a shortcut?*, J. Appl. Phys. **78**, 1058 (1995).

[35] D. Haneman, *Surfaces of silicon*, Rep. Prog. Phys. **50**, 1045 (1987).

[36] V. G. Lifshits, A. A. Saranin, and A. V. Zotov, *Surface phases on silicon* (Wiley, Chichester, 1994).

[37] W. Mönch, *Semiconductor surfaces and interfaces*, 2nd ed. (Springer, Berlin, 1995).

[38] R. E. Schlier and H. E. Farnsworth, *Structure and adsorption characteristics of clean surfaces of germanium and silicon*, J. Chem. Phys. **30**, 917 (1959).

[39] K. Takayanagi, Y. Tanishiro, S. Takahashi, and M. Takahashi, *Structure analysis of Si(111)-7×7 reconstructed surface by transmission electron diffraction*, Surf. Sci. **164**, 367 (1985).

[40] G. Binnig, H. Rohrer, C. Gerber, and E. Weibel, *7×7 reconstruction on Si(111) resolved in real space*, Phys. Rev. Lett. **50**, 120 (1983).

[41] R. J. Hamers, R. M. Tromp, and J. E. Demuth, *Surface electronic structure of Si(111)-(7×7) resolved in real space*, Phys. Rev. Lett. **56**, 1972 (1986).

[42] R. J. Hamers, R. M. Tromp, and J. E. Demuth, *Electronic and geometric structure of Si(111)-(7×7) and Si(001) surfaces*, Surf. Sci. **181**, 346 (1987).

[43] R. Erlandsson, L. Olsson, and P. Mårtensson, *Inequivalent atoms and imaging mechanisms in ac-mode atomic-force microscopy of Si(111)7×7*, Phys. Rev. B **54**, R8309 (1996).

[44] T. Uchihashi, Y. Sugawara, T. Tsukamoto, M. Ohta, S. Morita, and M. Suzuki, *Role of a covalent bonding interaction in noncontact-mode atomic-force microscopy on Si(111)7×7*, Phys. Rev. B **56**, 9834 (1997).

[45] N. Nakagiri, M. Suzuki, K. Okiguchi, and H. Sugimura, *Site discrimination of adatoms in Si(111)-7×7 by noncontact atomic force microscopy*, Surf. Sci. **373**, L329 (1997).

[46] I. K. Robinson, W. K. Waskiewicz, P. H. Fuoss, J. B. Stark, and P. A. Bennett, *X-ray diffraction evidence of adatoms in the Si(111)7×7 reconstructed surface*, Phys. Rev. B **33**, 7013 (1986).

[47] R. J. Culbertson, L. C. Feldman, and P. J. Silverman, *Atomic displacements in the Si(111)-(7×7) surface*, Phys. Rev. Lett. **45**, 2043 (1980).

[48] R. M. Tromp, E. J. van Loenen, M. Iwami, and F. W. Saris, *On the structure of the laser irradiated Si(111)-(1×1) surface*, Solid State Commun. **44**, 971 (1982).

[49] R. M. Tromp and E. J. van Loenen, *Ion beam crystallography of silicon surfaces: III. Si(111)-(7×7)*, Surf. Sci. **155**, 441 (1985).

[50] H. Huang, S. Y. Tong, W. E. Packard, and M. B. Webb, *Atomic geometry of Si(111)7×7 by dynamical low-energy electron diffraction*, Phys. Lett. A **130**, 166 (1988).

[51] S. Y. Tong, H. Huang, C. M. Wei, W. E. Packard, F. K. Men, G. Glander, and M. B. Webb, *Low-energy electron diffraction analysis of the Si(111)7×7 structure*, J. Vac. Sci. Technol. A **6**, 615 (1988).

[52] K. Takayanagi, Y. Tanishiro, M. Takahashi, and S. Takahashi, *Structural analysis of Si(111)-7×7 by UHV-transmission electron diffraction and microscopy*, J. Vac. Sci. Technol. A **3**, 1502 (1985).

[53] J. E. Northrup, *Origin of surface states on Si(111)(7×7)*, Phys. Rev. Lett. **57**, 154 (1986).

[54] G.-X. Qian and D. J. Chadi, *Si(111)-7×7 surface: Energy-minimization calculations for the dimer–adatom–stacking-fault model*, Phys. Rev. B **35**, 1288 (1987).

[55] R. D. Meade and D. Vanderbilt, *Adatoms on Si(111) and Ge(111) surfaces*, Phys. Rev. B **40**, 3905 (1989).

[56] G. B. Adams and O. F. Sankey, *Ab initio molecular-dynamical relaxation applied to the silicon(111)-5×5 surface reconstruction*, Phys. Rev. Lett. **67**, 867 (1991).

[57] I. Štich, M. C. Payne, R. D. King-Smith, J.-S. Lin, and L. J. Clarke, *Ab initio total-energy calculations for extremely large systems: Application to the Takayanagi reconstruction of Si(111)*, Phys. Rev. Lett. **68**, 1351 (1992).

[58] K. D. Brommer, M. Needels, B. E. Larson, and J. D. Joannopoulos, *Ab initio theory of the Si(111)-(7×7) surface reconstruction: A challenge for massively parallel computation*, Phys. Rev. Lett. **68**, 1355 (1992).

[59] K. D. Brommer, B. E. Larson, M. Needels, and J. D. Joannopoulos, *Modeling large surface reconstructions on the Connection Machine*, Jpn. J. Appl. Phys. (Part 1) **32**, 1360 (1993).

[60] K. D. Brommer, M. Galván, A. Dal Pino, Jr., and J. D. Joannopoulos, *Theory of adsorption of atoms and molecules on Si(111)-(7×7)*, Surf. Sci. **314**, 57 (1994).

[61] J. Kim, M.-L. Yeh, F. S. Kahn, and J. W. Wilkins, *Surface phonons of the Si(111)-7×7 reconstructed surface*, Phys. Rev. B **52**, 14709 (1995).

[62] H. Lim, K. Cho, I. Park, J. D. Joannopoulos, and E. Kaxiras, *Ab initio study of hydrogen adsorption on the Si(111)-(7×7) surface*, Phys. Rev. B **52**, 17231 (1995).

[63] C. Noguez, A. I. Shkrebtii, and R. Del Sole, *Microscopic theory of electron transitions at Si(111)7×7: Optical properties and energy-loss spectra*, Surf. Sci. **331–333**, 1349 (1995).

[64] I. Štich, K. Terakura, and B. E. Larson, *First-principles finite-temperature characterization of dynamics of the Si(111)-7×7*, Phys. Rev. Lett. **74**, 4491 (1995).

[65] I. Štich, J. Kohanoff, and K. Terakura, *Low-temperature atomic dynamics of the Si(111)-7×7*, Phys. Rev. B **54**, 2642 (1996).

[66] D. R. Alfonso, C. Noguez, D. A. Drabold, and S. E. Ulloa, *First-principles studies of hydrogenated Si(111)-7×7*, Phys. Rev. B **54**, 8028 (1996).

[67] H. Lim, K. Cho, R. B. Capaz, J. D. Joannopoulos, K. D. Brommer, and B. E. Larson, *Ab initio studies of adatom vacancies on the Si(111)-(7×7) surface*, Phys. Rev. B **53**, 15421 (1996).

[68] K. Cho, E. Kaxiras, and J. D. Joannopoulos, *Theory of adsorption and desorption of H_2 molecules on the Si(111)-(7×7) surface*, Phys. Rev. Lett. **79**, 5078 (1997).

[69] S. H. Ke, T. Uda, and K. Terakura, *Surface topography of the Si(111)-7×7 reconstruction*, Phys. Rev. B **62**, 15319 (2000).

[70] T. F. Heinz, in *Nonlinear Surface Electromagnetic Phenomena*, edited by H.-E. Ponath and G. I. Stegeman (North-Holland, Amsterdam, 1991), pp. 353–416.

[71] M. S. Hybertsen and S. G. Louie, *Theory of quasiparticle surface states in semiconductor surfaces*, Phys. Rev. B **38**, 4033 (1988).

[72] K. Hricovini, R. Günther, P. Thiry, A. Taleb-Ibrahimi, G. Indlekofer, J. E. Bonnet, P. Dumas, Y. Petroff, X. Blase, X. Zhu, S. G. Louie, Y. J. Chabal, and P. A. Thiry, *Electronic structure and its dependence on local order for H/Si(111)-(1×1) surfaces*, Phys. Rev. Lett. **70**, 1992 (1993).

[73] P. Mårtensson, W.-X. Ni, G. V. Hansson, J. M. Nicholls, and B. Reihl, *Surface electronic structure of Si(111)7×7-Ge and Si(111)5×5-Ge studied with photoemission and inverse photoemission*, Phys. Rev. B **36**, 5974 (1987).

[74] U. Höfer, *Nonlinear optical investigations of the dynamics of hydrogen interaction with silicon surfaces*, Appl. Phys. A **63**, 533 (1996).

[75] R. I. G. Uhrberg, T. Kaurila, and Y.-C. Chao, *Low-temperature photoemission study of the surface electronic structure of Si(111)7×7*, Phys. Rev. B **58**, R1730 (1998).

[76] F. J. Himpsel, D. E. Eastman, P. Heimann, B. Reihl, C. W. White, and D. M. Zehner, *Electronic structure of annealed Ge(111) and Si(111) surfaces: Similarities in local bonding*, Phys. Rev. B **24**, 1120 (1981).

[77] H. Neddermeyer, U. Misse, and P. Rupieper, *Photoemission study of the surface electronic structure of Si(111)1×1 and Si(111)7×7*, Surf. Sci. **117**, 405 (1982).

[78] J. E. Demuth, B. N. J. Persson, and A. J. Schell-Sorokin, *Temperature-dependent surface states and transitions of Si(111)-7×7*, Phys. Rev. Lett. **51**, 2214 (1983).

[79] R. I. G. Uhrberg, G. V. Hansson, U. O. Karlsson, J. M. Nicholls, P. E. S. Persson, , S. A. Flodström, R. Engelhardt, and E.-E. Koch, *Bulk and surface electronic structures of Si(111)2×1 and Si(111)7×7 studied by angle-resolved photoelectron spectroscopy*, Phys. Rev. B **31**, 3795 (1985).

[80] R. I. G. Uhrberg, G. V. Hansson, J. M. Nicholls, P. E. S. Persson, and S. A. Flodström, *Photoemission study of the surface and bulk electronic structures of Si(111)7×7 and Si(111)*$\sqrt{3} \times \sqrt{3}$*:Al*, Phys. Rev. B **31**, 3805 (1985).

[81] J. E. Demuth, W. J. Thompson, N. J. DiNardo, and R. Imbihl, *Photoemission-based photovoltage probe of semiconductor surface and interface electronic structure*, Phys. Rev. Lett. **56**, 1408 (1986).

[82] G. V. Hansson and R. I. G. Uhrberg, *Photoelectron spectroscopy of surface states on semiconductor surfaces*, Surf. Sci. Rep. **9**, 197 (1988).

[83] R. Losio, K. N. Allmann, and F. J. Himpsel, *Fermi surface of Si(111)7×7*, Phys. Rev. B **61**, 10845 (2000).

[84] T. Fauster and F. J. Himpsel, *Momentum-resolved bremsstrahlung spectroscopy with a tunable photon detector*, J. Vac. Sci. Technol. A **1**, 1111 (1983).

[85] F. J. Himpsel and T. Fauster, *Probing valence states with photoemisssion and inverse photoemission*, J. Vac. Sci. Technol. A **2**, 815 (1984).

[86] J. M. Nicholls and B. Reihl, *Adatom electronic structure of the Si(111)7×7 surface*, Phys. Rev. B **36**, 8071 (1987).

[87] F. J. Himpsel, *Inverse photoemission from semiconductors*, Surf. Sci. Rep. **12**, 1 (1990).

[88] R. M. Tromp, R. J. Hamers, and J. E. Demuth, *Quantum states and atomic structure of silicon surfaces*, Science **234**, 304 (1986).

[89] R. Wolkow and P. Avouris, *Atom-resolved surface chemistry using scanning tunneling microscopy*, Phys. Rev. Lett. **60**, 1049 (1988).

[90] P. Avouris and R. Wolkow, *Atom-resolved surface chemistry studied by scanning tunneling microscopy and spectroscopy*, Phys. Rev. B **39**, 5091 (1989).

[91] J. E. Rowe and H. Ibach, *Surface-state transitions of silicon in electron energy-loss spectra*, Phys. Rev. Lett. **31**, 102 (1973).

[92] U. Backes and H. Ibach, *Evidence for a 2D-metallic state of the clean 7×7 Si(111) surface*, Solid State Commun. **40**, 575 (1981).

[93] J. M. Layet, J. Y. Hoarau, H. Lüth, and J. Derrien, *Dispersion of the dangling-bond surface states of Si(111)-(7×7)*, Phys. Rev. B **30**, 7355 (1984).

[94] B. N. J. Persson and J. E. Demuth, *Inelastic scattering of slow electrons from Si(111) surfaces*, Phys. Rev. B **30**, 5968 (1984).

[95] T. Umeda, M. Nishizawa, T. Yasuda, J. Isoya, S. Yamasaki, and K. Tanaka, *Electron spin resonance observation of the Si(111)-(7×7) surface and its oxidation process*, Phys. Rev. Lett. **86**, 1054 (2001).

[96] F. J. H. G. Hollinger and R. A. Pollack, *Determination of the Fermi-level pinning position at Si(111) surfaces*, Phys. Rev. B **28**, 7014 (1983).

[97] J. Viernow, M. Henzler, W. L. O'Brien, F. K. Men, F. M. Leibsle, D. Y. Petrovykh, J. L. Lin, and F. J. Himpsel, *Unoccupied surface states on Si(111)*$\sqrt{3}\times\sqrt{3}$*-Ag*, Phys. Rev. B **57**, 2321 (1998).

[98] D. Fick, R. Veith, H. D. Ebinger, H. J. Jänsch, C. Weindel, H. Winnefeld, and J. J. Paggel, *Electron correlations in the clean and hydrogen-covered Si(111)-(7×7) surface at extremely low Li coverages*, Phys. Rev. B **60**, 8783 (1999).

[99] S. Heike, S. Watanabe, Y. Wada, and T. Hashizume, *Electron conduction through surface states of the Si(111)-(7×7) surface*, Phys. Rev. Lett. **81**, 890 (1998).

[100] J. J. Lander, *Chemisorption and ordered surface structures*, Surf. Sci. **1**, 125 (1964).

[101] U. Höfer, L. Li, G. A. Ratzlaff, and T. F. Heinz, *Nonlinear optical study of the Si(111)7×7 to 1×1 phase transition: Superheating and the nature of the 1×1 phase*, Phys. Rev. B **52**, 5264 (1995).

[102] R. M. Tromp, R. J. Hamers, and J. E. Demuth, *Si(001) dimer structure observed with scanning tunneling microscopy*, Phys. Rev. Lett. **55**, 1303 (1985).

[103] R. Wolkow, *Direct observation of an increase in buckled dimers on Si(001) at low temperatures*, Phys. Rev. Lett. **68**, 2636 (1992).

[104] D. Badt, H. Wengelnik, and H. Neddermeyer, *Scanning tunneling microscopy at low temperatures on the c(4×2)/(2×1) phase transition of Si(001)*, J. Vac. Sci. Technol. B **12**, 2015 (1994).

[105] H. Okada, Y. Fujimoto, K. Endo, K. Hirose, and Y. Mori, *Detailed analysis of scanning tunneling microscopy images of the Si(001) reconstructed surface with buckled dimers*, Phys. Rev. B **63**, 195324 (2001).

[106] P. C. Weakliem, G. W. Smith, and E. A. Carter, *Subpicosecond interconversion of buckled and symmetric dimers on Si(100)*, Surf. Sci. **232**, L219 (1990).

[107] Z.-H. Huang, J. Gryko, and R. E. Allen, *Kinetics and dynamics on Si(001)*, J. Vac. Sci. Technol. B **9**, 685 (1991).

[108] J. Gryko and R. E. Allen, *Energy surface and dynamics of Si(100)*, J. Vac. Sci. Technol. A **10**, 2052 (1992).

[109] A. I. Shkrebtii, R. D. Felice, C. M. Bertoni, and R. Del Sole, *Ab initio study of structure and dynamics of the Si(100) surface*, Phys. Rev. B **51**, 11201 (1995).

[110] J. Pollmann, P. Krüger, M. Rohlfing, M. Sabisch, and D. Vogel, *Ab initio calculations of structural and electronic properties of prototype surfaces of group IV, III-V and II-VI semiconductors*, Appl. Surf. Sci. **104–105**, 1 (1996).

[111] R. I. G. Uhrberg, G. V. Hansson, J. M. Nichols, and S. A. Flodström, *Experimental studies of the dangling- and dimer-bond-related surface electron bands on Si(100)2×1*, Phys. Rev. B **24**, 4684 (1981).

[112] L. S. O. Johansson, R. I. G. Uhrberg, P. Mårtensson, and G. V. Hansson, *Surface-state band structure of the Si(100)2×1 surface studied with polarization-dependent angle-resolved photoemission on single-domain surfaces*, Phys. Rev. B **42**, 1305 (1990).

[113] L. S. O. Johansson and B. Reihl, *Unoccupied surface-state bands on the single-domain Si(100)2×1 surface*, Surf. Sci. **269–270**, 810 (1992).

[114] Y. Enta, S. Suzuki, and S. Kono, *Angle-resolved-photoemission study of the electronic structure of the Si(001)c4×2 surface*, Phys. Rev. Lett. **65**, 2704 (1990).

[115] J. E. Ortega and F. J. Himpsel, *Inverse-photoemission study of Ge(100), Si(100), and GaAs(100): Bulk bands and surface states*, Phys. Rev. B **47**, 2130 (1993).

[116] H. H. Farrell, F. Stucki, J. Anderson, D. J. Frankel, G. J. Lapeyre, and M. Levinson, *Electronic excitations on Si(100)2×1*, Phys. Rev. B **30**, 721 (1984).

[117] R. J. Hamers and U. K. Köhler, *Determination of the local electronic structure of atomic-sized defects on Si(001) by tunneling spectroscopy*, J. Vac. Sci. Technol. A **7**, 2854 (1989).

[118] A. W. Munz, C. Ziegler, and W. Göpel, *Atomically resolved scanning tunneling spectroscopy on Si(001)-(2×1) asymmetric dimers*, Phys. Rev. Lett. **74**, 2244 (1995).

[119] J. Pollmann, P. Krüger, and A. Mazur, *Self-consistent electronic structure of semi-infinite Si(001)2×1 and Ge(001)2×1 with model calculations for scanning tunneling microscopy*, J. Vac. Sci. Technol. B **5**, 945 (1987).

[120] Z. Zhu, N. Shima, and M. Tsukuda, *Electronic states of Si(100) reconstructed surfaces*, Phys. Rev. B **40**, 11868 (1989).

[121] P. Krüger and J. Pollmann, *Ab initio calculations of Si, As, S, Se, and Cl adsorption on Si(001) surfaces*, Phys. Rev. B **47**, 1898 (1993).

[122] J. E. Northrup, *Electronic structure of Si(100)c(4×2) calculated wihtin the GW approximation*, Phys. Rev. B **47**, 10032 (1993).

[123] G. Li and Y.-C. Chang, *Planar-basis pseudopotential calculations of the Si(001)2×1 surface with and without hydrogen passivation*, Phys. Rev. B **48**, 12032 (1993).

[124] G. Li, Y.-C. Chang, R. Tsu, and J. E. Greene, *Electronic structure of the Si(001)2×1:H surface and pathway for H_2 desorption*, Surf. Sci. **330**, 20 (1995).

[125] P. Kratzer, E. Pehlke, M. Scheffler, M. B. Raschke, and U. Höfer, *Highly site-specific H_2 adsorption on vicinal Si(001) surfaces*, Phys. Rev. Lett. **81**, 5596 (1998).

[126] P. A. Franken, A. E. Hill, C. W. Peters, and G. Weinreich, *Generation of optical harmonics*, Phys. Rev. Lett. **7**, 118 (1961).

[127] N. Bloembergen and P. S. Pershan, *Light waves at the boundary of nonlinear media*, Phys. Rev. **128**, 606 (1962).

[128] F. Brown, R. E. Parks, and A. M. Sleeper, *Nonlinear optical reflection from a metallic boundary*, Phys. Rev. Lett. **14**, 1029 (1965).

[129] Y. R. Shen, *Surfaces probed by second-harmonic and sum-frequency generation*, Nature **337**, 519 (1989).

[130] Y. R. Shen, *Nonlinear optical studies of surfaces*, Appl. Phys. A **59**, 541 (1994).

[131] Y. R. Shen, *Surfaces probed by nonlinear optics*, Surf. Sci. **299**, 551 (1994).

[132] J. Hohlfeld, U. Conrad, and E. Matthias, *Does femtosecond time-resolved second-harmonic generation probe electron temperatures at surfaces?*, Appl. Phys. B **63**, 541 (1996).

[133] M. A. J. Mauerer, *Frequenzverdopplung ultrakurzer Laserimpulse an hochangeregten Siliziumoberflächen und physisorbierten Edelgasschichten*, Doctoral thesis, Technische Universität München, 1996.

[134] G. A. Schmitt, *Untersuchungen der nichtlinearen optischen Eigenschaften von Siliziumoberflächen im nahen Infrarot: Frequenzabhängigkeit und mikroskopische Mechanismen*, Doctoral thesis, Technische Universität München, 1996.

[135] K. Pedersen and P. Morgen, *Dispersion of optical second-harmonic generation from Si(111)7×7*, Phys. Rev. B **52**, R2277 (1995).

[136] K. Pedersen and P. Morgen, *Dispersion of optical second-harmonic generation of Si(111)7×7 during oxygen adsorption*, Phys. Rev. B **53**, 9544 (1996).

[137] K. Pedersen and P. Morgen, *Optical second-harmonic spectroscopy on Si(111)7×7*, Surf. Sci. **377–379**, 393 (1997).

[138] T. Suzuki, D. E. Milovzorov, S. Kogo, M. Tsukakoshi, and M. Aono, *Surface second-harmonic generation spectra of Si(111)7×7 in the 1.0–1.7-eV fundamental photon energy*, Appl. Phys. B **68**, 623 (1999).

[139] T. Suzuki, S. Kogo, M. Tsukakoshi, and M. Aono, *Thermally enhanced second-harmonic generation from Si(111)7×7 and "1×1"*, Phys. Rev. B **59**, 12305 (1999).

[140] T. Suzuki, *Surface-state transitions of Si(111)7×7 probed using nonlinear optical spectroscopy*, Phys. Rev. B **61**, R5117 (2000).

[141] F. Rebentrost, *Second-harmonic generation and effect of adsorbates for free-electron metal and semiconductor surfaces*, Progr. Surf. Sci. **48**, 71 (1995).

[142] S. Hollemann and F. Rebentrost, *Tight-binding model calculations of the nonlinear optical response of free and hydrogenated Si(111) surfaces*, Surf. Sci. **331–333**, 1342 (1995).

[143] V. I. Gavrilenko and F. Rebentrost, *Nonlinear optical susceptibility of the (111) and (001) surfaces of silicon*, Appl. Phys. A **60**, 143 (1995).

[144] V. I. Gavrilenko and F. Rebentrost, *Nonlinear optical susceptibility of the surfaces of silicon and diamond*, Surf. Sci. **331–333**, 1355 (1995).

[145] W. Daum, H.-J. Krause, U. Reichel, and H. Ibach, *Identification of strained silicon layers at Si-SiO_2 interfaces and clean Si surfaces by nonlinear optical spectroscopy*, Phys. Rev. Lett. **71**, 1234 (1993).

[146] U. Höfer, P. Morgen, W. Wurth, and E. Umbach, *Initial stages of oxygen adsorption on Si(111). II. The molecular precursor*, Phys. Rev. B **40**, 1130 (1989).

[147] T. Sakurai, Y. Hasegawa, T. Hashizume, I. Kamiya, T. Ide, I. Sumita, H. W. Pickering, and S. Hyodo, *Atomic hydrogen chemisorption on the Si(111)7× 7 surface*, J. Vac. Sci. Technol. A **8**, 259 (1990).

[148] K. Mortensen, D. M. Chen, P. J. Bedrossian, J. A. Golovchenko, and F. Besenbacher, *Two reaction channels directly observed for atomic hydrogen on the Si(111)-7× 7 surface*, Phys. Rev. B **43**, 1816 (1991).

[149] J. J. Boland, *The driving force behind the chemistry of hydrogen on the Si(111)-7× 7 surface*, J. Vac. Sci. Technol. B **9**, 764 (1991).

[150] J. J. Boland, *The importance of structure and bonding in semiconductor surface chemistry: Hydrogen on the Si(111)-7× 7 surface*, Surf. Sci. **244**, 1 (1991).

[151] J. F. McGilp, M. Cavanagh, J. R. Power, and J. D. O'Mahoney, *Spectroscopic optical second-harmonic generation from semiconductor interfaces*, Appl. Phys. A **59**, 401 (1994).

[152] J. R. Power, J. D. O'Mahony, S. Chandola, and J. F. McGilp, *Resonant optical second harmonic generation at the steps of vicinal Si(001)*, Phys. Rev. Lett. **75**, 1138 (1995).

[153] Z. Xu, X. F. Hu, D. Lim, J. G. Ekerdt, and M. C. Downer, *Second-harmonic spectroscopy of Si(001) surfaces: Sensitivity to surface hydrogen and doping, and applications to kinetic measurements*, J. Vac. Sci. Technol. B **15**, 1059 (1997).

[154] J. I. Dadap, Z. Xu, X. F. Hu, M. C. Downer, N. M. Russell, J. G. Ekerdt, and O. A. Aktsipetrov, *Second-harmonic spectroscopy of a Si(001) surface during calibrated variations in temperature and hydrogen coverage*, Phys. Rev. B **56**, 13367 (1997).

[155] P. S. Parkinson, D. Lim, R. Büngener, J. G. Ekerdt, and M. C. Downer, *Second-harmonic spectroscopy of Ge/Si(001) and* $Si_{1-x}Ge_x$*(001)/Si(001)*, Appl. Phys. B **68**, 641 (1999).

[156] P. T. Wilson, Y. Jiang, O. A. Aktsipetrov, E. D. Mishina, and M. C. Downer, *Frequency-domain interferometric second-harmonic spectroscopy*, Opt. Lett. **24**, 496 (1999).

[157] L. Mantese, K. Selinidis, P. T. Wilson, D. Lim, Y. Y. Jiang, J. G. Ekerdt, and M. C. Downer, *In situ control and monitoring of doped and compositionally graded SiGe films using spectroscopic ellipsometry and second harmonic generation*, Appl. Surf. Sci. **154–155**, 229 (2000).

[158] V. I. Gavrilenko, R. Q. Wu, M. C. Downer, J. G. Ekerdt, D. Lim, and P. Parkinson, *Optical second-harmonic spectra of silicon-adatom surfaces: Theory and experiment*, Thin Solid Films **364**, 1 (2000).

[159] V. I. Gavrilenko, R. Q. Wu, M. C. Downer, J. G. Ekerdt, D. Lim, and P. Parkinson, *Optical second-harmonic spectra of Si(001) with H and Ge adatoms: First-principles theory and experiment*, Phys. Rev. B **63**, 165325 (2001).

[160] B. S. Mendoza, A. Gaggiotti, and R. Del Sole, *Microscopic theory of second harmonic generation at Si(100) surfaces*, Phys. Rev. Lett. **81**, 3781 (1998).

[161] B. S. Mendoza, A. Gaggiotti, and R. Del Sole, *Microscopic theory of second harmonic generation at the Si(100)2×1 surface*, phys. stat. sol. (a) **170**, 343 (1998).

[162] N. Arzate, J. E. Mejía, B. S. Mendoza, and R. Del Sole, *DC-electric-field-modified second-harmonic generation at the Si(100) surface*, Appl. Phys. B **68**, 629 (1999).

[163] D. Lim, M. C. Downer, J. G. Ekerdt, N. Arzate, B. S. Mendoza, V. I. Gavrilenko, and R. Q. White, *Optical second harmonic spectroscopy of boron-reconstructed Si(001)*, Phys. Rev. Lett. **85**, 3406 (2000).

[164] D. Lim, M. C. Downer, and J. G. Ekerdt, *Second-harmonic spectroscopy of bulk boron-doped Si(001)*, Appl. Phys. Lett. **77**, 181 (2000).

[165] N. Arzate and B. S. Mendoza, *Polarizable bond model for optical spectra of Si(001) reconstructed surfaces*, Phys. Rev. B **63**, 113303 (2001).

[166] N. Arzate and B. S. Mendoza, *Microscopic study of surface second-harmonic generation from a clean Si(100)c(4×2) surface*, Phys. Rev. B **63**, 125303 (2001).

[167] B. S. Mendoza, M. Palummo, G. Onida, and R. Del Sole, *Ab initio calculation of second-harmonic-generation at the Si(100) surface*, Phys. Rev. B **63**, 205406 (2001).

[168] M. Rohlfing, (unpublished).

[169] A. M. Weiner, S. De Silvestri, and E. P. Ippen, *Three-pulse scattering for femtosecond dephasing studies: theory and experiment*, J. Opt. Soc. Am. B **2**, 654 (1985).

[170] S. Mukamel and R. F. Loring, *Nonlinear response function for time-domain and frequency-domain four-wave mixing*, J. Opt. Soc. Am. B **3**, 595 (1986).

[171] N. A. Kurnit, I. D. Abella, and S. R. Hartmann, *Observation of a photon echo*, Phys. Rev. Lett. **13**, 567 (1964).

[172] I. D. Abella, N. A. Kurnit, and S. R. Hartmann, *Photon Echoes*, Phys. Rev. **141**, 391 (1966).

[173] S. R. Hartmann, *Photon, Spin, and Raman Echoes*, IEEE J. Quantum Electron. **4**, 802 (1968).

[174] A. Laubereau, in *Ultrashort Laser Pulses – Generation and Applications*, Vol. 60 of *Topics in Applied Physics*, 2nd ed., edited by W. Kaiser (Springer-Verlag, Berlin, 1993), pp. 35–102.

[175] T. Sjodin, C.-M. Li, H. Petek, and H.-L. Dai, *Ultrafast transient grating scattering studies of carrier dynamics at a silicon surface*, Chem. Phys. **251**, 205 (2000).

[176] T. Kikteva, D. Star, A. M. D. Lee, G. W. Leach, and J. M. Papanikolas, *Five wave mixing: Surface-specific transient grating spectroscopy as a probe of low frequency intermolecular adsorbate motion*, Phys. Rev. Lett. **85**, 1906 (2000).

[177] W. T. Berthold, *Zeitaufgelöste Zweiphotonen-Photoemission an Si(111)7×7 mit UV-Pulsen im Femtosekundenbereich*, Diploma thesis, Technische Universität München, 1995.

[178] W. Berthold, M. Mauerer, U. Höfer, B. Kassühlke, and P. Feulner, (unpublished).

[179] P. Bratu, *Optische Frequenzverdopplung an Si(111)7×7: Adsorption, Dissoziation und Desorption von Sauerstoff*, Doctoral thesis, Ludwig-Maximilians-Universität München, 1994.

[180] S. M. Sze, *Physics of Semiconductor Devices*, 2nd ed. (Wiley, New York, 1981).

[181] B. S. Swartzentruber, Y.-W. Mo, M. B. Webb, and M. G. Lagally, *Scanning tunneling microscopy studies of structural disorder*, J. Vac. Sci. Technol. A **7**, 2901 (1989).

[182] T. Brabec, C. Spielmann, and F. Krausz, *Limits of pulse shortening in solitary lasers*, Opt. Lett. **17**, 748 (1993).

[183] M. T. Asaki, C.-P. Huang, D. Garvey, J. Zhou, H. C. Kapteyn, and M. M. Murnane, *Generation of 11-fs pulses from a self-mode-locked Ti:sapphire laser*, Opt. Lett. **18**, 977 (1993).

[184] M. S. Pshenichnikov, W. P. de Boeij, and D. A. Wiersma, *Generation of 13-fs, 5-MW pulses from a cavity-dumped Ti:sapphire laser*, Opt. Lett. **19**, 572 (1994).

[185] J.-C. Diels and W. Rudolph, *Ultrashort Laser Pulse Phenomena: Fundamentals, Techniques, and Applications on a Femtosecond Time Scale* (Academic Press, San Diego, 1996).

[186] T. Meier, *Theorie kohärenter optischer Anregungen in Halbleiter-Heterostrukturen: Vier-Wellen-Mischen und Bloch-Oszillationen*, Doctoral thesis, Philipps-Universität Marburg, 1994.

[187] F. Bloch, *Nuclear induction*, Phys. Rev. **70**, 460 (1946).

[188] R. H. Dicke, *Coherence in spontaneous radiation processes*, Phys. Rev. **93**, 99 (1954).

[189] T. Yajima and Y. Taira, *Spatial optical parametric coupling of picosecond light pulses and transverse relaxation effect in resonant media*, J. Phys. Soc. Jpn. **47**, 1620 (1979).

[190] T. Meier, *Zum Vier-Wellen-Mischen an Halbleiterheterostrukturen mit endlichen Laser-Pulsbreiten*, Diploma thesis, Philipps-Universität Marburg, 1992.

[191] P. Bratu and U. Höfer, *Phonon-assisted sticking of molecular hydrogen on Si(111)-(7×7)*, Phys. Rev. Lett. **74**, 1625 (1995).

[192] G. A. Schmitt, P. Bratu, and U. Höfer, (unpublished).

[193] P. Gupta, C. H. Mak, P. A. Coon, and S. M. George, *Oxidation kinetics of Si(111)7×7 in the submonolayer regime*, Phys. Rev. B **40**, 7739 (1989).

[194] A. Zangwill, *Physics at surfaces* (Cambridge Universtiy Press, Cambridge, 1988).

[195] A. L. Harris and L. Rothberg, *Surface vibrational energy relaxation by sum frequency generation: Five-wave mixing and coherent transients*, J. Chem. Phys. **94**, 2449 (1991).

[196] M. Mauerer, I. L. Shumay, and U. Höfer, (unpublished).

[197] O. L. Alerhand and E. J. Mele, *Surface reconstruction and vibrational excitation of Si(100)*, Phys. Rev. B **35**, 5533 (1987).

[198] T. F. Boggess, A. L. Smirl, and B. S. Wherrett, *Picosecond transient grating measurement of orientational effects in semiconductors*, Opt. Commun. **43**, 128 (1982).

[199] B. S. Wherrett, A. L. Smirl, and T. F. Boggess, *Theory of degenerate four-wave mixing in ps excitation–probe experiments*, IEEE J. Quantum Electron. **19**, 680 (1983).

[200] A. L. Smirl, T. F. Boggess, B. S. Wherrett, G. P. Perryman, and A. Miller, *Picosecond transient orientational and concentration gratings in germanium*, IEEE J. Quantum Electron. **19**, 690 (1983).

[201] R. Buhleier, G. Lüpke, G. Marowsky, Z. Gogolak, and J. Kuhl, *Anisotropic interference of degenerate four-wave mixing in crystalline silicon*, Phys. Rev. B **50**, 2425 (1994).

[202] H. Bergner, V. Brückner, and M. Supianek, *Ultrafast processes in silicon studied by transient gratings*, IEEE J. Quantum Electron. **22**, 1306 (1986).

[203] C. V. Shank, R. Yen, and C. Hirlimann, *Femtosecond-time-resolved surface structural dynamics of optically excited silicon*, Phys. Rev. Lett. **51**, 900 (1993).

[204] H. W. K. Tom, G. D. Aumiller, and C. H. Brito-Cruz, *Time-resolved study of laser-induced disorder of Si surfaces*, Phys. Rev. Lett. **60**, 1438 (1988).

[205] S. V. Govorkov, I. L. Shumay, W. Rudolph, and T. Schröder, *Time-resolved second-harmonic study of femtosecond laser-induced disordering of GaAs surfaces*, Opt. Lett. **16**, 1013 (1991).

[206] P. Saeta, J.-K. Wang, Y. Siegal, N. Bloembergen, and E. Mazur, *Ultrafast electronic disordering during femtosecond laser melting of GaAs*, Phys. Rev. Lett. **67**, 1023 (1991).

[207] K. Sokolowski-Tinten, H. Schulz, J. Bialkowski, , and D. von der Linde, *Two distinct transitions in ultrafast solid–liquid phase transformations of GaAs*, Appl. Phys. A **53**, 227 (1991).

[208] S. V. Govorkov, T. Schröder, I. L. Shumay, and P. Heist, *Transient gratings and second-harmonic probing of the phase transformation of a GaAs surface under femtosecond laser irradiation*, Phys. Rev. B **46**, 6864 (1992).

[209] E. N. Glezer, Y. Siegal, L. Huang, and E. Mazur, *Behavior of $\chi^{(2)}$ during a laser-induced phase transition in GaAs*, Phys. Rev. B **51**, 9589 (1995).

[210] K. Sokolowski-Tinten, J. Bialkowski, and D. von der Linde, *Ultrafast laser-induced order–disorder transitions in semiconductors*, Phys. Rev. B **51**, 14186 (1995).

[211] I. L. Shumay and U. Höfer, *Phase transformations of an InSb surface induced by strong fs-laser pulses*, Phys. Rev. B **54**, 15878 (1996).

[212] H. Kwak, K. C. Chou, J. Guo, and H. W. K. Tom, *Femtosecond laser-induced disorder of the (1×1)-relaxed GaAs(110) surface*, Phys. Rev. Lett. **83**, 3745 (1999).

[213] J. A. Prybyla, H. W. K. Tom, and G. D. Aumiller, *Femtosecond time-resolved surface reaction: Desorption of CO from Cu(111) in $<$ 325 fsec*, Phys. Rev. Lett. **68**, 503 (1992).

[214] J. Hohlfeld, D. Grosenick, U. Conrad, and E. Matthias, *Femtosecond time-resolved reflection second-harmonic generation on polycrystalline copper*, Appl. Phys. A **60**, 137 (1995).

[215] J. Hohlfeld, E. Matthias, R. Knorren, and K. H. Bennemann, *Nonequilibrium magnetization dynamics of nickel*, Phys. Rev. Lett. **78**, 4861 (1997), Erratum: Phys. Rev. Lett. **79**, 960 (1997).

[216] U. Conrad, J. Güdde, V. Jähnke, and E. Matthias, *Ultrafast electron and magnetization dynamics of thin Ni and Co films on Cu(001) observed by time-resolved SHG*, Appl. Phys. B **68**, 511 (1999).

[217] J. Güdde, U. Conrad, V. Jähnke, J. Hohlfeld, and E. Matthias, *Magnetization dynamics of Ni and Co films on Cu(001) and of bulk nickel surfaces*, Phys. Rev. B **59**, R6608 (1999).

[218] J. Hohlfeld, J. Güdde, U. Conrad, O. Dühr, G. Korn, and E. Matthias, *Ultrafast magnetization dynamics of nickel*, Appl. Phys. B **68**, 505 (1999).

[219] J. Hohlfeld, S.-S. Wellershoff, J. Güdde, U. Conrad, V. Jähnke, and E. Matthias, *Electron and lattice dynamics following optical excitation of metals*, Chem. Phys. **251**, 237 (2000).

[220] T. M. Crawford, T. J. Silva, C. W. Teplin, and C. T. Rogers, *Subnanosecond magnetization dynamics measured by the second-harmonic magneto-optic Kerr effect*, Appl. Phys. Lett. **74**, 3386 (1999).

[221] H. Regensburger, R. Vollmer, and J. Kirschner, *Time-resolved magnetization-induced second-harmonic generation from the Ni(110) surface*, Phys. Rev. B **61**, 14716 (2000).

[222] F. Bentivegna, P. Yvernault, A. V. Petukhov, and T. Rasing, *Time-resolved photo-induced nonlinear magneto-optical Kerr efffect for the study of spin dynamics at a GaAs(001) surface*, Appl. Phys. B **68**, 519 (1999).

[223] W. de Jong, A. F. van Etteger, C. A. van 't Hof, P. J. van Hall, and T. Rasing, *Time-resolved optical second-harmonic generation study of the electric field dynamics at a metal–semiconductor interface*, Surf. Sci. **352–354**, 807 (1996).

[224] A. Nahata, T. F. Heinz, and J. A. Misewich, *High-speed electrical sampling using optical second-harmonic generation*, Appl. Phys. Lett. **69**, 746 (1996).

[225] A. Nahata and T. F. Heinz, *Detection of freely propagating terahertz radiation by use of optical second-harmonic generation*, Opt. Lett. **23**, 67 (1998).

[226] Y.-M. Chang, L. Xu, and H. W. K. Tom, *Observation of local-interfacial optical phonons at buried interfaces using time-resolved second-harmonic generation*, Phys. Rev. B **59**, 12220 (1999).

[227] H. W. K. Tom, Y. M. Chang, and H. Kwak, *Coherent phonon and electron spectroscopy on surfaces using time-resolved second-harmonic generation*, Appl. Phys. B **68**, 305 (1999).

[228] Y.-M. Chang, L. Xu, and H. W. K. Tom, *Coherent phonon spectroscopy of GaAs surfaces using time-resolved second-harmonic generation*, Chem. Phys. **251**, 283 (2000).

[229] P. J. van Hall, W. de Jong, A. van Etteger, and T. Rasing, *Coherent plasmon–phonon oscillations in a GaAs Schottky barrier sample*, phys. stat. sol. (b) **204**, 91 (1997).

[230] C. Guo, G. Rodriguez, and A. J. Taylor, *Ultrafast dynamics of electron thermalization in gold*, Phys. Rev. Lett. **86**, 1638 (2001), Erratum: Phys. Rev. Lett. **86**, 3457 (2001).

[231] Y. Siegal, E. N. Glezer, and E. Mazur, *Dielectric constant of GaAs during a subpicosecond laser-induced phase transition*, Phys. Rev. B **49**, 16403 (1994).

[232] U. Höfer, *Time-resolved coherent spectroscopy of surface states*, Appl. Phys. B **68**, 383 (1999).

[233] M. Baeumler and R. Haight, *Ultrafast electron dynamics at the Ge(111)2×1 surface*, Phys. Rev. Lett. **67**, 1153 (1991).

[234] M. Kutschera, M. Weinelt, and T. Fauster, (in preparation).

[235] G. F. Giuliani and J. J. Quinn, *Lifetime of a quasiparticle in a two-dimensional electron gas*, Phys. Rev. B **26**, 4421 (1982).

[236] P. A. Maksym and C. J. Hearn, in *Semiconductors Probed by Ultrafast Laser Spectroscopy*, edited by R. R. Alfano (Academic Press, Orlando, 1984).

[237] J. J. Quinn and R. A. Ferrell, *Electron self-energy approach to correlation in a degenerate electron gas*, Phys. Rev. **112**, 812 (1958).

[238] J. M. Luttinger, *Analytic properties of single-particle propagators for many-fermion systems*, Phys. Rev. **121**, 942 (1961).

[239] A. V. Chaplik, *Energy spectrum and electron scattering processes in inversion layers*, Sov. Phys.–JETP **33**, 997 (1971).

[240] F. Flores, A. L. Yeyati, and J. Ortega, *Metal-insulator transition in the Si(111)-(7×7) surface*, Surf. Rev. Lett. **4**, 281 (1997).

[241] J. Ortega, F. Flores, and A. L. Yeyati, *Electron correlation effects in the Si(111)-7×7 surface*, Phys. Rev. B **58**, 4584 (1998).

[242] J. Ortega, A. L. Yeyati, and F. Flores, *Electron correlation effects in the Si(111)-5×5 and -7×7 surface*, Appl. Surf. Sci. **123–124**, 131 (1998).

[243] R. Atanasov, A. Haché, J. C. P. Hughes, H. M. van Driel, and J. E. Sipe, *Coherent control of photocurrent generation in bulk semiconductors*, Phys. Rev. Lett. **76**, 1703 (1996).

[244] A. Haché, Y. Kostoulas, R. Atanasov, J. L. P. Hughes, J. E. Sipe, and H. M. van Driel, *Observation of coherently controlled photocurrent in unbiased, bulk GaAs*, Phys. Rev. Lett. **78**, 306 (1997).

[245] J. J. Heberle, A. P. Baumberg, and K. Köhler, *Ultrafast coherent control and destruction of excitons in quantum wells*, Phys. Rev. Lett. **75**, 2598 (1995).

[246] W. Niggemeier, G. von Plessen, S. Sauter, and P. Thomas, *Current echoes*, Phys. Rev. Lett. **71**, 770 (1993).

[247] M. Weinelt, C. Reuss, M. Kutschera, U. Thomann, I. L. Shumay, T. Fauster, U. Höfer, F. Theilmann, and A. Goldmann, *Decay and dephasing of image-potential states due to surface defects and disorder*, Appl. Phys. B **68**, 377 (1999).

[248] C. Voelkmann, M. Mauerer, W. Berthold, and U. Höfer, *Second-harmonic diffraction from a transient population grating of silicon dangling bonds*, phys. stat. sol. (a) **175**, 169 (1999).

[249] H. Petek and S. Ogawa, *Femtosecond time-resolved two-photon photoemission studies of electron dynamics in metals*, Progr. Surf. Sci. **56**, 239 (1997).

[250] M. Simon, F. Träger, A. Assion, B. Lang, S. Voll, and G. Gerber, *Femtosecond time-resolved second harmonic generation at the surface of alkali metal clusters*, Chem. Phys. Lett. **296**, 579 (1998).

[251] T. Meier, A. Schulze, P. Thomas, H. Vaupel, and K. Maschke, *Signatures of Fano resonances in four-wave-mixing experiments*, Phys. Rev. B **51**, 13977 (1995).

[252] M. Koch, J. Feldmann, G. von Plessen, E. O. Göbel, P. Thomas, and K. Köhler, *Quantum beats versus polarization interference: An experimental distinction*, Phys. Rev. Lett. **69**, 3631 (1992).

[253] J. J. Yeh and J. H. Eberly, *Irreversibility of energy-conservative dipole dephasing in a simple model*, Phys. Rev. A **22**, 1124 (1980).

[254] M. Reichelt, *Mikroskopische und phänomenologische Beschreibung ausgewählter kohärenter optischer Phänomene in Halbleitern*, Diploma thesis, Philipps-Universität Marburg, 2001.

[255] A. C. Hindmarsh, in *Scientific Computing*, edited by R. S. Stepleman *et al.* (North-Holland, Amsterdam, 1983), pp. 55–64.

Acknowledgements

This thesis would not have been possible without the help of many other people.

First of all, I would like to thank my advisor Prof. Ulrich Höfer not only for the opportunity to set up, conduct, and interpret a fascinating experiment within his group of highly talented individuals, but also for his continuous attention to my work. I profited exceedingly from his scientific knowledge and intuition to discern the experimentally feasible from the unfeasible.

Furthermore, I am obliged to Prof. Karl-Ludwig Kompa for his steady support, that I always could rely on.

I thank Prof. Dietrich Menzel for his interest in my work and his willingness to participate in its evaluation.

An integral part of this thesis was made possible through the intellectually stimulating as well as personally enjoyable interaction with my collegues and friends within our reasearch group: Dr. Wolfram Berthold, Dr. Michael Dürr, Dr. Jens Güdde, Michael Hartmann, Dr. Markus Mauerer, Dr. Markus Raschke, and Dr. Georg Schmitt. Together as a team and also each one of them individually helped to pursue my experiment ranging from in-depth explanations to practical assistance. Thanks to you all.

My understanding of coherent processes has benefitted a lot from discussions with Dr. Torsten Meier and Matthias Reichelt, who were always willing to share their knowlegdeable insight with me.

The pleasant interaction with Dr. Frank Rebentrost and Dr. Jochen Wanner on topics inside and outside physics helped me sophisticate my comprehension of electronic surface states and personal states in hierarchical organizations (, respectively).

The skillful technical assistance that Karl Bauer and Manfred Preis provided for me represents an invaluable part of this work. Together with the people in the machine shops in Garching and in Marburg, they contributed substantially to the efficiency of the experimental progress.

Without the organizational talent of Margot Nagl and Inge Schmidt, the conduction of the day-to-day administrative work would have required much more time and effort.

Many ideas were stimulated by the warm scientific atmosphere of both the Max-Planck-Institut für Quantenoptik in Garching and the physics department of the

Philipps-Universität Marburg. I am indebted to all people in these institutions, who generated such a productive, (research-)friendly environment.

The successful conductance of the work summarized in this thesis has benefitted from the caring guidance of Dr. Vesselinka Petrova-Koch during my initial exposure to experimental physics, and from the introduction to the field of nonlinear optics, that I was fortunate to receive in the group of Prof. Yuen-Ron Shen.

Most of all, I thank my parents for helping me be what I am, and Imke for taking me how I am.

Vita

Carsten Voelkmann

January 25, 1970	Born in Ingolstadt, Germany
1980–89	Christoph-Scheiner-Gymnasium in Ingolstadt, Germany
1989–90	compulsory military service
1990–97	Technische Universität München, Munich, Germany, majoring in physics
1992	”Vordiplom” in physics, Technische Universität München
1996	Diploma thesis at the department of physics, University of California at Berkeley, USA
1997	”Diplom” in physics, Technische Universität München
1997–2001	Doctoral thesis at the Max-Planck-Institut für Quantenoptik, Garching, Germany, at the Technische Universität München, Munich, Germany, and at the Philipps-Universität Marburg, Germany
2001	”Dr. rer. nat.” in physics, Technische Universität München